

OPTICAL PROPERTIES
OF SILICON BASED AMORPHOUS
THIN FILMS

A THESIS SUBMITTED TO
THE GRADUATE SCHOOL OF NATURAL AND APPLIED SCIENCES
OF
MIDDLE EAST TECHNICAL UNIVERSITY

BY

BARIŞ AKAOĞLU

IN PARTIAL FULFILLMENT OF THE REQUIREMENTS
FOR
THE DEGREE OF DOCTOR OF PHILOSOPHY
IN
PHYSICS

SEPTEMBER 2004

Approval of the Graduate School of Natural and Applied Sciences

Prof. Dr. Canan Özgen
Director

I certify that this thesis satisfies all the requirements as a thesis for the degree of Doctor of Philosophy.

Prof. Dr. Sinan Bilikmen
Head of Department

This is to certify that we have read this thesis and that in our opinion it is fully adequate, in scope and quality, as a thesis for the degree of Doctor of Philosophy.

Prof. Dr. Bayram Katircioğlu
Supervisor

Examining Committee Members

Prof. Dr. Şenay Yurdakul	(GÜ, PHYS)	_____
Prof. Dr. Bayram Katircioğlu	(METU, PHYS)	_____
Prof. Dr. Bülent Akınoğlu	(METU, PHYS)	_____
Assoc. Prof. Dr. Serhat Çakır	(METU, PHYS)	_____
Assoc. Prof. Dr. İsmail Atılgan	(METU, PHYS)	_____

I hereby declare that all information in this document has been obtained and presented in accordance with academic rules and ethical conduct. I also declare that, as required by these rules and conduct, I have fully cited and referenced all material and results that are not original to this work.

Name, Last name : Barış Akaoglu

Signature :

ABSTRACT

OPTICAL PROPERTIES OF SILICON BASED AMORPHOUS THIN FILMS

Akaoğlu, Barış

Ph.D., Department of Physics

Supervisor: Prof. Dr. Bayram Katircioğlu

September 2004, 248 pages

Silicon based hydrogenated amorphous semiconducting (intrinsic and n/p doped a-Si:H and a-Si_{1-x}C_x:H) thin films have been deposited by plasma enhanced chemical vapor deposition (PECVD) system. In order to analyze the optical response of these amorphous films, intrinsic optical absorption mechanisms have resumed and spectral variations of absorption coefficient $\alpha(E)$ are derived. The exponential variation of absorption coefficient for energies below the band edge is discussed in the frame of randomly distributed square well like potential fluctuations of localized states. Urbach constant E_U and the slope B are deduced as disorder parameters. Both intensity sensitive transmittance and reflectance, and amplitude/phase sensitive ellipsometric techniques for multilayer thin films are theoretically and practically treated. Various methodologies are developed for the determination of thickness, refractive index and absorption coefficient of the films. A reflectance unit is adapted to the spectrometer and all the measuring instruments are computerized and relevant software packets have been developed. IR spectroscopy has been used for determination of mainly hydrogen concentrations and bonding properties. Establishing the “production-characterization-improved growth conditions” cycle successfully, the following results are obtained: (a) determination of lateral inhomogeneity of films along the radial direction of the plasma reactor, (b) determination of vertical inhomogeneity due to both substrate and air ambient, (c) perfect adjustment of refractive index and band gap of a-Si_{1-x}C_x:H films by changing

carbon content of the films, (d) effect of plasma power density on both growth and carbon content.

Keywords: Amorphous silicon, transmittance, reflectance, ellipsometry, optical constants, inhomogeneity.

ÖZ

SİLİSYUM TABANLI AMORF İNCE FİLMLEİN OPTİK ÖZELLİKLERİ

Akaođlu, Barıř

Doktora, Fizik Bölümü

Tez Yöneticisi: Prof. Dr. Bayram Katırcıođlu

Eylül 2004, 248 sayfa

Plazma destekli kimyasal buhar biriktirme düzeneğinde (PECVD) silisyum tabanlı hidrojenlenmiş amorf yarı iletken (katkılanmamış ve n/p tipi katkılanmış a-Si:H ve a-Si_{1-x}C_x:H) ince filmler büyütülmüştür. Amorf filmlerin optik tepkilerini anlamak için optik sođurma mekanizmaları ele alınmış, ve sođurma katsayısında tayfsal deđişimler ortaya çıkarılmıştır. Bant eteđinin altındaki enerjilerde, sođurma katsayısının üstel deđişimi, yerel durumların geliřigüzel dađılmış kare çukur tipi potansiyel oynamaları çerçevesinde tartışılmıştır. Urbach sabiti ve eđim B düzensizlik parametreleri olarak belirlenmiştir. Çok katmanlı ince filmler için ışık řiddetine hassas olan geçirgenlik ve yansıma ile genlik / faz'a hassas olan ellipsometre teknikleri teorik ve pratik yönlerden ele alınmıştır. Filmlerin kalınlıklarının, kırılma indislerinin ve sođurma katsayılarının belirlenmesi için çeřitli metodlar geliřtirilmiştir. Bir yansıma birimi spektrometreye adapte edilmiş, bütün ölçüm aletleri bilgisayarlaştırılmış ve ilgili yazılım paketleri geliřtirilmiştir. Kızıl ötesi spektrometre esas olarak hidrojen konsantrasyonlarının ve bağlanma özelliklerinin belirlenmesi için kullanılmıştır. 'Üretim-karakterizasyon-büyüme koşullarının iyileřtirilmesi' döngüsü başarı ile kurulmuş ve řu sonuçlar elde edilmiştir: (a) plazma reaktörünün çapı boyunca yanal düzensizlikler gösterdiđinin belirlenmesi, (b) taban ve dıř ortam nedeniyle oluşan dikey düzensizliklerin belirlenmesi, (c) a-Si_{1-x}C_x:H filmlerinin kırılma indisi ve yasak enerji aralıkları

filmlerdeki karbon içeriğinin deęiştirilmesi ile kusursuzca ayarlanabilmesi, (d) plazma güç yoğunluęunun filmlerdeki karbon içeriğini etkileyebilmesi.

Anahtar kelimeler: Amorf silisyum, geçirgenlik, yansıma, elipsometri, optik sabitler, düzensizlik.

TABLE OF CONTENTS

ABSTRACT.....	iv
ÖZ.....	vi
ACKNOWLEDGMENTS.....	viii
TABLE OF CONTENTS.....	x
LIST OF TABLES.....	xvi
LIST OF FIGURES.....	xviii
CHAPTER	
1. INTRODUCTION.....	1
2. INTERACTION OF LIGHT WITH AMORPHOUS MATERIALS.....	5
2.1 Introduction.....	5
2.2 Optical absorption in crystals.....	6
2.2.1 Motion of Electrons in an Electromagnetic Field in the Frame of Quantum Mechanics.....	7
2.2.2 Time Dependent Perturbation Approach.....	9
2.2.3 Interband Transitions.....	10
2.2.4 Electric-Dipole Approximation.....	12
2.2.5 Connection with Optical Constants.....	14
2.2.6 Direct Transitions.....	15
2.3 Optical Absorption in Amorphous Solids.....	18
2.3.1 Transitions Between Valence and Conduction Band Extended States.....	20
2.3.2 Transitions Between Valence Band Tail and Conduction Band Extended States.....	22
2.3.3 Results.....	26
2.4 Exponential Spectrum (Urbach edge) of Optical Absorption in Amorphous Semiconductors.....	29

2.4.1 Potential Energy Distributions of Atoms.....	30
2.4.2 Potential Well Model.....	32
3. OPTICS OF HOMOGENEOUS MULTILAYER THIN FILMS.....	41
3.1 Introduction.....	41
3.2 Maxwell's equations, wave equation and plane waves in a conducting medium.....	42
3.3 Reflection and Transmission of a Plane Wave.....	44
3.3.1 Reflection and Transmission of Electromagnetic Waves at a Plane Interface between Two Media.....	44
3.3.2 Transmission and Reflection of a Thin Film on a substrate...	47
3.3.3 Incoherent Interaction of the Light with the Substrate Layer.	49
3.3.4 Characteristic Matrix Approach in Determining Transmission and Reflection Coefficients.....	51
3.4 Methods of Determining the Optical Constants from Transmittance and Reflectance.....	59
3.4.1 Determination of Optical Constants and Thickness of Thin Films by Using the Transmission and Reflection Spectra: Method of Envelopes.....	59
3.4.2 Determination of Optical Parameters by Numerical Inversion Techniques.....	66
4. ELLIPSOMETRY.....	68
4.1 Introduction.....	68
4.2 Polarization Properties of Light.....	69
4.2.1 Polarization Ellipse.....	69
4.2.2 Main states of polarization: Linear and Circular Polarization.	73
4.2.3 Jones Matrix Formalism.....	73
4.2.4 Interaction of Light with Polarizing Optical Systems.....	74
4.2.5 Measurement of the Ratio of Eigenvalues of an Optical System.....	76
4.3 Fundamentals of Ellipsometry	79
4.3.1 Definition of Ellipsometry Angles.....	79

4.3.2 Two Phase (Substrate-Ambient) Optical System.....	80
4.3.3 Three Phase (Substrate-Film-Ambient) Optical System.....	80
5. EQUIPMENTS AND THEIR IMPLEMENTATIONS.....	83
5.1 Plasma Enhanced Chemical Vapor Deposition	83
5.1.1 Collisions of particles in the Plasma.....	83
5.1.2 Radio Frequency Discharges (Plasma).....	84
5.2 UV/VIS Spectrometer.....	90
5.2.1 RS-232-C Interface.....	91
5.2.2 Computer Control of the Spectrometer via a RS-232-C Interface.....	94
5.3 Single/Multi-Wavelength Ellipsometer.....	94
5.3.1 Calibration.....	97
5.3.2 Sample Alignment.....	97
5.3.3 Measurement Steps.....	98
5.3.4 Measurement on a Silicon wafer: Effects of surface conditions.....	100
5.4 Spectroscopic Ellipsometry.....	102
5.4.1 Fourier Analysis.....	103
5.4.2 Measurement on a Silicon Wafer.....	105
6. EFFECTS OF INHOMOGENEITIES ON TRANSMITTANCE AND REFLECTANCE SPECTRA.....	107
6.1 Introduction.....	107
6.2 Approximate Solutions to the Wave Equation.....	109
6.2.1 Slightly inhomogeneous thin film (small wavelength limit)...	109
6.2.2 Some useful parameters in the analysis of inhomogeneity.....	114
6.2.3 First order approximation theory.....	115
6.2.4 Approximation of Characteristic Matrix for an Inhomogeneous Layer.....	117
6.3 Surface Roughness.....	118
6.3.1 Determination of Optical Constants of Thin Films with a Rough Surface.....	119

6.4 Correlation between optical path modulations and transmittance spectra of a-Si:H thin films.....	121
6.4.1 Sample preparation.....	121
6.4.2 Experiment.....	122
6.4.3 Discussion and conclusion.....	128
7. THICKNESS AND OPTICAL CONSTANT DISTRIBUTIONS OF PECVD A-SiC _x :H THIN FILMS ALONG ELECTRODE RADIAL DIRECTION.....	130
7.1 Introduction.....	131
7.2 Outline of dielectric function representations used in the characterization.....	131
7.2.1 Forouhi-Bloomer Model.....	131
7.2.2 Tauc-Lorenz Model.....	132
7.2.3 Lorentz Oscillator Model.....	133
7.3 Experimental.....	134
7.3.1 Preparation of a-SiC _x :H thin films.....	134
7.3.2 Measuring procedures and equipments.....	135
7.4 Results.....	136
7.4.1 Numerical determination of optical constants.....	136
7.4.2 Inhomogeneity assessment.....	139
7.4.3 Discussion.....	144
7.5 Conclusion.....	147
8. MODULATION OF OPTICAL CONSTANTS OF HYDROGENATED AMORHOUS SILICON CARBON ALLOY (a-Si _{1-x} C _x :H) BY CARBON CONTENT.....	149
8.1 Introduction.....	149
8.1.1 Deposition of a-Si:H thin films in SiH ₄ plasma.....	150
8.1.2 Deposition of a-C:H thin films in C ₂ H ₄ plasma.....	152
8.1.3 Deposition of a-Si _{1-x} C _x :H thin films.....	155
8.2 Experimental	156
8.2.1 Preparation of a-Si _{1-x} C _x :H thin films.....	156

8.2.2 Measuring procedures and equipments.....	158
8.2.3 Determination of optical constants.....	158
8.2.4 Dispersion relations used in the characterization.....	160
8.3. Results.....	162
8.3.1 The influence of carbon content and rf power on deposition rate.....	162
8.3.2 Carbon incorporation in the films: Statistical approach for compositional analysis.....	164
8.3.3 UV-VIS Transmittance Analysis of the Films	167
8.3.4 Reflectance and Ellipsometry analysis of the films.....	177
8.3.5 FTIR spectroscopy analysis of the films.....	182
8.4 Conclusion.....	189
9. EFFECTS OF DOPING ON THE OPTICAL CONSTANTS OF SILICON BASED AMORPHOUS THIN FILMS.....	190
9.1 Introduction.....	190
9.2 Preparation of Samples.....	191
9.3 UV-VIS Transmittance and Reflectance Analysis.....	192
9.4 Spectroscopic Ellipsometry Analysis.....	195
9.5 Atomic Force Microscopy Analysis.....	199
9.5.1 Principles of Atomic Force Microscopy.....	199
9.5.2 Vertical Roughness Parameter: Root Mean Square (rms) Roughness.....	200
9.5.3 Lateral Roughness Parameter: Power Spectral Density.....	201
9.5.4 Height Distributions: Skewness and Kurtosis.....	202
9.5.5 AFM Measurement Results.....	203
9.6 FTIR Spectroscopy Analysis.....	205
9.7 XPS Analysis.....	208
9.7.1 Fundamentals of XPS.....	208
9.7.2 XPS measurements and results.....	210
9.8 Discussion and Conclusion.....	214

10. CONCLUSION.....	216
APPENDICES	
A. Inclusion of Material Properties in Maxwell's Equations.....	220
B. Definitions of Coefficients Appearing in Expressions of Transmittance and Reflectance.....	224
C. Definitions of Coefficients Given by Equation (5.15).....	226
D. Normalized reflectance spectra of a-Si _{1-x} C _x :H thin films with simulated reflectances.....	227
REFERENCES.....	231
VITA.....	248

LIST OF TABLES

TABLE

5.1	Pin Assignments in RS-232-C with signal travel direction.....	92
7.1	Deposition parameters such as gas concentration of source gases (M), total gas flow rate (F), pressure (P), substrate temperature (T), power density (P) and the residence time (t) of samples 1C and 2C.....	134
7.2	Optical gaps obtained by various methods [155] and corresponding carbon fractions x [156-158]. E_{04} is defined as an energy point in the absorption spectrum where the absorption coefficient reaches 10^4 cm^{-1} .	138
8.1	Eight different depositions under a pressure of 0.5 Torr at substrate temperature of 250 °C for the following deposition parameters such as relative C_2H_4 concentration ($M_{\text{C}_2\text{H}_4}$), SiH_4 (F_{SiH_4}) and C_2H_4 ($F_{\text{C}_2\text{H}_4}$) flow rates and power density (P). The last two letters “lp” and “hp” denote films grown at low and high powers, respectively.....	157
8.2	Table of optical constants and carbon content x of various films determined by comparing these optical constants with relevant published results in the literature. For each film, a set of x values is first determined either from E_g^{Tauc} or E_{04} values and listed in the column denoted by E_{04} , E_g . Similarly, the x values which are determined either from refractive indices at $E=2\text{eV}$ (n_1) or $\lambda = 1100 \text{ nm}$ (n_2) are listed in the column denoted by n . The average values $\langle x \rangle$ of x together with their standard deviations σ are added at the bottom of the table. The indices lp and hp are used for low power (30 mW/cm^2) and high power (90 mW/cm^2).....	165
8.3	Table of thicknesses of samples obtained by fitting the normalized reflectance and single wavelength ellipsometry measurements simultaneously by TL dispersion relations.....	181

8.4	Assignments of absorption peaks in FTIR spectra of a-Si _{1-x} C _x :H thin films.....	183
9.1	Deposition parameters such as doping ratios ($M_B = B_2H_6/SiH_4$, $M_P = PH_3/SiH_4$), relative gas concentration of the C ₂ H ₄ ($M_{C_2H_4} = C_2H_4/(C_2H_4+SiH_4)$), total gas flow rates (F), pressure (p), substrate temperature (T) and power density (P) for eight different depositions.....	192
9.2	Optical gaps E_g^{Cody} , E_{04} and film thicknesses d_1 calculated from transmittance and reflectance measurements. Thicknesses d_1 (bulk layer) and d_2 (roughness layer) of the films calculated from spectroscopic ellipsometry measurements.....	194
9.3	Rms, skewness and kurtosis values of the film surfaces.....	203
9.5	The relative intensities of both Si-C peak to Si-Si/Si-H peak in Si 2p spectra and C-Si peak to C-C/C-H peak in C1s spectra of the films.....	211

LIST OF FIGURES

FIGURE

2.1	Schematic energy band diagram. The functional forms of the energy bands are approximated as parabolic functions of \vec{k} around the maxima and minima at $\vec{k} = 0$ in the frame effective mass approximation. Vertical transitions are produced by an external electromagnetic field....	16
2.2	(a) An illustration of typical absorption coefficient as a function of photon energy with 3 main energy regions A, B, C. (b) A schematic diagram illustrating roughly the density of states. It should be noted that density of the localized valence band tail states is exaggerated for easy readability [21].....	18
2.3	Nonzero optical matrix elements for a-Si and c-Si from a particular valence band state (from Jackson <i>et al.</i> [23]).....	25
2.4	Illustration of the wavefunctions of (a) crystal extended, (b) amorphous extended and (c) amorphous localized states [2].....	31
2.5	Spherically symmetric potential well of depth V_0 and radius L	33
2.6	Binding energy $ E $ and decay length λ of the ground state in a steplike spherical potential well of depth V_0 and volume a^3	34
3.1	Incident wave is reflected and transmitted at a boundary separating two media.....	44
3.2	Multiple reflections and transmissions of a plane wave by an air-film-substrate system with parallel-plane boundaries.....	47
3.3	Multiply reflected and transmitted elements including the reflections at the back interface of the substrate [62].....	49
3.4	A plane wave incident on a multilayer coating with m homogeneous and isotropic layers surrounded by an outer space and substrate with refractive indices N_a and N_s	53

3.5	Simulated transmittance spectrum with $d = 1100$ nm, $n_s = 1.51$, $n_a = 1$, $n = 3 + 3 \times 10^5 / \lambda^2$ (λ in nm) and $k = (\lambda / 4\pi) \times 10^{1.45 \times 10^6 / \lambda^2 - 8}$ (λ in nm).	61
3.6	Flowchart of Swanepoel's procedure for the determination of optical constants in 8 steps.....	64
4.1	The polarization ellipse which is the most general state of polarization of any electromagnetic field that is monochromatic. The electric field vector at a fixed point traces the same ellipse in a regular repetitive fashion for an elliptically (most general state of polarization) polarized light [89].....	70
4.2	An optical arrangement of a polarizer, optical system S, analyzer and photodetector. The light emerging from the light source L falls on the polarizer, passes through it and reflects from the optical system S. The reflected light reaches the photodetector after passing through the analyzer. P and A represent the azimuthal positions of the polarizer and analyzer measured from the plane of incidence.....	76
4.3	(a) Unit circle in the complex X-plane for a transparent film. (b) Constant angle of incidence contour of ρ at $\phi_0 = 60^\circ$ for air-SiO ₂ -Si system at wavelength $\lambda = 632.8$ nm when the film is transparent. (c) Logarithmic spiral of X when the film is absorbing. (d) Constant angle of incidence contour of ρ at $\phi_0 = 60^\circ$ for air-SiO ₂ -Si system at wavelength $\lambda = 632.8$ nm when the film is absorbing.....	82
5.1	Schematic diagram of a capacitively coupled radio frequency discharge. Spatial distribution of the average potential between the electrodes is given just below the inter-electrode region. I_e and I_{ions} denote electron and ion currents, respectively.....	85
5.2	Schematic diagram of the PECVD system used in the production of thin films [98].....	88
5.3	Gas cabinet system associated to the PECVD system shown in Figure 5.2 [98].....	89

5.4	Illustration of optical path of the Perkin Elmer Lambda 2 Spectrometer [99]. Reflectance unit, shown as an inset, is positioned on the sample platform for reflectance measurements.....	90
5.5	Null modem cable.....	93
5.6	Single wavelength ellipsometer system.....	95
5.7	Receiver unit.....	96
5.8	(A) Reflection of light from the sample hitting the four photodetectors in the center and perpendicular direction. (B) Reflection of light from the sample hitting the four photodetectors unsuccessfully.....	97
5.9	A representative diagram on the program window which are used in the alignment of the sample.....	99
5.10	Measured ellipsometric angles Ψ and Δ as a function of angle of incidence ϕ_i for silicon wafer p-type Si (100) with different surface conditions.....	101
5.11	A shematic diagram of the spectroscopic ellipsometer [101].....	102
5.12	Variation of transmitted intensity by the rotating analyzer in time for unpolarized and linearly, elliptically polarized incident light [105-106].	103
5.13	Measured $\langle \varepsilon_2 \rangle$ spectra of various silicon wafers with orientations $\langle 111 \rangle$ and $\langle 100 \rangle$. The results denoted by circles are measured by the setup shown in Figure 5.11. The others are spectra of previously published data [108-110].....	105
6.1	An inhomogeneous layer with arbitrary dielectric function surrounded by homogeneous media, the ambient and the substrate with constant dielectric functions.....	109
6.2	An optical model of an inhomogeneous layer surrounded by an ambient and substrate.....	111
6.3	Thin film with a thickness variation on a transparent substrate [70].....	119
6.4	Transmittance of a-Si:H with its envelopes, and transmittance T_s of the substrate alone.....	122

6.5	Thickness variation Δd computed by solution of equations (4.23) and (4.24) numerically at each extremum point.....	123
6.6	(a) Refractive index of the substrate calculated from the transmittance spectrum of the substrate alone as shown in Figure 6.4. (b) Graph of $l/2$ versus θ	124
6.7	(a) Extrema of the transmittance spectrum with corrected extrema values from which the film has no thickness variation ($\Delta d = 0$ nm). (b) Thicknesses d_1 and d_2 calculated from equations from (3.62) and (3.57), respectively.....	125
6.8	(a) Fringe order numbers calculated from equation (3.57) and from exact integer and half integer values that are found from calculated ones. (b) Refractive indices n_1 and n_2 calculated from equation (3.61) and from equation (3.57) with exact fringe numbers and average thickness $\bar{d}_2 = 1264.9$ nm, respectively. The continuous curve denotes fitted dispersion relation (equation (6.27)).....	126
6.9	(a) Transmittance B is the spectrum of the film that is obtained by correction of curve A (original measured data) from the thickness modulation. (b) Transmittance C of a film that has refractive index inhomogeneities at its interfaces, as shown in (c), fitted to curve A. (c) Refractive index profile of the film that gives transmittance spectrum C.	127
7.1	Transmittance spectra of samples 1C and 2C [128].....	136
7.2	Retrieved values of refractive indices and absorption coefficients from transmittance spectra, fitting of these optical constants to Forouhi-Bloomer (FB), Jellison-Modine (TL) and single Lorentz oscillator (L) dispersion relations.....	137
7.3	Schematic gas flow diagram in the plasma enhanced chemical vapor deposition system (PECVD). The electrode diameter and the interelectrode distance are 24 cm and 4 cm, respectively. Two samples are shown symbolically on the grounded bottom electrode.....	139

7.4	The distributions of film thickness (d), refractive index (n) at a wavelength of 632.8 nm and optical gap E_{04} along the sample 1C as a function of radial distance. Stars denote the results obtained from ellipsometry measurements at 632.8 nm, circles and squares denote the results obtained from transmittance measurements.....	140
7.5	The distributions of film thickness (d), refractive index (n) at a wavelength of 632.8 nm and optical gap E_{04} along the sample 2C as a function of radial distance. Stars denote the results obtained from ellipsometry measurements at 632.8 nm, circles and squares denote the results obtained from transmittance measurements.....	141
7.6	Optical gap (E_g) and resonance energies (E_0) of depositions 1C (a) and 2C (b) plotted as a function of radial distance. E_g values are obtained by fitting FB and TL dispersion relations (7.1-7.2), while E_0 values are obtained from L dispersion relations (7.3). Similarly, refractive index at high energy, $n(\infty)$, as a function of radial distance are obtained from FB, TL and L models for depositions 1C (c) and 2C (d).....	142
7.7	IR spectra of two a-Si $_x$ C $_x$:H samples, 1C-a and 1C-b, grown at positions 3 cm and 8 cm radially apart from the center of the bottom electrode of the PECVD system, respectively. The IR spectra are normalized according to the thicknesses of the films.....	143
7.8	Deposition rates $R(t)$ for samples 1C and 2C as a function of residence time (t).....	145
8.1	The thicknesses d_{fit} is plotted as a function of thicknesses d_{env} to exhibit the agreement in thicknesses determined from fitting and envelope method.....	159
8.2	Deposition rate of a-Si $_{1-x}$ C $_x$:H thin films as function of C $_2$ H $_4$ relative gas concentration $M_{C_2H_4} = C_2H_4 / (C_2H_4 + SiH_4)$	161
8.3	Carbon content of a-Si $_{1-x}$ C $_x$:H thin films as function of C $_2$ H $_4$ gas concentration $M_{C_2H_4}$	166

8.4	Refractive indices of a-Si _{1-x} C _x :H thin films as function photon energy together with fittings of dispersion relations by Lorentz (L), Modified Lorentz (ML), Forouhi-Bloomer (FB) and Tauc-Lorentz (TL) models. (a) low and (b) high power.....	168
8.5	(a) $1/(n^2-1)$ is plotted as a function E^2 to determine the static refractive indices $n(E=0)$ of a-Si _{1-x} C _x :H thin films from the intercept of the linear fitting. (b)Refractive indices at both $E=0$ (diamonds) and $E=2$ eV (circles) are plotted as a function of carbon content. The resonance energies found from the fittings are plotted as a function of x as an inset. Full diamonds, circles and triangles denote films produced at high power density whereas the empty markers denote films produced at low power density.....	170
8.6	Absorption coefficients as a function of energy for a-Si _{1-x} C _x :H thin films grown at (a) low and (b) high power densities together with fittings of dispersion relations of Lorentz (L), Modified Lorentz (ML), Forouhi-Bloomer (FB) and Tauc-Lorentz (TL) models. Close-up drawings of the Urbach edges of the films are plotted as insets where the arrows along the absciss point the corresponding Tauc optical gaps.....	172
8.7	(a) E_g^{Tauc} , E_g^{Cody} and E_{04} optical gap values for a-Si _{1-x} C _x :H thin films grown at low (empty markers) and high (full markers) power densities are plotted as function of carbon content x . The variation of slope parameters B^{Tauc} and B^{Cody} are given as an inset. (b) Urbach parameters E_U is plotted as a function of x for both power densities together with suitable representative fittings.....	174
8.8	Reflectance spectrum (open circles) of the sample 0lp is normalized (full circles) by a common factor for all samples. Solid line denotes the reflectance spectrum simulated by using the optical constants obtained from the analysis of transmittance spectrum. Dashed line denotes the fitting of TL dispersion relations to the normalized reflectance spectrum (full circles) and single wavelength ellipsometry.....	178

8.9	Measured ellipsometric angles ψ and Δ of samples (a) 0lp, 0hp; (b) 2lp, 2hp; (c) 5lp, 5hp; (d) 7lp, 7hp. The solid and dash-dot (-.) lines denote the fitting results of the normalized reflectance and ellipsometry angles simultaneously of films grown at low power (empty circles) and high power (full circles), respectively.....	180
8.10	Comparison of optical constants obtained from transmittance and reflectance/ellipsometry measurements. Solid lines denote the optical constants retrieved by fitting the normalized reflectance spectra and single wavelength ellipsometry results simultaneously. Circles, squares, pluses, reverse triangles, crosses, stars, diamonds, triangles denote optical constants (Figures 8.4 and 8.6)of the samples 0lp, 2lp, 5lp, 7lp, 0hp, 2hp, 5hp and 7hp, respectively, obtained from the transmittance measurements.....	181
8.11	First IR absorption band of a-Si _{1-x} C _x :H thin films grown at low and high power with deconvolutions of the peaks according to the assignments given in Table 8.4.....	184
8.12	Second (a) and third (b) IR absorption bands of a-Si _{1-x} C _x :H thin films grown at low and high power with deconvolutions of the peaks according to the assignments given in Table 8.4.....	185
8.13	The change of peak parameters as a function of carbon content in a-Si _{1-x} C _x :H thin films.(a) the concentration of the vibration mode at about 770 cm ⁻¹ , (b) FWHM of the absorption peak at 770 cm ⁻¹ , (c) the sum of concentrations of vibration modes at about 640 and 670 cm ⁻¹ , (d) peak position of Si-H stretching mode at 2090 cm ⁻¹	186
8.14	Sum of the relative concentrations of symmetric and asymmetric stretching modes of (a) C-H ₂ and (b) C-H ₃ bonds.....	188
9.1	(a) Spectral dependence of refractive index n and absorption coefficient α for undoped a-Si:H, B ₂ H ₆ doped a-Si:H, undoped a-SiC _x :H, B ₂ H ₆ doped a-SiC _x :H and PH ₃ doped a-SiC _x :H thin films, obtained from transmittance and reflectance measurements.....	193

9.2	Determination of optical gaps E_g^{Cody} of the films by fitting $\epsilon_2^{1/2}$ to a linear function and extrapolating to $\epsilon_2^{1/2} = 0$	195
9.3	Real and imaginary parts of the pseudodielectric functions ($\epsilon = \epsilon_1 - i\epsilon_2$) of the (a) B_2H_6 doped a-Si:H, (b) B_2H_6 doped a-SiC _x :H and (c) PH ₃ doped a-SiC _x :H thin films (circles) together with the fitting results (solid lines).....	196
9.4	(a) Spectral dependence of refractive index n and absorption coefficient α for undoped a-Si:H, B_2H_6 doped a-Si:H, undoped a-SiC _x :H, B_2H_6 doped a-SiC _x :H and PH ₃ doped a-SiC _x :H thin films, obtained from spectroscopic ellipsometry measurements.....	199
9.5	(a) One dimensional sectional surface profile and (b) two dimensional isotropic power spectrum density of B_2H_6 doped a-Si:H, undoped a-SiC _x :H, B_2H_6 doped a-SiC _x :H, PH ₃ doped a-SiC _x :H thin films.....	204
9.6	IR absorption spectra of unpoded a-Si:H (thick solid line), B_2H_6 doped a-Si:H (dotted line), undoped a-SiC _x :H (dashed line), B_2H_6 doped a-SiC _x :H (dash-dotted line) and PH ₃ doped a-SiC _x :H (thin solid line) thin films in two different wavenumber intervals of (a) 500-1200 cm ⁻¹ and (b) 1900-2200 cm ⁻¹ . IR absorption spectrum of undoped a-SiC _x :H in wavenumber interval of 2800-3000 cm-1 is given as an inset in (a).....	206
9.7	Si 2p peaks of (a) B_2H_6 doped a-Si:H (b) undoped a-SiC _x :H (c) B_2H_6 doped a-SiC _x :H (d) PH ₃ doped a-SiC _x :H.....	212
9.8	C 1s peaks of (a) B_2H_6 doped a-Si:H (b) undoped a-SiC _x :H (c) B_2H_6 doped a-SiC _x :H (d) PH ₃ doped a-SiC _x :H.....	212
9.9	O 1s peaks of (a) B_2H_6 doped a-Si:H (b) undoped a-SiC _x :H (c) B_2H_6 doped a-SiC _x :H (d) PH ₃ doped a-SiC _x :H.....	213
D.1	Reflectance spectra of the sample 0hp.....	227
D.2	Reflectance spectra of the sample 2lp.....	228
D.3	Reflectance spectra of the sample 2hp.....	228
D.4	Reflectance spectra of the sample 5lp.....	229
D.5	Reflectance spectra of the sample 5hp.....	229

D.6	Reflectance spectra of the sample 7lp.....	230
D.7	Reflectance spectra of the sample 7hp.....	230

ACKNOWLEDGMENTS

I would like to express my gratitude to my supervisor Prof. Dr. Bayram Katirciođlu for his guidance, fruitful discussions and encouraging vision. I benefited very much from his insights and experiences in general on wide spread of subjects during my study.

I would like to thank Assoc. Prof. Dr. İsmail Atılgan for his endless support and advice in the laboratory. This work would not have been possible without his experience on thin film production.

I would like to acknowledge my lab colleagues Orhan Özdemir, Kıvanç Sel and Oben Sezer.

I would also like to thank the Scientific and Technical Research Council of Turkey for financial support during my study in Middle East Technical University and North Carolina State University at Chapel Hill.

I am grateful to Prof. Dr. Eugene A. Irene for giving me the opportunity to study in his laboratory in North Carolina State University at Chapel Hill. I would like to thank my colleagues and friends Roshan, Natalya, Jason, Ciro, Isaac, Alex and Todd for their help, friendness and hospitality.

I would also like to thank İsmet Yurduşen and İsmail Turan for their continuous friendship and support during my study.

I would like to express my gratitude to my parents for their guidance, support and encouragement.

Finally, I would like to thank my wife Tlay for her patience, understanding and continuous support during my Ph.D. study. Special thanks are due to our son zgr with whom I have enjoyable time playing games and feel myself very happy.

CHAPTER 1

INTRODUCTION

Nowadays, information systems are built by rather two complementary constituents [1],

1. electronic processors (microelectronics)
2. input/output devices (large area electronics)

Although the first group of devices is continuously developing with unbelievable miniaturization on the crystalline silicon chip, the second class has to stay large dimensions as a necessity of man/machine interface such as document scanners, electronic displays, printers etc...The crystalline silicon could not satisfy the requirement of these large area opto-electronic devices due to its poor optical properties and limited dimensions. The solutions developed on the semiconductors other than the crystalline silicon have created mismatching problems with the existing silicon based microelectronic technologies.

Amorphous silicon whose huge amount of dangling bond states at midgap ($10^{20} \text{ cm}^{-1} \text{ eV}^{-1}$) are reduced to a minute amount ($10^{15} \text{ cm}^{-1} \text{ eV}^{-1}$) by the hydrogen compensation process, becomes able to be selectively doped both n and p types leading to a large number of devices practically useful such as p-n, p-i-n, Schottky diodes etc...[2]. Consequently, the hydrogenated amorphous silicon (a-Si:H) seems to be a solution to the large area problem of crystalline silicon because it can be deposited at low temperatures ($<300 \text{ K}^\circ$) by the glow discharge method at reasonable cost as large area thin films on low cost substrate [3].

Besides, the control of electrical conductivity over 10 orders of magnitude [4] due to its dopability, the field effect allows the sheet conductance of a-Si:H layer to be switched over 6 orders of magnitude [5]. As a result, the development of thin film transistors for addressing circuits on large area electronics is facilitated by the fact that the gate dielectric layer (mostly SiN_x :H film), the channel layer of a-Si:H film and the ohmic source and drain n^+ -contact layers can all be deposited in the same plasma CVD reactor [6].

In addition to the above outlined electronic behaviour of a-Si:H material, its optical properties are substantially improved compared with the ones of crystalline silicon. The optical gap of a-Si:H is widened up to the visible region (~ 1.75 eV) leading to the photoconductivity spectrum, shifted to shorter light wavelength compared with crystalline silicon. In other words, the a-Si:H spectrum coincides better with the sensitivity range of human eye (the alloying ability of a-Si:H with Ge, Sn, C, N and O creates a flexibility of adjusting the optical gap from IR to UV). Moreover, the optical absorption of a-Si:H in the visible range is greater by about a factor of 20 than in the case of crystalline silicon [7,8]. As this will be discussed later in this work, this increase in optical absorption is a consequence of the irrelevance of the selection rules for optical transitions in amorphous semiconductors (non-conservation of k-vector) [9]. Thus, a thin film of only 1 μm thickness absorbs most of the visible light, facilitating the fabrication of high efficiency photosensors.

At present there is an increasing need for a accurate knowledge of the optical constants of thin absorbing films over a wide range. Since the optical constants of the materials are not well known or determined only in a narrow wavelength range. Optical constants may be determined by a large variety of techniques which basically fall into two [10,11]:

1. photometry: film is illuminated by unpolarized radiation and the intensities of reflected or transmitted beams are measured as a function of wavelength (this

method is well suited to the determination of optical constants over a wide wavelength range).

2. ellipsometry: polarized radiation is used and both intensity and phase of the reflected or transmitted beam is determined (even though the spectral range has been increased, it remains limited for this last technique).

In general, the first category, the photometric method is chosen for the determination of optical constants because of the wider availability of the necessary instrumentation. On the other hand, the most accurate values of dielectric function of any material (even if it is only a few atomic layer) is obtained by spectroscopic ellipsometry measurements because such measurements are mostly free of errors due to presence of overlayers (contaminant oxides, microrough surface layers or any microstructural defects) [12]. In addition, spectroscopic ellipsometry has the capability of analyzing depth profile of multilayer structures together with their surface microroughness properties. For example, depth profile measurements on the same sample (implanted crystalline silicon) are performed by spectroscopic ellipsometry and cross-section transmission electron microscopy (XTEM) [13]. It seen that the thicknesses obtained by two methods are in excellent agreement and in contrast to XTEM, the spectroscopic ellipsometry provides quantitative estimates of relative amounts of amorphous and crystalline phase in each layer. Moreover, spectroscopic measurements are non-destructive and non-invasive which can be useful for real-time material analyses. Evolutionary improving changes (improved accuracy, extending spectral ranges, parallel data acquisition) on ellipsometry is being experienced to achieve more accurate control over decreasingly thick gate oxides, to characterize wide band gap materials and to control the dynamic processes [14].

The second chapter of this thesis describes the concepts mainly on interaction of light with the electronic states of amorphous solids within the frame of semi-classical approach of quantum mechanics. Absorption properties, determined by transitions between bands, are discussed by introducing and assessing some physical parameters such as absorption coefficient, band gap, Urbach parameter, density of states of the

amorphous materials. Chapter 3 covers the optics of multilayer thin films in the frame of photometric measurement techniques. Various methodologies are discussed for the determination of optical constants, such as thickness, refractive index and absorption coefficient, of the thin films. In Chapter 4, the fundamentals of ellipsometry are summarized by describing the polarization properties of light. In Chapter 5, the equipments and their implementations are summarized. In Chapter 6, various kinds of inhomogeneities in the thin films and their eventual effects on the results of photometric measurements are discussed. The correlation between optical path modulations and the transmittance spectra of plasma deposited hydrogenated amorphous silicon (a-Si:H) thin film is interpreted in terms of thickness irregularities and vertical film inhomogeneities (refractive index distribution). In Chapter 7, the influence of the pressure on the distribution of thicknesses, refractive indices at 632.8 nm and optical gaps of amorphous silicon carbide (a-SiC_x:H) thin films from the edge to the center of the bottom electrode of plasma enhanced chemical vapor deposition system (PECVD) is examined by transmission, single wavelength ellipsometry and Fourier transform infrared spectroscopy (FTIR). In Chapter 8, effect of carbon content and power density on optical constants of silicon carbon alloys is analyzed by transmittance, reflectance, ellipsometry and FTIR measurements. In Chapter 9, effects of doping on the optical constants of silicon based amorphous thin films are studied together with surface sensitive measurement techniques such as spectroscopic ellipsometry, atomic force microscopy, x-ray photoemission spectroscopy.

CHAPTER 2

INTERACTION OF LIGHT WITH AMORPHOUS MATERIALS

2.1 Introduction

The interaction between external electromagnetic field and electrons in a semiconductor can be examined by using semi-classical approach, that is, the electromagnetic field is treated classically whereas the atomic states are considered in the frame of nonrelativistic quantum mechanics. Although this approach is not appropriate for describing spontaneous emission, it leads to many correct results relatively simply [15].

The response of electrons to an electromagnetic field can be obtained by approximating the response of many-electron wave functions as the response of one-electron wave functions. In this approach, each electron moves independent from the other electrons both in a field due to the nuclei and the average repulsion effect of the other electrons. The motion of any given electron depends on the motion of all electrons; but since it itself affects the motion of other electrons there is a self consistence. Moreover, on average, a large fraction of electron-electron interaction can be considered to be radial, that is, spherically symmetric (central field approximation).

Response of the medium does not depend on the light intensity of the incident light because incident light intensity is weak (less than few W/cm^2). Besides, in the presence of weak fields, any nonlinear behavior of the medium can be neglected.

2.2 Optical absorption in crystals

Neglecting spin-orbit interaction; one-electron Hamiltonian, in the absence of external electromagnetic field, has the form of

$$H_0 = \frac{-\hbar^2}{2m} \nabla^2 + U(\vec{r}) \quad (2.1)$$

$U(\vec{r})$ is the potential energy for an arbitrary electron and can be expressed as

$$U(\vec{r}) = \Omega(\vec{r}) + U(\vec{r}, \vec{R}_1, \vec{R}_2, \dots) \quad (2.2)$$

where $\Omega(\vec{r})$ is the self consistent potential energy of an electron at position r due to the rest of the electrons and $U(\vec{r}, \vec{R}_1, \vec{R}_2, \dots)$ is the potential energy of the electron at position \vec{r} due to the field created by ions at positions $\vec{R}_1, \vec{R}_2, \dots$. An ideal crystal lattice can be formed by translating minimal number of atoms (basis set) by integer multiples of three primitive translational vectors \vec{a} , \vec{b} , \vec{c} . This periodicity of the lattice leads to a periodic crystal potential and the effect of the periodic potential $U(r)$ can be introduced within the effective mass m^* as

$$H_0 = \frac{-\hbar^2}{2m^*} \nabla^2 \quad (2.3)$$

Effective mass m^* is used instead of electron rest mass m and this approach is known as effective mass approximation. As long as electrons can be treated as quasi-free in the effective mass approximation, the complete set of solutions of

$$H_0 \phi_{\vec{k}}^0 = E^0(\vec{k}) \phi_{\vec{k}}^0 \quad (2.4)$$

can be determined and are of the form of plane waves (Bloch wave function) with amplitudes varying periodically in space as the crystal potential:

$$\phi_{\vec{k}}^0(\vec{r}) = u_{\vec{k}}^0(\vec{r})e^{i\vec{k}\cdot\vec{r}} \quad (2.5)$$

where $u_{\vec{k}}^0(\vec{r}) = u_{\vec{k}}^0(\vec{r} + n_1\vec{a} + n_2\vec{b} + n_3\vec{c})$, $n_{1,2,3} = 0,1,2,\dots$

2.2.1 Motion of Electrons in an Electromagnetic Field in the Frame of Quantum Mechanics

In order to express the motion of charged particles in the frame of quantum mechanics, it is needed to replace the canonical coordinate pairs in the classical Hamiltonian with the Hermitian operators [16]. For this purpose let's first write the force acting on an electron of charge q with a mass m that is moving with velocity $d\vec{r}/dt$ in an electromagnetic field:

$$m\frac{d^2\vec{r}}{dt^2} = q\vec{E} + \frac{q}{c}\frac{d\vec{r}}{dt} \times \vec{B} \quad (2.6)$$

where \vec{E} and \vec{B} denote electric field and magnetic induction, respectively. This equation of motion of the charged particle can be derived by using Eulerian equations from the following Lagrangian L or Hamiltonian H :

$$L(\vec{r}, \frac{d\vec{r}}{dt}, t) = \frac{1}{2}m\left(\frac{d\vec{r}}{dt}\right)^2 + \frac{q}{c}\frac{d\vec{r}}{dt} \cdot \vec{A} - q\phi \quad (2.7)$$

$$H(\vec{r}, \vec{p}, t) = \frac{d\vec{r}}{dt} \cdot \vec{p} - L = \frac{1}{2}m\left(\frac{d\vec{r}}{dt}\right)^2 + q\phi \quad (2.8)$$

where ϕ and \vec{A} are the scalar and vector potentials, respectively. Since the canonical momentum is $\vec{p} = \frac{\partial L}{\partial(\vec{d}\vec{r}/dt)} = m \frac{d\vec{r}}{dt} + \frac{q}{c} \vec{A}$, the velocity $d\vec{r}/dt$ can be expressed as

$\frac{d\vec{r}}{dt} = \frac{1}{m} \left(\vec{p} - \frac{q}{c} \vec{A} \right)$. Consequently, Hamiltonian can be written as

$$H(\vec{r}, \frac{d\vec{r}}{dt}, t) = \frac{1}{2m} \left(\vec{p} - \frac{q}{c} \vec{A} \right)^2 + q\phi \quad (2.9)$$

It should be noted that \vec{p} is the canonical momentum at the canonical coordinate \vec{r} and can be expressed as $-i\hbar\vec{\nabla}$ whereas $m \frac{d\vec{r}}{dt}$ is kinematical (or mechanical) momentum [17]. For an electron charge $q = -e$ in the frame of effective mass approximation, the Hamiltonian become

$$H = \frac{(\vec{p} + \frac{e}{c} \vec{A})^2}{2m^*} = \frac{\vec{p}^2}{2m^*} + \frac{e}{2m^*c} \vec{p} \cdot \vec{A} + \frac{e}{2m^*c} \vec{A} \cdot \vec{p} + \frac{e^2}{2m^*c^2} \vec{A}^2 \quad (2.10)$$

If Coulomb gauge, $\vec{\nabla} \cdot \vec{A} = 0$, is chosen, $[\vec{p}, \vec{A}] = \vec{p}\vec{A} - \vec{A}\vec{p} = 0$. Consequently, H becomes

$$H = \frac{\vec{p}^2}{2m^*} + \frac{e}{m^*c} \vec{A} \cdot \vec{p} \quad (2.11)$$

where nonlinear term ($\propto \vec{A}^2$) is neglected. The second term, $\frac{e}{m^*c} \vec{A} \cdot \vec{p}$, can be treated as a time dependent perturbation on the electronic states of the crystals.

2.2.2 Time Dependent Perturbation Approach

The problem is to find a solution to the following Schrödinger equation:

$$i\hbar \frac{\partial \psi(\vec{r}, t)}{\partial t} = \left(H_0 + \frac{e}{m^* c} \vec{A} \cdot \vec{p} \right) \psi(\vec{r}, t) \quad (2.12)$$

Let's expand $\psi(\vec{r}, t)$ as a sum of the solutions to the unperturbed problem:

$$\psi(\vec{r}, t) = \sum_{\vec{k}} c_{\vec{k}}(t) e^{-iE^0(\vec{k})t/\hbar} \phi_{\vec{k}}^0(\vec{r}) \quad (2.13)$$

If above expansion (2.13) is substituted into the Schrödinger equation (2.12),

$$\sum_{\vec{k}} i\hbar \frac{dc_{\vec{k}}(t)}{dt} e^{-iE^0(\vec{k})t/\hbar} \phi_{\vec{k}}^0(\vec{r}) = \sum_{\vec{k}} \frac{e}{m^* c} \vec{A} \cdot \vec{p} c_{\vec{k}}(t) e^{-iE^0(\vec{k})t/\hbar} \phi_{\vec{k}}^0(\vec{r}) \quad (2.14)$$

is obtained. Taking the scalar product with $\phi_{\vec{k}'}^0(\vec{r})$ and integrate over crystal volume (V), one can obtain

$$i\hbar \frac{dc_{\vec{k}'}(t)}{dt} = \sum_{\vec{k}} c_{\vec{k}}(t) e^{i(E^0(\vec{k}') - E^0(\vec{k}))t/\hbar} \int_V d\vec{r}' \phi_{\vec{k}'}^{0*}(\vec{r}') \frac{e}{m^* c} \vec{A} \cdot \vec{p} \phi_{\vec{k}}^0(\vec{r}') \quad (2.15)$$

Supposing before the perturbation is switched on at $t=0$, the system is in a stationary state $\phi_{\vec{k}'}^0$, that is, $c_{\vec{k}'}(0) = 1$ ($c_{\vec{k}}(0) = 0$ for all $\vec{k} \neq \vec{k}'$), the above differential equation (2.15) becomes

$$i\hbar \frac{dc_{\vec{k}'}(t)}{dt} = e^{i(E^0(\vec{k}') - E^0(\vec{k}''))t/\hbar} \int_V d\vec{r}' \phi_{\vec{k}'}^{0*}(\vec{r}') \frac{e}{m^* c} \vec{A} \cdot \vec{p} \phi_{\vec{k}''}^0(\vec{r}') \quad (2.16)$$

Finally, $c_{\vec{k}'}(t)$ can be expressed as

$$c_{\vec{k}'}(t) = \frac{1}{i\hbar} \int_0^t dt' e^{i(E^0(\vec{k}') - E^0(\vec{k}'))t'/\hbar} \underbrace{\int_V d\vec{r}' \phi_{\vec{k}'}^{0*}(\vec{r}') \frac{e}{m^* c} \vec{A} \cdot \vec{p} \phi_{\vec{k}''}^0(\vec{r}')}_{\equiv I} \quad (2.17)$$

2.2.3 Interband Transitions

Let's consider transitions from valence band (v) to conduction band (c) and define Bloch wave functions with two indices denoting the corresponding bands and k vectors:

$$\phi_{c,\vec{k}_c}^0(\vec{r}) = u_{c,\vec{k}_c}^0(\vec{r}) e^{i\vec{k}_c \cdot \vec{r}} \quad \phi_{v,\vec{k}_v}^0(\vec{r}) = u_{v,\vec{k}_v}^0(\vec{r}') e^{i\vec{k}_v \cdot \vec{r}} \quad (2.18)$$

Substitution of these Bloch wave functions into the integral I defined in the expression (2.17) leads to

$$I = \int_V d\vec{r}' u_{c,\vec{k}_c}^{0*}(\vec{r}') e^{-i\vec{k}_c \cdot \vec{r}'} \frac{e}{m^* c} \vec{A} \cdot \vec{p} u_{v,\vec{k}_v}^0(\vec{r}') e^{i\vec{k}_v \cdot \vec{r}'} \quad (2.19)$$

Using Maxwell's equations given in Appendix 1, magnetic induction \vec{B} can be given in terms of a vector potential \vec{A} as $\vec{B} = \vec{\nabla} \times \vec{A}$ and electric field \vec{E} can be expressed in terms of the vector potential \vec{A} and scalar potential ϕ as $\vec{E} = -\frac{1}{c} \frac{\partial \vec{A}}{\partial t} - \vec{\nabla} \phi$. Scalar potential may be chosen to be zero by means of gauge transformation. Then, in vacuum where charge and current densities are zero, electric field and vector potential can be expressed as $\vec{E} = \vec{E}_0 e^{-i\omega t + i\vec{g} \cdot \vec{r}} + \vec{E}_0 e^{i\omega t - i\vec{g} \cdot \vec{r}}$ and $\vec{A} = \vec{A}_0 e^{-i\omega t + i\vec{g} \cdot \vec{r}} + \vec{A}_0 e^{i\omega t - i\vec{g} \cdot \vec{r}}$ where \vec{g} is the momentum of light. Only the first term in \vec{A} , which gives rise to absorption, is considered and the second term (emissive transitions) is neglected. Substituting

$\vec{A} = \vec{A}_0 e^{-i\alpha t + i\vec{g}\cdot\vec{r}}$ and electron generalized momentum $\vec{p} = -i\hbar\vec{\nabla}$ in equation (2.19), the integral I becomes

$$\begin{aligned}
I &= \frac{\hbar e}{im^*c} |\vec{A}_0| e^{-i\alpha t} \int_V d\vec{r}' u_{c,\vec{k}_c}^{0*}(\vec{r}') e^{-i\vec{k}_c\cdot\vec{r}' + i\vec{g}\cdot\vec{r}'} \vec{a}_0 \cdot \vec{\nabla} u_{v,\vec{k}_v}^0(\vec{r}') e^{i\vec{k}_v\cdot\vec{r}'} \\
&= \frac{\hbar e}{im^*c} |\vec{A}_0| e^{-i\alpha t} \left[\int_V d\vec{r}' u_{c,\vec{k}_c}^{0*}(\vec{r}') e^{i(\vec{g}-\vec{k}_c+\vec{k}_v)\cdot\vec{r}'} \left[\vec{a}_0 \cdot (\vec{\nabla} u_{v,\vec{k}_v}^0(\vec{r}')) + i\vec{a}_0 \cdot \vec{k}_v u_{v,\vec{k}_v}^0(\vec{r}') \right] \right] \quad (2.20)
\end{aligned}$$

where $\vec{a}_0 = \vec{A}_0 / |\vec{A}_0|$.

On the other hand, one can express \vec{r} as $\vec{r}' = \vec{r} + \vec{R}_j$ where \vec{r} lies within one unit cell of the crystal and \vec{R}_j is a lattice vector. If the integral I is separated according to this new definition, that is, expressing the integral I as a sum of integrals over unit cells, the integral I becomes [18, 19]

$$I = \frac{\hbar e}{im^*c} |\vec{A}_0| e^{-i\alpha t} \left(\sum_j e^{i(\vec{g}-\vec{k}_c+\vec{k}_v)\cdot\vec{R}_j} \right) \int_{\text{unit cell}} d\vec{r} u_{c,\vec{k}_c}^{0*}(\vec{r}) e^{i(\vec{g}-\vec{k}_c+\vec{k}_v)\cdot\vec{r}} \left[\vec{a}_0 \cdot (\vec{\nabla} u_{v,\vec{k}_v}^0(\vec{r})) + i\vec{a}_0 \cdot \vec{k}_v u_{v,\vec{k}_v}^0(\vec{r}) \right] \quad (2.21)$$

As a consequence of translational symmetry of the crystal, one can write

$$\sum_j e^{i(\vec{g}-\vec{k}_c+\vec{k}_v)\cdot\vec{R}_j} = \delta(\vec{g} - \vec{k}_c + \vec{k}_v) \quad (2.22)$$

Consequently, one can conclude that $\vec{A}\cdot\vec{p}$ may have non-vanishing matrix elements only among Bloch wave functions with \vec{k} vectors satisfying $\vec{k}_c = \vec{k}_v + \vec{g}$. However, one

should note that \vec{k}_c and $\vec{k}_v + \vec{g}$ may differ by a reciprocal lattice vector [20]. Using this selection rule in the transitions, the integral I becomes

$$\begin{aligned}
I &= \frac{\hbar e}{im^* c} |\vec{A}_0| e^{-i\omega t} \int_{\text{unit cell}} d\vec{r} u_{c,\vec{k}_c}^{0*}(\vec{r}) \left[\vec{a}_0 \cdot (\vec{\nabla} u_{v,\vec{k}_v}^0(\vec{r})) + i\vec{a}_0 \cdot \vec{k}_v u_{v,\vec{k}_v}^0(\vec{r}) \right] \\
&= \frac{\hbar e}{im^* c} |\vec{A}_0| e^{-i\omega t} \int_{\text{unit cell}} d\vec{r} u_{c,\vec{k}_v+\vec{g}}^{0*}(\vec{r}) \vec{a}_0 \cdot \vec{\nabla} u_{v,\vec{k}_v}^0(\vec{r})
\end{aligned} \tag{2.23}$$

where the second term in the integral is vanished since $u_{c,\vec{k}_c}^0(\vec{r})$ and $u_{v,\vec{k}_v}^0(\vec{r})$ are orthogonal.

2.2.4 Electric-Dipole Approximation

Since at typical wavelengths of the incident field ($\lambda=500$ nm) and interatomic distances ($a=0.2-0.3$ nm)

$$\frac{p_{\text{photon}}}{p_{\text{electron}}} = \frac{h/\lambda}{\hbar k} = \frac{h/\lambda}{(h/2\pi)(\pi/a)} = \frac{2a}{\lambda} \approx 10^{-3} \tag{2.24}$$

which shows that the momentum of photon is much less than that of electron, one can neglect \vec{g} . Then, $u_{c,\vec{k}_v+\vec{g}}^0$ can be approximated as $u_{c,\vec{k}_v+\vec{g}}^0 = u_{c,\vec{k}_v}^0 + \vec{g} \cdot \vec{\nabla} u_{c,\vec{k}_v}^0 + \dots \approx u_{c,\vec{k}_v}^0$.

This reasonable approximation is known as electric-dipole approximation [electron-photon interaction Hamiltonian (perturbation term) $\frac{e}{m^* c} \vec{A} \cdot \vec{p}$ is equivalent to $e\vec{r} \cdot \vec{E}$ in the limit $\vec{g} \rightarrow 0$] [19].

Finally, replacing $u_{c,\vec{k}_v+\vec{g}}^0$ with u_{c,\vec{k}_v}^0 in expression (2.23) within the electric-dipole approximation, $c_{c,\vec{k}_c}(t)$ given by expression by (2.17) can be expressed as

$$c_{c,\vec{k}_c}(t) = -\frac{e}{m^*c} |\vec{A}_0| \int_0^t dt' e^{i(E_c^0(\vec{k}_c) - E_v^0(\vec{k}_v))t'/\hbar} e^{-i\omega t'} \int_{\substack{\text{unit} \\ \text{cell}}} d\vec{r} u_{c,\vec{k}_c}^{0*}(\vec{r}) \vec{a}_0 \cdot \vec{\nabla} u_{v,\vec{k}_v}^0(\vec{r}) \quad (2.25)$$

Transition probability within the time t can be expressed as

$$|c_{c,\vec{k}_c}(t)|^2 = \left(\frac{e}{m^*c}\right)^2 |\vec{A}_0|^2 \left| \int_{\substack{\text{unit} \\ \text{cell}}} d\vec{r} u_{c,\vec{k}_c}^{0*}(\vec{r}) \vec{a}_0 \cdot \vec{\nabla} u_{v,\vec{k}_v}^0(\vec{r}) \right|^2 \left| \int_0^t dt' e^{i(E_c^0(\vec{k}_c) - E_v^0(\vec{k}_v) - \hbar\omega)t'/\hbar} \right|^2 \quad (2.26)$$

For large t ,

$$\left| \int_0^t dt' e^{i(E_c^0(\vec{k}_c) - E_v^0(\vec{k}_v) - \hbar\omega)t'/\hbar} \right|^2 = 2\pi\hbar t \delta(E_c^0(\vec{k}_c) - E_v^0(\vec{k}_v) - \hbar\omega) \quad (2.27)$$

Then, transition probability per unit time (Fermi-Golden rule) can be obtained as the following:

$$R_{v \rightarrow c} = \frac{d}{dt} |c_{c,\vec{k}_c}(t)|^2 = \frac{2\pi}{\hbar} \left(\frac{e}{m^*c}\right)^2 |\vec{A}_0|^2 |P_{c\vec{k}_c, v\vec{k}_v}|^2 \delta(E_c^0(\vec{k}_c) - E_v^0(\vec{k}_v) - \hbar\omega) \quad (2.28)$$

where

$$P_{c\vec{k}_c, v\vec{k}_v} = \int_{\substack{\text{unit} \\ \text{cell}}} d\vec{r} u_{c,\vec{k}_c}^{0*}(\vec{r}) \vec{a}_0 \cdot \vec{p} u_{v,\vec{k}_v}^0(\vec{r}) \quad (2.29)$$

is called momentum matrix element.

In order to obtain the number of transitions $R(\hbar\omega)$ per unit time we must sum over all possible states in valence band (occupied) and conduction band (empty) in the unit volume of crystal. Each electron is associated with a six-dimensional phase space: three

positional coordinates x, y, z and three components of momenta p_x, p_y, p_z . Considering Heisenberg uncertainty relations ($\Delta x \Delta p_x \approx h, \Delta y \Delta p_y \approx h, \Delta z \Delta p_z \approx h$), the density of the allowed \vec{k} vectors in the Brillouin zone can be obtained as $V/(2\pi)^3$ where V is the crystal volume. Consequently, $R(\hbar\omega)$ per unit volume of crystal can be expressed as

$$R(\hbar\omega) = \frac{2\pi}{\hbar} \left(\frac{e}{m^* c} \right)^2 |\bar{A}_0|^2 \int_{BZ} \frac{2d\vec{k}}{(2\pi)^3} |P_{c\vec{k}, v\vec{k}}|^2 \delta(E_c^0(\vec{k}) - E_v^0(\vec{k}) - \hbar\omega) \quad (2.30)$$

where the integral is performed over the first Brillouin zone and the factor of 2 arises due to the electron spin degeneracy.

2.2.5 Connection with Optical Constants

Absorption coefficient can be defined as:

$$I(r) = I(0)e^{-\alpha r} \quad (2.31)$$

where $I(r)$ and $I(0)$ are the intensities of the light beam per unit volume at the depth r and surface, respectively. On the other hand, power lost by the field due to absorption in unit volume of the medium can be given as $R(\hbar\omega) = -dI/dt$. Rate of decrease in the energy of the incident beam per unit volume can be expressed as follows:

$$-\frac{dI}{dt} = -\frac{dI}{dx} \frac{dx}{dt} = \alpha I \frac{c}{n} \quad (2.32)$$

where c and n are speed of light and refractive index of the medium, respectively. Time-averaged energy density is related to the electric field amplitude as

$$I = \frac{n^2}{8\pi} |\bar{E}|^2 \quad (2.33)$$

Then, one can write

$$-\frac{dI}{dt} = R\hbar\omega = \alpha \frac{cn}{8\pi} |\vec{E}|^2 \quad (2.34)$$

Using expression (2.30), absorption coefficient can be expressed as

$$\begin{aligned} \alpha &= \frac{8\pi\hbar\omega}{cn|\vec{E}|^2} R = \frac{16\pi^2\omega}{cn} \left(\frac{e}{m^*c}\right)^2 \frac{|\vec{A}_0|^2}{|\vec{E}_0|^2} \int_{BZ} \frac{2d\vec{k}}{(2\pi)^3} |P_{c\vec{k},v\vec{k}}|^2 \delta(E_c^0(\vec{k}) - E_v^0(\vec{k}) - \hbar\omega) \\ &= \left(\frac{4\pi e}{m^*}\right)^2 \frac{1}{cn\omega} \int_{BZ} \frac{2d\vec{k}}{(2\pi)^3} |P_{c\vec{k},v\vec{k}}|^2 \delta(E_c^0(\vec{k}) - E_v^0(\vec{k}) - \hbar\omega) \end{aligned} \quad (2.35)$$

where $|\vec{E}_0| = \frac{\omega}{c} |\vec{A}_0|$ is substituted for $|\vec{E}_0|$.

Since $\varepsilon_2 = \frac{nc}{\omega} \alpha$, ε_2 can be expressed as

$$\varepsilon_2 = \left(\frac{4\pi e}{m^*\omega}\right)^2 \int_{BZ} \frac{2d\vec{k}}{(2\pi)^3} |P_{c\vec{k},v\vec{k}}|^2 \delta(E_c^0(\vec{k}) - E_v^0(\vec{k}) - \hbar\omega) \quad (2.36)$$

2.2.6 Direct Transitions

It was seen above in the text that a charge carrier can be made free by associating it with an effective mass through effective mass approximation. In this approach, one can probe the characteristics (e.g. localized or extended states) of the charge carriers by examining their effective masses. A direct transition (the transition of type where \vec{k} is conserved) from the parabolic region of the valence band to parabolic region of the conduction band in presence of external electromagnetic field is schematically illustrated in Figure 2.1. It is assumed that the maximum of the valence band is located at the point $\vec{k} = 0$. Then, electron energy in the conduction band is

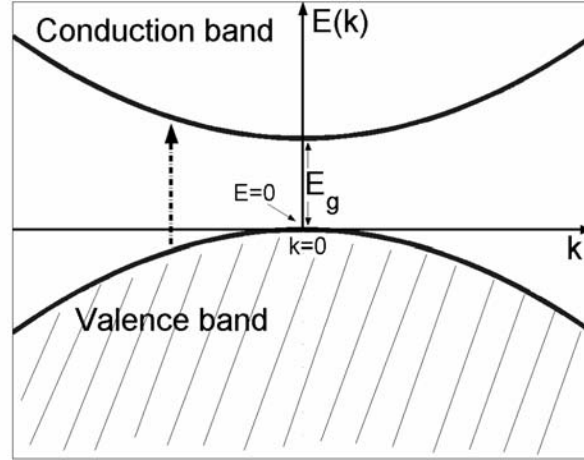


Figure 2.1 Schematic energy band diagram. The functional forms of the energy bands are approximated as parabolic functions of \vec{k} around the maxima and minima at $\vec{k} = 0$ in the frame effective mass approximation. Vertical transitions are produced by an external electromagnetic field.

$$E_c = E_g + \frac{\hbar k^2}{2m_e^*} \quad (2.37)$$

and in the valence band is

$$E_v = -\frac{\hbar k^2}{2m_h^*} \quad (2.38)$$

where E_g is the so called band gap. m_e^* and m_h^* are effective masses for electrons in the conduction band and holes in the valence band, respectively. For such a direct transition, conservation of energy requires

$$E = E_c - E_v = E_g + \frac{\hbar k^2}{2m_e^*} + \frac{\hbar k^2}{2m_h^*} = E_g + \frac{\hbar k^2}{2m_r^*} \quad (2.39)$$

where m_r^* is called effective reduced mass and defined as $\frac{1}{m_r^*} = \frac{1}{m_e^*} + \frac{1}{m_h^*}$. In the frame of effective mass approximation, absorption coefficient can be expressed as

$$\alpha = \left(\frac{4\pi e}{m^*}\right)^2 \frac{1}{cn\omega} \int_{BZ} \frac{8\pi k^2 dk}{(2\pi)^3} |P_{c\vec{k},v\vec{k}}|^2 \delta(E_g + \frac{\hbar k^2}{2m_r^*} - \hbar\omega) \quad (2.40)$$

In most cases, the momentum matrix element $|P_{c\vec{k},v\vec{k}}|^2$ is not strongly dependent on \vec{k} . One can expand $P_{c\vec{k},v\vec{k}}$ around $k = 0$ and retain the first term of expansion $P_{c0,v0}$ as an approximate value of this matrix element. Doing so, the absorption coefficient takes a simpler form as:

$$\alpha = \left(\frac{4e}{m^*}\right)^2 \frac{|P_{c0,v0}|^2}{cn\omega} \int_{BZ} dk k^2 \delta(E_g + \frac{\hbar k^2}{2m_r^*} - \hbar\omega) \quad (2.41)$$

By changing variables as $u = \frac{\hbar k^2}{2m_r^*}$ absorption coefficient becomes

$$\alpha = \left(\frac{4e}{m^*}\right)^2 \frac{|P_{c0,v0}|^2}{cn\omega} \left(\frac{2m_r^*}{\hbar^2}\right)^{3/2} \int_{BZ} du u^{1/2} \delta(u - (\hbar\omega - E_g)) = \frac{B}{n\hbar\omega} (\hbar\omega - E_g)^{1/2} \quad (2.42)$$

where $B = \left(\frac{4e}{m^*}\right)^2 \frac{|P_{c0,v0}|^2}{c\hbar^2} (2m_r^*)^{3/2}$

Up to this point, we assumed that valence band maximum and conduction band minimum occur at the same point in the Brillouin zone. However, there are crystals such as silicon and germanium whose valence band maximum and conduction band minimum do not coincide at the same point of the Brillouin zone. It is known that such experimentally observed transitions, forbidden by momentum conservation, are due to

interaction of electrons with the vibrations of the lattice (phonons) which is not considered in this discussion.

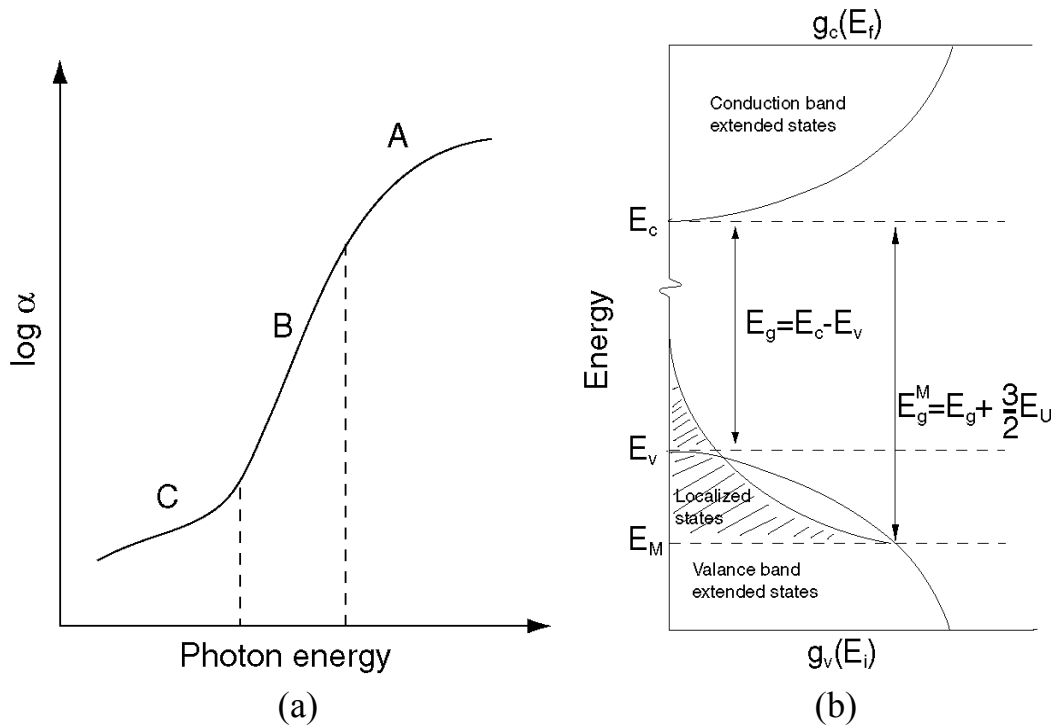


Figure 2.2 (a) An illustration of typical absorption coefficient as a function of photon energy with 3 main energy regions A, B, C. (b) A schematic diagram illustrating roughly the density of states. It should be noted that density of the localized valence band tail states is exaggerated for easy readability [21].

2.3 Optical Absorption in Amorphous Solids

The question, which triggered the interest in amorphous solids, was “Why is glass transparent?”. The studies on these materials showed that, for example in amorphous silicon, short-range order is almost equivalent to the crystalline silicon. In other words, the local bond configuration or coordination number of the atoms in crystalline silicon is preserved in amorphous silicon. D. Weaire demonstrated by using tight binding model that the existence of a gap in a material, which has a short range order, is not dependent on the periodicity of the structure [22]. Many studies on this

subject concluded that short range order in the atomic arrangement is responsible for the absorption edge or band gap in amorphous solids, which explains the puzzling transparency of amorphous solids.

An illustrative typical spectral dependence of absorption coefficient of an amorphous solid is shown in Figure 2.2(a). Although there is no long-range order in amorphous solids it is seen clearly, there exists an absorption edge in the absorption spectra, which suggests the presence of an optical gap. It should be noted that the absorption edge of amorphous solids are broader in comparison to the sharp absorption edge of their crystal counterparts and this broad behavior of absorption edges in amorphous solids do not let to assign a definite threshold energy for optical gap.

In crystals, energy $E(k)$ is defined as a function of k in different directions in the Brillouin zone. However, in amorphous phase, periodicity is absent and the wavenumber k cannot be used to define the electron states since it is undefined in the absence of the reciprocal lattice. Therefore, band structure $E(k)$ cannot be constructed. Since amorphous solids are macroscopically structurally isotropic, an isotropic quantity independent of k , is needed to describe the electronic structure. In this respect, a scalar function called density of states, $g(E)$, which is number of electron states per unit volume lying in unit energy interval around the average energy E has been adopted for the description of the electronic structure of the amorphous phase. However, $g(E)$ describing extended states is not enough due to topological disorder leading to localized electron states. Therefore, states are needed to be labeled according to whether they are localized or extended. In general, fluctuations in bond lengths and angles raise (lower) the energy level of states at the top (bottom) of the valence (conduction) band so that “tail” localized state distributions in the gap result. However, since valence band tailing is found experimentally to be broader than conduction band tailing and consequently, the number of valence band tail states in a-Si is considerably larger, conduction band tail states are neglected in the model shown in Figure 2.2(b). Besides, optical measurements are known to be dominated by the largest of the two band tails. Localization means that electron does not diffuse away from its site at very long times due to the strong

electronic scattering and short coherence length of the wave functions. Coherence length is of the order of the lattice spacing and the resulting uncertainty in the wave vector is of order of the wave vector itself. There exists a mobility edge separating localized and extended states in a band and at this energy the conductivity is expected to change substantially.

Types of optical transitions can be itemized as follows:

- (a) transitions between valence and conduction band extended states,
- (b) transitions between valence band tail and conduction band extended states,
- (c) transitions between valence band extended and conduction band tail states
- (d) transitions between valence and conduction band tail states.
- (e) transitions between mid-gap states (dangling bonds) and extended states.

Transitions of types (c), (d) and (e) are neglected in this study. The latter is neglected because the transition matrix elements between localized states are very small. Let's, first, examine transitions of type (a).

2.3.1 Transitions Between Valence and Conduction Band Extended States

Similar to crystalline phase, using the effective mass approximation, density of final and initial energies of the extended states in conduction band and valence band, respectively, for a unit volume of space can be written at least around the band edge regions as

$$g_v(E_i) = \frac{1}{2\pi^2} \left(\frac{2m_h^*}{\hbar^2} \right)^{3/2} (E_v - E_i)^{1/2} \quad (2.43)$$

$$g_c(E_f) = \frac{1}{2\pi^2} \left(\frac{2m_e^*}{\hbar^2} \right)^{3/2} (E_f - E_c)^{1/2} \quad (2.44)$$

where m_h^* and m_e^* are hole and electron effective masses, respectively. The absorption coefficient derived for crystalline materials

$$\alpha = \left(\frac{4e}{m^*} \right)^2 \frac{|P_{c0,v0}|^2}{cn\omega} \int_{BZ} dk k^2 \delta(E_g + \frac{\hbar k^2}{2m_r^*} - \hbar\omega), \quad (2.45)$$

by omitting momentum selection rule ($\Delta k = 0$) in the formulation, can be reformulated as

$$\alpha = \left(\frac{4e}{m_e^*} \right)^2 \frac{|P_{c,v}|^2}{cn\omega} \int dE_f g_v(E_f - \hbar\omega) g_c(E_f) \quad (2.46)$$

where energy is conserved during the transition and $|P_{c,v}|^2 = P(E)$ is the square of momentum matrix element which is assumed to be independent of photon energy ($P_{c,v} = \int d\vec{r} u_{c,E_c,f}^{0*}(\vec{r}) \vec{a}_0 \cdot \vec{p} u_{v,E_f-\hbar\omega}^0(\vec{r})$). Substituting corresponding density of states in equation (2.46), the following expression is obtained:

$$\alpha = \frac{32e^2 |P_{c,v}|^2}{\pi^2 \hbar^6 m_e^{*2} cn\omega} (m_e^* m_h^*)^{3/2} \int dE_f (E_f - E_c)^{1/2} (E_v + \hbar\omega - E_f)^{1/2} \quad (2.47)$$

E_f must lie in the range $E_c < E_f < E_v + \hbar\omega$. Let's define a new variable as

$y = \frac{E_f - E_c}{\hbar\omega - E_g}$. Substituting y into the integral in expression (2.47) and noting that

$$\int dy y^{1/2} (1-y)^{1/2} = \frac{\Gamma(3/2)\Gamma(3/2)}{\Gamma(3)} = \frac{\pi}{8}, \quad \alpha \text{ and } \varepsilon_2 (= \frac{nc}{\omega} \alpha) \text{ can be expressed as}$$

$$\alpha = B_\alpha^a (\hbar\omega - E_g)^2, \quad \varepsilon_2 = B_\varepsilon^a (\hbar\omega - E_g)^2 \quad (2.48)$$

where, $B_\alpha^a = \frac{4e^2 |P_{c,v}|^2 \bar{m}^3}{\pi \hbar^6 m_e^{*2} c n \omega}$, $B_\varepsilon^a = \frac{4e^2 |P_{c,v}|^2 \bar{m}^3}{\pi \hbar^6 m_e^{*2} \omega^2}$ and $\bar{m} = (m_e^* m_h^*)^{1/2}$. The superscript a

associated with coefficient B is used to indicate amorphous case.

The above expressions (2.48) arise by transitions between fully coordinated bonds (extended states) without translational symmetry of the structure due to the fluctuations both in bond lengths and bond angles (ideal amorphous structure). Let's, second, examine transitions of type (b).

2.3.2 Transitions Between Valence Band Tail and Conduction Band Extended States

As it is seen from Figure 2.2(b), at a particular energy, E_M , valence density of states starts to decrease exponentially and conduction density of states is a parabolic function. Densities of states in the tail and in the parabolic region of the valence band are defined as

$$g_{vt}(E_i) = K e^{\frac{-(E_i - E_M)}{E_V}} \quad \text{for } E_i > E_M \text{ (tail region)} \quad (2.49)$$

$$g_{vb}(E_i) = N_v (E_v - E_i)^{1/2} \quad \text{for } E_i < E_M \text{ (band region)} \quad \text{with } N_v = \frac{1}{2\pi^2} \left(\frac{2m_h^*}{\hbar^2} \right)^{3/2} \quad (2.50)$$

Since $g_{vt}(E_i)$ and $g_{vb}(E_i)$ must be equal to each other at $E_i = E_M$, K may be expressed as $K = N_v (E_v - E_g^M)^{1/2}$. One more condition on this exponential tail states distribution is that their total number for $E > E_M$ should be equal to the total number of parabolic

states that would exist in the interval $E_M < E < E_v$. Thus, $\int_{E_M}^{\infty} dE_i g_{vt}(E_i) = \int_{E_M}^{E_v} dE_i g_{vb}(E_i)$

leads to $E_v - E_M = \frac{3}{2} E_U$.

The density of states in the conduction band edge is expressed as

$$g_{cb}(E_f) = N_c (E_f - E_c)^{1/2} \quad \text{with} \quad N_c = \frac{1}{2\pi^2} \left(\frac{2m_e^*}{\hbar^2} \right)^{3/2} \quad (2.51)$$

Within these approximations, the expression of the absorption coefficient α given by the relation (2.46) can be written in the following form:

$$\begin{aligned} \alpha &= \left(\frac{2e}{m_e^* \pi^2 \hbar} \right)^2 \frac{|P_{c,v}|^2}{cn\omega} (2\bar{m})^3 \left(\frac{3}{2} E_U \right)^{1/2} \int dE_f e^{-\frac{(E_f - E_M - \hbar\omega)}{E_U}} (E_f - E_c)^{1/2} \\ &= \left(\frac{2e}{m_e^* \pi^2 \hbar} \right)^2 \frac{|P_{c,v}|^2}{cn\omega} (2\bar{m})^3 \left(\frac{3}{2} \right)^{1/2} (E_U)^2 e^{\frac{(E_M - E_c + \hbar\omega)}{E_U}} \int_0^{\infty} dt e^{-t} t^{1/2} \quad \text{with} \quad t = \frac{E_f - E_c}{E_U} \quad (2.52) \end{aligned}$$

Noting that $\int_0^{\infty} dt e^{-t} t^{1/2} = \Gamma(3/2) = \frac{\sqrt{\pi}}{2}$, absorption coefficient α can be expressed as

$$\alpha(\hbar\omega) = K_{tb} e^{\frac{\hbar\omega}{E_U}} \quad \text{with} \quad K_{tb} = \left(\frac{2e}{m_e^* \pi^2 \hbar} \right)^2 \frac{|P_{c,v}|^2}{cn\omega} (2\bar{m})^3 \left(\frac{3}{2} \right)^{1/2} \frac{\sqrt{\pi}}{2} (E_U)^2 e^{-\frac{E_g^M}{E_U}} \quad (2.53)$$

As a result, optical transition from exponentially distributed valence band tail states would give an exponential spectral dependence of $\alpha(\hbar\omega)$, notably different from the previous case. This difference may be used for determining the tail state distribution from the $\alpha(\hbar\omega)$ spectrum.

Up to this point, square of momentum matrix element is assumed to be independent of photon energy. Using the following commutation $m \frac{d\vec{r}}{dt} = \vec{p} = \frac{im_e^*}{\hbar} [H, \vec{r}]$, momentum matrix element $P_{c,v} = \int d\vec{r}' u_{c,E_c,f}^{0*}(\vec{r}') \vec{a}_0 \cdot \vec{p} u_{v,E_c,f-\hbar\omega}^0(\vec{r}')$ becomes:

$$P_{c,v} = \frac{im_e^*}{\hbar} \int d\vec{r}' u_{c,E_c,f}^{0*}(\vec{r}') (H\vec{a}_0 \cdot \vec{r}' - \vec{a}_0 \cdot \vec{r}' H) u_{v,E_c,f-\hbar\omega}^0(\vec{r}') = im_e^* \omega \vec{a}_0 R_{c,v} \quad (2.54)$$

where $R_{c,v} = \int d\vec{r}' u_{c,E_c,f}^{0*}(\vec{r}') \vec{r}' u_{v,E_c,f-\hbar\omega}^0(\vec{r}')$

Using the last relation, the expression of α (2.46) becomes:

$$\alpha = (4e)^2 \frac{\omega}{cn} \int dE_f |\vec{a}_0 \cdot R_{c,v}|^2 g_v(E_f - \hbar\omega) g_c(E_f) \quad (2.55)$$

The directional average of $|R_{c,v}|^2$ yields $\frac{1}{3} R_{c,v}^2$. For amorphous materials and unpolarized light, $|R_{c,v}|^2$ can be replaced with the $\frac{1}{3} |R_{c,v}|^2$. Moreover, one can average square of the dipole matrix element over all transitions. Then, α becomes [23]

$$\alpha = (4e)^2 \frac{\omega}{3cn} \left[|R_{c,v}|^2 \right]_{av} \int dE_f g_v(E_f - \hbar\omega) g_c(E_f) \quad (2.56)$$

where $\left[|R_{c,v}|^2 \right]_{av} = \frac{\int dE_f |R_{c,v}|^2 g_v(E_f - \hbar\omega) g_c(E_f)}{\int dE_f g_v(E_f - \hbar\omega) g_c(E_f)}$

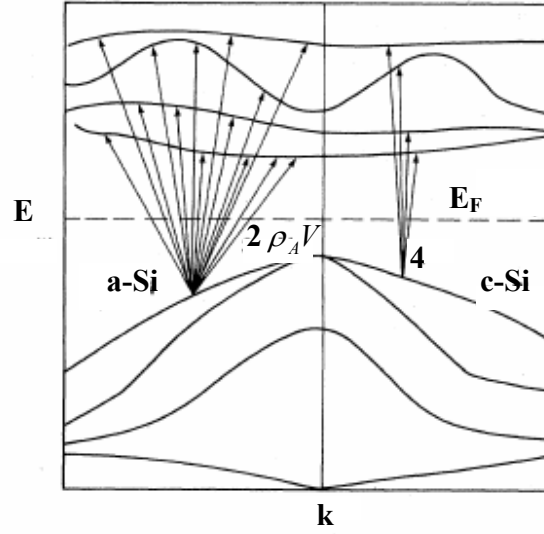


Figure 2.3 Nonzero optical matrix elements for a-Si and c-Si from a particular valence band state (from Jackson *et al.* [23]).

$\left| \left[R_{c,v} \right]_{av}^2 \right|$ is the square of the dipole matrix element averaged over all transitions separated by the energy $\hbar\omega$. In crystals where \vec{k} is a good quantum number, averaging is performed only over the transitions conserving \vec{k} . This \vec{k} -conserving average is expected to be larger in comparison to non- \vec{k} -conserving average which is the case for amorphous silicon. In amorphous silicon, Jackson *et al.* [23] argued that there can be possibly $2\rho_A V$ number of transitions, as shown in Figure 2.3, between a particular single spin valence band state with a wave vector \vec{k} and $2\rho_A V$ number of single spin conduction band states with a general wave vector \vec{k}' for a range of photon energy where ρ_A and V is approximately the atomic density of c-Si and the illuminated volume, respectively. However, for c-Si, only 4 of $2\rho_A V$ transitions from a particular valence band are nonzero if \vec{k} -conservation is taken into account. In other words, a single matrix element for an individual transition in amorphous material is roughly $\frac{\rho_A V}{2}$ times smaller than an allowed matrix element for c-Si. In this respect, it would be useful to define normalized average matrix element $R(E)^2$ as

$$R(E)^2 = \frac{\rho_A V}{2} \left[|R_{c,v}|^2 \right]_{av} \quad (2.57)$$

$R(E)^2$ can be used to directly compare non-k-conserving c-Si with a-Si:H and with c-Si band structure calculations where k-conservation is taken into account. It is shown experimentally for a-Si:H by Jackson *et al.* that $R(E)^2$ has no appreciable energy dependence for energies between 0.6 and 3.0 eV. In this energy interval $R(E)^2$ has a magnitude of $\approx 10 \text{ \AA}^{-2}$. On the other hand, it should be noted that theoretical analysis done by S.K. O'Leary [24] do not predict the spectral dependence of $R(E)^2$ that is observed experimentally by Jackson *et al.* Numerical calculations in this study shows that spectral dependence of $R(E)^2$ depends on the relative positions of abrupt mobility edges at valence and conduction bands with respect to critical points at which exponential and square-root distributions of density of states interface. It is found that spectral variation of $R(E)^2$ saturates beyond the mobility gap but decreases very sharply just below the mobility gap. If the mobility edges are at the below and above the conduction and valence bands, respectively, it is observed that the spectral dependence of $R(E)^2$ is small. However, although Jackson *et al.* determined a large mobility gap their results show no spectral dependence of $R(E)^2$ whereas S.K. O'Leary's analysis predicts a significant spectral dependence of $R(E)^2$.

2.3.3 Results

For transitions of type (a), the expressions for α and ε_2 becomes

$$\alpha = B_\alpha^{a'} (\hbar\omega - E_g)^2, \quad \varepsilon_2 = B_\varepsilon^{a'} (\hbar\omega - E_g)^2 \quad (2.58)$$

where $\varepsilon_2 = \frac{nc}{\omega} \alpha$, $B_\alpha^{a'} = \frac{4e^2 |R_{c,v}|^2 \bar{m}^3 \omega}{3\pi\hbar^6 cn}$ and $B_\varepsilon^{a'} = \frac{4e^2 |R_{c,v}|^2 \bar{m}^3}{3\pi\hbar^6}$.

Let us note that if densities of states instead of parabolic variations are defined in the following more general form $g_v(E) \approx \text{const} \times (E_v - E)^p$, $g_c(E) = \text{const} \times (E - E_c)^s$, α and ε_2 can be expressed as

$$\alpha \approx \text{const} \times \omega(\hbar\omega - E_g)^{s+p+1}, \quad \varepsilon_2 \approx \text{const} \times (\hbar\omega - E_g)^{s+p+1} \quad (2.59)$$

Note that for linear bands ($p = s = 1$) the spectral variation of α becomes superquadratic, that is, cubic.

Optical gaps, within the frame of effective mass approximation (square root dependence of density of state distributions of both around the extrema of valence and conduction bands), can be determined by assuming two approximate approaches:

- 1- Constant momentum matrix approximation (Tauc's method) [25].
- 2- Constant dipole matrix approximation (Cody's method) [26].

In Tauc's method, where the momentum matrix element is approximated to be independent of photon energy, α and ε_2 is expressed as

$$\sqrt{\hbar\omega\alpha} = B_\alpha^{\text{Tauc}} (\hbar\omega - E_g^{\text{Tauc}}) \quad B_\alpha^{\text{Tauc}} = \sqrt{B_\alpha^a / \hbar\omega} \quad (2.60)$$

$$\sqrt{\varepsilon_2} = B_\varepsilon^{\text{Tauc}} (\hbar\omega - E_g^{\text{Tauc}}) \quad B_\varepsilon^{\text{Tauc}} = \sqrt{B_\varepsilon^a} \quad (2.61)$$

In this method, first, $\sqrt{\hbar\omega\alpha}$ or $\sqrt{\varepsilon_2}$ is plotted as a function of photon energy $\hbar\omega$. Then, the linear functional dependence of $\sqrt{\hbar\omega\alpha}$, which is observed at energies greater than optical gap (where distribution of density of states is significant), is fitted to a linear function and extrapolated to $\sqrt{\hbar\omega\alpha} = 0$. The intercept gives the threshold energy value (band gap) for optical absorption between valence and conduction band extended states.

In Cody's method, where the dipole matrix element is approximated to be independent of photon energy, α and ε_2 is expressed as

$$\sqrt{\frac{\alpha}{\omega}} = B_{\alpha}^{Cody} (\hbar\omega - E_g^{Cody}) \quad \text{with} \quad B_{\alpha}^{Cody} = \sqrt{B_{\alpha}^{a'}} \hbar\omega \quad (2.62)$$

$$\sqrt{\varepsilon_2} = B_{\varepsilon}^{Cody} (\hbar\omega - E_g^{Cody}) \quad \text{with} \quad B_{\varepsilon}^{Cody} = \sqrt{B_{\varepsilon}^{a'}} \quad (2.63)$$

The determination procedure of the optical gap in this approximation is same as Tauc's method except the functional forms of α and ε_2 given above.

Any deviation from the linear behavior in the low energy part of the above plotting suggests that other types (e.g. localized to extended, extended to localized and localized to localized) of transitions are becoming dominant for this energy range.

If the absorption data follow a superquadratic [27] rather than quadratic energy dependence, one can conclude that different functional dependences of density of states need to be used in the analysis instead of parabolic density of states. For example, cubic dependence of α or ε_2 suggests that energy dependence of densities of states in the bands is linear. On the other hand, if constant behavior of matrix elements is considered to be doubtful, one can conclude that superquadratic dependence of α or ε_2 may occur due to enhancement of absorption by an energy dependent matrix element. In order to understand the origin of excess absorption, one must use additional experimental information or choose the most reasonable explanation in the light of relevant literature.

An alternative measure of optical gap (E_{04}) is defined as an energy point in the absorption spectrum where the absorption coefficient reaches 10^4 cm^{-1} . Determination of E_{04} is possible even from only a limited range of optical absorption data, without any

approximations on momentum or dipole matrix elements. This practical aspect of E_{04} may be envisaged as simplicity but it should be noted that E_{04} does not give any information about nature of the density of state distribution in the relevant bands and transitions. It is sometimes easier to measure and interpret the changes rather than the absolute magnitude of the quantity itself. In this respect, E_{04} is probably more useful for comparing band gaps of different materials.

For transitions of type (b), functional behavior of absorption coefficient given by expression (2.53) alternatively can be expressed as $\log \alpha = \log(K_{tb}) + \frac{1}{E_U} \hbar \omega$ leading to the Urbach slope E_U from the inverse logarithmic slope. The inverse logarithmic slope of the trap distribution for a-Si:H is found to be identical within the experimental error to the quantity E_U [21]. Drift mobility measurements also show that localized states tailed from conduction band into the gap exhibits a similar exponential behavior with a $E_U^c \approx \frac{1}{2} E_U^v$ where superscripts c and v denote the conduction and valence bands, respectively. Photomodulated infrared absorption measurements also confirm this result [28].

Cody claims that Tauc gap and Urbach slope are linearly related [29] and it makes little difference whether the Tauc gap or Urbach slope is used as a measure of disorder in the amorphous material at hand [21]. Now let us discuss a bit more in detail the Urbach edge.

2.4 Exponential Spectrum (Urbach edge) of Optical Absorption in Amorphous Semiconductors

Exponential dependence of absorption coefficient was first pronounced for the alkali halide crystal AgBr [30]. Similar exponential relationships have been observed for many insulators and crystalline semiconductors. Various models predicted such an exponential tail in the absorption spectrum. W. Franz and L.V. Keldish [31, 32]

independently have considered the effect of internal electric fields on the absorption edge of a semiconductor and showed that the absorption edge tails off exponentially at energies lower than the forbidden gap. Later, Dow and Redfield have considered electron-hole interaction and internal electric fields together, and found that internal electric fields cause broadening in the direct exciton transitions leading to an exponential tail. In the meantime, it is concluded that the dominant sources of electric fields vary from material to material and may be optical phonons, impurities and dangling bonds, or other potential fluctuations associated with disorder [33]. Eventually, such an exponential dependence concluded to be a universally observed behavior and Dow and Redfield [34] have asserted that a single physical mechanism must be the cause of all the exponential absorption edges although, even today, the mechanism is considered to be unclear despite extensive experimental and theoretical studies [35]. Recently, a first principle theory has been developed by C.H. Grein and S. John who present the effect of thermal and static site disorder on the absorption edge of crystalline and amorphous semiconductors and predicts an exponential edge. Exponential edge is believed to be arising from three fundamental effects [36]:

- (i) static potential wells arising from impurities or structural disorder,
- (ii) quasi-static potential wells arising from phonons,
- (iii) effect of electric field on excitons

2.4.1 Potential Energy Distributions of Atoms

On the other hand, the above physical mechanisms, which are introduced to explain the exponential tail in the density of the states, generally tend to obscure a common feature. This quasi-universal property arises from Gaussian distribution of local potential wells.

In the presence of long-range order (translational symmetry) electrons (or other quantum objects such as phonons) can move unrestrictedly (Bloch type) throughout the whole system. There is a constant phase relation between the wavefunction at different lattice sites as shown in Figure 2.4(a). However, in reality, there are always distortions

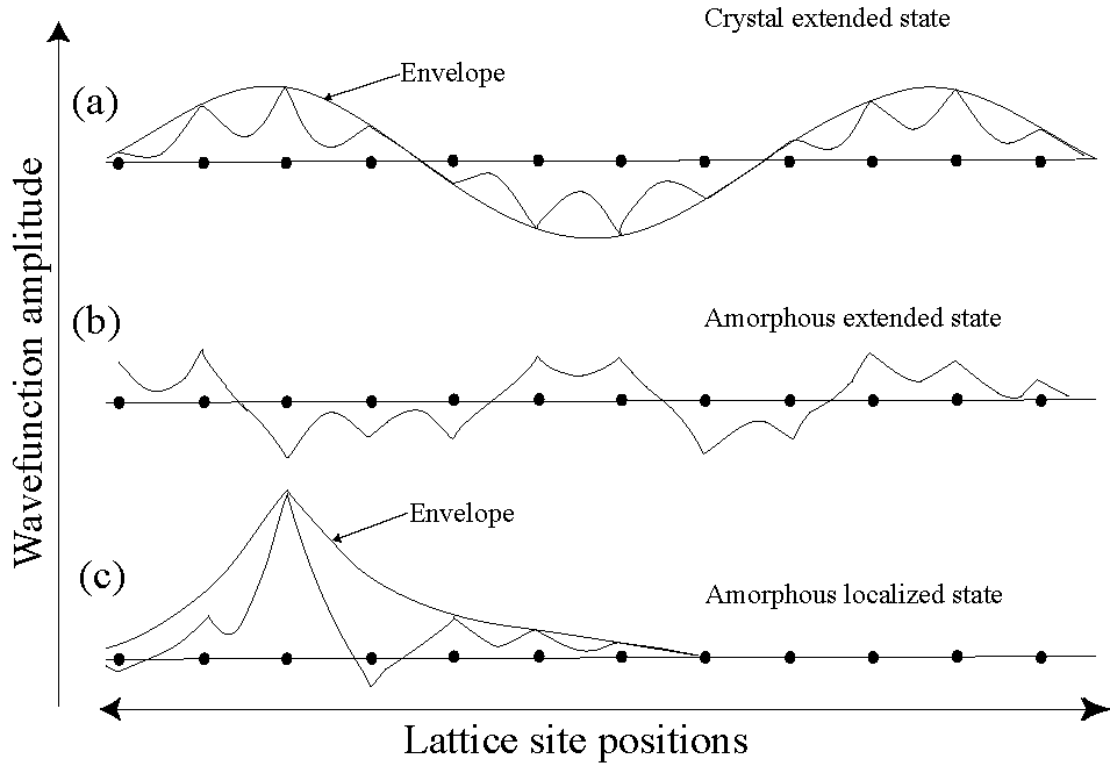


Figure 2.4. Illustration of the wavefunctions of (a) crystal extended , (b) amorphous extended and (c) amorphous localized states [2].

of the ideal order due to the presence of impurities, dislocations, vacancies and other defects. This disordering causes scattering of electrons and the wavefunction loses its phase coherence over a distance of one or two inter-atomic distances as shown in Figure 2.4(b). A stronger disorder potential confines the wavefunction to a small volume of material rather than being extended and causes electron localization as shown in Figure 2.4(c). As long as the concentration of any kind of distortions of the ideal order is small, one can construct the wave functions of an electron or hole in an amorphous solid as linear combinations of the Bloch functions in the same band of the corresponding crystal [37]. In a disordered medium, an electron can be described by a Hamiltonian in the form:

$$H = H_0 + H_1 \quad (2.64)$$

where $H_0 = \frac{p^2}{2m^*}$ is unperturbed Hamiltonian which is valid within the neighborhood of a band edge and

$$H_1 = \sum_{j=1}^N V_j(r - R_j) \quad (2.65)$$

which represents the perturbation of the effective potential in which the electron moves and is sufficiently small. V_j is the potential energy of an atom at the site R_j and N is the number of atoms. H_1 can be expressed in terms of some matrix elements V_j which are random variables possessing probability distribution $p(V_j)$. As a very large number of defects constituting randomly the disorder, the corresponding amount of the potential V_j of each one might reasonably have a distribution $p(V_j)$ of Gaussian type. Central limit theorem holds saying that when a random process results from the summation of infinitely many random elementary events, then this process will tend to have Gaussian probability distribution [38-40]:

$$p(V_j) = \frac{1}{\sqrt{2\pi}\sigma} \exp\left(-\frac{V_j^2}{2\sigma^2}\right) \quad (2.66)$$

where σ^2 is the standard deviation of independent local potentials V_j from the average potential $\bar{V} = 0$.

2.4.2 Potential Well Model

One can simply model one-particle potentials V_j ($j = 1, 2, \dots, N$) as a collection of local (i.e., of atomic scale) potential wells by which the particle can be scattered or trapped. Let's consider a three dimensional spherical symmetric potential well of depth V_0 as shown in Figure 2.5 [41].

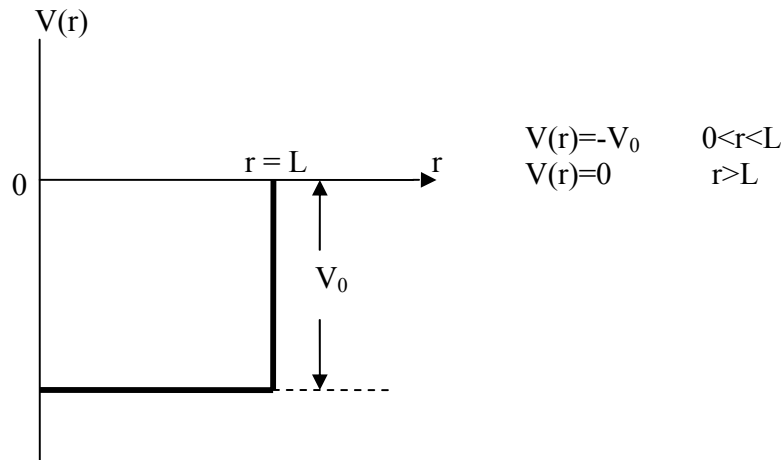


Figure 2.5. Spherically symmetric potential well of depth V_0 and radius L .

It is well known that one can express the relatively complex radial Schrödinger equation, by appropriate change of variables, in a similar form of one-dimensional Schrödinger equation [42]. If one restricts the problem to lowest energy of a given well (that is, with orbital quantum number $l=0$), the solution to the spherically symmetric potential well can be expressed in the following form

$$\tan \sqrt{\frac{2m^*(V_0 - |E|)}{\hbar^2}} L = -\sqrt{\frac{V_0 - |E|}{|E|}} \quad (2.67)$$

where $|E|$ is the binding energy.

Defining energy scales as

$$\varepsilon_L = \frac{\hbar^2}{2mL^2} \quad (2.68)$$

or

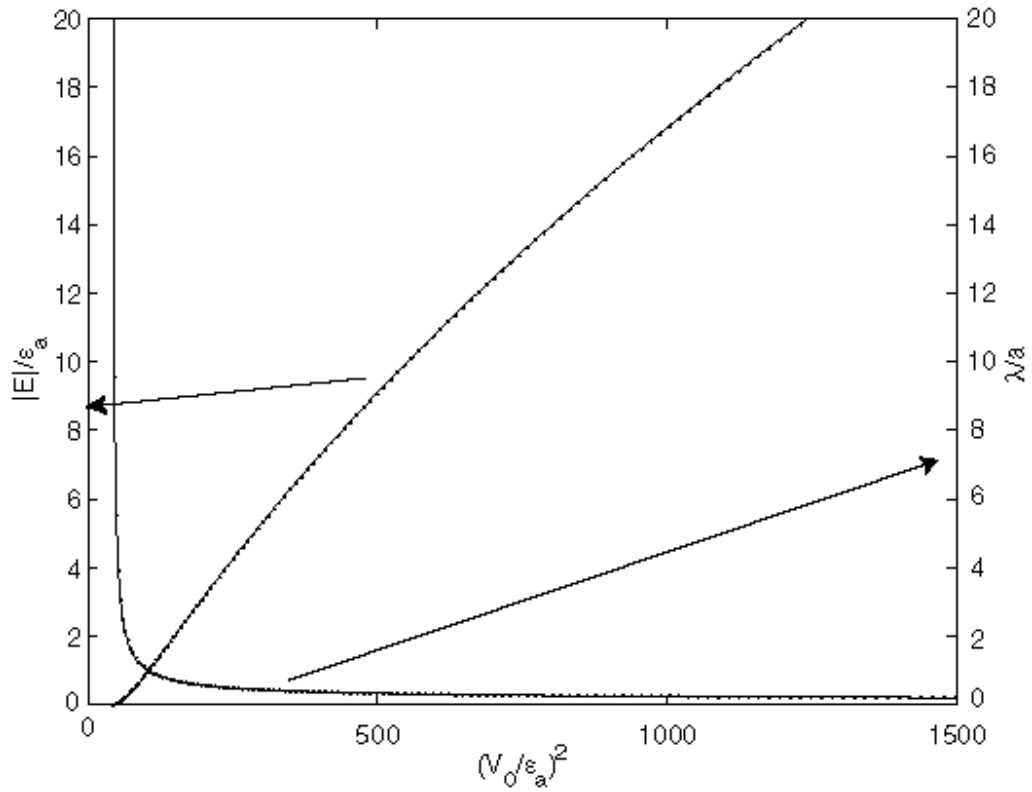


Figure 2.6. Binding energy $|E|$ and decay length λ of the ground state in a steplike spherical potential well of depth V_0 and volume a^3 .

$$\varepsilon_a = \frac{\hbar^2}{2ma^2}, \quad (2.69)$$

where $a^3 = \frac{4\pi}{3}L^3$, one can rewrite the equation (2.67) in the following form [43]:

$$\tan \sqrt{(w-f)} = -\sqrt{\frac{w-f}{f}} \quad (2.70)$$

where $w = \frac{V_0}{\varepsilon_L}$ and $f = \frac{|E|}{\varepsilon_L}$ which are dimensionless parameters. $\frac{|E|}{\varepsilon_a}$ can be plotted as

a function of $\left(\frac{V_0}{\varepsilon_a}\right)^2$ as shown in Figure 2.6. The decay length

$$\lambda = \frac{\hbar}{\sqrt{2m|E|}} = \frac{a}{\sqrt{|E|/\varepsilon_a}}$$

of the bound state is also shown in the length scale of a in Figure 2.6. For $V_0 < V_c = 6.41\varepsilon_a$ (or $V_0 < 2.47\varepsilon_L$), there is no bound state. As V_0 just exceeds $6.41\varepsilon_a$ (or $2.47\varepsilon_L$), a bound state appears with a huge decay length.

Depending on the depth parameter $\left(\frac{V_0}{\varepsilon_a}\right)^2$ and decay length parameter $\frac{\lambda}{a}$, three different functional forms can be assigned to $V(|E|)$:

Region 1: $\frac{\lambda}{a} \gg 1$, very large decay length, weakly bound regime :

$$|E| \sim (V_0 - V_c)^2 \quad (2.71)$$

or

$$\begin{aligned} V_0^2 &\sim (|E|^{1/2} + V_c)^2 = |E| + 2V_c |E|^{1/2} + V_c^2 \\ &\sim |E|^{1/2} \end{aligned} \quad (2.72)$$

where $|E| \ll |E|^{1/2}$ for $|E| \ll 1$, thus $|E|$ term is neglected.

Region 2: $\frac{\lambda}{a} \sim 1$, decay length is of the order of inter-atomic distance:

$$|E| \sim AV_0^2 + B \quad (2.73)$$

Region 3: $\frac{\lambda}{a} \ll 1$, for large binding energies ($|E| > 100V_c$), that is, for short decay

lengths ($\frac{\lambda}{a} < 0.1$):

$$|E| \sim CV_0 + D, \text{ very low density of states.} \quad (2.74)$$

On the other hand, one can express one-electron density of states as follows [43]:

$$\rho(E) = 2\chi p(V(E)) \left| \frac{dV(E)}{dE} \right| \quad (2.75)$$

where the factor of 2 accounts for the spin degeneracy, χ denote the average number of wells per unit volume and $p(V(E))$ is the probability of occurrence of $V(E)$, that is, the distribution function. Using this equation, it is possible to find one-electron density of states (DOS) for three regions seen in Figure 2.6:

DOS for region 1:

$$\rho(E) \propto \exp\left(-\frac{|E|^{1/2}}{2\sigma^2}\right) \quad \text{Halparin-Lax (HL) regime} \quad (2.76)$$

DOS for region 2:

$$\rho(E) \propto \exp\left(-\frac{|E|}{E_U}\right) \quad (2.77)$$

where $E_U = 2A\sigma^2$ is the Urbach parameter.

DOS for region 3:

$$\rho(E) \propto \exp\left(-\frac{|E|^2}{2\sigma^2}\right) \quad (2.78)$$

The energy width of the exponential behavior linear in energy (Urbach tail), in region 2, is much larger than the HL regime which is found by experiment [44]. The near tails (HL regime) are dominated by states trapped in clusters of atomic sites. These

cluster-trapped states dominate over a very narrow range of energies. The deeper tails are usually dominated by single-site bound states [45].

The general behavior can be written as follows:

$$\rho(E) \propto \exp\left(-\frac{|E|^n}{2\sigma^2}\right) \quad (2.79)$$

where n is equal to 1 for Urbach tail. In the energy range over which absorption spectrum exhibits an exponential behavior linear in energy, n is shown to be varying from $n \approx 1$ to 1.2 for the screened Coulomb potential and from 0.7 to 0.9 for a Gaussian potential as energy decreases [46]. It is illustrated that $n \approx 1$ is expected for reasonable potentials in the observed energy range for a-Si:H by Abeles *et. al.* [47]. The deviations from $n \approx 1$ are shown to be in the direction of smaller n at high E and larger n at low E which is consistent with the deviations observed in the typical experimental result shown in Figure 2.2(a) [46]. Transient-photocurrent measurements on As_2Se_3 showed independently from assumptions about optical matrix elements that density of states is exactly exponential over almost five decades of density [44]. Besides, the validity of equation, $|E| \sim AV_0^2 + B$, in region 2 does not depend on the validity of the effective mass approximation. This is proved by various models such as tight binding model in a simple cubic lattice with single site potential well, tight binding model considering a semicircular density of states with single site potential well and tight binding model for hydrogenated amorphous silicon [48]. In all cases it is found that there is an energy range of validity of this equation.

It should be remembered that lattice oscillations produce fluctuating time dependent local potentials with a Gaussian distribution and with an extent of atomic size. Because of the short time scale of optical absorption events, lattice displacements due to thermal fluctuations may be considered frozen in, that is static. Such thermal fluctuations contribute to the disorder which is probed by the electron. In other words, they give rise to another independent contribution leading to Gaussian distribution [45,

48]. Consequently, in the presence of both Gaussian static disorder and phonon-induced fluctuations, one obtains a Gaussian distribution with a total variance given by the sum of the static disorder variance σ_s^2 and the thermal variance σ_T^2 :

$$\sigma^2 = \sigma_s^2 + \sigma_T^2 \quad (2.80)$$

For $\sigma \cong 1.6$ eV one finds from equation $E_0 = 2A\sigma^2$ that, by substituting the constant A from numerical calculations, $E_U = 16$ meV for the conduction band and $E_V = 36$ meV for the valence band [48]. These results are in agreement with experimental estimates [21].

Finally, let's briefly review some results. B. I Halperin and M. Lax [49] considered Gaussian statistic for potential fluctuations for shallow-energy tail states near the band edge to explain linear exponential edge. J.D. Dow and D. Redfield [33] claimed that electric field induced ionization of the exciton is the only mechanism consistent with existing data which can explain exponential edges in both ionic and covalent solids in a unified manner. In this model, the dominant sources of electric microfields are potential fluctuations of various kinds associated with disorder. M. Schreiber and Y. Toyozawa [50] demonstrate that the Urbach tail can be explained as an effect of the phonon field on the translational form of the exciton. In this model, they considered the thermal distribution of exciton-phonon interaction modes as Gaussian distribution. C.H. Grein and S. John [36, 51-53] presents a first principles theory of the effect of thermal and static Gaussian site disorder on the absorption edge of crystalline and disordered semiconductors. Their theory is remarkably in agreement with experiment. They conclude the universality of the linear exponential edge is essentially the universality of short range order in disordered solids. S. Abe and Y. Toyozawa [54] developed a theory within the frame of coherent potential approximation which concludes that the exponential behaviour results from a interplay between transfer energy and Gaussian distributed site energies. The most remarkable aspect of the above

models apart from their detailed physical mechanisms that all these models have a common feature of a fluctuating potential associated with Gaussian statistics.

In conclusion, although various physical mechanisms have been assumed and different formalisms have been employed, the implicit basic position is that the exponential tail of $\rho(E)$ should be explainable solely on the basis of random potential fluctuations [55].

Next, let's review some interesting observations:

- 1) Logarithmic slope of the absorption coefficient in the Urbach regime is about 50 meV for many amorphous semiconductors [a-Si:H, Se, As₂S₃, As₂S₅, As₂Se₃, As₂SeTe₂, As₂Se₂Te, CdGeAs₂ [56], a-Ge-Se compounds [57]. Moreover, this value is of the same order of magnitude of E_U in some crystalline semiconductors. In this respect, one is faced with the following question: Why do the band gaps of amorphous semiconductors with the same E_U vary in a broad range?

The answer to above, Tauc's question asked in 1972, is clear in the frame of above discussion. All these materials have a common property of potential fluctuations due to various kinds of disorder.

- 2) It is observed that absorption edge of a-Si:H broadens (E_U increases) and shifts to lower energy (E_g decreases) either with increasing thermal disorder or with structural disorder. There is a striking similarity between the temperature dependences of E_U and E_g . The linear relationship between E_U and E_g suggests that their temperature dependences have the same functional form. Such a relationship is satisfied either by hydrogen evolution (structural disorder) or by changing the measurement temperature. This result suggests a model explaining the observations that takes the equivalence of thermal and structural disorder into account [29].

- 3) The results of different experimental techniques (photoelectric total yield, dispersive transport, capacitance, photothermal deflection spectroscopy and photoconductivity measurements) agree remarkably on the shape of the density of states of a-Si:H. Particularly, band tails have been observed to have exponential forms [23, 58].

CHAPTER 3

OPTICS OF HOMOGENEOUS MULTILAYER THIN FILMS

3.1 Introduction

Optical measurements on solids can provide information if one develops a relationship for the interaction between the response of the external electromagnetic field and the physical model of the solid. The physical model is not unique and determined by the length and time scale of the light. For example, in the infrared wavelengths solid is modeled rather by atomic interactions whereas in the ultraviolet and visible spectral range mainly by electronic interactions.

Apart from the energy scale of electromagnetic field, although there are different measurement methods to determine optical properties of a solid, these methods may be sensitive to different properties even in the same energy scale. For example, a phase sensitive measuring technique (e.g., ellipsometry) may not be envisaged at first as a suitable technique for determining the bulk properties, whereas phase sensitivity can be useful to extract the surface properties. Moreover, the solid may put some limitations on the choice of the experimental techniques. For example, for solids with ‘dirty’ surfaces (not specially prepared, cleaned), it is not possible to describe the surface exactly due to their unpredictable surface properties which affects in complicating ways the measured optical response. Therefore many forms of spectroscopy techniques are useful for obtaining different types of complementary information.

In the first part of this chapter, the theoretical description of the interaction of electromagnetic radiation with solid is discussed on the basis of Maxwell's equations. The material parameters such as complex refractive index and dielectric function are introduced. Next, since the knowledge of optical functions, complex refractive indices or dielectric function, defines the optical behavior of the solid, the method of evaluation of such functions from the transmittance and reflectance measurements is given by the description of the optical phenomena occurring at the interface of ambient medium and the solid. Electromagnetic radiation is treated classically since the number of photons is large and the momentum of the photon is small compared to the momentum of the particle (e.g., electron) in the solid.

3.2 Maxwell's equations, wave equation and plane waves in a conducting medium

If the medium is ohmic, isotropic, far away from the charge sources ($\rho_{ext} = 0$) and there is no spatial variation in dielectric constant ϵ_1 and magnetic permeability μ , the Maxwell's equations in Gaussian units (cgs) become

$$\vec{\nabla} \cdot \vec{E} = 0, \quad (3.1) \quad \vec{\nabla} \cdot \vec{H} = 0, \quad (3.2)$$

$$\vec{\nabla} \times \vec{E} = -\frac{\mu}{c} \frac{\partial \vec{H}}{\partial t}, \quad (3.3) \quad \vec{\nabla} \times \vec{H} = \frac{4\pi\sigma}{c} \vec{E} + \frac{\epsilon_1}{c} \frac{\partial \vec{E}}{\partial t} \quad (3.4)$$

where σ is the electrical conductivity, \vec{E} is electric field, \vec{H} is the magnetic field, $\vec{B} = \mu\vec{H}$ is magnetic induction and c is the velocity of light in free space. How some material parameters enter the Maxwell's equations (3.1-3.4) are briefly summarized in Appendix A.

The wave equations are derived by taking the curl of equations (3.3) and (3.4) as follows:

$$\nabla^2 \vec{E} - \frac{4\pi\mu\sigma}{c^2} \frac{\partial \vec{E}}{\partial t} - \frac{\mu\varepsilon_1}{c^2} \frac{\partial^2 \vec{E}}{\partial t^2} = 0, \quad \nabla^2 \vec{H} - \frac{4\pi\mu\sigma}{c^2} \frac{\partial \vec{H}}{\partial t} - \frac{\mu\varepsilon_1}{c^2} \frac{\partial^2 \vec{H}}{\partial t^2} = 0 \quad (3.5)$$

The solutions of the wave equations are in the form of plane waves, $e^{-i(\vec{k}\cdot\vec{x}-\omega t)}$, where the frequency ω and the magnitude of the wave vector \vec{k} are related by $k^2 = \frac{\mu\omega^2 \tilde{\varepsilon}}{c^2}$ where complex dielectric constant $\tilde{\varepsilon}$ is defined by $\tilde{\varepsilon} = \varepsilon_1 - i \frac{4\pi\sigma}{\omega} = \varepsilon_1 - i\varepsilon_2$. The wave vector can be written as $k = \frac{\omega}{c} N$ where $N = \sqrt{\mu\tilde{\varepsilon}}$ is the complex refractive index. N can be written in terms of its real and imaginary parts as $N = n - i\kappa$ where n and κ are called the refractive index and the extinction coefficient of the medium, respectively. Plane wave solutions of the wave equations are of the form

$$\vec{E}(\vec{x}, t) = \vec{E}_0 e^{-i(\vec{k}\cdot\vec{x}-\omega t)} = \vec{E}_0 e^{-i(\frac{\omega}{c}n\hat{k}\cdot\vec{x}-\omega t)} e^{-\frac{\omega}{c}\kappa\hat{k}\cdot\vec{x}}, \quad \vec{H}(\vec{x}, t) = \vec{H}_0 e^{-i(\vec{k}\cdot\vec{x}-\omega t)} \quad (3.6)$$

where $\hat{k} = \frac{\vec{k}}{k}$ and, \vec{E}_0 and \vec{H}_0 are constant in time and space. Using equations (3.1) and (3.2) it can be shown that \vec{k} , \vec{E} and \vec{H} form an orthogonal set: $\vec{k} \perp \vec{E}$, $\vec{E} \perp \vec{H}$, $\vec{H} \perp \vec{k}$. If \vec{E} propagates in the positive direction of the z-axis, that is $\hat{k} = \hat{z}$, \vec{E} becomes

$$\vec{E}(\vec{x}, t) = E e^{-i(\frac{\omega}{c}nz - \omega t)} e^{-\frac{1}{2}\alpha z} \quad (3.7)$$

where $\alpha = \frac{2\omega}{c} \kappa = \frac{4\pi}{\lambda} \kappa$ is absorption coefficient.

3.3 Reflection and Transmission of a Plane Wave

3.3.1 Reflection and Transmission of Electromagnetic Waves at a Plane Interface between Two Media

To determine the light reflected and transmitted at a boundary separating two media, boundary conditions are applied to the solutions of the Maxwell's equations. Consider a plane electromagnetic wave incident on a planar interface at $z = 0$ where plane of incidence is the plane xOz as shown in Figure 3.1. The angle of incidence is ϕ_i and angle of refraction ϕ_r . The media above and below the plane $z = 0$ have dielectric constants ϵ_0, ϵ_1 and permeabilities μ_0, μ_1 , respectively. \hat{z} is a unit vector, normal to the interface and directed in the positive z -direction. The boundary conditions require that the tangential components of both \vec{E} and \vec{H} are continuous at the boundary.

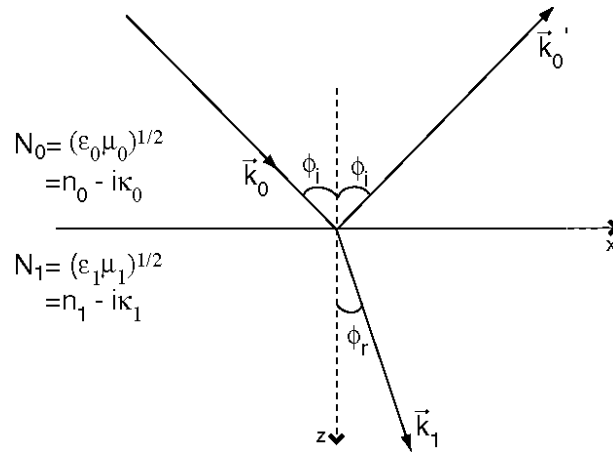


Figure 3.1 Incident wave is reflected and transmitted at a boundary separating two media.

The \vec{E} for incident, reflected and refracted electric field wave can be given as $\vec{E}_0 = E_{00} e^{-i(\vec{k}_0 \cdot \vec{x} - \omega t)}$, $\vec{E}_0' = E_{00}' e^{-i(\vec{k}_0' \cdot \vec{x} - \omega t)}$ and $\vec{E}_1 = E_{01} e^{-i(\vec{k}_1 \cdot \vec{x} - \omega t)}$, respectively. At the

interface $z = 0$ between two media there must be no difference in the spatial and time variation of the incident, reflected and transmitted waves. Therefore the exponents at $z = 0$ must be equal: $(\vec{k}_0 \cdot \vec{x})_{z=0} = (\vec{k}'_0 \cdot \vec{x})_{z=0} = (\vec{k}_1 \cdot \vec{x})_{z=0}$. For the boundary conditions to be satisfied: (1) the directions of propagation of the incident, reflected and transmitted waves must lie in one plane. (2) Since $k_0 = k'_0$, the angle of incident ϕ_i must be equal to the angle of reflection ϕ'_i . (3) The angles ϕ_i and ϕ_r is related by $k_0 \sin \phi_i = k_1 \sin \phi_r$, (Snell's law) [59].

If the amplitude and polarization of the incident wave is known, the amplitude and the polarization of the reflected and transmitted waves can be determined by using the continuity of the tangential components of the \vec{E} and \vec{H} across the interface. When the incident wave is linearly polarized with electric vector vibrating parallel (p) to the plane of incidence, the reflected and transmitted waves are polarized with their electric vectors also vibrating parallel to the plane of incidence. Similarly, when the incident beam wave is linearly polarized perpendicular (s) to the plane of incidence, the reflected and transmitted waves are also linearly polarized perpendicular to the plane of incidence. This condition is only valid when the medium is isotropic which is already assumed up to this point [60]. Since any arbitrarily polarized light can be expressed in terms of its s- and p-components, consideration of only these two components is sufficient to determine the amplitudes of the reflected and transmitted waves in terms of the incident waves.

As a result of the continuity of tangential components of \vec{E} and \vec{H} , one can derive the reflected amplitude $r = \frac{E'_{00}}{E_{00}}$ and transmitted amplitude $t = \frac{E_{01}}{E_{00}}$ for s- and p-polarized light as follows:

$$r_s = \frac{N_0 \cos \phi_i - N_1 \cos \phi_r}{N_0 \cos \phi_i + N_1 \cos \phi_r}, \quad r_p = \frac{N_1 \cos \phi_i - N_0 \cos \phi_r}{N_1 \cos \phi_i + N_0 \cos \phi_r}, \quad (3.8)$$

$$t_s = \frac{2N_0 \cos \phi_i}{N_0 \cos \phi_i + N_1 \cos \phi_r}, \quad t_p = \frac{2N_0 \cos \phi_i}{N_1 \cos \phi_i + N_0 \cos \phi_r}$$

where it is assumed that $\mu_0 = \mu_1$. The amplitudes r and t are also known as Fresnel coefficients.

Flow of energy is described by the Poynting vector, \vec{S} , and its magnitude value is called intensity:

$$\vec{S} = \frac{c}{4\pi} (\vec{E} \times \vec{H}), \quad |S| = \frac{c}{4\pi\mu} |N||E|^2 \quad (3.9)$$

Transmittance, which is the ratio of transmitted to incident intensity, and reflectance, which is the ratio of reflected intensity to the incident intensity, are given by

$$T = \frac{n_1}{n_0} t^2, \quad R = r^2 \quad (3.10)$$

Expressions for transmittance and reflectance hold for both of the polarizations. For p-polarized incident wave, r_p (equation (3.8)) can be written alternatively as $r_p = \tan(\phi_i - \phi_r) / \tan(\phi_i + \phi_r)$. r_p becomes zero when $\tan(\phi_i + \phi_r) = \infty$, that is, $\phi_i + \phi_r = \pi/2$. In other words, If the both media are non-absorbing ($\kappa = 0$), the incident angle ϕ_i , using Snell's law, satisfies the following relation $\phi_i = \tan^{-1}(\frac{n_2}{n_1})$. This

special angle of incidence where there is no p-polarized reflected wave is called Brewster angle. If the reflecting surface is absorbing ($\kappa \neq 0$), then the reflectance of a p-polarized incident light can only reaches a minimum at a particular angle of incidence which is called principle angle of incidence. In this respect, principle angle of incidence and Brewster angle are equal for $\kappa = 0$.

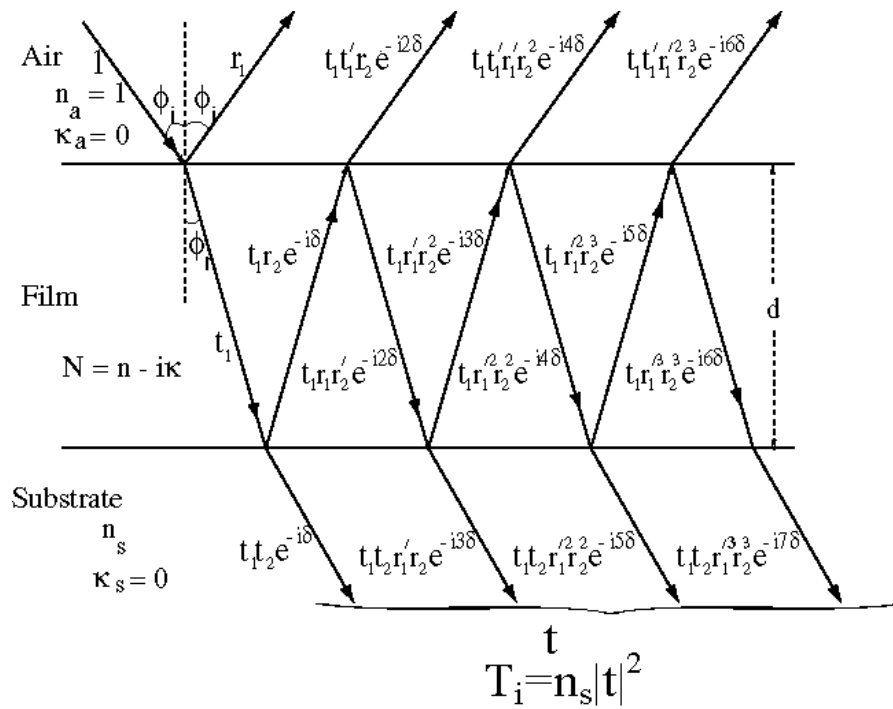


Figure 3.2 Multiple reflections and transmissions of a plane wave by an air-film-substrate system with parallel-plane boundaries.

3.3.2 Transmission and Reflection of a Thin Film on a substrate

A light beam is incident on a thin film of parallel plate boundaries sandwiched between air and infinitely long transparent ($\kappa = 0$) substrate as shown in Figure 3.2. The film of thickness d is assumed absorbing with a complex refractive index N and with a. The air and the substrate refractive indices are 1 and n_s , respectively. The beam is divided into reflected and transmitted parts at each interface. Incident wave is reflected and part of it transmitted at the air-film interface. The transmitted wave inside the film is multiply-reflected and multiply-transmitted at the film-substrate and film-air interfaces. Amplitudes of the transmitted and reflected beams are obtained by summing the Fresnel coefficients of multiply-reflected and multiply-transmitted beam elements [61]. The multiply reflected and multiply-transmitted beams can be written in terms of Fresnel coefficients. Fresnel reflection and transmission coefficients at the air-film and film-

substrate interfaces are denoted by r_1 , t_1 and r_2 , t_2 , respectively. The corresponding coefficients for propagation from the film to the air are r_1' and t_1' .

As the wave traverses the film from one boundary to the other, a constant phase change is added to its phase. In terms of the free space wavelength λ , d , N and ϕ_r , the phase change is given by $\delta = \frac{2\pi}{\lambda} Nd \cos \phi_r$. After summing the partial waves and using expressions $r_1' = -r_1$ and $t_1' = \frac{1-r_1^2}{t_1}$, the transmitted (t) and reflected (r) amplitudes of an air-film-substrate system can be obtained, respectively, as follows:

$$t = \frac{t_1 t_2 e^{-i\delta}}{1 + r_1 r_2 e^{-i2\delta}}, \quad r = \frac{r_1 + r_2 e^{-i2\delta}}{1 + r_1 r_2 e^{-i2\delta}} \quad (3.11)$$

Transmittance T_i and reflectance R_i for this system at normal angle of incidence, where substrate is assumed to be infinitely thick (semi-infinite medium), can be expressed as

$$T_i = \frac{A_i x}{B_i - C_i x + D_i x^2}, \quad R_i = \frac{E_i - C_i^+ x + G_i x^2}{B_i - C_i^- x + D_i x^2} \quad (3.12)$$

The transmittance, T_i' , for a beam incident normally on the film from the substrate side is equal to the transmittance for a beam incident normally on the film from the air side, that is, $T_i' = T_i$. However, this is not true correspondingly for reflectance, that is, $R_i' \neq R_i$. Reflectance for a beam incident normally on the film from the substrate side can be given as

$$R_i' = \frac{E_i' - C_i^{+'} x + G_i' x^2}{B_i' - C_i^{-'} x + D_i' x^2} \quad (3.13)$$

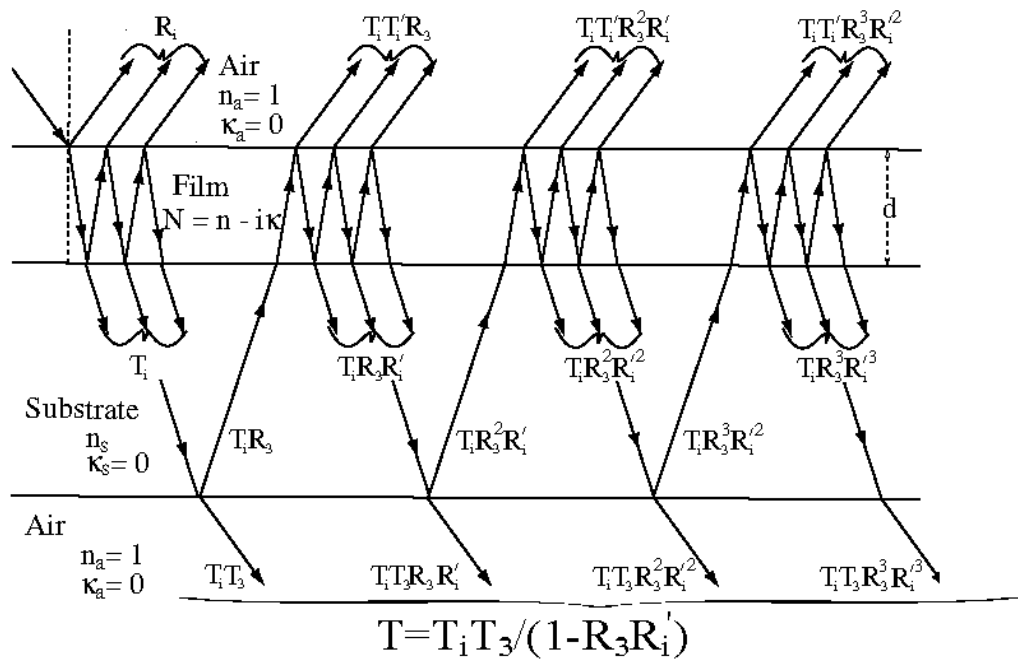


Figure 3.3 Multiply reflected and transmitted elements including the reflections at the back interface of the substrate [62].

All coefficients denoted by capital letters are functions of n, κ, n_s, d and λ and are explicitly given in Appendix B. x is defined as $x = e^{-\alpha d}$.

3.3.3 Incoherent Interaction of the Light with the Substrate Layer

There are no perfectly monochromatic sources because light has discontinuous changes in its phase. Only within a short period of time, time dependence of any light can be approximated by a sine wave. The length of this time is called the coherence time, $\Delta\tau$. The coherence time can be related to the spectral bandwidth by the uncertainty principle,

$$\Delta\tau \Delta\omega \approx 1 \tag{3.14}$$

The greater the coherence time, the narrower the spectral bandwidth, that is, the more monochromatic light [63]. The coherence length, $\Delta\ell$ is the length of the traveling coherent wave and equal to

$$\Delta\ell = c\Delta\tau \approx \frac{c}{\Delta\omega} = \frac{\lambda^2}{\Delta\lambda} \quad \text{with} \quad \omega = \frac{c}{\lambda} \quad (3.15)$$

As long as the coherence length of the light satisfies the following relation [64]:

$$2nd \ll \Delta\ell \ll 2n_s d_s \quad (3.16)$$

where d_s is the thickness of the substrate, incident light interacts coherently with the film and incoherently with the substrate. This means that the character of the transmittance or reflectance spectrum is not affected by the phase changes of the wave in the substrate since phase changes occur randomly. The factor 2 in the above inequality takes the distance traveled in the substrate or in the film into account and since the speed of light is c/n and c/n_s in the film and substrate, respectively, n and n_s is apparently involved in the above inequality. Consequently, only the intensities of the beams are important in the substrate because the interaction of light beam with the substrate does not change the behavior of the curve representing the transmittance and reflectance versus wavelength graph. Figure 3.3 illustrates the total transmittance and reflectance with a substrate of finite thickness d_s . The transmittance T^i at the film-substrate interface is reflected and transmitted at the substrate-air interface with intensities $T_i R_3$ and $T_i T_3$, respectively. Then the reflected beam is multiply-reflected at the substrate-film interface and is multiply-transmitted at the film-air interface. Total transmittance and reflectance can be calculated by adding all the separate partial intensities. Consequently, the transmittance can be expressed in terms of T_i as the following:

$$T = \frac{T_i T_3}{1 - R_3 R_i'}, \quad \text{or} \quad T = \frac{Ax}{B - Cx + Dx^2} \quad (3.17)$$

Similarly, reflectance can be expressed as

$$R = R_i + \frac{T_i^2 R_3}{1 - R_3 R_i}, \quad (3.18)$$

or

$$R = \frac{E_i - C_i^+ x + G_i x^2}{B_i - C_i^- x + D_i x^2} + \frac{1}{B_i - C_i^- x + D_i x^2} \frac{A_r x}{B_r - C_r x + D_r x^2} \quad (3.19)$$

Coefficients (capital letters in the expressions) for this system are also given explicitly in Appendix B.

3.3.4 Characteristic Matrix Approach in Determining Transmission and Reflection Coefficients.

Let us consider a multilayer coating consisting of m number of homogeneous and isotropic layers as shown in Figure 3.4. Stratification is parallel to xy -plane and each medium is defined by a thickness (d_j) and complex refractive index ($N_j = n_j - \kappa_j$). A plane wave, incident on the $z = 0$ plane with an angle of incidence ϕ_a , propagates through the stratified medium and the transmitted wave propagates in the substrate with an angle of ϕ_s . Let's first consider linearly polarized light with its electric field vector is perpendicular (s-polarized) to the plane of incidence ($E_y = E_z = 0$). For this s-component of the light, Maxwell's equations (3.3) and (3.4) can be expressed as follows [65-66]:

$$\frac{\partial H_z}{\partial y} - \frac{\partial H_y}{\partial z} = \frac{i\tilde{\epsilon}\omega}{c} E_x, \quad (3.20a)$$

$$H_x = 0, \quad (3.20b)$$

$$\frac{\partial H_z}{\partial x} = 0, \quad (3.20c)$$

$$\frac{i\mu\omega}{c} H_y + \frac{\partial E_x}{\partial z} = 0, \quad (3.20d)$$

$$\frac{\partial H_y}{\partial x} = 0, \quad (3.20e)$$

$$\frac{-i\mu\omega}{c} H_z + \frac{\partial E_x}{\partial y} = 0 \quad (3.20f)$$

By using equations (3.20a), (3.20b) and (3.20c), and eliminating \vec{H} , the following differential equation for \vec{E} can be obtained:

$$\frac{\partial^2 E_x}{\partial y^2} + \frac{\partial^2 E_x}{\partial z^2} + N^2 k_0^2 E_x = \frac{d(\ln \mu)}{dz} \frac{\partial E_x}{\partial z} \quad (3.21)$$

where $N^2 = \tilde{\epsilon}\mu$ and $k_0 = \omega/c$. Introducing a trial solution in the form of $E_x(y, z, t) = Y(y)U(z)e^{i\omega t}$, the differential equation becomes

$$\frac{1}{Y} \frac{\partial^2 Y}{\partial y^2} = -\frac{1}{U} \frac{d^2 U}{dz^2} - N^2 k_0^2 + \frac{d(\ln \mu)}{dz} \frac{1}{U} \frac{dU}{dz} \quad (3.22)$$

Equating both sides of the above equation to $-k_0^2 \alpha^2$, one can express E_x , H_y and H_z as

$$E_x = U(z)e^{-i(k_0 \alpha y - \omega t)}, \quad (3.23)$$

$$H_y = V(z)e^{-i(k_0 \alpha y - \omega t)}, \quad (3.24)$$

$$H_z = W(z)e^{-i(k_0 \alpha y - \omega t)} \quad (3.25)$$

where U and V must satisfy the following second-order differential equations:

$$\frac{d^2 U}{dz^2} - \frac{d(\ln \mu)}{dz} \frac{dU}{dz} + (N^2 - \alpha^2) k_0^2 U = 0 \quad (3.26)$$

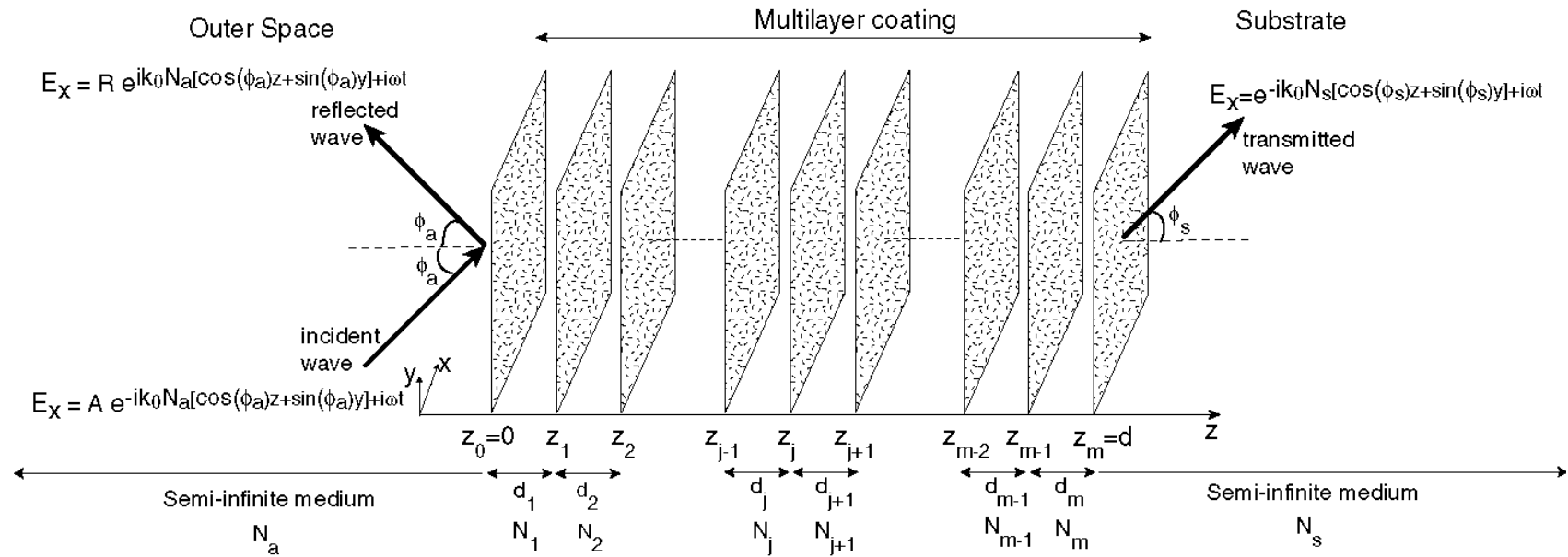


Figure 3.4 A plane wave incident on a multilayer coating with m homogeneous and isotropic layers surrounded by an outer space and substrate with refractive indices N_a and N_s .

$$\frac{d^2V}{dz^2} - \frac{d\left[\ln\left(\tilde{\varepsilon} - \frac{\alpha^2}{\mu}\right)\right]}{dz} \frac{dV}{dz} + (N^2 - \alpha^2)k_0^2V = 0 \quad (3.27)$$

Substituting the expressions for E_x , H_y and H_z in Maxwell's equations (3.3) and (3.4), U , V and W can be interrelated by first-order differential equations:

$$\frac{dV}{dz} = ik_0(\alpha W + \tilde{\varepsilon}U) = ik_0\left(\tilde{\varepsilon} - \frac{\alpha^2}{\mu}\right)U, \quad (3.28)$$

$$\frac{dU}{dz} = ik_0\mu W, \quad (3.29)$$

$$\alpha U + \mu W = 0 \quad (3.30)$$

Let us now determine the constant α . The electric field incident in the outer space can be expressed as

$$\vec{E}_A = \vec{E}_A e^{-i(\vec{k}_0 N_a - \omega t)} = \vec{E}_A e^{-i[k_0 N_a (\hat{z} z \cos(\phi_a) + \hat{y} y \sin(\phi_a)) - \omega t]} = U(z) e^{-i(k_0 \alpha y - \omega t)} \quad (3.31)$$

Then, it is seen that $\alpha = N_a \sin(\phi_a)$. The constancy of α is equivalent to Snell's law of refraction. α is same in all layers, outer space and substrate; that is,

$$\alpha = N_a \sin(\phi_a) = \dots = N_{j-1} \sin(\phi_{j-1}) = N_j \sin(\phi_j) = \dots = N_m \sin(\phi_m) = N_s \sin(\phi_s) \quad (3.32)$$

In a homogeneous medium and say the j^{th} layer, where $\tilde{\varepsilon}$ and μ are constants, one can write for a s-polarized wave

$$\frac{d^2U}{dz^2} + k_0^2 N_j^2 \cos^2(\phi_j) U = 0 \quad (3.33)$$

General solution of this differential equation has two independent (particular) solutions U_1, U_2 and can be given in the following form:

$$\begin{aligned} U(z) &= U_1(z) + U_2(z) \\ &= c_1 \cos(k_0 N_j \cos(\phi_j)(z_{j-1} - z)) + c_2 \sin(k_0 N_j \cos(\phi_j)(z_{j-1} - z)) \end{aligned} \quad (3.34)$$

where z_{j-1} is the left boundary of the j^{th} layer. Using equation $\frac{dU}{dz} = ik_0 \mu V$ one can write $V(z)$ as

$$V(z) = \frac{1}{i} \sqrt{\frac{\tilde{\epsilon}_j}{\mu_j}} \cos(\phi_j) [c_1 \sin(k_0 N_j \cos(\phi_j)(z_{j-1} - z)) - c_2 \cos(k_0 N_j \cos(\phi_j)(z_{j-1} - z))] \quad (3.35)$$

At $z = z_{j-1}$, $U(z_{j-1}) = c_1$ and $V(z_{j-1}) = -\frac{c_2}{i} \sqrt{\frac{\tilde{\epsilon}_j}{\mu_j}} \cos(\phi_j)$. Consequently, $U(z)$ and $V(z)$ can be given by

$$U(z) = U(z_{j-1}) \cos(k_0 N_j \cos(\phi_j)(z_{j-1} - z)) - V(z_{j-1}) i \sqrt{\frac{\mu_j}{\tilde{\epsilon}_j}} \frac{1}{\cos(\phi_j)} \sin(k_0 N_j \cos(\phi_j)(z_{j-1} - z)) \quad (3.36)$$

$$V(z) = -U(z_{j-1}) i \sqrt{\frac{\tilde{\epsilon}_j}{\mu_j}} \cos(\phi_j) \sin(k_0 N_j \cos(\phi_j)(z_{j-1} - z)) + V(z_{j-1}) \cos(k_0 N_j \cos(\phi_j)(z_{j-1} - z)) \quad (3.37)$$

The equations (3.36) and (3.37) can be written for $z = z_j$ in a matrix form as

$$\begin{pmatrix} U(z_j) \\ V(z_j) \end{pmatrix} = \begin{pmatrix} \cos(\phi_j) & -\frac{i}{p_j} \sin(\phi_j) \\ -ip_j \sin(\phi_j) & \cos(\phi_j) \end{pmatrix} \begin{pmatrix} U(z_{j-1}) \\ V(z_{j-1}) \end{pmatrix} \quad (3.38)$$

where

$$\varphi_j = k_0 N_j \cos(\phi_j)(z_j - z_{j-1}) = k_0 N_j \cos(\phi_j) d_j \quad (3.39)$$

$$p_j = \sqrt{\frac{\tilde{\epsilon}_j}{\mu_j}} \cos(\phi_j). \quad (\text{for s-polarized incident light}) \quad (3.40)$$

Alternatively, equation (3.28) can be written as

$$\begin{pmatrix} U(z_{j-1}) \\ V(z_{j-1}) \end{pmatrix} = M_j \begin{pmatrix} U(z_j) \\ V(z_j) \end{pmatrix} \quad (3.41)$$

where

$$M_j = \begin{pmatrix} \cos(\varphi_j) & \frac{i}{p_j} \sin(\varphi_j) \\ ip_j \sin(\varphi_j) & \cos(\varphi_j) \end{pmatrix} \quad (3.42)$$

and is called characteristic matrix of the j^{th} medium. It can be shown that determinant of M_j is constant ($\frac{d|M_j|}{dz} = 0$) and this property of $|M|$ is equivalent to the conservation of energy. In addition to the j^{th} layer, if one considers the next medium $j-1$, it is possible to interrelate media j and $j-2$ as

$$\begin{pmatrix} U(z_{j-2}) \\ V(z_{j-2}) \end{pmatrix} = M_{j-1} \begin{pmatrix} U(z_{j-1}) \\ V(z_{j-1}) \end{pmatrix} = M_{j-1} M_j \begin{pmatrix} U(z_j) \\ V(z_j) \end{pmatrix} \quad (3.43)$$

Since characteristic matrix of the multilayer coating is seen to be $M = M_1 M_2 M_3 \dots M_m$,

then

$$\begin{pmatrix} U(0) \\ V(0) \end{pmatrix} = M \begin{pmatrix} U(d) \\ V(d) \end{pmatrix} \quad \text{with} \quad M = \begin{pmatrix} m_{11} & m_{12} \\ m_{21} & m_{22} \end{pmatrix} \quad (3.44)$$

Denoting A , R and T as amplitudes of the electric field vectors of the incident, reflected and transmitted waves, respectively, one can write tangential components of the field for the incident medium (outer space) as

$$E_x = A e^{-ik_0 \sqrt{\mu_a \epsilon_a} (\cos(\phi_a)z + \sin(\phi_a)y) + i\omega t}, H_y = p_a A e^{ik_0 \sqrt{\mu_a \epsilon_a} (\cos(\phi_a)z + \sin(\phi_a)y) + i\omega t} \quad (\text{incident waves})$$

$$E_x = R e^{ik_0 \sqrt{\mu_a \epsilon_a} (\cos(\phi_a)z + \sin(\phi_a)y) + i\omega t}, H_y = -p_a R e^{-ik_0 \sqrt{\mu_a \epsilon_a} (\cos(\phi_a)z + \sin(\phi_a)y) + i\omega t} \quad (\text{reflected waves})$$

and obtain tangential field components in the substrate as

$$E_x = T e^{-ik_0 \sqrt{\mu_s \epsilon_s} (\cos(\phi_s)z + \sin(\phi_s)y) + i\omega t}, H_y = p_s T e^{ik_0 \sqrt{\mu_s \epsilon_s} (\cos(\phi_s)z + \sin(\phi_s)y) + i\omega t} \quad (\text{transmitted waves})$$

Then amplitude of the fields can be written as

$$U(z=0) = A + R, \quad V(z=0) = p_a (A - R) \quad (\text{incident waves})$$

$$U(z=d) = T, \quad V(z=d) = p_s T \quad (\text{transmitted waves})$$

Consequently, it is possible to relate $U(0)$, $V(0)$, $U(d)$ and $V(d)$ by equation (3.41) as

$$A + R = (m_{11} + m_{12} p_s) T \quad (3.45)$$

$$p_a (A - R) = (m_{21} + m_{22} p_s) T \quad (3.46)$$

From equations (3.45-3.46), one can obtain transmission and reflection coefficients as

$$t = \frac{T}{A} = \frac{2p_a}{p_a m_{11} + p_s m_{22} + p_a p_s m_{12} + m_{21}}, \quad (3.47)$$

$$r = \frac{R}{A} = \frac{p_a m_{11} - p_s m_{22} + p_a p_s m_{12} - m_{21}}{p_a m_{11} + p_s m_{22} + p_a p_s m_{12} + m_{21}} \quad (3.48)$$

Maxwell's equations (3.3) and (3.4) remain unchanged after the following substitutions:

$$\vec{E} \rightarrow \vec{H}, \quad \tilde{\varepsilon} \rightarrow \mu, \quad -\vec{H} \rightarrow \vec{E}, \quad \mu \rightarrow \tilde{\varepsilon}$$

By using this property of Maxwell's equations, an equation for \vec{E} can be changed to a corresponding equation for \vec{H} . For a linearly polarized light with its electric field vector is parallel (p) to the plane of incidence ($H_y = H_z = 0$), the nonvanishing components of the field vectors can be expressed as

$$H_x = U(z)e^{-i(k_0 \alpha y - \omega t)}, \quad E_y = -V(z)e^{-i(k_0 \alpha y - \omega t)}, \quad E_z = -W(z)e^{-i(k_0 \alpha y - \omega t)} \quad (3.49)$$

where U and V must satisfy the following second-order differential equations:

$$\frac{d^2 U}{dz^2} - \frac{d(\ln \tilde{\varepsilon})}{dz} \frac{dU}{dz} + (N^2 - \alpha^2)k_0^2 U = 0 \quad (3.50)$$

$$\frac{d^2 V}{dz^2} - \frac{d\left[\ln\left(\mu - \frac{\alpha^2}{\tilde{\varepsilon}}\right)\right]}{dz} \frac{dV}{dz} + (N^2 - \alpha^2)k_0^2 V = 0 \quad (3.51)$$

Similarly, U , V and W can be interrelated by the following first-order differential equations:

$$\frac{dV}{dz} = ik_0(\alpha W + \mu U) = ik_0\left(\mu - \frac{\alpha^2}{\tilde{\varepsilon}}\right)U, \quad \frac{dU}{dz} = ik_0 \tilde{\varepsilon} V, \quad \alpha U + \tilde{\varepsilon} W = 0 \quad (3.52)$$

For p-polarized incident wave, the same characteristic matrix equation (3.42) and same expressions (3.47) and (3.48) hold, with p_j replaced by

$$p_j = \sqrt{\frac{\mu_j}{\tilde{\varepsilon}_j}} \cos(\phi_j) \quad (\text{for p-polarized incident light}) \quad (3.53)$$

3.4 Methods of Determining the Optical Constants from Transmittance and Reflectance

There is an increasing need for accurate knowledge of the optical constants of absorbing films not only because of fundamental but also due to a technological point of view. In order to improve the characteristics of different types of semiconductor devices, which are mainly consisting of interfaces of two materials or doping types, it is important to know the refractive indices and their absorption properties together with the thicknesses of the individual layers.

3.4.1 Determination of Optical Constants and Thickness of Thin Films by Using the Transmission and Reflection Spectra: Method of Envelopes

There are different types of characterization techniques to determine the optical parameters of thin films from spectral photometric data. Among those techniques, measuring the transmittance of a film illuminated by an unpolarized light at normal angle of incidence is a common method for determining the thickness and complex refractive index. Optical constants of thin films displaying at least two interference fringes in their transparent spectral region can be determined by using envelopes of transmittance spectra [67-68]. This method provides optical parameters of the thin films to an accuracy of 1%.

In a four-phase problem (ambient-substrate-film-ambient) there are four unknowns: n , α , d and n_s . It is possible to obtain n_s from the transmission spectrum of the substrate alone. If the multiply-reflected and transmitted beams through the substrate do not interfere, existence of incoherent light interaction in the substrate can be concluded. This result may come out because of two closely related reasons: Thickness of the substrate d_s can be very large according to the coherence length of the light or the two interfaces of the substrate may not be perfectly parallel to each other. The latter is an expected result when d_s is large. Assuming the substrate is transparent and presence of incoherent interaction in the substrate, T_s can be calculated summing multiply-reflected and transmitted intensities of beams:

$$T_s = \frac{T_1 T_2}{1 - R_2 R_1}, \quad \text{or} \quad T_s = \frac{2n_s}{n_s^2 + 1} \quad (3.54)$$

Since the substrate is transparent, $R_s = 1 - T_s$, and reflectance R_s and n_s can be given by

$$R_s = \frac{(n_s - 1)^2}{n_s^2 + 1}, \quad n_s = \frac{1}{T_s} + \left(\frac{1}{T_s^2} - 1 \right)^{1/2} \quad (3.55)$$

The equation for T becomes simpler if $\kappa = 0$. This is an acceptable approximation because κ is very small in comparison to n over most of the transmission spectrum of semiconductors. The transmittance equation reduces to the following:

$$T = \frac{Ax}{B - C \cos(4\pi md / \lambda)x + Dx^2} \quad (3.56)$$

where $A = 16n_s n^2$, $B = (n + 1)^3 (n + n_s^2)$, $C = 2(n^2 - n_s^2)(n^2 - 1)$, $D = (n - 1)^3 (n - n_s^2)$, $x = e^{-\alpha d}$. A simulated transmittance spectrum is given Figure 3.5.

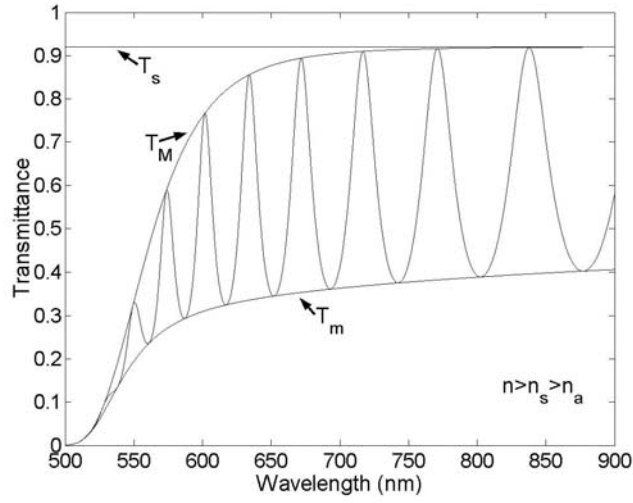


Figure 3.5 Simulated transmittance spectrum with $d = 1100$ nm, $n_s = 1.51$, $n_a = 1$, $n = 3 + 3 \times 10^5 / \lambda^2$ (λ in nm) and $k = (\lambda / 4\pi) \times 10^{1.45 \times 10^6 / \lambda^2 - 8}$ (λ in nm).

When the optical path difference is integer and half integer multiples of λ , constructive and destructive interference occurs, respectively. The equation for these extrema is

$$2nd = m\lambda \quad (3.57)$$

where $m = 0, 0.5, 1, 1.5, \dots$. Equation (3.57) is valid only for a dispersion-free film, however, small dispersion do not invalidate the expression [69]. Alternatively, equation (3.57) can be expressed as

$$2nd = \left(\frac{\ell}{2} + m_1\right)\lambda \quad (3.58)$$

where m_1 is the fringe order number of the first extremum ($\ell = 0$) starting from the long wavelength.

Substituting integer and half-integer values of m into transmittance expression gives envelopes T_M for maxima and T_m for minima, respectively:

$$T_M = \frac{Ax}{B - Cx + Dx^2} \quad (\text{for maxima}), \quad (3.59)$$

$$T_m = \frac{Ax}{B + Cx + Dx^2} \quad (\text{for minima}) \quad (3.60)$$

T_M and T_m are slowly varying, monotonic functions of λ whereas T varies very fast with λ . These functions are called envelopes of the transmittance spectrum. In the transparent region ($x = 1$), T_M reduces to the transmittance of the substrate alone, that is, $T_M = T_s$. If the reciprocal of T_M is subtracted from the reciprocal of T_m , n can be expressed independent of x as follows:

$$n = (L + (L^2 + (L^2 - n_s^2)^{1/2})^2) \quad \text{where} \quad L = 2n_s \frac{T_M - T_m}{T_M T_m} + \frac{n_s^2 + 1}{2} \quad (3.61)$$

For every interference fringe whether it is maximum or minimum at any λ there exists a maximum T_M for a minimum or a minimum T_m for a maximum. Since the difference of the fringe order numbers of the two adjacent maxima or minima is 1, one can express thickness of the film as

$$d = \frac{\lambda_1 \lambda_2}{2(\lambda_1 n_2 - \lambda_2 n_1)} \quad (3.62)$$

The envelopes T_M and T_m are quadratic equations in x and can be solved for x . The solution is

$$x = \frac{E - (E^2 - (n^2 - 1)^3 (n^2 - n_s^4))}{(n - 1)^3 (n - n_s^2)} \quad (3.63)$$

where $E = \frac{8n^2 n_s}{T_M} + (n^2 - 1)(n^2 - n_s^2)$ for T_M and $E = \frac{8n^2 n_s}{T_M} - (n^2 - 1)(n^2 - n_s^2)$ for T_m .

Determination of optical constants by Swanepoel's method can be summarized in 8 steps as shown in Figure 3.5 [68]. In order to apply this procedure to a transmittance spectrum of a thin film, the spectrum needs to be consisting of sufficient number of interference fringes. If the measured spectra do not cover the spectral interval where the film is transparent, then transmittance of bare substrate is needed to be measured, otherwise refractive index can only be determined from a database of optical constants for frequently used standard substrates. In step 3, some dispersion in thickness values is obtained. If there are some values of thickness which deviate considerably from the others, those values should be omitted in the analysis. In Step 5, if it is not possible to correct the calculated fringe order numbers easily with certainty, thickness values are determined for different sets of m and the correct set of m can be found from the set of m that gives the least dispersion in thickness.

In our experience, application of these steps first in the transparent region for the determination of thickness and then, performing the analysis through all the spectrum interval including the absorbing region is a more reliable procedure. The envelopes should be drawn very carefully in the absorbing region of the spectrum because the equation (3.57) refers to the wavelengths at the points of the spectrum where $dT/d\lambda = 0$ in the transparent region. However, in the absorbing region this is no longer correct because absorption cause to shift the maxima and the minima to the larger and smaller wavelengths, respectively. Drawing the envelopes tangent to the actual spectrum and using these tangential points, instead of maxima and minima of the spectrum, in the analysis can correct this effect [70]. The maxima and minima of the spectrum coincide with the tangential points in the transparent region. Therefore, it is relatively unambiguous to draw envelopes in the transparent region and, consequently, determine

optical constants. The envelopes can be drawn generally by polynomial interpolation of three adjacent extrema and even by linear interpolation between adjacent extrema in the transparent region.

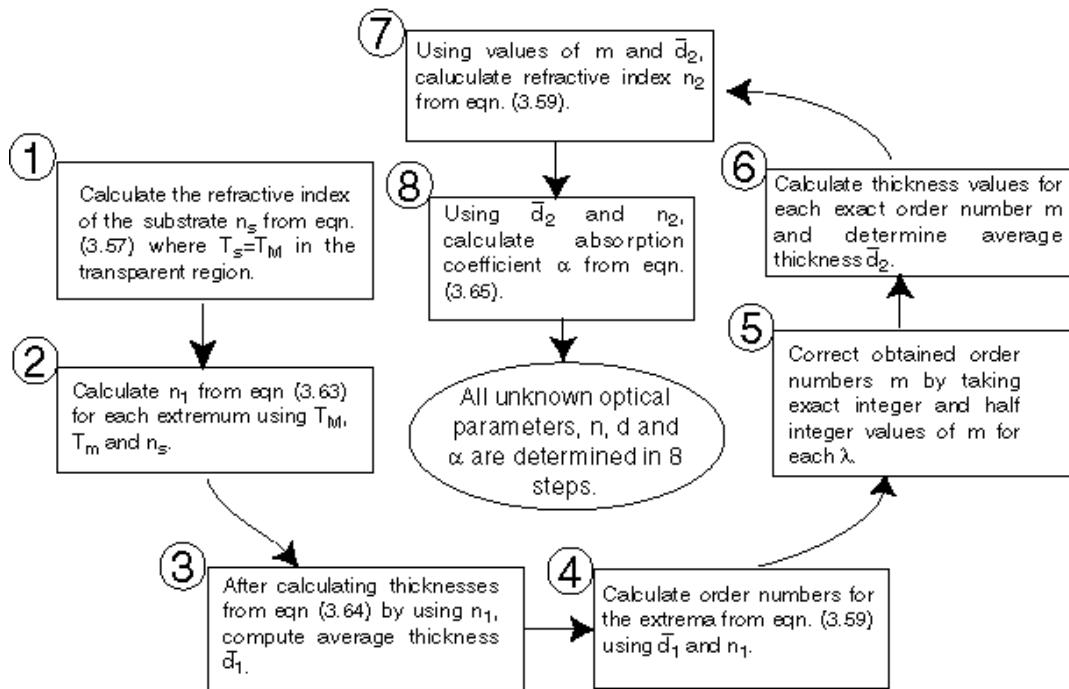


Figure 3.6 Flowchart of Swanepoel's procedure for the determination of optical constants in 8 steps.

Thicker films are preferable for determining the optical properties of the film in the low absorbing and transparent region. On the other hand, if one needs to examine mainly the absorption properties, thinner films would be preferable. However, it should be noted that as film thickness is reduced the number of the interference fringes decreases in turn diminishing the accuracy of the optical constants determined within this approach. Transmittance measurements may be preferable for the determination of κ because the beam is expected to interact more strongly with the material in the

transmittance measurements. However, it should be noted that this argument may not be true for a thin film because large amount of loss in the transmitted intensity may be due to reflection at the interfaces rather than to absorption in the film [71].

In the literature, different optical constants have been obtained depending on the model assumed for the films and the experimental method that is used, even for nominally the same films [71]. Optical constants sometimes may substantially scatter, even 30%. On the other hand, it is known that photometry measurements such as transmittance and reflectance have generally accepted accuracies of 0.1% [72]. Such an uncertainty is meaningless unless it is possible to measure the film thicknesses to accuracies that are unrealistically small. Therefore the major cause of the scattering in photometrically determined values of n and κ is not the uncertainty in the photometric data but rather the uncertainty in the thickness. Accuracies of optical constants obtained from transmittance and reflectance measurements can be improved by decreasing the uncertainty in the determination of the film thickness [71].

Interference fringes may not be resolved because of several reasons. For example, thickness variations of the sample and coherence length of the light may cause to an observation of a slowly varying smooth transmission. If the transmission T is integrated over phase angles between a minimum and an adjacent maximum and divided by the corresponding phase difference, an interference-free transmission T_α can be obtained. If all the parameters n , n_s and x are assumed to be constant between integration limits $[0, \pi]$, it can be shown that $T_\alpha = \sqrt{T_M T_m}$.

In the strong absorption region ($x \ll 1$), the term $\cos(4\pi nd / \lambda)x \sim 1$ and consequently, interference fringes can not be resolved. In this part of the spectrum, transmittance can be approximated as $T = T_0 \approx Ax / B$ [68]. This expression can be solved for x as

$$x = \frac{(n+1)^3 (n+n_s^2)}{16n^2 n_s} T_0 \quad (3.64)$$

Similarly, envelope functions of a reflectance spectrum can be determined and calculations of optical parameters by use of envelopes can be performed as it is done for the transmittance spectrum [73-74]. In the reflection spectrum, there is a greater number of fringes in comparison to the transmittance spectrum. Such an advantage results in reduced errors especially in d and m .

3.4.2 Determination of Optical Parameters by Numerical Inversion Techniques:

Optical constants of thin films which are displaying at least two interference fringes in their highly transparent spectral region can be determined with various methods using envelopes of the transmittance and reflectance. Recently, one more method consisting of a numerical constrained minimization has been developed for relatively thin films that do not exhibit a clear fringe pattern [75-76]. In this method some physical constraints that both refractive index $n(E)$ and extinction coefficient $\kappa(E)$ of amorphous solids must satisfy in the measured spectral energy range are used instead of imposing functional forms upon these optical constants. In the neighbourhood of the fundamental absorption edge of amorphous semiconductors it is known that:

- (a) $n(\lambda) \geq 1$ and $\kappa(\lambda) \geq 0$.
- (b) The functions of $n(\lambda)$ and $\kappa(\lambda)$ are decreasing.
- (c) $n(\lambda)$ is a convex function.
- (d) There exists $\lambda_{\text{infl}} \in [\lambda_{\text{min}}, \lambda_{\text{max}}]$ such that $\kappa(\lambda)$ is convex if $\lambda \geq \lambda_{\text{infl}}$ and concave if $\lambda < \lambda_{\text{infl}}$

If the above restrictions on some of the optical properties are considered in the numerical inversion procedure, it is possible to drastically reduce the range of variability of the unknowns $n(\lambda)$ and $\kappa(\lambda)$. Later, apart from this constrained formulation, an

“unconstrained” one of this method has been developed avoiding most of the constraints by suitable change of variables [77-78]. In other words, the optimization problem is formulated in a way such that the constraints are implicitly included in the minimization problem.

The reliability of these two formulations has been tested with various experimental measurement methods such as Swanpoel’s method using exclusively transmittance data [75], photothermal deflection spectroscopy, ellipsometry [75,77] and comparison of optical constants of thin films grown with the same deposition conditions [79]. The results of these tests have shown that these formulations seem successful for film thicknesses larger than about 75 nm. Very recently, a new optimization technique is introduced which is efficient for recovering the optical parameters of very thin computer generated films with thicknesses larger than 30 nm [80].

CHAPTER 4

ELLIPSOMETRY

4.1 Introduction

Ellipsometry is a type of optical spectroscopy which measures the change in polarization state of light upon reflection from a surface. First experimental studies start with Paul Drude in 1887 [81-82] although it was not called “ellipsometry” at that time. Since ellipsometry deals with polarization states rather than intensity as in reflectance and transmittance measurements, it is a highly sensitive to the presence of thin films on reflecting surfaces which are main elements of modern microelectronics technology. There are various process steps (crystal growth, wafering, oxidation, chemical vapor deposition, cleaning and etching) in silicon microelectronics where ellipsometry is benefited to identify various properties (surface quality, thickness, complex refractive index) of the film and film surface [83]. For example, each Pentium computer chip goes through a spectroscopic ellipsometry at least 40 times during fabrication [84].

The advantages of this diagnostic technique for thin film characterization can be summarized as follows [85-86]

- (a) Two parameters instead of one are independently determined in a single measurement.
- (b) Nondestructive (weak light sources) and consequently it can be used for in situ measurements.
- (c) Relatively insensitive to both intensity fluctuations of the source and macroscopic roughness (light loss by scattering).

- (d) Phase sensitive technique, that is, more sensitive to surface conditions (this property may be sometimes envisaged as a disadvantage)

On the negative side, light is needed to be transmitted through various optical elements such as polarizer, analyzer etc., which may not be good-quality transmitting elements in some wavelength ranges. Moreover, it requires careful expert alignment and calibration [83]. Among the different types of ellipsometers, rotating analyzer ellipsometer without a compensator has not wavelength dependent elements (achromatic) which makes this particular measurement configuration attractive and popular [87].

4.2 Polarization Properties of Light

Polarization concept is related to the vectorial nature of waves. Although, explanation of interference and diffraction phenomena does not generally require this nature of light, that is, scalar approach is sufficient, concept of polarization of light does require to enrolment of the vectorial aspect of the electromagnetic field. Emissions from light sources such as thermal source, arc-lamp and LED are incoherent by nature because the electric field emitted from a natural light source, which consists of emitting centres, is an incoherent addition of waves. For example, laser is a coherent light source and constrains the emitting centres to radiate coherently [88].

4.2.1 Polarization Ellipse

Plane wave solutions of the wave equations (3.5) are given in Section 3.2. Within the Maxwell's theory of electromagnetic field, wave consists of an oscillating electric field and oscillating magnetic field with the same frequency but oriented perpendicularly to each other. However, electric field component of light can be chosen to define the state of polarization, since the electric field affects the molecules by redistributing the charges much stronger than magnetic fields do. Besides, once the polarization of electric

field is determined, the polarization of remaining field vectors can be determined by using the Maxwell's equations.

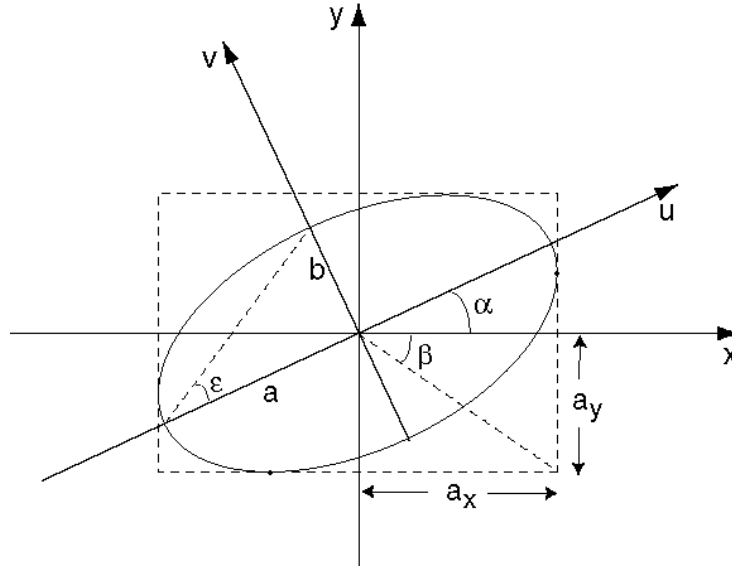


Figure 4.1 The polarization ellipse which is the most general state of polarization of any electromagnetic field that is monochromatic. The electric field vector at a fixed point traces the same ellipse in a regular repetitive fashion for an elliptically (most general state of polarization) polarized light [89].

A general time-harmonic (monochromatic) plane wave propagating along the z -direction can be defined as a real solution of the wave equation, of the form

$$\vec{E}(\vec{x}, t) = \text{Re}[(E_x \hat{x} + E_y \hat{y}) e^{-i(kz - \omega t)}] = \text{Re}[(a_x e^{i\delta_x} \hat{x} + a_y e^{i\delta_y} \hat{y}) e^{-i(kz - \omega t)}] \quad (4.1)$$

where E_x and E_y are the complex field components describing the amplitude (real, positive constants a_x and a_y) and the phase of the projections of $\vec{E}(\vec{x}, t)$ (δ_x and δ_y) along the x and y axes. As shown in Figure 4.1, the end point of the electric field vector $\vec{E}(\vec{x}, t)$ traces an ellipse (polarization ellipse) in time at any fixed plane $z = z_j$ which satisfies the following equation:

$$\left(\frac{E_x}{a_x}\right)^2 + \left(\frac{E_y}{a_y}\right)^2 - 2\frac{E_x}{a_x}\frac{E_y}{a_y}\cos(\delta) = \sin^2(\delta) \quad (4.2)$$

where $\delta = \delta_y - \delta_x$ and in order to avoid complex notation, the real field and associated complex field are represented by the same notation ($\text{Re}[E_x] = a_x \cos(\omega t - kz + \delta_x)$ and $\text{Re}[E_y] = a_y \cos(\omega t - kz + \delta_y)$ are represented by E_x and E_y , respectively) [60, 65]. The polarization ellipse is determined by the relative amplitude and the relative phase of one oscillating component with respect to the other orthogonal component. In general, the axes of the ellipse are not in the Ox and Oy directions. New coordinate axes Ou and Ov along the axes of the ellipse can be defined as shown in Figure 4.1 where the angle between Ou and Ox is denoted by α (azimuth). All physically distinguishable azimuths can be obtained by limiting α to the range of $-\pi/2 < \alpha < \pi/2$. The rotated ellipse can be described as the sum of u and v components of the electric vector with maximum amplitudes of a and b , respectively and relative phases of $\pm \pi/2$. Then the electric field components at a reference plane $z=0$ can be written as $E_u = a \cos(\omega t + \delta_u)$ and $E_v = b \cos(\omega t + \delta_v)$, or $E_u = a \cos(\omega t + \delta_u)$ and $E_v = b \cos(\omega t + \delta_u \pm \pi/2) = \pm b \sin(\omega t + \delta_u)$. The lengths of the axes of the ellipse in the new coordinate frame are a and b . If a_x , a_y and δ is known, a , b can be determined for any α ; or conversely, if a , b and α are known, a_x , a_y and δ can be determined by using the following equations:

$$a^2 + b^2 = a_x^2 + a_y^2, \quad \tan 2\alpha = \tan 2\beta \cos \delta, \quad \sin 2\varepsilon = \sin 2\beta \sin \delta \quad (4.3)$$

where $\tan 2\beta = a_y/a_x$, $\tan \varepsilon = \pm b/a = e$ is called ellipticity which is a measure of “fatness” of the ellipse ($-1 < e < 1$ where handedness of the ellipse is defined by the sign of e) and ε is called the ellipticity angle ($-\pi/4 > \varepsilon > \pi/4$) [65, 89]. It is evident from the above second equation that one needs only to know the relative, not absolute, amplitudes and phases of the x and y components of the the electric field vector in

order to determine the azimuth of the ellipse described by these components. Similarly, from the third equation, the ellipticity can be determined from the relative amplitudes and phases of the x and y components of the electric field vector. Moreover, it is possible to write the following relation

$$ab = \pm a_x a_y \sin \delta \quad (4.4)$$

Since a , b , a_x and a_y are positive, + sign and - sign indicate $\sin \delta > 0$ and $\sin \delta < 0$, respectively. If δ is defined as $-180^\circ < \delta < 180^\circ$, + sign and - sign correspond to $0^\circ < \delta < 180^\circ$ and $-180^\circ < \delta < 0^\circ$, respectively. $0^\circ < \delta < 180^\circ$ means y component is “ahead” of the x component and $-180^\circ < \delta < 0^\circ$ means y component is “behind” of the x component. In the case of $0^\circ < \delta < 180^\circ$, as time passes, the ellipse is traced out in a clockwise direction, that is called right-handed polarization; whereas in the case of $-180^\circ < \delta < 0^\circ$, as time passes, the ellipse is traced out in a counter-clockwise fashion, that is called left-handed polarization.

The parameters needed to describe the shape of the ellipse of polarization (intensity independent quantity) are listed as follows:

- (1) The azimuth α
- (2) The ellipticity e or ellipticity angle ε .
- (3) Handedness of the polarization ellipse

On the other hand, the amplitude (a scalar quantity) is related to the size of the ellipse of polarization and the absolute phase is related to the angle that the electric field vector makes with the x axis.

4.2.2 Main states of polarization: Linear and Circular Polarization

The shape of the ellipse of polarization can be represented by the polarization state $\chi = E_y / E_x$ and some special types of polarization can be given accordingly as follows:

Linearly polarized light: $\text{Im}\left[\frac{E_y}{E_x}\right] = 0$ (no phase difference between two components. In other words, they are in phase).

Circularly polarized light: $|E_x| = |E_y|$. $\frac{E_y}{E_x} = -i$, right-handed, or $\frac{E_y}{E_x} = i$, left-handed (the two components have identical magnitudes but are 90° out of phase).

Circularly polarized light can be described by the orthogonal components of linearly polarized light and vice versa. Elliptical polarized light can be thought of as combinations of orthogonal components of either linear and circularly polarized light. Most generally, any polarization form can be represented as the sum of two orthogonally polarized components.

4.2.3 Jones Matrix Formalism

Jones matrix approach is a kind of mathematical tool to describe the interaction of light with several types of optical systems such as polarizers and retarders [60, 89]. Such a tool is very useful to determine the evolution of a state of polarization in an optical system. The only information that is needed to be sought is the determination of the amplitude and phase of oscillation of each component of the electric field vector, because time dependence of each component (periodic sinusoidally with time at all points in space at the same frequency) is known. Electric field vector of a light at a certain point along the z-axis can be given in a column vector notation as

$$\vec{E} = e^{i\omega t} \begin{pmatrix} a_x e^{i\delta_x} \\ a_y e^{i\delta_y} \end{pmatrix} \quad (4.5)$$

If the time dependent term is suppressed, the following vector

$$\vec{J} = \begin{pmatrix} a_x e^{i\delta_x} \\ a_y e^{i\delta_y} \end{pmatrix} \quad (4.6)$$

is called Jones vector. All possible states of polarization of all possible values of intensity and phase can be defined by the Jones vector. For a unit amplitude and zero phase, Jones vector of an arbitrary linearly polarized light wave of which the electric vector oscillates along a general direction x' inclined to the direction of the x axis by an azimuth angle α can be expressed as $\vec{J} = \begin{pmatrix} \cos \alpha \\ \sin \alpha \end{pmatrix}$. The state of polarization that is

orthogonal to the state given by the above Jones vector can be given by $\vec{J}' = \begin{pmatrix} \sin \alpha \\ -\cos \alpha \end{pmatrix}$ where α is replaced by $\alpha - \pi/2$.

4.2.4 Interaction of Light with Polarizing Optical Systems

As a result of interaction of an incident wave and a polarizing system, the Jones vector of the incident wave is transformed. An optical system may attenuate the amplitude and/or change the phase relation between two orthogonal components of the light differently, such as by dichroism (unequal absorption of two orthogonally polarized components) or birefringence (unequal retardation of orthogonal components). If the optical system is assumed to be linear, not frequency-changer (frequency of the incident light is conserved) and non-depolarizing, that is, it does not randomize the time-dependent amplitudes and phases of the orthogonal electric field components of the incident light wave, the incident Jones vector J_0 is linearly transformed under the effect of optical system as

$$J_1 = TJ_0 \quad \text{with} \quad T = \begin{pmatrix} T_{11} & T_{12} \\ T_{21} & T_{22} \end{pmatrix} \quad (4.7)$$

J_1 is the Jones vector of the wave emerged (outgoing) from the optical system and T is called the Jones matrix of the optical system (transformation matrix that converts J_0 to J_1) [60, 89].

The relation between state of polarizations of incoming ($\chi_0 = E_{0y}/E_{0x}$) and outgoing light ($\chi_1 = E_{1y}/E_{1x}$) can be given as $\chi_1 = (T_{22}\chi_0 + T_{21})/(T_{12}\chi_0 + T_{11})$. It is seen that the polarization state of the outgoing light can be given by the polarization state of the incident wave irrespective of the amplitude and the phase of the incident wave. If the polarization state (ellipticity, azimuth and handedness) of the incident wave is not changed ($\chi_1 = \chi_0$, intensity may be changed), the two solutions (roots) χ_{e1} and χ_{e2} of equation $\chi_0 = (T_{22}\chi_0 + T_{21})/(T_{12}\chi_0 + T_{11})$ are called eigenpolarizations (eigenvectors) of the optical system. An optical system can be described by its eigenpolarizations. For example, the Jones matrix of a isotropic and non-optically active reflecting surface (reflector) can be given as

$$T = \begin{pmatrix} r_p & 0 \\ 0 & r_s \end{pmatrix} \quad (4.8)$$

where r_p and r_s are reflection coefficients of an incident light polarized parallel and perpendicular to the plane of incidence. It is seen that if the electric field vector of the incident wave is parallel to the plane of incidence, the reflected wave is also have an electric field vector parallel to the plane of incidence. Likewise, if the electric field vector is oscillating perpendicular to the plane of incidence, the reflected field vector has also a vibration perpendicular to the plane of incidence. Consequently, s and p linear polarization states are eigenpolarizations of this optical system. r_p and r_s are

eigenvalues associated to the eigenvector. At the Brewster angle, $|r_p| = 0$, the reflecting surface becomes an ideal linear polarizer.

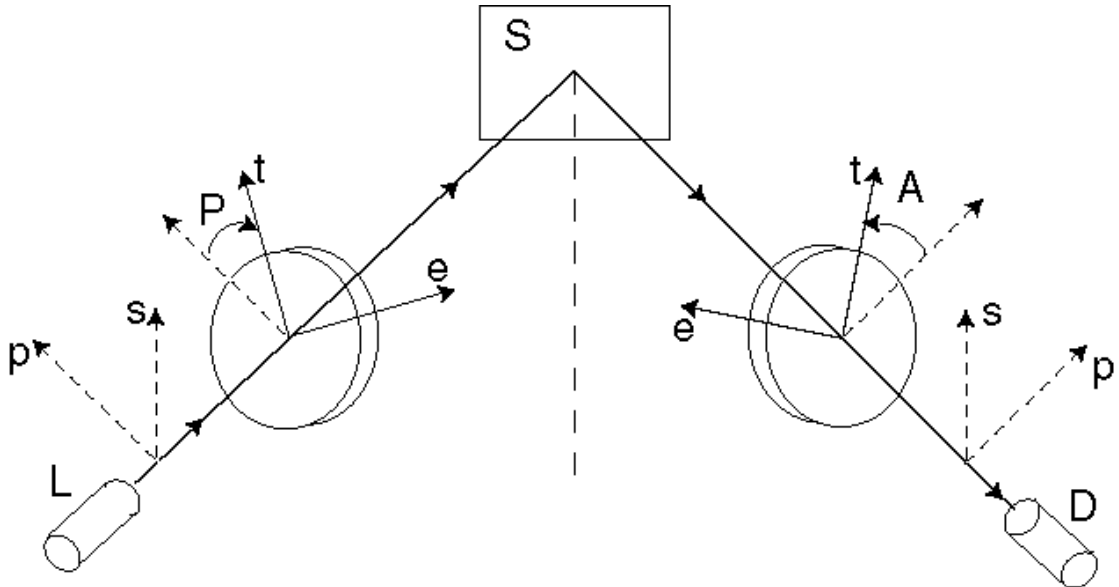


Figure 4.2 An optical arrangement of a polarizer, optical system S , analyzer and photodetector. The light emerging from the light source L falls on the polarizer, passes through it and reflects from the optical system S . The reflected light reaches the photodetector after passing through the analyzer. P and A represent the azimuthal positions of the polarizer and analyzer measured from the plane of incidence.

4.2.5 Measurement of the Ratio of Eigenvalues of an Optical System

Let's consider an optical arrangement, consisting of a light source, a linear polarizer, an optical system, an analyzer and a photodetector as shown in Figure 4.2. Azimuth positions (orientation of the transmission axes) of the polarizer and analyzer are denoted by P and A , respectively, which are measured from the plane of incidence, positive in a counterclockwise sense looking into the beam. After the beam of light (e.g, unpolarized light) passes through the polarizer, the state of polarization of light emerging from the polarizer is changed according to the azimuth position of the linear

polarizer. Then, the state of polarization of the incident light beam is modified upon reflection from the optical system S when that state is different from either one of its eigenpolarizations. The modified state of polarization of the light beam is analyzed by a linear analyzer followed by a photodetector.

The light incident on the linear polarizer becomes linearly polarized as it emerges. The Jones vector of the emerging wave is given by $J_{Po}^{te} = C_p \begin{pmatrix} 1 \\ 0 \end{pmatrix}$ where C_p is the term containing the information of intensity and absolute phase of the wave emergent from the polarizer. The superscript te denotes the transmission-extinction principle frame of reference of the polarizer. The principle frame is the coordinate system in which the Jones matrix of the optical component is diagonal. The first letter of the subscript P (A) denotes the optical element, that is, polarizer (analyzer) and the second letter o (i) denote output (input) of the polarizer. The emerging wave is incident on the optical system and its Jones vector can be given as $J_{Si}^{te} = J_{Po}^{te}$. The subscript S denotes the optical system. In order to calculate the Jones vector of the outgoing reflected wave, one needs to change the reference coordinate system from te principle frame of the polarizer to the sp principle frame of the optical system S . Such a coordinate rotation, transform J_{Si}^{te} to the Jones vector J_{Si}^{sp} as $J_{Si}^{sp} = \begin{pmatrix} \cos P & -\sin P \\ \sin P & \cos P \end{pmatrix} J_{Si}^{te}$. Recalling equation (4.8), the Jones matrix of the optical system can be given by $T_S^{sp} = \begin{pmatrix} r_p & 0 \\ 0 & r_s \end{pmatrix}$. Consequently, the Jones vector J_{So}^{sp} of the reflected wave can be written as $J_{So}^{sp} = T_S^{sp} J_{Si}^{sp}$. Similarly, transforming the reference frame to the principle frame of the analyzer (te) one can express J_{Ai}^{te} as $J_{Ai}^{te} = \begin{pmatrix} \cos A & \sin A \\ -\sin A & \cos A \end{pmatrix} J_{So}^{sp}$. In analyzer's principle frame, the Jones matrix of the analyzer is $T_A^{te} = C_A \begin{pmatrix} 1 & 0 \\ 0 & 0 \end{pmatrix}$ where the factor C_A accounts for amplitude and phase changes experienced by the transmitted linear eigenpolarization and the Jones vector of

the wave transmitted by the analyzer can be given as $J_{Ao}^{te} = C_A \begin{pmatrix} 1 & 0 \\ 0 & 0 \end{pmatrix} J_{Ai}^{te}$. The electric field of the wave reaching the photodetector in the principle frame of the analyzer can be expressed as

$$\begin{aligned}
\begin{pmatrix} E_t \\ E_e \end{pmatrix} &= e^{i\omega t} \begin{pmatrix} a_t e^{i\delta_t} \\ a_e e^{i\delta_e} \end{pmatrix} = C_A C_P \begin{pmatrix} 1 & 0 \\ 0 & 0 \end{pmatrix} \begin{pmatrix} \cos A & \sin A \\ -\sin A & \cos A \end{pmatrix} \begin{pmatrix} r_p & 0 \\ 0 & r_s \end{pmatrix} \begin{pmatrix} \cos P & -\sin P \\ \sin P & \cos P \end{pmatrix} \begin{pmatrix} 1 \\ 0 \end{pmatrix} \\
&= C_A C_P \begin{pmatrix} r_p \cos P \cos A + r_s \sin P \sin A \\ 0 \end{pmatrix} \\
&= C_A C_P r_s \begin{pmatrix} \rho \cos P \cos A + \sin P \sin A \\ 0 \end{pmatrix} \tag{4.9}
\end{aligned}$$

where ρ is defined as

$$\rho = \frac{r_p}{r_s} = \tan \Psi e^{i\Delta} \tag{4.10}$$

The dedected intensity of the light by the photodetector is proportional to $I = |E_t|^2 + |E_e|^2$:

$$\begin{aligned}
I &= |C_A|^2 |C_P|^2 |r_s|^2 |\rho \cos P \cos A + \sin P \sin A|^2 \\
&= I_0 (1 + \alpha_2 \cos 2A + \beta_2 \sin 2A) \tag{4.11}
\end{aligned}$$

where I_0 is the average irradiance, $\alpha_2 = \frac{\tan^2 \Psi - \tan^2 P}{\tan^2 \Psi + \tan^2 P}$ and $\beta_2 = \frac{2 \tan P \tan \Psi \cos \Delta}{\tan^2 \Psi + \tan^2 P}$.

It is seen that the signal dedected by the photodetector is a function of azimuth angle settings P and A , and the complex eigenvalues r_p and r_s of the optical system.

In such an optical arrangement of various optical elements, the coefficients α_2 and β_2 needed to be determined in order to obtain the ratios of eigenpolarizations of the optical system S , that is $\rho = r_p / r_s$. In principle, for a given polarizer angle, it is possible to determine ρ from two measurements of detected intensity at two different analyzer angles.

4.3 Fundamentals of Ellipsometry

Since reflection and transmission coefficients at each interface for s and p polarized waves are different, total reflection and transmission coefficients for an air-film-substrate system will also be different. The change of polarization upon reflection and transmission due to the difference in amplitude attenuation and phase shift experienced by the p and s components is the basis of ellipsometry.

4.3.1 Definition of Ellipsometry Angles

Ellipsometry measurement determines the complex reflectance ratio ρ which can be defined in terms of angles Ψ and Δ as $\rho = \tan \Psi e^{i\Delta}$ (equation (4.10)). ρ is equivalent to the ratio of polarization states: $\chi_{reflected} / \chi_{incident} = [(r_p E_p / r_s E_s) / (E_p / E_s)] = r_p / r_s = \rho$. The angles Ψ and Δ determine changes in the amplitude and phase, respectively, of the p and s components of the wave upon reflection, and can be expressed as

$$\Psi = \tan^{-1} \frac{|r_p|}{|r_s|}, \quad \Delta = \delta_p - \delta_s \quad (4.12)$$

4.3.2 Two Phase (Substrate-Ambient) Optical System

Two phase system is an ideal case which consists of an optically thick substrate and a transparent ambient with isotropic dielectric functions ε and ε_a , respectively, as shown in Figure 3.1. If the expressions for r_p and r_s (equations (3.8)) are substituted into equation (4.10) and making use of Snell's law, $\varepsilon/\varepsilon_a$ can be expressed in terms of ρ and ϕ_i only, as follows:

$$\frac{\varepsilon}{\varepsilon_a} = \sin \phi_i \left[1 + \left(\frac{1-\rho}{1+\rho} \right)^2 \tan^2 \phi_i \right] \quad \text{or,} \quad \frac{\varepsilon}{\varepsilon_a} = \tan \phi_i \left[1 - \frac{4\rho}{(1+\rho)^2} \sin^2 \phi_i \right] \quad (4.13)$$

In reality, it is extremely difficult to have a film with mathematically sharp surface (more generally interface) without any oxide layer, adsorbed contaminant and microscopic roughness on it. Calculating optical parameters from equation (4.13) by neglecting such properties of surfaces which are encountered in typical laboratory conditions may result in incorrect results. Instead, assuming simple two-phase model, one can compute the pseudodielectric function $\langle \varepsilon \rangle$ from the measured ρ using equation (4.13). The pseudodielectric function is an average dielectric responses of substrate and overlayer. Its difference from actual ε depends on how two-phase model represents the sample. In other words, $\langle \varepsilon \rangle$ is the dielectric function of the hypothetical uniform isotropic material with a clean mathematically sharp surface boundary that gives the same ellipsometric data as the actual sample [90].

4.3.2 Three Phase (Substrate-Film-Ambient) Optical System

Three phase system consists of a substrate, film and ambient as shown in Figure 3.2. If we substitute the values of r_p and r_s from equations (3.16) into equation (4.10), we obtain ρ as

$$\tan \Psi e^{i\Delta} = \rho = \frac{r_{1p} + r_{2p} e^{-i2\delta}}{1 + r_{1p} r_{2p} e^{-i2\delta}} \frac{1 + r_{1s} r_{2s} e^{-i2\delta}}{r_{1s} + r_{2s} e^{-i2\delta}} \quad (4.14)$$

It is not possible to solve equation (4.14) in general as it is done for a two phase system. If we write r_p and r_s as $r_p = (a + bX)/(1 + abX)$ and $r_s = (c + dX)/(1 + cdX)$, equation (4.14) can be given by [60]

$$\rho = \frac{A + BX + CX^2}{D + EX + FX^2} \quad (4.15)$$

where $X = e^{-i2\delta}$ and the coefficients of X is given in Appendix 3. It is seen that ρ is a rational function of X with coefficients which are functions of Fresnel reflection coefficients. By using the Snell's law, one can write phase thickness in the following form:

$$\delta = 2\pi \left(\frac{d}{\lambda} \right) \left(N_1^2 - N_0^2 \sin^2 \phi_0 \right)^{1/2} \quad (4.16)$$

If δ is substituted in X , X becomes

$$X = \exp \left[-i2\pi \left(\frac{d}{D_\phi} \right) \right] \quad \text{with} \quad D_\phi = \frac{1}{2} \lambda \left(N_1^2 - N_0^2 \sin^2 \phi_0 \right)^{1/2} \quad (4.17)$$

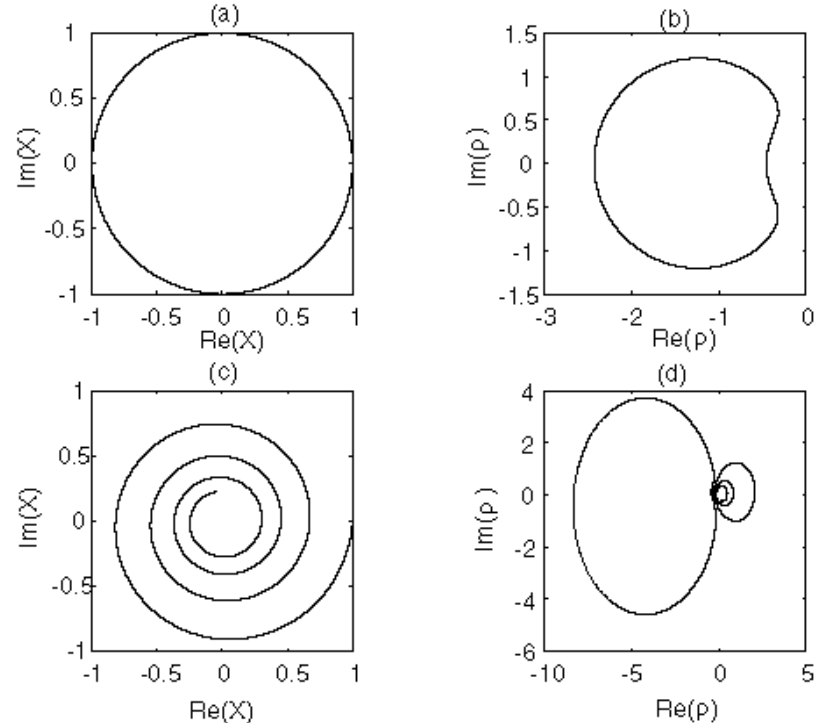


Figure 4.3. (a) Unit circle in the complex X -plane for a transparent film. (b) Constant angle of incidence contour of ρ at $\phi_0=60^\circ$ for air-SiO₂-Si system at wavelength $\lambda=632.8$ nm when the film is transparent. (c) Logarithmic spiral of X when the film is absorbing. (d) Constant angle of incidence contour of ρ at $\phi_0=60^\circ$ for air-SiO₂-Si system at wavelength $\lambda=632.8$ nm when the film is absorbing.

When the ambient and film media are transparent (N_0, N_1 ve D_ϕ are real), it can be seen from equation (4.17) and Figure 4.3(a) the representative point of the complex exponential function X moves uniformly in a clockwise direction around the unit circle in the complex X -plane for any angle of incidence as the film thickness d is increased starting from $d=0$ ($X=1$). X is a periodic function of d and the first revolution around the unit circle is completed as the film thickness reaches a value of D_ϕ . On the other hand, the point describing ρ on the complex ρ -plane trace a closed contour as X traces the unit circle in the complex X -plane as it is seen from Figure 4.3(b). When the film is absorbing, equation (4.18) becomes complex and the exponential function X exhibits a logarithmic spiral in the complex plane as it is shown in Figure 4.3(c). Similarly, the contour of ρ for an absorbing film is shown in Figure 4.3(d) [60].

CHAPTER 5

EQUIPMENTS AND THEIR IMPLEMENTATIONS

5.1 Plasma Enhanced Chemical Vapor Deposition

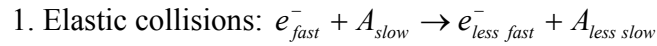
It is first observed in 1933 that material can be removed from the wall of a glass tube if it is subjected to a high frequency discharge. After similar investigations, in 1962, Anderson *et al.* applied radio frequency (RF) voltage to the inside of the tube and suggested that this method can be used for deposition of thin films since RF voltage is observed to be used to generate reactive species [91]. Since then (especially after the end of 1970s), RF discharges are widely used for deposition and etching of thin solid films which have important applications in all aspects of high technology, especially in large area electronics.

Plasma is an effective chemical medium because it consists of electrons, ions, radicals and other active species which make the plasma medium highly reactive [92]. Most deposition systems have been designed by confining the plasma between two electrodes where the electric field can be created by direct current (DC), RF and microwave. This type of deposition system is named as plasma enhanced or plasma assisted chemical vapor deposition (PECVD). RF discharges can be easily produced at larger dimensions which makes it more advantageous over other discharges [93].

5.1.1 Collisions of particles in the Plasma

At sufficiently high voltage (under electric field of sufficient magnitude), the gas in the reactor starts to breakdown via the collisions of accelerated free electrons which

are present in the reactor initially. Types of collisions between particles in the plasma can be given in most general as follows [94]:



2. Inelastic collisions: $e_{fast}^- + A \rightarrow e_{slower}^- + A^*$ (kinetic energy transferred to internal energy).

3. Superelastic collisions: $A_{slow}^* + B_{slow} \rightarrow A_{faster} + B_{faster}$ (internal energy is transferred to kinetic energy)

At all types of above collisions momentum is redistributed between particles.

5.1.2 Radio Frequency Discharges (Plasma)

The frequency of applied voltage in RF discharges must be sufficiently high that the created charged particles by the applied voltage are not lost when the voltage passes through zero. Typical frequencies for this purpose are above 50 kHz. Commonly used frequency is 13.56 Mhz. RF discharges are usually operated at low pressures, typically 0.1-1 Torr. Low and high pressures in this range are preferred for etching and deposition, respectively.

In the initial stage of the plasma process, accelerated electrons by the applied field lose their energy by elastic collisions with gas molecules. Then, as the electrons gain sufficient energy, they ionize and/or dissociate gas molecules. Consequently, secondary electrons are produced [91]. The electrons cannot transfer much energy to heavy ions because the energy transfer in an elastic collision is proportional to the (small) mass ratio. The electrons lose their energy mainly by inelastic collisions such as excitation (rotational, vibrational and electronic), dissociation and ionization of plasma species. Electronic excitation of molecules or atoms lead to luminous glow during recombination process. Ionizing collisions produce electron and ion pairs whereas molecular dissociation leads to highly reactive atoms and free radicals. A free radical is

an atom or group of atoms which is electrically neutral and in state of incomplete chemical bonding (unpaired electron) which makes it very reactive. As charged particles (electrons, ions) are generated by inelastic collisions, some of them are lost from the plasma by various reasons such as drift and diffusion to the reactor walls (boundaries), recombination (ion-ion recombination, electron-ion recombination) and attachment to electronegative molecules to form negative ions. At steady state (stable-plasma), charged particle generation and loss processes balance each other, that is, plasma is self sustained.

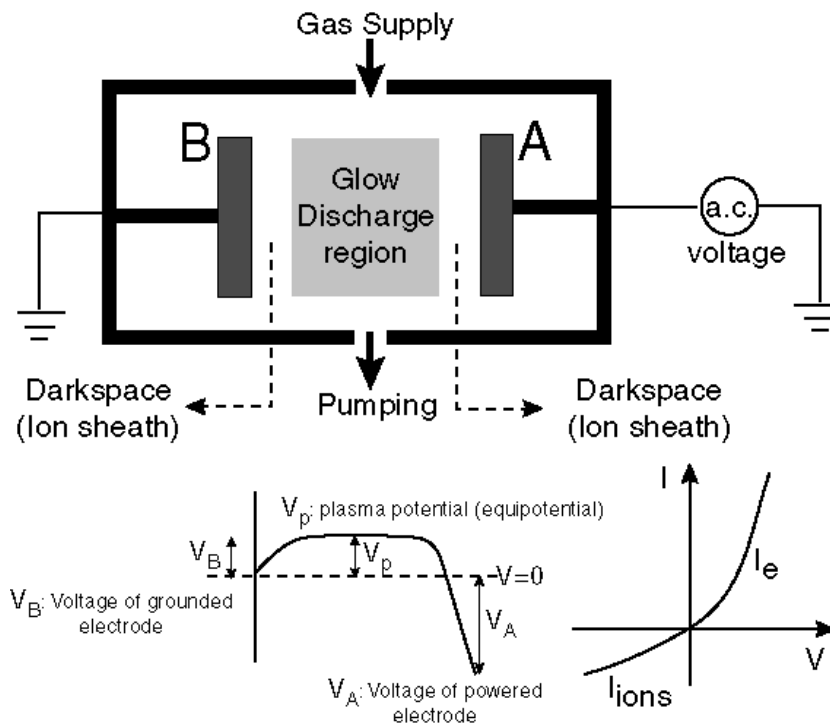


Figure 5.1. Schematic diagram of a capacitively coupled radio frequency discharge. Spatial distribution of the average potential between the electrodes is given just below the inter-electrode region. I_e and I_{ions} denote electron and ion currents, respectively.

A schematic diagram of capacitively coupled radio frequency discharge is given in Figure 5.1. For a gas pressure of about 1 torr, a weakly ionized medium (10^{10} electrons or ions per cm^3 , 10^{16} neutral molecules per cm^3) is obtained between the electrodes. As the plasma is obtained, current starts to flow between electrodes. If the potential is positive at a given electrode, electrons are collected from the plasma leading to current I_e . Similarly, if the potential is negative at a given electrode, positive ions are collected from the plasma leading to current I_{ions} .

Since electrons are much more mobile than the heavier ions, $I_e > I_{ions}$. I-V characteristic of the plasma is like a leaky diode as it is illustrated in Figure 5.1. As the frequency of the applied field increases from very low (dc) to higher values (ac), beyond a certain value, the ions created during the breakdown cannot be fully extracted from the inter-electrode gap in one half of the field but electrons are easily extracted due to their lighter masses. If the frequency increases further, a large fraction of electrons have insufficient time to drift to the positive electrode during a half cycle. Instead, these electrons oscillate in the inter-electrode gap and undergo collisions with gas molecules. This range of frequency is called RF range (typically 25 kHz-25 MHz).

Let's suppose a potential (e.g. square like) at the RF generator is applied to the electrode A. At negative half-cycle positive ions are accelerated towards the electrode A. These ions become neutralized by removing electrons from the electrode surface. A positive charge is left on the electrode as a result of this flow and neutralization. During the positive half-cycle, the electrode collects electrons which are much lighter than ions. Such a difference in masses results in collection of many more electrons than ions during the first full-cycle. Electron and ion concentration becomes equal for subsequent cycles because negative charge building increases up to the steady state where at negative cycles, as incoming electrons are repelled, incoming ions are attracted more strongly. This average negative charge built-up at the electrode causes a negative dc offset voltage (self bias voltage) between the electrode and the discharge. There are three main regions in potential distribution: grounded electrode with potential V_B , glow discharge region with a potential V_p and power electrode with potential V_A [95-96]. The

larger potential drop occurs at the powered electrode which is more negative with respect to ground than the grounded electrode. Therefore powered electrode is called the cathode and the grounded electrode is called anode. The substrate is usually placed on the anode in FR discharges. Since the potential of grounded electrode is always negative with respect to the plasma potential, substrate's surface on the grounded electrode suffers bombardment by the positive ions. However, ion bombardment is stronger at the cathode which experiences more ion bombardment than films grown on the grounded electrode (anode). Glow discharge region corresponds to the region where the potential is approximately equal to the plasma potential. The regions between the glow discharge and the electrodes are called dark space or ion sheath [97].

There are two types of plasma parameters for any plasma deposition system:

1. Plasma related variables such as electron and ion densities, energies, and distribution.
2. Process related variables such as frequency, excitation power, gas mixtures and flow rates, pressures and substrate temperature.

Process related variables are adjusted for a particular production and are easier to measure and control than plasma related parameters [97].

The schematic diagram of the PECVD reactor which is used in the deposition of the various films is given in Figure 5.2. Gas cabinet system associated to the PECVD reactor is shown in Figure 5.3.

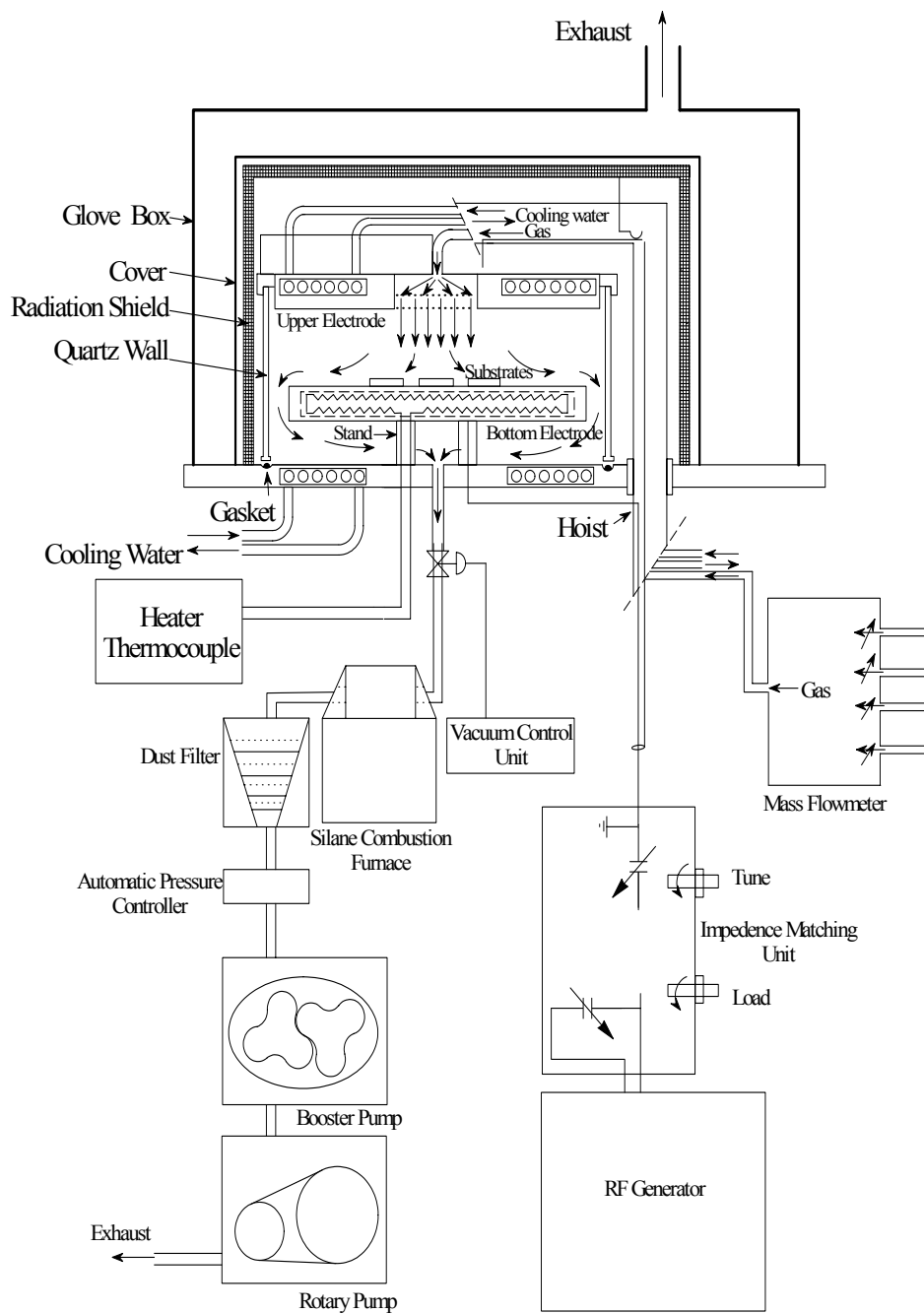


Figure 5.2. Schematic diagram of the PECVD system used in the production of thin films [98].

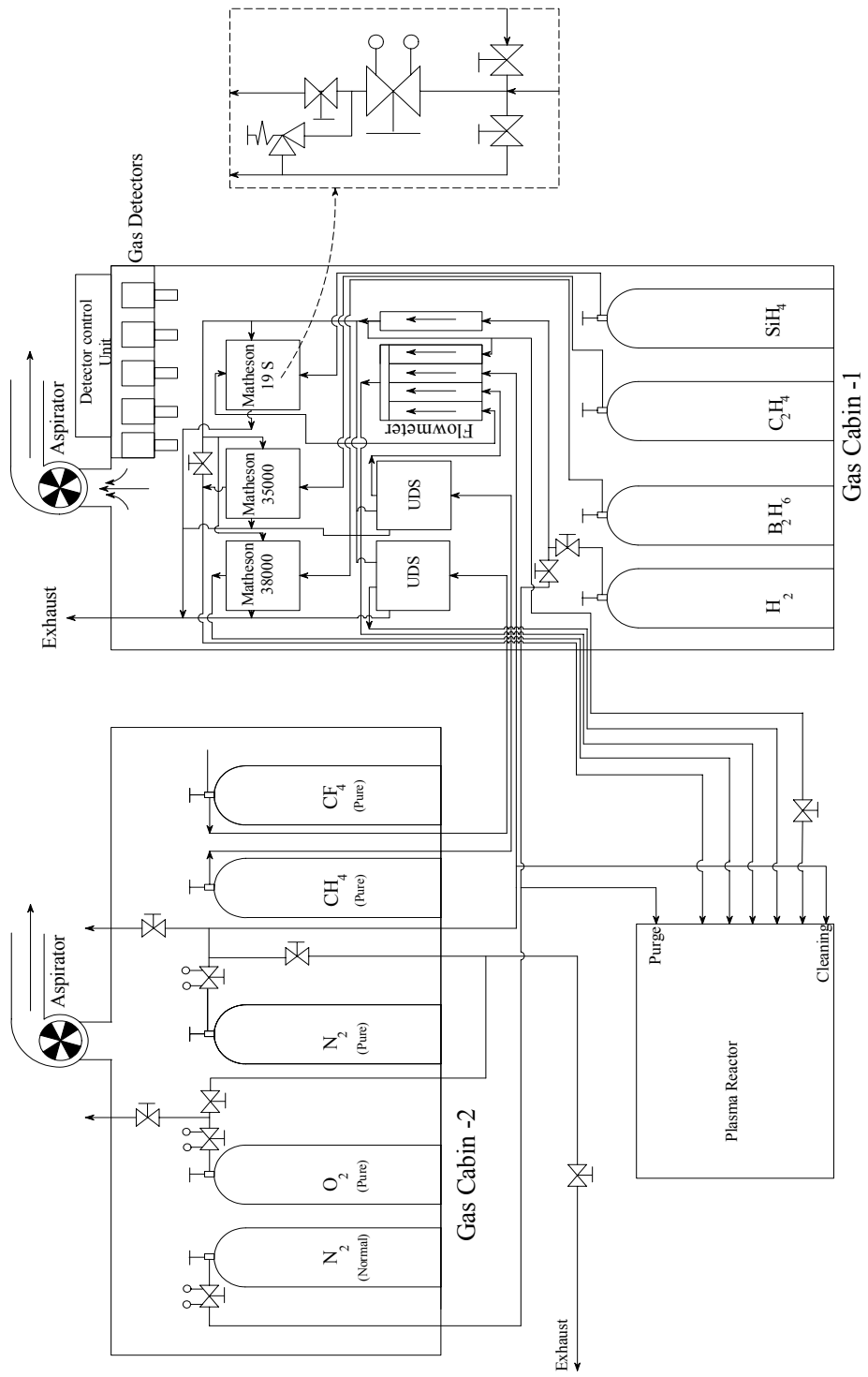


Figure 5.3. Gas cabinet system associated to the PECVD system shown in Figure 5.2 [98].

5.2 UV/VIS Spectrometer

Perkin Elmer Lambda 2 Spectrometer is used for transmission and reflection measurements. It is a double beam spectrometer for Ultraviolet/Visible (UV/VIS) region with a wavelength range of 200-1100 nm. A deuterium and a Tungsten-halogen lamp are used as radiation sources.

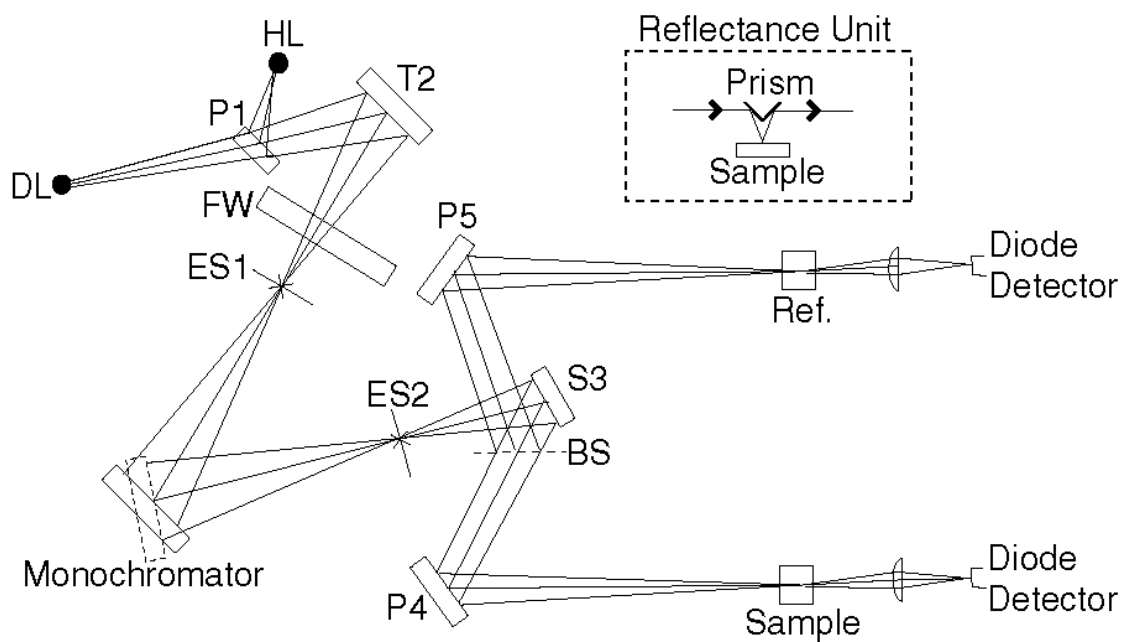


Figure 5.4. Illustration of optical path of the Perkin Elmer Lambda 2 Spectrometer [99]. Reflectance unit, shown as an inset, is positioned on the sample platform for reflectance measurements.

The optical system is illustrated in Figure 5.4. The monochromator has a grating with 1053 lines/mm. A movable planar mirror P1 is positioned to block the light emerging from one of the light sources and the light emerging from the other light source is reflected onto the mirror T2. Source changes, performed by positioning the mirror P1, occur in synchronization with the monochromator. Radiation, focused by T2

onto the entry slit ES1, first passes through some filters (FW) to limit the wavelength range reaching to the monochromator. As the light beam reaches to the monochromator it is spectrally dispersed and focused on the exit slit ES2. After the light beam passes through a spherical mirror S3, the light beam is reflected onto the beam splitter BS which allows 50% of the light to pass through to the planar mirror P4 and 50% of the light is reflected onto the planar mirror P5. After the mirror P4 focuses the radiation in the sample platform, the emerging light is focused onto the sample photo-diode by a convex lens. Similarly, after the mirror P5 focuses the light beam onto the reference platform is then focused onto the reference photo-diode dedector by a convex lens [99]. For reflectance measurements the reflectance unit shown in Figure 5.4 needs to be positioned onto the sample platform. Reflectance measurements at approximately normal angle of incidence are performed first with a calibrating mirror in place of the sample and then with the sample.

A standard developed by Electronic Industry Association with Bell Laboratories in 1969 to simplify interfacing a Data Terminal Equipment (DTE) with a Data Communications Equipment (DCE) that are manufactured by different firms. This standard is shortly called as RS-232-C and it is an interface between DTE and DCE employing serial binary data exchange.

5.2.1 RS-232-C Interface

Serial interfaces use a single line to transmit one bit at a time. RS-232-C consists of 25 data lines and the signals going through each pin of the connector are specialized [100]. The pin definitions are given in Table 5.1. The directions are specified relative to the DTE end of the connection. This means that when DTE transmits data it is an output whereas in terms of the DCE it becomes an input.

Table 5.1 Pin Assignments in RS-232-C with signal travel direction.

Pin Number	Signal Name	Definition	Direction
1	Protective Ground	Connected to the frame of one of the devices to protect against electrical shock.	-
2	Transmit Data	Data is sent on this line.	Output
3	Receive Data	Data is received in this line.	Input
4	Request to Send	is used when DTE wants to transmitting.	Output
5	Clear to Send	Answer signal telling DTE that it can now start transmitting.	Input
6	Data Set Ready	DCE tells DTE that the communication channel is available.	Input
7	Signal Ground	Reference ground for all other signals, data and control.	-
8	Data Carrier Detect	DCE tells DTE that a good signal is received.	Input
20	Data Terminal Ready	Tells DCE that DTE is available for receiving.	Output
22	Ring Indicator	DCE tells DTE that there is an incoming call.	Input

Transmitted data go through pin 2, whereas the received data go through pin 3. Transmitted data that originates from pin 2 of the DTE becomes a received data arrived on pin 3. For example two Data Terminal Equipments are connected through telephone lines where each DTE has modem (DCE). If the telephone number of one of the modem is dialed, the DTE is indicated that there is an incoming call to the modem through pin 22. Data Terminal Ready signal is sent to the modem and then modem answers the call. After the modem answers the call, each modem sets Data Set Ready (DSR) "On" which indicates two modems are ready to communicate. If the DTR of the other end is "On", connection is established. Half duplex transmission means that signals can travel on both directions but only one at a time. In this environment, after the connection is established, suppose that one of the DTE has data to transmit. This DTE (local) sets Request To Send (RTS) "On" through pin 4 and this signal is received by pin 8 at the other end. The modem checks whether Data Carriage Detect (DCD) is "On" or not. If it is "Off" then Clear To Sent (CTS) signal is sent to DTE. If it is "On" it means that RTS signal of the

DTE at the other end is “On” and local DTE sets RTS “Off” and then sets it “On” again. This interaction continues until DCD is “Off”. After CTS signal is received by the DTE, the DTE transmits the data to the modem through pin 2 and the modem transmits to the other modem. This receiving modem transmits the data to the pin 3 of the DTE. Until the data is transmitted RTS signal of the local DTE is held “On”. Then DTE sets RTS “Off” and DCD is set “Off” at the other end. Finally, CTS is set “Off” and now any one of the Data Terminal Equipments can set RTS “On”.

If two Data Terminal Equipments are connected without using any Data Communications Equipment, a cable which simulates the existence of the two Data Communication Equipments (typically modems) is needed between the ports of the two Data Terminal Equipments. This type of cable is called null modem. Since the spectrometer and the computer are on a table, any DCE like a modem using telephone lines is not needed to connect these two equipments.

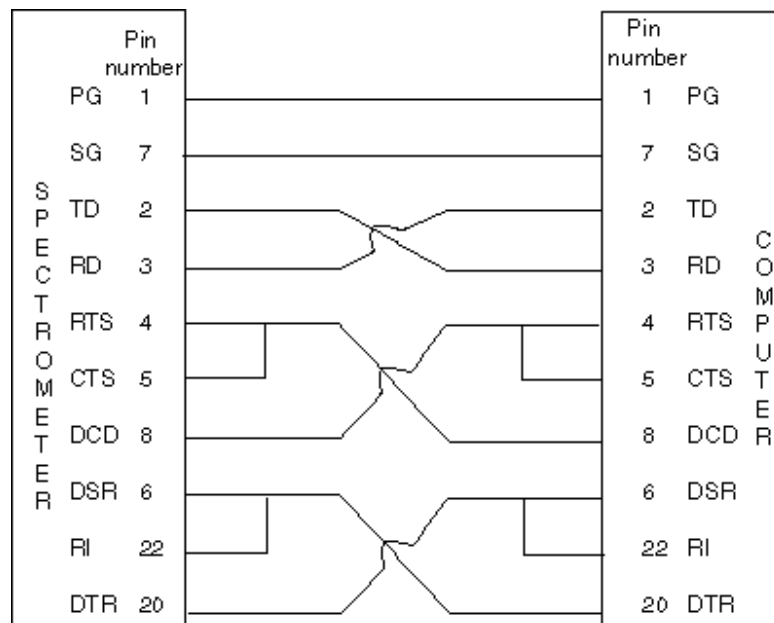


Figure 5.5 Null modem cable.

5.2.2 Computer Control of the Spectrometer via a RS-232-C Interface

Since no DCE is used between the PC and the Spectrometer, a null modem is needed to be used. The Protective Ground (PG) and Signal Ground (SG) of the spectrometer are connected to the corresponding PG and SG on the computer directly without any cross connections as shown in Figure 5.5. Data are transmitted through pin 2 from the spectrometer and received through pin 3 at the computer. Similarly, data are transmitted through pin 2 from the computer and received through pin 3 at the spectrometer. In the absence of the DSR, CTS and DCD signals provided by the DCE, RTS and DTR signals must be used to provide those signals. DTR is generally “On” when the power of the corresponding equipment is “On”. DSR signal must be “On” to provide connection. When DTR is “On”, DSR on the other end must be “On”; therefore DTR and DSR signals on both ends are crossed. When RTS signal is sent, CTS signal must be received for data transmission to be allowed. If pin 4 and 5 are connected on the same equipment, CTS signal is granted. On the other hand, the receiving device must be indicated that data will be arriving. Therefore DCD signal can be provided by RTS signal by also connecting pin 4 with pin 8 at the other equipment. These connections are repeated at the spectrometer and the computer as shown in Figure 5.5. Each setting that can be selected on the keyboard of the spectrometer can be selected also by using commands in a program. These commands are begun with a \$ and followed by two capital letters. Some of these commands must have an input parameter which must follow the command, separated by one space. A programme is written to control the spectrometer by a computer which lets to see the spectrum interactively while the spectrometer runs.

5.3 Single/Multi-Wavelength Ellipsometer

This system consists of a transmitter unit and a receiver unit fixed at the end of adjustable arms as it is shown in Figure 5.6. The transmitter unit consists of a helium-neon laser with a wavelength of 632.8 nm. The receiver unit consists of a polarizer which is controlled by a motor and four photodetectors (see Figure 5.7).

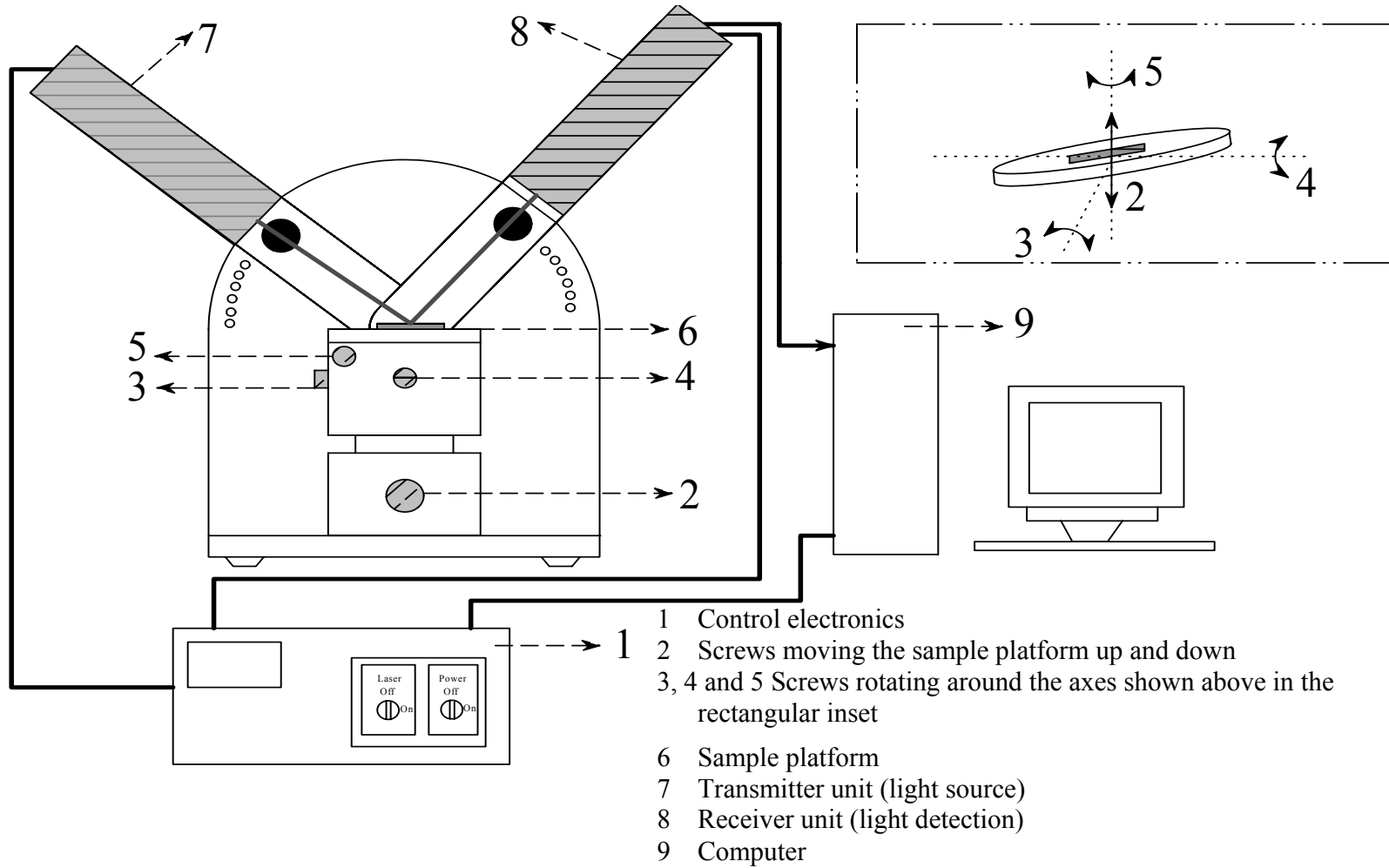


Figure 5.6 Single wavelength ellipsometer system.

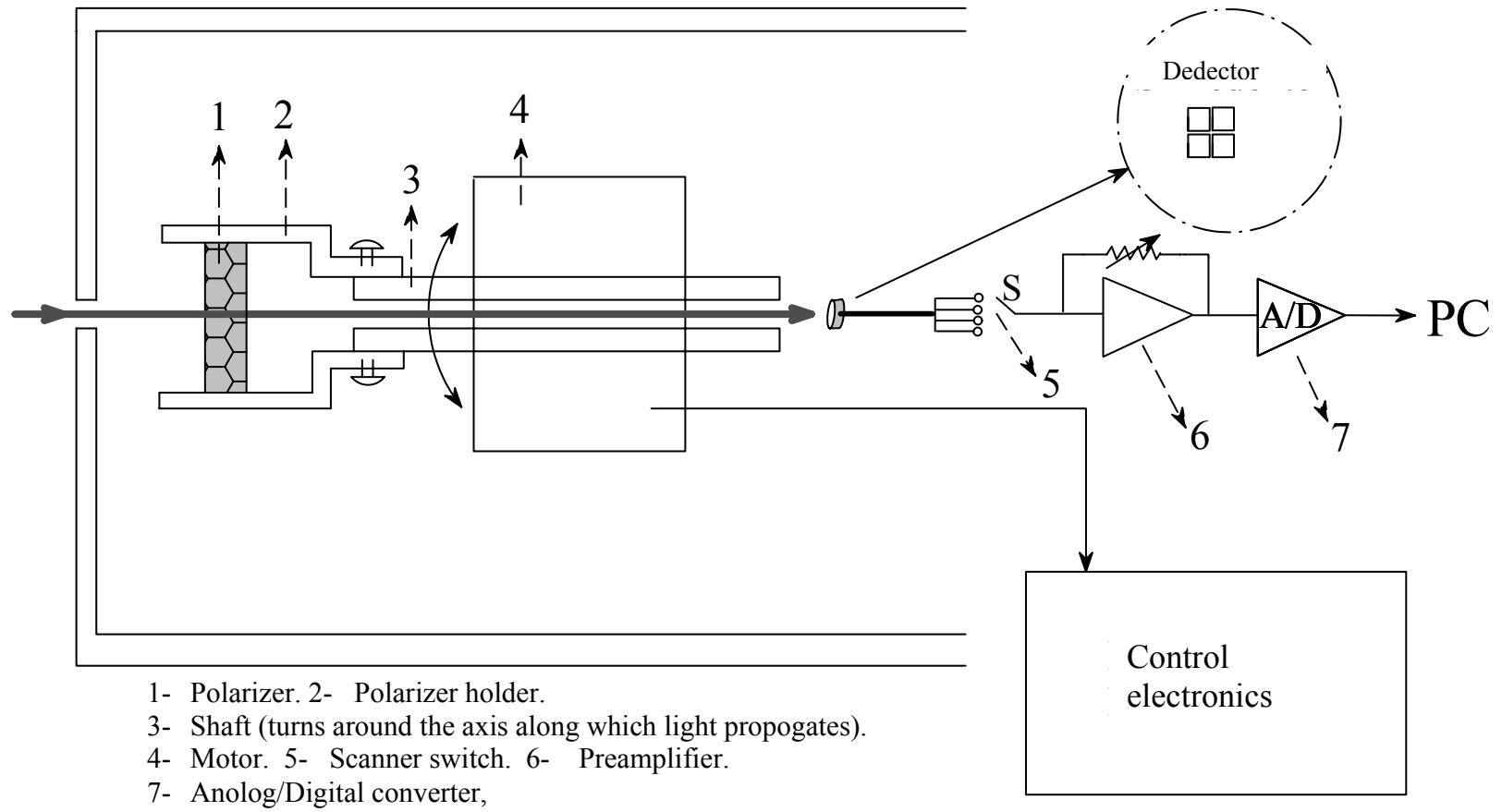


Figure 5.7 Receiver unit.

5.3.1 Calibration

Before putting the sample, on which we want to make measurements, onto the sample platform, the arms of the ellipsometer must be brought into horizontal position and laser must be aligned so that laser beam hits each of photodetectors at equal and sufficient intensity. For this purpose the screws on the transmitter unit must be loosen or tighten in different directions in order to change the direction of the laser beam and besides, the sensitivity of the amplifiers of the ellipsometer has to be adjusted with potentiometer at the receiver unit.

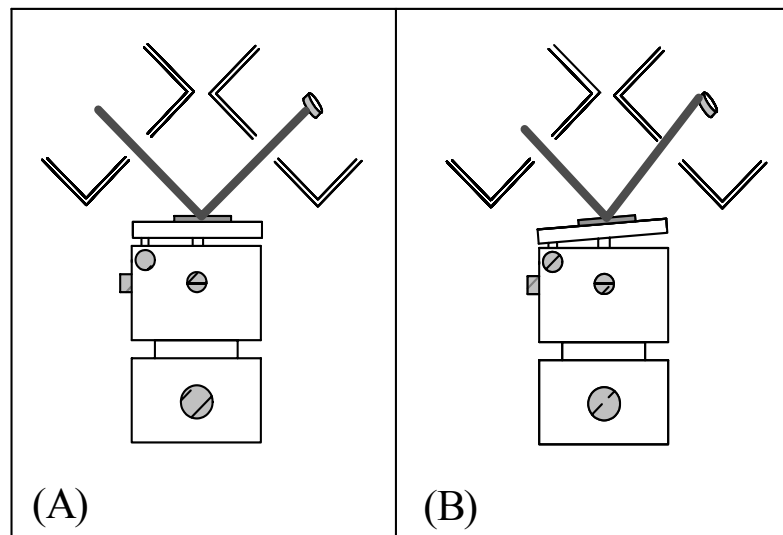


Figure 5.8 (A) Reflection of light from the sample hitting the four photodetectors in the center and perpendicular direction. (B) Reflection of light from the sample hitting the four photodetectors unsuccessfully.

5.3.2 Sample Alignment

After this calibration process, the arms of the transmitter and receiver units can be adjusted to any desired angular position. The reflected light from the sample also

must hit each of photodetectors at equal and sufficient intensity. In order to achieve this, the sample platform must be rotated in three different axes (3, 4 and 5) and moved up and down (2) as it is shown in Figure 5.6. One must be very careful throughout this adjustment because laser beam must hit the four photodetectors in the same and perpendicular direction as it was in the calibration process. In Figure 5.8(A), since the reflected light hits the photodetector unit in the center, equal amounts of intensity detection by each photodetector may be expected. Circular hole (a small window through which light enters the receiver unit and reach photodetectors) with a radius of about 1 mm on the receiver unit is exaggeratedly drawn in Figures 5.8(A) and 5.8(B). Although the beam enters through this small hole in Figure 5.8(B), it does not hit the photodetectors successfully. Therefore, a careful adjustment is needed even the beam enters through the hole and for this purpose the sample platform must be rotated in different axes and moved up and down as it is pointed out before.

If the light intensity is low, to minimize the error in analog/digital converter sensitivity of the amplifiers can be adjusted with the potentiometer. Such an adjustment is mostly needed when measurement is taken at small angles of incidence on absorbing samples because as the angle of incidence increases, the component of the light which is perpendicular to the surface decreases.

5.3.3 Measurement Steps

The adjustments explained above are controlled by a software written for the ellipsometer. Before taking measurements on the sample, the following steps have to be followed:

1. **Intensity test:** After bringing the arms of the ellipsometer to the horizontal position, sensitivity of the amplifiers must be adjusted by the potentiometer. First, the potentiometer button has to be turned into the position of minimal amplification. Next, by activating the function “Measurement/Before.../Intensity Test” from the program menu the amount of light intensity reaching to the photodetectors can be

controlled with the potentiometer. While light intensity level of 50% is sufficient for measurement the optimal adjustment is reached when the intensity level is about 95% or near below.

2. **Measurement of rest intensity:** The light in a room where ellipsometer is (such as daylight and/or lamp to illuminate the room) must be measured. By activating the function “Measurement/Before.../Rest Intensity” from the program menu the light intensity not originated from the laser source in the room can be measured. While this measurement is being taken the shutter of the laser must be hold closed. This measuring takes about 15 seconds and the rest intensity is stored for taking into account for the following measurements.

3. **Sample Alignment:** After the rest intensity measured the angle of incidence can be selected by changing the angular positions of the transmitter and receiver unit. By activating the function “Measurement/Before.../Sample Alignment” from the program menu how the intensity of the reflected beam is shared by the four photodetectors can be seen on a program window as shown in Figure 5.9.

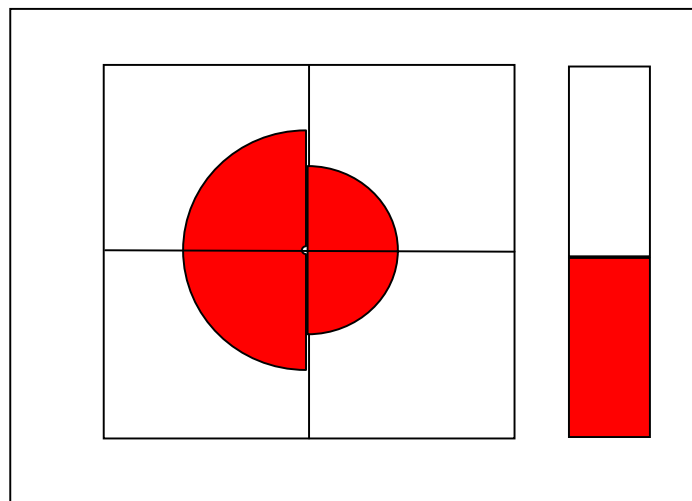


Figure 5.9 A representative diagram on the program window which are used in the alignment of the sample.

The relative amount of light intensity reaching each photodetector is represented by quadrants of a circle as shown in Figure 5.9. If it is succeeded to adjust the sample alignment properly (equal amount of light intensity is received by each of the four photodetectors) by rotating the sample platform in 3 different axes (3, 4 and 5) and moving it up and down (2), then all four quadrants detect the same intensity and four segments together will build a circle. If the intensity in all four quadrants is almost the same, the color of the segments change from red to green. Similarly, if the total amount light intensity reaching to the detectors is sufficient, the segment in rectangular diagram on the right side in Figure 5.9 will change its color from red to green also. Insufficient light intensity problem can be solved with the potentiometer.

- 4. Accuracy setting:** By calling the function “Measurement /Before.../Set Accuracy” from the program menu the measuring algorithm can be chosen. Algorithms can be listed from fast to slow and lowest accuracy to highest accuracy as follows: Standard harmonic analysis, advanced harmonic analysis, high precision harmonic analysis, precision minimum search, high precision minimum search, very high precision minimum search.

5.3.4 Measurement on a Silicon wafer: Effects of surface conditions

A p-type silicon (100) wafer is analyzed by using single wavelength ellipsometry at various angles of incidence. Different chemical treatments are applied the surfaces and their effects are observed. First, a measurement is performed on the wafer with various contaminants such as grease, dust and natural oxide on its surface (denoted by circles in Figure 5.10). Second, the wafer is left in boiling trichloroethylene (TCE) solution for 5 minutes and rinsed in ultrasonically agitated deionized water (water with high resistivity) for 5 minutes. The wafer is measured (denoted by squares) after exposing nitrogen gas on its surface to make it dry. Third, the wafer is again treated by the same cleaning procedure and measured then (denoted by triangles). Such a chemical treatment using TCE removes grease from the surface. Finally, the wafer is dipped in deionized water-HF solution (diluted HF) with 10:1 volume ratio for 15 seconds at room

temperature to remove oxide layer on the surface. After rinsing in deionized water, the silicon wafer is measured (denoted by crosses).

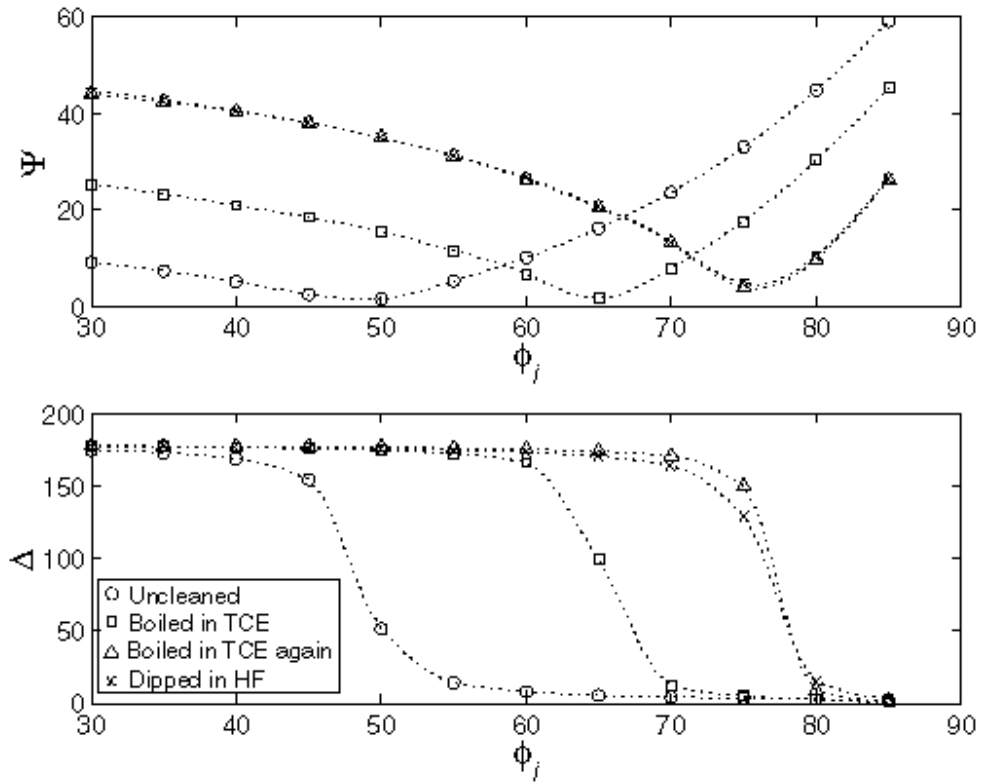


Figure 5.10 Measured ellipsometric angles Ψ and Δ as a function of angle of incidence ϕ_i for silicon wafer p-type Si (100) with different surface conditions.

The angles of incidence at which Ψ is minimum for absorbing films and Δ is 90° are called pseudo-Brewster angle and principle angle, respectively. If the material under study is non-absorbing these two angles coincide. It is observed that as the film is cleaned these angles shifted towards higher angles except final oxide removal step by using HF solution. The reverse effect by HF is probably due to the surface roughness created during etching oxides from the surface.

The measurement results shown in Figure 5.10 demonstrates the high sensitivity of ellipsometry technique to the contaminants, surface conditions or in other words, to

very thin overlayers. Since the cleanliness and interface properties are crucial for device characteristics in microelectronics, the information obtained from ellipsometry is very valuable in this respect.

5.4 Spectroscopic Ellipsometry

This system consists of a Xe high pressure Arc lamp (light source), a collimating lens, low-pass filters, electric shutter, a Glan-Taylor polarizer prism, a sample stage, an optical encoder, a rotating analyzer, an auto-collimating telescope, a fiber optic bundle, a monochromator and a photomultiplier tube (PMT) as shown in Figure 6.11 [101-102]. The originating light from the xenon light source, which is featureless in the ultraviolet and visible region, is collimated by a fused silica lens. Low-pass filters are used to eliminate interference effects at long wavelengths. Electric shutter is used to subtract the external light (background light) and PMT dark current. The analyzer prism is in hollow shaft mounted on a sealed ball bearing assembly [103].

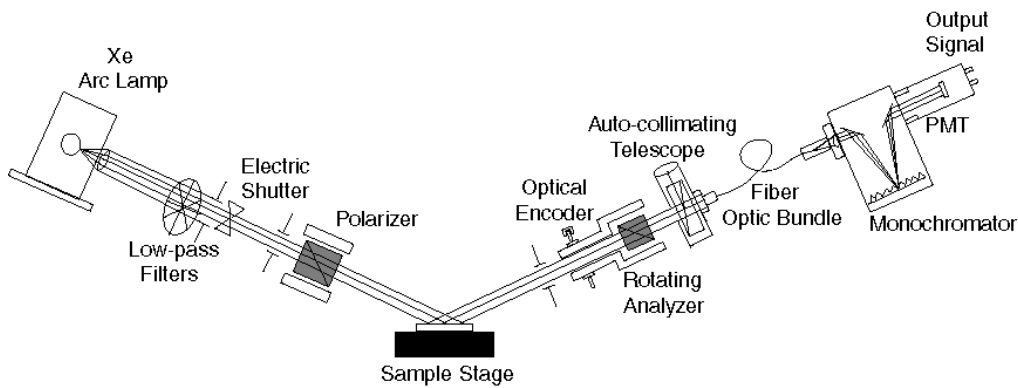


Figure 5.11 A schematic diagram of the spectroscopic ellipsometer [101].

The shaft is rotated at a constant speed of 300 rpm by a motor. The optical encoder, which has 360 small lines arranged in a radial pattern and is mounted on the hollow shaft, determines the instantaneous analyzer azimuth. The encoder has two outputs: One of them gives a single “start” pulse (reference pulse) per rotation and another gives 360

pulses at equally spaced angular intervals. Data are taken for several rotations to suppress noise due to random fluctuations of the light source by averaging (total number of data points is 360 times the number of rotations) [104]. The number of revolutions is limited for real time measurements and single revolution gives the maximum possible time resolution. The light transmitted through the analyzer is directed to the monochromator by a fiber optic bundle. The fiber optic bundle acts also as depolarizer of the light reaching the monochromator so that any artifact due to polarization of light in the monochromator is prevented. However, since fiber optic bundle depolarize the light not completely but partially, an additional calibration is necessary [101].

5.4.1 Fourier Analysis

The intensity of the light incident on the analyzer is given by equation (4.11) for a measurement configuration shown in Figure 4.2. A is defined as the azimuth position (orientation of the transmission axis) of the analyzer measured from the plane of incidence. As the analyzer is rotated at a constant frequency, the transmitted intensity I varies in time as shown in Figure 5.12. For unpolarized light the intensity is constant whereas the intensity varies sinusodially for elliptically and linearly polarized light.

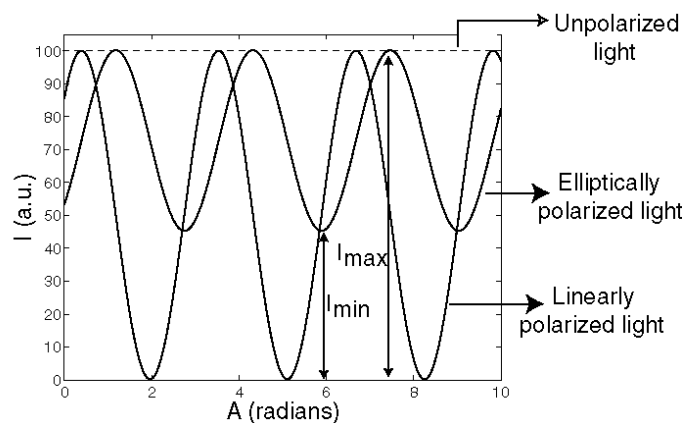


Figure 5.12 Variation of transmitted intensity by the rotating analyzer in time for unpolarized and linearly, elliptically polarized incident light [105-106].

The normalized Fourier coefficients α_2 and β_2 represent the polarization information available by the measurement. They are determined by Fourier transform method of photometric analysis [105,107]:

$$I_0 = \frac{1}{N} \sum_{i=1}^N I_i \quad (5.1)$$

$$\alpha_2 = \frac{2}{N} \sum_i^N I_i \cos \left[\frac{2\pi(i-1)}{N} \right] \quad (5.2)$$

$$\beta_2 = \frac{2}{N} \sum_i^N I_i \sin \left[\frac{2\pi(i-1)}{N} \right] \quad (5.3)$$

where N is half of the number of measurements for each revolution . If α_2 and β_2 is determined from measurement, they can be related to the ellipsometric parameters Ψ and Δ as

$$\tan \psi = \tan P \sqrt{\frac{1+\alpha_2}{1-\alpha_2}}, \quad \cos \Delta = \frac{\beta_2}{\sqrt{1-\alpha_2^2}} \quad (5.4)$$

It is seen that such a rotating-analyzer ellipsometry measures $\cos \Delta$ instead of Δ . Alternatively, α_2 and β_2 can be expressed in terms of azimuth α and $\tan \varepsilon$ as [104]

$$\alpha_2 = \cos 2\varepsilon \cos 2\alpha, \quad \beta_2 = \cos 2\varepsilon \sin 2\alpha \quad (5.5)$$

Since cosine is an even function the sign of ε and Δ is indeterminate. Therefore, it can be concluded that the coefficients α_2 and β_2 describe the polarization completely except for the handedness.

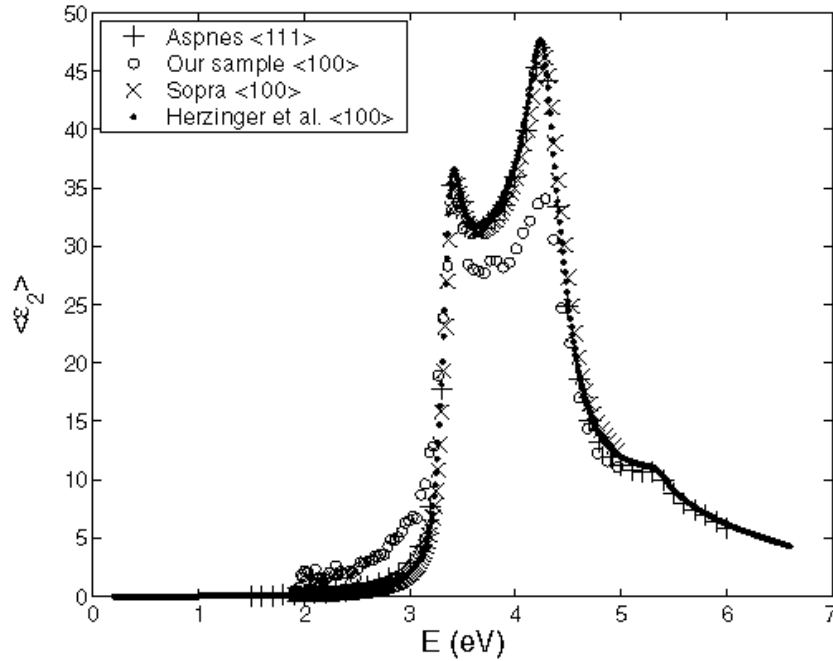


Figure 5.13 Measured $\langle \varepsilon_2 \rangle$ spectra of various silicon wafers with orientations $\langle 111 \rangle$ and $\langle 100 \rangle$. The results denoted by circles are measured by the setup shown in Figure 5.11. The others are spectra of previously published data [108-110].

5.4.2 Measurement on a Silicon Wafer

The measured $\langle \varepsilon_2 \rangle$ spectra for various silicon wafers with orientations $\langle 111 \rangle$ and $\langle 100 \rangle$ are shown in Figure 5.13. The measurement results of Aspnes *et al.* [108], Herzinger *et al.* [109], SOPRA [110] are almost similar. These $\langle \varepsilon_2 \rangle$ values are almost representing the bulk properties of silicon (almost no overlayer and/or roughness on the surface) and can be denoted as ε_2 . On the other hand, the $\langle \varepsilon_2 \rangle$ spectra of our sample (denoted by circles) measured at an angle of incidence of 70° by the setup shown in Figure 5.11 is quite different from the others. Although the amplitudes of the two peaks at about 3.4 eV and 4.2 eV are decreased, the relative decrease at 4.2 eV is larger. Since at high energies the penetration depth of the light is shorter, any surface related artifact is expected to affect the spectrum strongly at high energies. In this respect,

apparent decrease in $\langle \varepsilon_2 \rangle$ is most probably due to presence of contamination and/or roughness on the surface. If it is reminded that $\langle \varepsilon_2 \rangle$ is defined in terms of dipole moment per unit volume, the decrease in $\langle \varepsilon_2 \rangle$ can be envisaged as decrease in the dipole moment per unit volume. Therefore, roughness on the surface can be expected to be a density deficit that lowers the $\langle \varepsilon_2 \rangle$ [111].

CHAPTER 6

EFFECTS OF INHOMOGENEITIES ON TRANSMITTANCE AND REFLECTANCE SPECTRA

6.1 Introduction

A single layer deposited thin film on a substrate is generally supposed to be a homogeneous film which has constant refractive index between sharp, plane parallel boundaries. In practice, although the deposition parameters of thin films may be optimized to reduce inhomogeneities, it is unavoidable for practical reasons to have microstructures across a film leading a gradient of refractive index or to a small variation in the refractive index near film/substrate or near film/ambient interfaces. In addition to these refractive index irregularities in the film, there may be also a roughness on the surface of the film. Such inhomogeneities are not exclusively due to a given process condition, in some cases, the surrounding medium, for example substrate, might be influent.

Inhomogeneous thin films are sometimes intentionally produced for concrete applications such as anti-reflecting coating where the refractive index is wanted to vary smoothly from that of the substrate to that of the external surrounding medium (air). In many other cases, inhomogeneities in the deposited thin films are considered as source of problems and degradations. It is a priori impossible to predict the thin film growth conditions for obtaining a homogeneous structure. Consequently, it is indispensable to establish a 'film-growth-test measurement' cycle in order to carry out the interdependence between optical properties and film deposition parameters. As test

measurements the spectral transmittance and reflectance both might be a suitable choice due to their nondestructive, rapid and powerful nature.

Inhomogeneities in the films result in modifications in absolute values of spectrophotometric measurements such as transmittance and reflectance. In order to carry out the optical characterization of inhomogeneous thin films, at first, one obviously needs to observe a satisfactory evidence for the presence of any kind of inhomogeneity from the spectrum at hand. Second, any affect in the measured spectrum, which is not predicted by the ideal optical model, need to be assigned to a specific type of inhomogeneity. Finally, the resulting inhomogeneity that is predicted to be present in the film can be included in the model and optical constants can be extracted from the measured data. The optical constants obtained within this approach depend on the optical model and can be close to the true values of constants as much as the optical model is close to the true model no matter how accurate the measurement. Generally, the formulas for transmittance and reflectance for films having inhomogeneities are quite complex which makes the experimental analysis difficult. However, numerical procedures do not suffer from such a disadvantage. It should be noted that as the number of unknown parameters increase in the optical model, the correlation between the parameters, which are numerically retrieved, increase. Correlation between parameters result in equivalent optical models, that is, the uniqueness of the solution is questionable. Another drawback of numerical procedures is the computation speed limits of computer at hand.

Transmittance measurements at normal angle of incidence are commonly used not only because of its power but also because of the wide availability of the necessary instrument. On the other hand, reflectance measurements may suffer numerous problems. First, most reflectance setups needs a calibration mirror of which the optical properties may degrade due to ageing affects. Second, it is not easy to measure normal-incidence reflectance. Third, reflectance measurements are very sensitive to surface properties of the film. It may not be possible to obtain sufficiently accurate specular reflectance data [112]. Consequently, various behaviors in the reflectance spectrum

which are not predicted by the optical model may be attributed to inhomogeneity in the film but in reality it may not be so. In this respect, most focus is given on variations in transmittance measurements. However, it should be noted that reflectance measurements is useful especially for absorbing films which cannot be prepared as thin specimens.

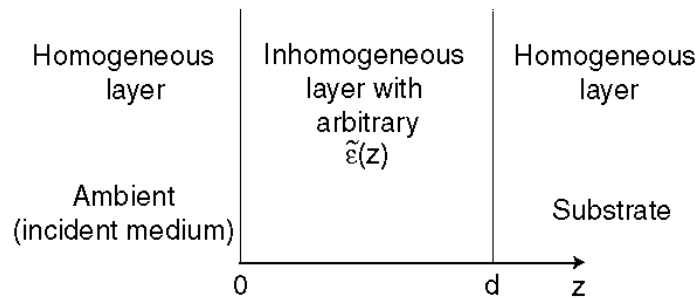


Figure 6.1 An inhomogeneous layer with arbitrary dielectric function surrounded by homogeneous media, the ambient and the substrate with constant dielectric functions.

6.2 Approximate Solutions to the Wave Equation

If we consider an optical model as shown in Figure 6.1, it may be possible to find the reflection and transmission coefficients for a particular dielectric function from the wave equation but the resulting solutions are generally very complex. One can rarely find simple, exact solutions. On the other hand, some approximate solutions to a given problem can be developed [113-114].

6.2.1 Slightly inhomogeneous thin film (small wavelength limit)

Wave equation can be approximately solved for arbitrary inhomogeneity where the inhomogeneity is considered as a small perturbation to the homogenous behavior and not a dominant factor. For this purpose, let's represent first order wave equations as

$$U' = ik_0 \gamma \beta V, \quad V' = ik_0 \frac{\gamma}{\beta} U \quad (6.1)$$

where

$$\gamma(z) = [\varepsilon(z)\mu(z)]^{1/2} \cos(\phi(z)), \quad \beta(z) = \begin{cases} \frac{\sqrt{\mu/\varepsilon}}{\cos \phi(z)} & (s - \text{polarization}) \\ \frac{\sqrt{\varepsilon/\mu}}{\cos \phi(z)} & (p - \text{polarization}) \end{cases} \quad (6.2)$$

Moreover, let us introduce a new dimensionless parameter $\nu(z) = k_0 \int_0^z \gamma(z) dz$ and new wave functions \bar{U} , \bar{V} as $\bar{U} = \frac{U}{\sqrt{\beta(z)}}$, $\bar{V} = \sqrt{\beta(z)} V$. In this representation, the wave equations take the following forms

$$\bar{U}'' + \left[1 - 3 \left(\frac{\beta'}{2\beta} \right)^2 + \frac{\beta''}{2\beta} \right] \bar{U} = 0, \quad \bar{V}'' + \left[1 + \left(\frac{\beta'}{2\beta} \right)^2 + \frac{\beta''}{2\beta} \right] \bar{V} = 0 \quad (6.3)$$

where prime denotes differentiation with respect to the phase variable ν . If $\left(\frac{\beta'}{2\beta} \right)^2$ and $\frac{\beta''}{2\beta}$ are negligibly small then the above equations can be approximated as

$$\bar{U}'' + \bar{U} = 0, \quad \bar{V}'' + \bar{V} = 0 \quad (6.4)$$

Then, U and V can be given in the form of

$$U = \beta^{1/2} e^{\pm ik_0 \int_0^z \gamma(z) dz}, \quad V = \beta^{-1/2} e^{\pm ik_0 \int_0^z \gamma(z) dz} \quad (6.5)$$

Consequently, characteristic matrix of the medium can be written as

$$M = \begin{pmatrix} \sqrt{\frac{\beta(0)}{\beta(z)}} \cos \nu(z) & i\sqrt{\beta(0)\beta(z)} \sin \nu(z) \\ \frac{i}{\sqrt{\beta(0)\beta(z)}} \sin \nu(z) & \sqrt{\frac{\beta(z)}{\beta(0)}} \cos \nu(z) \end{pmatrix} \quad (6.6)$$

For a homogeneous film, this matrix reduces to the equation (3.42)

$$M = \begin{pmatrix} \cos k_0 \gamma z & i\beta \sin k_0 \gamma z \\ \frac{i}{\beta} \sin k_0 \gamma z & \cos k_0 \gamma z \end{pmatrix} \quad (6.7)$$

where β and γ are constants.

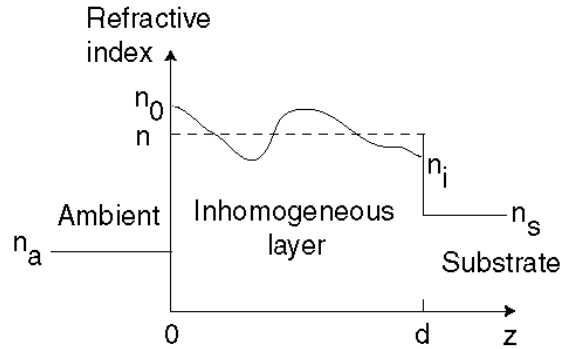


Figure 6.2 An optical model of an inhomogeneous layer surrounded by an ambient and substrate.

Within this approximation, reflection and transmission coefficients for a film with thickness d and surrounded by homogeneous media as shown in Figure 6.2, are given by

$$r = \frac{[\beta_s \beta(0) - \beta_a \beta(d)] \cos \nu(d) - i[\beta(0)\beta(d) - \beta_a \beta_s] \sin \nu(d)}{[\beta_s \beta(0) + \beta_a \beta(d)] \cos \nu(d) - i[\beta(0)\beta(d) + \beta_a \beta_s] \sin \nu(d)} \quad (6.8)$$

$$t = \frac{2\beta_s \sqrt{\beta(0)\beta(d)}}{[\beta_s \beta(0) + \beta_a \beta(d)] \cos \nu(d) - i[\beta(0)\beta(d) + \beta_a \beta_s] \sin \nu(d)} \quad (6.9)$$

Polarization information of the incident light is seen to be implicitly included in the parameter β .

Let's try to understand the meaning of approximations $(\beta'/2\beta)^2 \ll 1$ and $\beta''/2\beta \ll 1$. It can be seen that $(\beta'/2\beta)$ and $\beta''/2\beta$ are inversely proportional to wave number k :

$$\frac{\beta'}{2\beta} = \frac{1}{k_0 \gamma} \frac{d\beta/dz}{2\beta}, \quad \frac{\beta''}{2\beta} = \frac{1}{k_0^2 \gamma^2} \left[\frac{d}{dz} \left(\frac{1}{\gamma} \frac{d\beta}{dz} \right) \right] \quad (6.10)$$

Therefore, for large wavenumbers ($k \rightarrow \infty$, short wavelengths), $(\beta'/2\beta)$ and $\beta''/2\beta$ become infinitesimal, irrespective to the variations of ε and μ . It can be shown that the exact solutions of the wave equations approach the solutions of this approximation asymptotically as $k \rightarrow \infty$ [113]. On the other hand, apart from the magnitude of wave number, if the inhomogeneity in the film is small and negligible, it is possible to write $d\beta/dz = 0$. Consequently, $\beta'/2\beta = 0$ and $\beta''/2\beta = 0$.

Let's consider the optical model shown in Figure 6.2. For normal incidence, lossless medium (no absorption) and $\mu(z) = 1$, the reflection and transmission coefficients (equations 6.8-6.9) can be expressed as

$$r = \frac{\left(n_a \sqrt{\frac{n_i}{n_0}} - n_s \sqrt{\frac{n_0}{n_i}} \right) \cos \nu(d) - i \left(\frac{n_a n_s}{\sqrt{n_0 n_i}} - \sqrt{n_0 n_i} \right) \sin \nu(d)}{\left(n_a \sqrt{\frac{n_i}{n_0}} + n_s \sqrt{\frac{n_0}{n_i}} \right) \cos \nu(d) - i \left(\frac{n_a n_s}{\sqrt{n_0 n_i}} + \sqrt{n_0 n_i} \right) \sin \nu(d)} \quad (6.11)$$

$$t = \frac{2n_a}{\left(n_a \sqrt{\frac{n_i}{n_0}} + n_s \sqrt{\frac{n_0}{n_i}} \right) \cos \nu(d) - i \left(\frac{n_a n_s}{\sqrt{n_0 n_i}} + \sqrt{n_0 n_i} \right) \sin \nu(d)} \quad (6.12)$$

where n_s and n_a are the refractive indices of the substrate and the ambient media, respectively; and, $n_i = \beta(d)$ and $n_0 = \beta(0)$ are the refractive indices of the substrate and the ambient medium boundaries, respectively. It is seen that the variation in the refractive index in the film affects only the phase variable ν .

The expression (6.11) is a coefficient of an equivalent optical model which ignores the reflections in the inhomogeneous film and takes into account only interference due to the discontinuities at the boundaries. The equation (6.11) is seen to be derived if the reflection coefficient at the boundaries

$$r_1 = \frac{n_a - n_0}{n_a + n_0}, \quad r_2 = \frac{n_i - n_s}{n_i + n_s} \quad (6.13)$$

are substituted in the expression for r (equation (3.11)) which is given in Section 3.3.2. On the other hand, if the following transmission coefficients

$$t_1 = \frac{2n_a}{n_a + n_0}, \quad t_2 = \frac{2n_i}{n_i + n_s} \quad (6.14)$$

are substituted in the expression for t (equation (3.11)) for transmission amplitude, transmission coefficient is found to be $\sqrt{\frac{n_i}{n_0}} t$. It is seen that the expression (6.12) is not exactly equivalent to the same optical model apart from a factor $\sqrt{\frac{n_i}{n_0}}$.

6.2.2 Some useful parameters in the analysis of inhomogeneity

There may be wide range of forms of refractive index profiles in the growth direction such as linear, parabolic, exponential, etc. and it is generally difficult to extract exact profile from transmittance and reflectance measurements. However, it is possible to compute mean refractive index which is defined as

$$n = \frac{1}{d} \int_0^d n(z) dz \quad (6.15)$$

If the inhomogeneity is smooth enough, one can approximate mean refractive index as $n \approx \sqrt{n_0 n_i}$. In addition, if the film is slightly inhomogeneous, that is, $n_0 \approx n_i$, one can substitute $n \approx \sqrt{n_0 n_i}$ in expressions of r and t .

Moreover, one can define the degree of inhomogeneity by

$$r_{0i} = \frac{n_0 - n_i}{n_0 + n_i} \quad (6.16)$$

This ratio may be interpreted as the apparent reflection coefficient for a boundary between two hypothetical media of indices n_i and n_0 . If r_{0i} is small ($r_{0i} \ll 1$), the above expression becomes:

$$r_{0i} = -1 + \sqrt{\frac{n_0}{n_i}}, \quad r_{0i} = 1 - \sqrt{\frac{n_i}{n_0}} \quad (6.17)$$

Using this equations, r and t can be given in the forms of

$$r = \frac{[(n_a - n_s) - r_{0i}(n_a + n_s)]\cos\nu(d) + i\left(\frac{n_a n_s}{n} - n\right)\sin\nu(d)}{[(n_a + n_s) - r_{0i}(n_a - n_s)]\cos\nu(d) + i\left(\frac{n_a n_s}{n} + n\right)\sin\nu(d)} \quad (6.18)$$

$$t = \frac{2n_a}{[(n_a + n_s) - r_{0i}(n_a - n_s)]\cos\nu(d) + i\left(\frac{n_a n_s}{n} + n\right)\sin\nu(d)} \quad (6.19)$$

where $\nu(d) = k_0 \int_0^z n(z) dz = k_0 n d$. The relations (6.18) and (6.19) point out that the inhomogeneity of the film appears in the terms containing r_{0i} . If $r_{0i} = 0$, r and t become the coefficients of an ideal homogeneous film with refractive index n . The inhomogeneity is most apparent at the wavelengths for which $\cos\nu = \pm 1$ or $\lambda_m = 2nd/m$ with $m = 1, 2, 3, \dots$. If $n > n_s > n_a$, λ_m correspond to the reflectance minima (transmittance maxima). In other words, the envelope of these extrema is vertically shifted by the same amount for all wavelength, leading to erroneous substrate index value compared to the one obtained from the bare substrate reflectance (or transmittance). On the contrary, the transmittance minima (reflectance maxima) should not differ from the transmittance (reflectance) values of the homogenous film. These modifications on the transmittance maxima can be attributed to coherent multiple reflections between two boundaries n_a/n_s and n_0/n_i , but with a zero phase shift.

6.2.3 First order approximation theory

The approximate calculation for reflection and transmittance coefficients given in Section 6.2.1 is not adequate because it does not predict any modulation of interference fringes apart from a complete shift. There is a need for a valid first-order approximation that takes into account interference effects arising from the thin-film inhomogeneity. For this purpose, Tikhonravov *et al.* [115] derived transmittance and reflection expressions for small changes in the refractive index and extinction coefficient of a homogeneous thin film. They presented numerically calculated transmittance

spectra for different types of simple inhomogeneities. The results indicate that there is good agreement between the exact and their approximate calculations.

Important findings of this work can be given as follows:

- (a) It is possible to distinguish qualitatively between different types of inhomogeneity simply by examining experimental transmittance.
- (b) Although some particular types of inhomogeneities may not be distinguished easily from transmittance spectrum alone, additional measurement such as reflectance may resolve the problem. For example, particular type of refractive index inhomogeneity may bend transmittance curve downwards as if there is absorption present.
- (c) In the case of a small refractive increase and decrease in the substrate boundary result in widening and shrinking of interference fringes, respectively, as wavelength decreases in the transparent part of the spectrum.
- (d) In the case of a small refractive increase and decrease in the ambient boundary result in bending of interference fringes downwards and upwards, respectively, as wavelength decreases in the transparent part of the spectrum.
- (e) In case of small absorption in the film (no refractive index inhomogeneity), spectral transmittance and reflectance are not sensitive to the actual variation of the extinction coefficient with film thickness. Only the mean integral value of the extinction coefficient is important. Moreover, variation in transmittance is greater than that in the reflectance in this case.

6.2.4 Approximation of Characteristic Matrix for an Inhomogeneous Layer

Any inhomogeneous medium can be considered as a pile of very thin films with thicknesses $\delta z_1, \delta z_2, \delta z_3, \dots, \delta z_m$. If these thicknesses are sufficiently small, one can neglect any variation in $\tilde{\epsilon}, \mu, N$ in the each film [65]. Consequently, characteristic matrix of the j^{th} film using equation (3.42) can be approximately written as

$$M_j = \begin{pmatrix} 1 & \frac{i}{p_j} \varphi_j \\ ip_j \varphi_j & 1 \end{pmatrix} \quad \text{with} \quad \begin{matrix} \cos \varphi_j \approx 1 \\ \sin \varphi_j \approx \varphi_j \end{matrix} \quad (6.20)$$

Characteristic matrix of the multilayer (inhomogeneous medium) can be written as $M = M_1 M_2 M_3 \dots M_m$. Retaining terms up to first power of δz , M is approximately equal to

$$M = \begin{pmatrix} 1 & ik_0 B \\ ik_0 A & 1 \end{pmatrix} \quad \text{where} \quad A = \sum_{j=1}^m \frac{\varphi_j}{p_j}, \quad B = \sum_{j=1}^m p_j \varphi_j \quad (6.21)$$

As $m \rightarrow \infty$, the summations can be replaced with integration.

Let's assume that a linear variation of refractive index perpendicular to the film surface is predicted from the transmittance spectrum of a thin film. In order to decide how many layers are needed to model inhomogeneity, one needs to simulate the transmittance and check the amount of change in transmittance as one more layer added to the optical model. If the transmittance obtained with some number of layers, say 10, is equivalent to the one with, say 1000 layers, 10 layers is sufficient to define the linear variation and calculate optical parameters from transmittance spectrum. Since numerical calculations are very time consuming and even maybe practically impossible for very large number of layers, it is essential to approximate the medium with reasonable amount of layers [116].

6.3 Surface Roughness

It can happen that the film boundaries are not perfectly parallel, so that the cross section of the measuring light beam covers a sample area where the film thickness is not constant. Any geometric deviation at the boundaries from the ideal case can be visualized as a thickness variation and it has a strong influence on the transmittance and reflectance spectra. Consequently, one needs to identify and take the effect of such a thickness variation into account in the analysis of the experimental spectrum.

The phase of transmitted and reflected light is equal to $4\pi nd / \lambda$ and is seen to be depended on optical thickness nd and wavelength λ . Any variation in the phase can be equivalently created by

- (a) variation of thickness Δd
- (b) variation of refractive index Δn (variation parallel to the plane of surface)
- (c) wavelength bandwidth $\Delta\lambda$
- (d) variation of refractive index in the direction perpendicular to surface.

Variation of refractive index parallel to the plane of surface can be neglected because in practice it is not possible to conclude definitely such a variation occurs on a very limited surface area, typically at most $5 \times 5 \text{ mm}^2$. By choosing the slit width sufficiently narrow, for example 1 nm or less, the effect of slit width can be neglected [117].

If the experimental spectra do change by either changing the size of the beam cross-section or beam target on the sample surface, film interfaces are likely to be unparallel, that is, there is thickness variation. However, it should be kept in mind that all optical constants are assumed to be uniform over the investigated area of the sample [118].

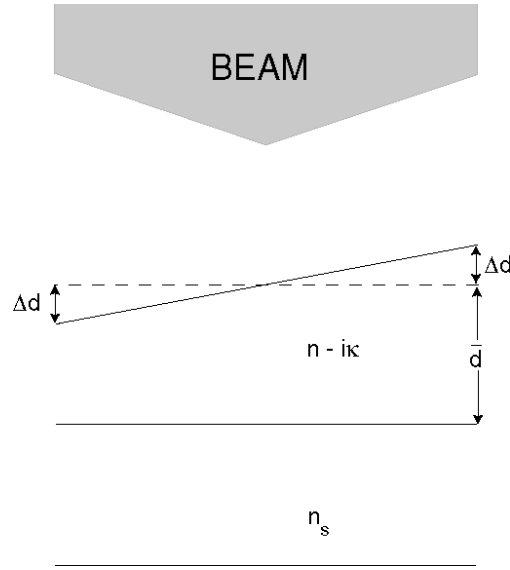


Figure 6.3 Thin film with a thickness variation on a transparent substrate [70].

6.3.1 Determination of Optical Constants of Thin Films with a Rough Surface

Transmittance expressions (3.12), (3.17) and (3.56) derived in Chapter 3 are valid for a thin film with uniform thickness. If the film has a thickness variation at the air-film interface as shown Figure 6.3, every individual element in the light beam travels the same film with different thicknesses [70]. Δd is the maximum variation in thickness with respect to the average thickness \bar{d} . The deviation of the thickness is considered to be symmetric with respect to the average thickness to define only a one parameter, Δd , in thickness variation. Consequently, every transmitted element travels with a different phase angle. To obtain the transmittance $T_{\Delta d}$ in the case of non-uniform thickness, transmittance T (equation (3.56)) can be summed over phase angle interval between $\phi_1 = (4\pi n(\bar{d} - \Delta d) / \lambda)$ and $\phi_2 = (4\pi n(\bar{d} + \Delta d) / \lambda)$, and divided by the corresponding phase interval. Eliminating the parameter x in the transparent region and $T_{\Delta d}$ can be obtained in this region as the following:

$$T_{\Delta d} = \frac{\lambda}{4\pi m \Delta d} \frac{a}{(1-b^2)^{1/2}} \left[\tan^{-1} \left(\frac{(1+b) \tan(\phi_2/2)}{(1-b^2)^{1/2}} \right) - \tan^{-1} \left(\frac{(1+b) \tan(\phi_1/2)}{(1-b^2)^{1/2}} \right) \right] \quad (6.22)$$

where $a = A/(B+D)$ and $b = C/(B+D)$. The terms $\tan(\phi_1/2)$ and $\tan(\phi_2/2)$ can be written as in the following form:

$$\tan\left(\frac{\phi_1}{2}\right) = \frac{\tan(2\pi m \bar{d} / \lambda) - \tan(2\pi m \Delta d / \lambda)}{1 + \tan(2\pi m \bar{d} / \lambda) \tan(2\pi m \Delta d / \lambda)}, \quad \tan\left(\frac{\phi_2}{2}\right) = \frac{\tan(2\pi m \bar{d} / \lambda) - \tan(2\pi m \Delta d / \lambda)}{1 - \tan(2\pi m \bar{d} / \lambda) \tan(2\pi m \Delta d / \lambda)}$$

It should be noted that thickness variation should be small enough so that angle of incidence of light is still considered as normal. At a maximum, $2\pi m \bar{d} / \lambda = m\pi$ where $m = 0, 1, 2, 3, \dots$. Then, $\tan(2\pi m \bar{d} / \lambda) = 0$ at a maximum. At a minimum, $2\pi m \bar{d} / \lambda = m\pi/2$ where $m = 1, 3, 5, \dots$. Then, $\tan(2\pi m \bar{d} / \lambda) = \infty$ for a minimum. It can be seen that $T_{\Delta d}$ blows up for minima. Therefore, the expression for $T_{\Delta d}$ can not be used for minima and can only be used for the wavelength region around maxima. If $T_{\Delta d}$ is simulated it is seen that this region decreases as Δd increases. Therefore, it can be concluded that borders of this region is a function of Δd . If $\tan(\phi_1/2)$ and $\tan(\phi_2/2)$ for maxima is substituted in $T_{\Delta d}$, the expression for the envelope passing through maxima can be obtained:

$$T_M^* = \frac{\lambda}{2\pi m \Delta d} \frac{a}{(1-b^2)^{1/2}} \tan^{-1} \left(\frac{1+b}{(1-b^2)^{1/2}} \tan^{-1} \left(\frac{2\pi m \Delta d}{\lambda} \right) \right) \quad (6.23)$$

Changing only the sign of C or b is enough to obtain T_m^* from T_M^* . Doing so, the expression for the envelope passing through minima can be obtained:

$$T_m^* = \frac{\lambda}{2\pi m \Delta d} \frac{a}{(1-b^2)^{1/2}} \tan^{-1} \left(\frac{1-b}{(1-b^2)^{1/2}} \tan^{-1} \left(\frac{2\pi m \Delta d}{\lambda} \right) \right) \quad (6.24)$$

The expressions for T_M^* and T_m^* are valid in the range of $0 < \Delta d < \frac{\lambda}{4n}$.

Assuming $\Delta d \ll \bar{d}$ and x is constant in the range $[\phi_1, \phi_2]$, the relations between the envelopes of transmittance for films with uniform and non-uniform thickness can be written as

$$T_M^* = \frac{\sqrt{T_M T_m}}{\theta} \tan^{-1} \left(\sqrt{\frac{T_M}{T_m}} \tan \theta \right), \quad T_m^* = \frac{\sqrt{T_M T_m}}{\theta} \tan^{-1} \left(\sqrt{\frac{T_m}{T_M}} \tan \theta \right) \quad (6.25)$$

where $\theta = 2\pi n \Delta d / \lambda$.

6.4 Correlation between optical path modulations and transmittance spectra of a-Si:H thin films

Optical constants of plasma-enhanced chemical vapor deposited amorphous silicon (a-Si:H) thin film upon a transparent substrate are determined within the UV-visible region by measurement of the transmittance spectrum [62].

6.4.1 Sample preparation

A-Si:H thin films is deposited onto a glass substrate ($d_s = 1 \text{ mm}$) by the plasma-enhanced chemical vapor deposition technique. Before deposition the substrate was cleaned *in situ* for 5 min by H_2 plasma with 35 mW/cm^2 rf power, $50 \text{ cm}^3/\text{min}$ H_2 flow, and 0.3 Torr reactor pressure. Then deposition is initiated by application of rf power of 15 mW/cm^2 after the process parameters, $30 \text{ cm}^3/\text{min}$ of SiH_4 flow, and 0.3 Torr of pressure were maintained. The substrate was held at $250 \text{ }^\circ\text{C}$ during the deposition process and then left in the chamber for cooling to room temperature.

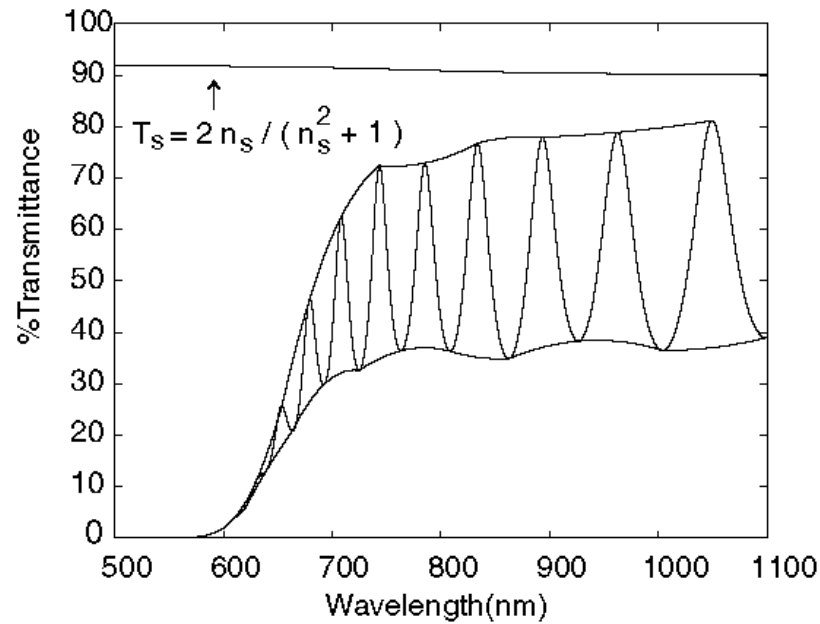


Figure 6.4 Transmittance of a-Si:H with its envelopes, and transmittance T_s of the substrate alone.

6.4.2 Experiment

The transmittance spectrum of a-Si:H and the envelopes of the interference fringes are shown in Figure 6.4. Perkin-Elmer Lambda 2s spectrum is used to obtain the spectrum at normal incidence. Extrema of the interference fringes were obtained directly from the data, and we interpolated these extremum points locally, by using at most three adjacent extrema, to draw the envelopes T_M and T_m . However, the transmittance spectrum deviated considerably from that of a uniform thin film, with abrupt changes in the refractive indices at the interfaces, which were parallel to each other. In other words, along the transparent region (700-1100 nm) of the spectrum the envelope T_M , instead of coinciding with the substrate transmittance T_s , lay below it and decayed substantially for decreasing λ , where as the overall spectral variation of the envelope T_m remained limited within the range as a result of the eventual refractive index dispersion, except for a slight oscillation as shown in Figure 6.4. Each one or combinations of factors such as

film thickness modulation, refractive index inhomogeneity, and absorption might lead to the deformation described above. The last factor, at least alone, may be omitted from consideration because eventual absorption in the film should affect both envelopes, T_M and T_m , equally. Here we evaluate the individual effects of the remaining factors for correcting the spectrum given in Figure 6.4.

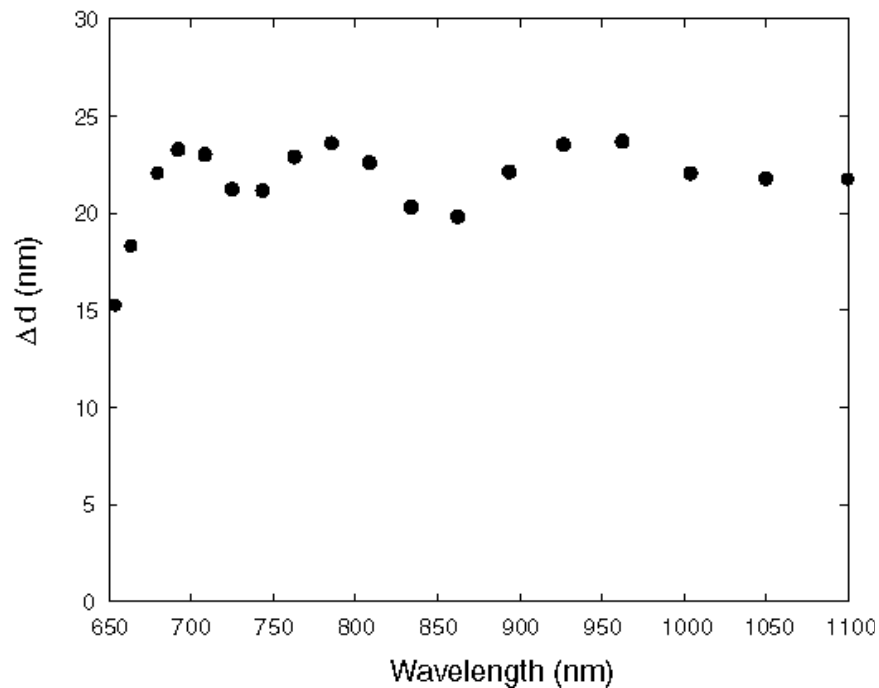


Figure 6.5 Thickness variation Δd computed by solution of equations (4.23) and (4.24) numerically at each extremum point.

Let us consider, first, a thickness variation at the air-film interface, as shown in Figure 6.3. Refractive index of the substrate, n_s , is obtained from the measured transmittance T_s of bare substrate as shown in Figure 6.6(a). In the transparent region, expressions (6.23) and (6.24) are two transcendental equations with two unknowns n and Δd . By solving these two equations numerically at the extremum points, one can compute Δd at each corresponding wavelength. As can be seen from Figure 6.5, the

resultant thickness variations calculated from different regions of the spectrum are distributed closely about a value of 20 nm. Two Δd values that deviate remarkably widely from the others indicate that absorption is present in that short wavelength region. Using the determined thickness variation $\Delta d = 20$ nm in equations (6.23) and (6.24), one can solve for n and x numerically.

The relations (6.25) involve two unknowns, T_m and θ , in the transparent region where $T_M = T_m$. Equation (3.64) can be expressed as

$$\frac{l}{2} = \left(\frac{\bar{d}}{\pi \Delta d} \right) \theta - m_1 \quad (6.26)$$

From the solution of equations (6.25) for θ_1 numerically for all wavelength regions, $l/2$ versus θ_1 is plotted in Figure 6.6(b). The points that deviate from the fitted function indicate the presence of absorption in that wavelength region. By using this equation one can calculate all θ values that are also valid in the absorption region.

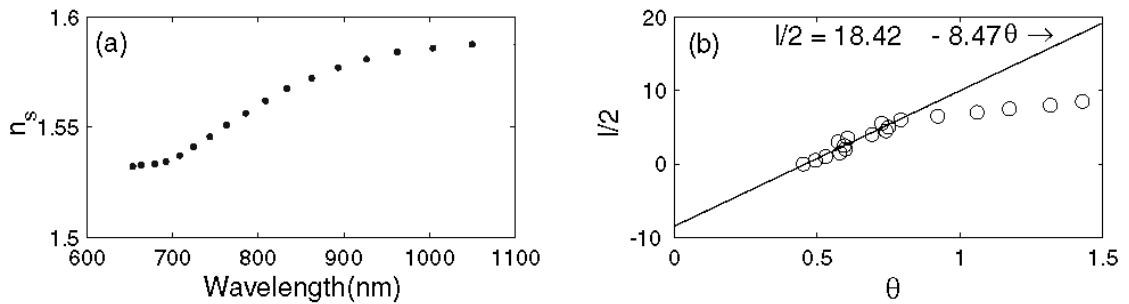


Figure 6.6 (a) Refractive index of the substrate calculated from the transmittance spectrum of the substrate alone as shown in Figure 6.4. (b) Graph of $l/2$ versus θ .

Finally, T_M and T_m values are calculated by solutions of equation (6.25) by use of values of T_M^* , T_m^* and θ , as shown in Figure 6.7(a). It can be seen that the maxima of the spectrum are more sensitive to thickness variation, in agreement with Swanepoel's simulated transmission [70]. The corrected spectrum can be interpreted as the spectrum that is due to a film of uniform thickness \bar{d} .

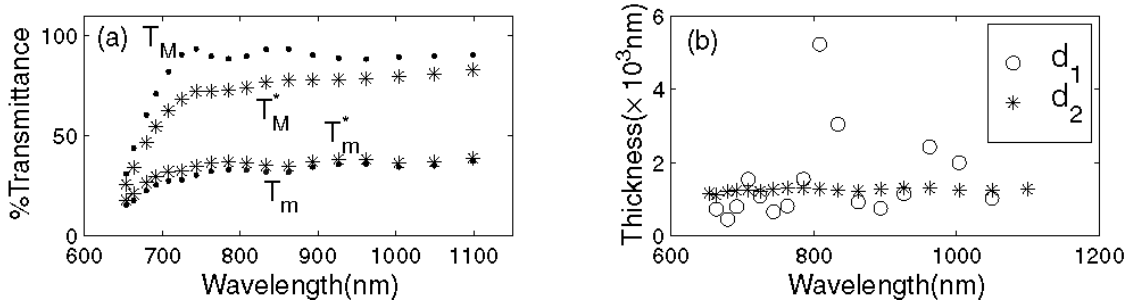


Figure 6.7 (a) Extrema of the transmittance spectrum with corrected extrema values from which the film has no thickness variation ($\Delta d = 0$ nm). (b) Thicknesses d_1 and d_2 calculated from equations from (3.62) and (3.57), respectively.

Equations (3.61) and (3.62) can be used for calculating the thickness n_1 and refractive index d_1 of the films as shown in Figure 6.7(b) and 6.8(b). Fringe order numbers are calculated from equation (3.57) with $\bar{d}_1 = 1320.2$ nm and n_1 as shown in Figure 6.8(a). Using exact integer and half-integer values instead of calculated ones and n_1 in equation (3.57), one can find a more accurate set of thicknesses \bar{d}_2 , as shown in Figure 6.7(b). Finally, using average thickness \bar{d}_2 and exact fringe numbers in equation (3.57), one can calculate refractive indices n_2 . These values were fitted to a function of the form $n = a + b/\lambda^2$:

$$n = 3.336 + \frac{434119}{\lambda^2} \quad (6.27)$$

n_2 and the fitted function are shown in Figure 6.8(b). By using refractive index function (6.27), \bar{d}_2 , n_s and taking $x = 1$ in equation (3.17), one can simulate transmittance curve B, which does not involve deformations on the fringes that originate from thickness variations on the surface of the film, as shown in Figure 6.9(a).

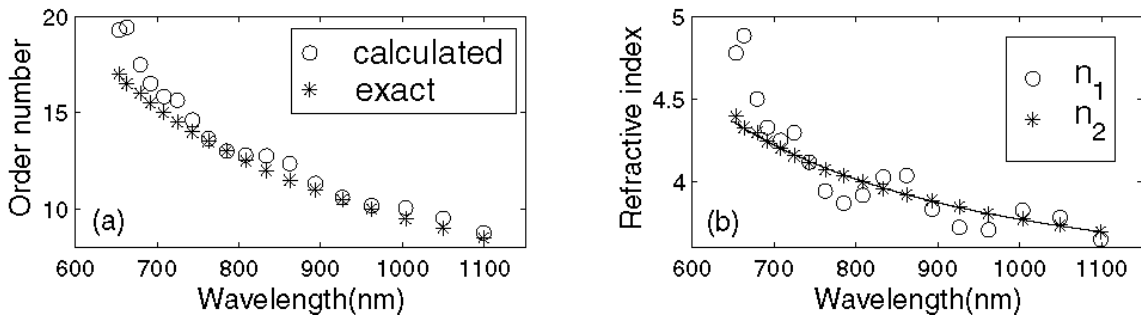


Figure 6.8 (a) Fringe order numbers calculated from equation (3.57) and from exact integer and half integer values that are found from calculated ones. (b) Refractive indices n_1 and n_2 calculated from equation (3.61) and from equation (3.57) with exact fringe numbers and average thickness $\bar{d}_2 = 1264.9$ nm, respectively. The continuous curve denotes fitted dispersion relation (equation (6.27)).

Finally, let us consider the possibility that such a deformation of the experimental spectrum might arise because of refractive index irregularities, which are thin transitional regions at the substrate/film and film/air interfaces [115]. Let us assume the film consists of three homogenous layers situated between substrate and air. The electromagnetic fields at the substrate/film interface and the film/air interface are connected by a characteristic matrix (equation (3.42)) and transmission amplitude can be expressed as in equation (3.47). Similarly, the characteristic matrix for the light incident at the substrate/film interface can be given as

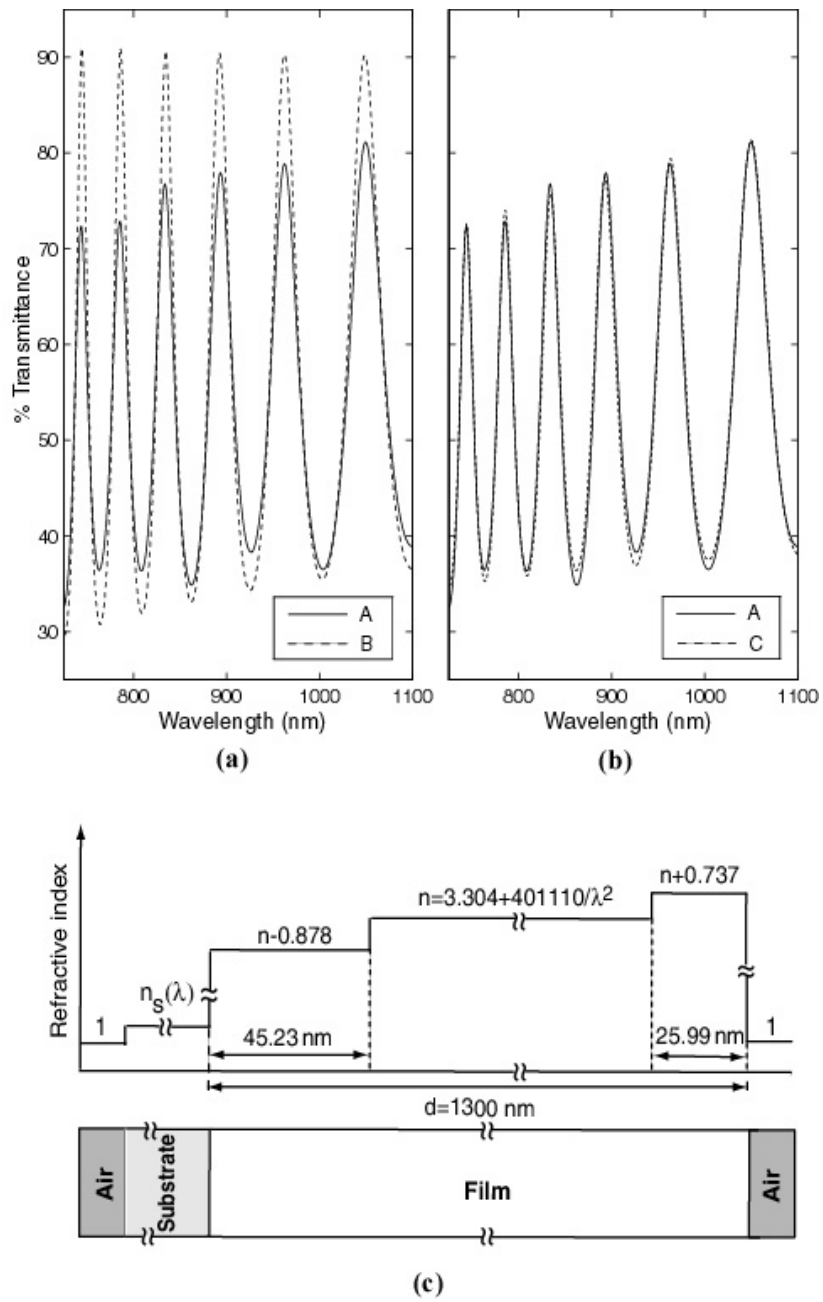


Figure 6.9 (a) Transmittance B is the spectrum of the film that is obtained by correction of curve A (original measured data) from the thickness modulation. (b) Transmittance C of a film that has refractive index inhomogeneities at its interfaces, as shown in (c), fitted to curve A. (c) Refractive index profile of the film that gives transmittance spectrum C.

$$M' = \begin{pmatrix} m'_{11} & m'_{12} \\ m'_{21} & m'_{22} \end{pmatrix} = \prod_{j=3}^1 M_j \quad (6.28)$$

for which the reflection amplitude is

$$r = \frac{n_s m'_{11} - n_a m'_{22} + n_a n_s m'_{12} - m'_{21}}{n_s m'_{11} + n_a m'_{22} + n_a n_s m'_{12} + m'_{21}} \quad (6.29)$$

Using these two amplitudes and taking reflections from the substrate-air interface and incoherent interaction of light in the substrate into account, one can express the transmittance as

$$T = \frac{T_i T_3}{1 - R_3 R_i'} = \frac{4n_s^2 |t|^2}{(n_s + 1)^2 - (n_s - 1)^2 |r'|^2} \quad (6.30)$$

This calculated expression for a film composed of three layers with different refractive indices and thicknesses is fitted to the original, experimental transmittance A by use of a simplex search algorithm, as shown in Figure 6.9(b). The refractive index profile of the film yields transmittance spectrum C is shown in Figure 6.9(c).

6.4.3 Discussion and conclusion

The spectral transmittance is a suitable choice for use in determining the optical constants of an amorphous silicon thin film upon a transparent due to its nondestructive, rapid and powerful nature. However, all the optical behavior of a film cannot be interpreted by an ideal model. Moreover, one type of irregularity of the film may not be responsible alone for anomalies in the experimental transmittance spectrum, which is the case for a-Si:H analyzed in this study. Although the thickness variation within the spot of the probe beam of an a-Si:H thin was determined, it was also determined that such a type of inhomogeneity was not the only type that can be used for correcting the

modulation of the extremum envelopes in the transparent region. Therefore an inhomogeneity of the refractive index with film depth was considered as an alternative correction. First, taking into account the thin transitional layer at either the substrate/film or the film/air boundary as inhomogeneity in the fitting procedure remained unsatisfactory. However a steplike refractive index distribution that was due to two thin transitional layers at both of these boundaries appeared to produce an acceptable correction of the spectrum, as shown in Figure 6.9(b). Use of this refractive index profile seems at least plausible, because the actual compositional and structural variations throughout the film from the substrate to the ambient boundaries might lead to refractive index changes [119-123]. On one hand, impurities such as oxygen and nitrogen, which are present more or less abundantly in the plasma reactor, can easily be incorporated into a-Si:H at the initial stage of the deposition process, drastically decreasing the refractive index [124-126]; consequently a negative steplike change in the refractive index profile at the substrate side may be envisaged for a first approximation. On the other hand, values of the refractive index vary from ~ 4.1 in unhydrogenated a-Si to ~ 2.8 in fully hydrogenated film [119]. In this respect, a possible out-diffusion of hydrogen from the film/air boundary would justify a positive steplike change in the refractive index profile at this boundary [127].

Although this speculative argument for the proposed index profile seems qualitatively reasonable, the amount of index change resides at the extreme limit of the possibility. Therefore a slight lateral thickness modulation together with a much more moderate refractive index profile along the depth would be a realistic combination to give rise to the transmittance spectrum deformation that is encountered.

CHAPTER 7

THICKNESS AND OPTICAL CONSTANT DISTRIBUTIONS OF PECVD A-SiC_x:H THIN FILMS ALONG ELECTRODE RADIAL DIRECTION

Two sets of hydrogenated amorphous silicon carbide (a-SiC_x:H) thin films were grown on glass and c-Si substrates by plasma enhanced chemical vapor deposition (PECVD) technique at pressures of 0.5 and 0.1 Torr [128]. The influence of the pressure on the distribution of thicknesses, refractive indices at 632.8 nm and optical gaps from the edge to the center of the bottom electrode of PECVD system is examined by transmission, single wavelength ellipsometry and Fourier transform infrared spectroscopy. A recently introduced optimization method considering some prior knowledge of common optical properties of amorphous semiconductor thin films has been applied to the optical transmission spectra for estimating thickness and optical constants of a-SiC_x:H thin films at hand. In addition, spectral characteristics of these constants are analyzed by fitting experimental data through Forouhi-Bloomer, Tauc-Lorentz and single Lorentz oscillator models. The retrieved results show that while the thicknesses and optical band gaps are decreasing towards the center of the electrode, refractive index is slightly increasing in that direction. Chemical processes occurring during the film deposition are discussed. These distributions of the film constants have been interpreted as due to the carbon incorporation whose efficiency might increase towards the edge of the electrode corresponding to a longest residence time of carbon radicals.

7.1 Introduction

Hydrogenated amorphous silicon carbide (a-SiC_x:H) film, prepared by the conventional plasma enhanced chemical vapor deposition (PECVD), apart from its use for solar cells becomes available material for visible light emitting devices due to both its adjustable band gap to any value in the visible range of energy spectrum and its ability for fabrication of large area flat panel displays. The properties of this Si, C and H alloy depend primarily on the value of x; that is, the bonding organization changes drastically from x=0 (pure a-Si where tetrahedral sp³ like hybrid covalent σ type bonding is dominant in short range order), to x=1 (pure a-C where all three types of covalent 2-center hybrid σ -like sp³, sp² and sp¹ bondings coexist together with π -like, delocalized (or multicenter) bonding) [129]. In this respect, for x<0.5, both Si-Si homonuclear bonds and Si-C heteronuclear bonds, for x \approx 0.5 (stoichiometry) mainly Si-C heteronuclear bonds, and for x>0.5 both Si-C and various types homonuclear C-C bond are expected. On passing from Si-rich alloy (x<0.5) to C-rich alloy (for x>0.5), apart from the bonding types, the configuration and the amount of both hydrogen and defects are qualitatively and quantitatively different. Consequently the short range and medium range structures of these amorphous alloys together with their resulting opto-electronic properties exhibit drastic changes [130-136]. In other words, the growth conditions may be used to tune the material properties for different applications.

7.2 Outline of dielectric function representations used in the characterization

7.2.1 Forouhi-Bloomer Model

Different approaches have been used to describe the spectral distributions of refractive index (n) and extinction coefficient (k) of amorphous thin films. Since spectral behavior of dielectric function of amorphous solids does not exhibit sharp features, a

model with few parameters is expected to be sufficient to simulate the experimental spectrum [137]. Forouhi-Bloomer (FB) model assumes finite lifetime for the excited state under illumination and a single type of electronic transition between parabolic conduction and valence bands in the derivation of dispersion relations. These resulting dispersion relations are given as [138]:

$$n_{FB}(E) = n(\infty) + \frac{B_0 E + C_0}{E^2 - BE + C} \quad , \quad k_{FB}(E) = \frac{A(E - E_g)^2}{E^2 - BE + C} \quad (7.1)$$

where E denotes the photon energy , E_g is the optical band gap and the remaining parameters can be expressed as follows:

$$B_0 = \frac{A}{Q} \left[-\frac{B^2}{2} + E_g B - E_g^2 + C \right], \quad C_0 = \frac{A}{Q} \left[(E_g^2 + C) \frac{B}{2} - 2E_g C \right], \quad Q = \frac{1}{2} (4C - B^2)^{1/2}$$

7.2.2 Tauc-Lorentz Model

Although FB dispersion relations have been widely used in the literature, Alterovitz *et al.* [139] remarked that these dispersion relations for hydrogenated amorphous carbon films (a-C:H) beyond 1.5-4.1 eV are questionable. Furthermore, McGahan *et al.* [140], Yamagucki *et al.* [141-142], Jellison and Modine [143-144] and Franta *et al.* [145-146] pointed out some fundamental problems in the FB formulation and then new parameterizations of the dielectric function ($\epsilon(E) = \epsilon_1(E) + i\epsilon_2(E)$) have been introduced. It should be kept in mind that the real and imaginary parts of the dielectric function, $\epsilon_1(E)$ and $\epsilon_2(E)$, together with absorption coefficient $\alpha(E)$ are related to refractive index $n(E)$ and extinction coefficient $k(E)$ as follows: $\epsilon_1(E) = n^2(E) - k^2(E)$, $\epsilon_2(E) = 2n(E)k(E)$, $\alpha(E) = 2\omega k(E)/c$.

In this respect, Jellison and Modine derived Tauc-Lorentz (TL) model by combining imaginary part of the Tauc dielectric function ($\epsilon_2(E) \propto (E - E_g)^2/E^2$) and a single Lorentz oscillator ($\epsilon_2(E) \propto CE/((E^2 - E_0^2)^2 + CE^2)$) in a form given below:

$$\varepsilon_{2TL}(E) = \frac{AE_0C(E - E_g)^2}{(E^2 - E_0^2)^2 + C^2E^2} \frac{1}{E} \quad E > E_g, \quad \varepsilon_{2TL}(E) = 0 \quad E \leq E_g \quad (7.2)$$

where E_0 is the resonance energy and C is the broadening term. The expression for the real part ε_{1TL} is not reported here, it is first given in equation (7.2) of [143] and corrected later in [144]. Although this formulation has been found to be a quite suitable analytic representation with relatively small number of parameters (only 5) for disordered materials, it was not used widely as FB model due probably to its relatively recent appearance in the literature together with its cumbersome expression for ε_{1TL} . The dispersion formulation of Franta *et al.* involves at least 7 parameters where this parameter number increases if the model contains more than one oscillator. The main disadvantage of this last approach and the one developed by Yamagucki *et al.* appears to be a large number of unknown parameters in the dispersion relations so that correlations between parameters become important.

7.2.3 Lorentz Oscillator Model

An alternative model is single Lorentz oscillator (L) [147]:

$$\varepsilon_L = \varepsilon(\infty) + \frac{A}{(E_0^2 - E^2) - i\Gamma E} \quad (7.3)$$

where $\varepsilon(\infty)$ is the high energy dielectric function, A is the amplitude of the oscillator, E_0 is the resonance energy and Γ is the full width of the ε_2 at half maximum. This is a general spectral representation for all dielectric functions [148-150]. In this model, resonance energy E_0 approximately corresponds to the maximum of ε_2 and represents the average separation between valence and conduction band [151-152].

All these parameterizations of the dielectric function are derived by using the fundamental principle that no signals are transmitted with a speed greater than that of

light in vacuum or equivalently, by using the analyticity of complex refractive index [153].

Table 7.1 Deposition parameters such as gas concentration of source gases (M), total gas flow rate (F), pressure (P), substrate temperature (T), power density (P) and the residence time (t) of samples 1C and 2C.

	$M=C_2H_4/(C_2H_4+SiH_4)$	F (ccm)	p (Torr)	T (C°)	P (mW/cm ²)	t (s)
1C	0.5	60	0.5	250	60	1.85
2C	0.5	60	0.1	250	60	0.35

7.3 Experimental.

7.3.1 Preparation of a-SiC_x:H thin films

a-SiC_x:H thin films are deposited on the grounded bottom electrode of a parallel plate PECVD system at 13.56 MHz (Plasma Lab μ P 80). Crystalline silicon and glass microscope slide substrates are used for infrared vibrational and ultraviolet-visible optical analyses, respectively. The Si substrates were cleaned by boiling in HNO₃ for 15 minutes, followed by dipping in HF for 30 seconds and rinsed in deionized water (DW). The glass substrates were dipped in KOH solution for 30 minutes and then, washed in ultrasonically agitated DW for at least 30 minutes. The process was finished by dipping in HF for 30 seconds and rinsing in DW. After the cleaning process, they were loaded into the deposition system as quick as possible to prevent the substrates from atmospheric contamination. Finally, the reactor was pumped down to a base pressure below 1 mTorr and the temperature of the bottom electrode was adjusted to 250°C before letting flow of source gases, ethylene (C₂H₄) and silane (SiH₄), into the system. Growth process was started by adjusting deposition parameters such as gas concentration of source gases (M), total gas flow rate (F), pressure (p), substrate

temperature (T), power density (P) and the residence time (t) during which the plasma species remain in plasma medium. Deposition parameters for two different depositions 1C and 2C are shown in Table 7.1. Here, t is defined by PV/F where V is active volume of the reactor chamber [154].

7.3.2 Measuring procedures and equipments.

Structural analysis of a-SiC_x:H films were performed by Fourier transform infrared (FTIR) spectroscopy (Nicolet 520). The thicknesses and the optical constants of the films are obtained by both the measurements of transmittance at normal incidence (Perkin Elmer Lambda 2s Spectrometer) and ellipsometry (EL X-02C Ellipsometer) at single wavelength (632.8 nm) and 5 incidence angles at least. The ellipsometer consists of a linearly polarized Helium-Neon laser light source and a rotating analyzer (Glan Thompson polarizing prism). In the ellipsometric analysis, the problem of multiplicity of solutions encountered in numerical inversion procedure of ellipsometry data is solved by the information obtained from the transmission results and the back reflection of the light beam, which is propagating to the photodetectors, is reduced by roughening the back surface of the substrates in a form of thin stripe along the long side of the rectangular substrate. The remaining parts of the substrates are used for transmission measurements.

During these transmission measurements, it is detected that the thickness and optical constants of a-SiC_x:H thin films change as a function of film position along the radial direction of the circular bottom electrode. On the other hand, optical model used in the analysis is an ideal case, that is, the films are assumed to have homogenous distributions of thicknesses and optical constants within the area of probing beam of the spectrometer. In this respect, in order to avoid these inhomogeneities during the measurement, the rectangular shaped probing beam is targeted in a geometric configuration such that the thinner side of the beam with thickness of about 1mm is aligned perpendicularly to radial direction. Examples of such a spectrum are given in Figure 7.1. Especially, for sample 1C, effect of inhomogeneity is negligible (It is well

known that eventual inhomogeneity causes shrinking of interference fringes and reduce their maxima or increase their minima with respect to the bare substrate transmittance [62]). Consequently, the optimization method can be applied to the measured spectra without inhomogeneity correction for a first order evaluation.

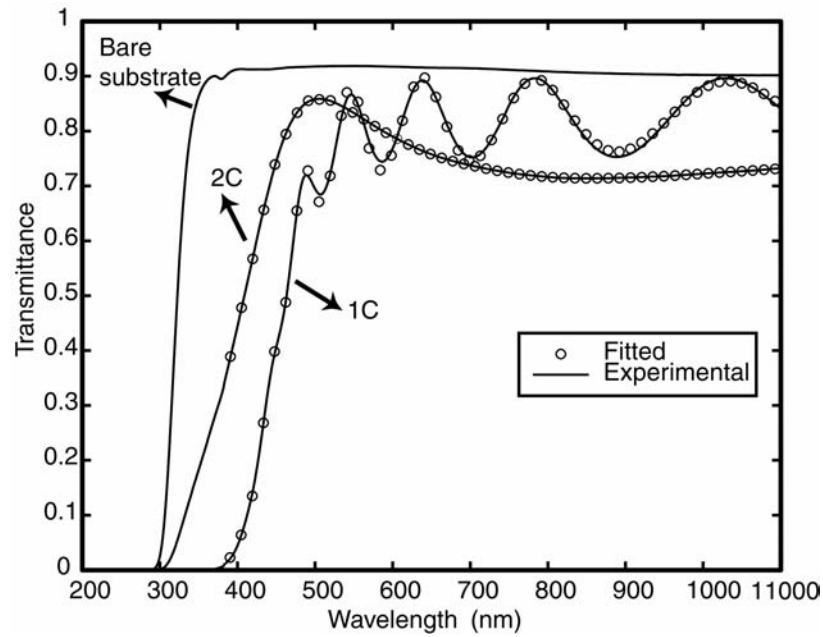


Figure 7.1 Transmittance spectra of samples 1C and 2C [128].

7.4 Results

7.4.1 Numerical determination of optical constants.

In this work, first the unconstrained formulation of the optimization method, as introduced previously in Subsection 3.4.2, is applied to the measured transmission spectra given in Figure 7.1. Since the glass substrate becomes absorbing for wavelengths below 380 nm, the optimization is always performed beyond 380 nm. Second, the results

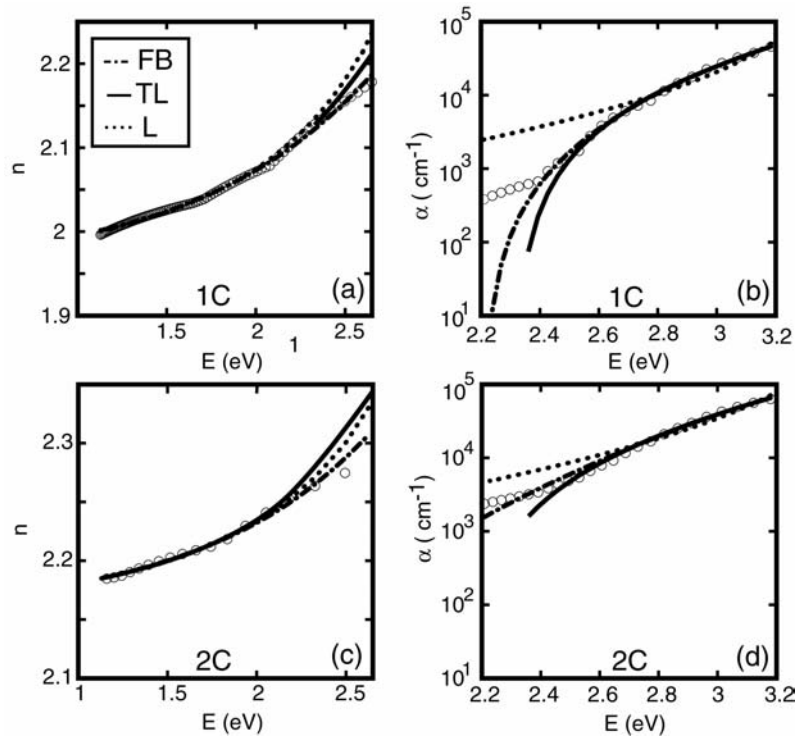


Figure 7.2 Retrieved values of refractive indices and absorption coefficients from transmittance spectra, fitting of these optical constants to Forouhi-Bloomer (FB), Jellison-Modine (TL) and single Lorentz oscillator (L) dispersion relations.

for these samples are examined by fitting FB, TL and L dispersion relations (7.1-7.3) to retrieved refractive index and absorption coefficient values as shown in Figure 7.2.

Although a smooth functional behavior is observed for refractive index (n) of sample 1C in Figure 7.2(a), absorption coefficient (α) displays relatively sharp behaviors in low energy part of the spectrum as shown in Figure 7.2(b). Such anomalies for energies $E < 2.4$ eV in $\alpha(E)$ and for energies $E > 2$ eV in $n(E)$, in fact, are known to be a result of insensitivity of transmittance measurements. Applications to gedanken and experimental measurements also show that this optimization method is mostly reliable in the transparent region for refractive index calculations and in the strong absorption region for absorption coefficient calculations [78-79]. Therefore dispersion relations are fitted to the retrieved refractive index and absorption coefficient data simultaneously for

different energy ranges of $E < 2$ eV and $E > 2.4$ eV, respectively. Similarly, the retrieved results for sample 2C are plotted in Figure 7.2(c) and 7.2(d). Refractive indices of sample 2C are observed to be slightly larger than the ones of sample 1C.

The relations between the optical gap values and the compositional properties of a-SiC_x:H thin films are quite essential to develop a light emitting device with desired optical and electrical properties. On the other hand, in amorphous solids there is not any definite threshold value for an optical gap as in their crystal counterparts, but different empirical measures, given in Section 2.3 and summarized briefly in [155], such as Tauc optical gap ($E_{g(Tauc)}$), Sokolov optical gap ($E_{g(Sokolov)}$) and Cody optical gap ($E_{g(Cody)}$) are widely used in the literature. In addition, an energy value E_{04} is another measure of optical gap which is defined as an energy point in the absorption spectrum where the absorption coefficient reaches 10^4 cm⁻¹. The optical gaps of a-SiC_x:H films obtained from both fittings of FB and TL models and the above quoted empirical measures together with the relevant carbon fraction x [156-158] are given in Table 7.2. Although FB model has fundamental problems as stated previously, it might be considered as a successful representation giving the best fitting to the optical constants apart from the optical gap values $E_{g(FB)}$ as shown in Figure 7.2. Whereas FB model gives underestimated optical gap values especially for sample 2C, TL model is not only observed to be a satisfactory representation, but also gives for both films consistent optical gaps with the values of $E_{g(Tauc)}$, $E_{g(Sokolov)}$ and $E_{g(Cody)}$. As for the L model, the fittings are more or less suitable to $\alpha(E)$ only for energies $E > 2.8$ eV. In the frame of single Lorentz oscillator model, the resulting retrieved parameters of the L model are envisaged as measures of the average oscillator.

Table 7.2 Optical gaps obtained by various methods [155] and corresponding carbon fractions x [156-158]. E_{04} is defined as an energy point in the absorption spectrum where the absorption coefficient reaches 10^4 cm⁻¹.

	$E_{g(FB)}$ (eV)	$E_{g(TL)}$ (eV)	$E_{g(Sokolov)}$ (eV)	$E_{g(Cody)}$ (eV)	$E_{g(Tauc)}$ (eV)	E_{04} (eV)	x
1C	2.21	2.32	2.27	2.42	2.50	2.80	0.45-0.50
2C	1.61	2.14	2.12	2.27	2.40	2.65	0.35-0.40

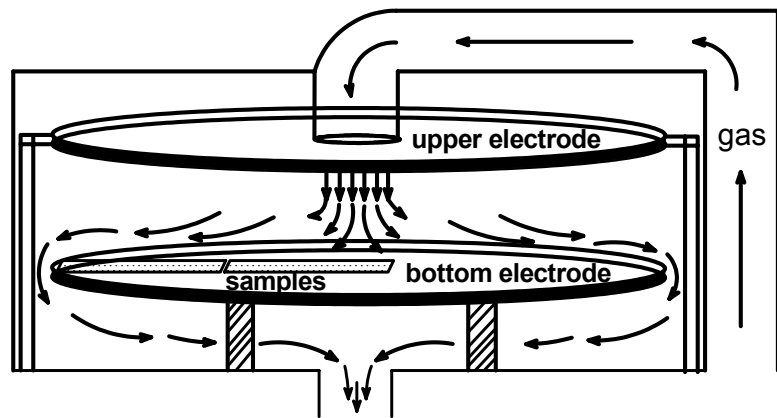


Figure 7.3 Schematic gas flow diagram in the plasma enhanced chemical vapor deposition system (PECVD). The electrode diameter and the interelectrode distance are 24 cm and 4 cm, respectively. Two samples are shown symbolically on the grounded bottom electrode.

For lower energies, the α values, supplied by L model, remains gradually above the retrieved values. This is not surprising because the L model uses lifetime broadening to give optical absorption. This Lorentzian broadening function has too wide wings leading to excessive absorption near the fundamental edge [159]. This approach has been relatively improved replacing constant broadening parameter C by an energy dependent one [159]. Both FB and TL models are more adequate since they use Tauc expression for α near the band edge as a starting point. On the other hand, the fitting along the subgap absorption might be improved by including an Urbach tail distribution but this was not done because in these regions, the experimental data might be extremely erroneous due to low sensitivity of the experimental technique at hand. Consequently, this region has been deliberately omitted in this work.

7.4.2 Inhomogeneity assessment.

After it is detected that there is a thickness variation on the a-SiC_x:H thin films depending their position on the bottom electrode of PECVD system as shown in Figure

7.3, this effect is analyzed by making systematic transmittance and ellipsometry measurements on different locations of the samples which, in turn, corresponds to different positions on the bottom electrode. A typical sample position within the PECVD reactor (long side along the radial direction of the bottom electrode) is depicted in Figure 7.3. The changes of the film properties as a function of radial distance from the edge of the bottom electrode to the center for depositions 1C and 2C are plotted in Figure 7.4 and 7.5.

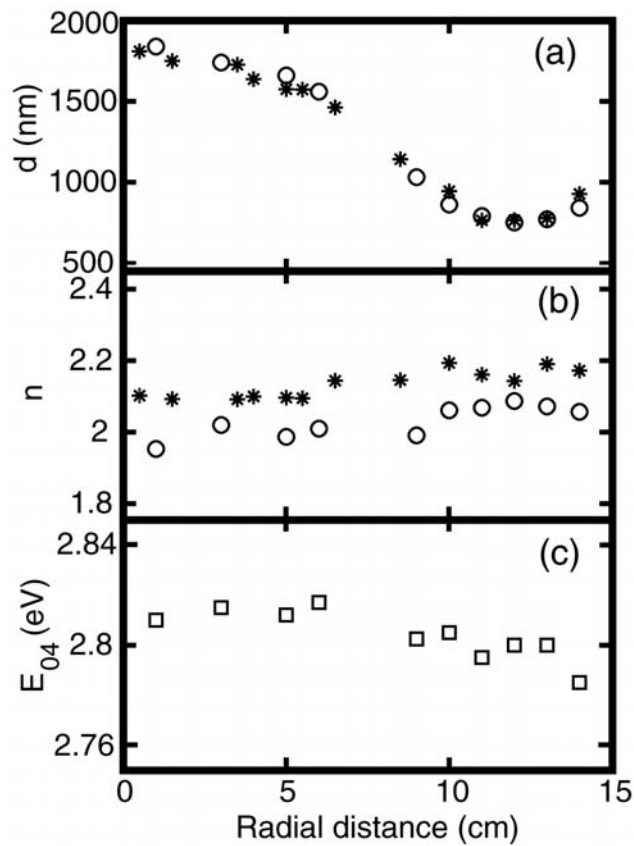


Figure 7.4 The distributions of film thickness (d), refractive index (n) at a wavelength of 632.8 nm and optical gap E_{04} along the sample 1C as a function of radial distance. Stars denote the results obtained from ellipsometry measurements at 632.8 nm, circles and squares denote the results obtained from transmittance measurements.

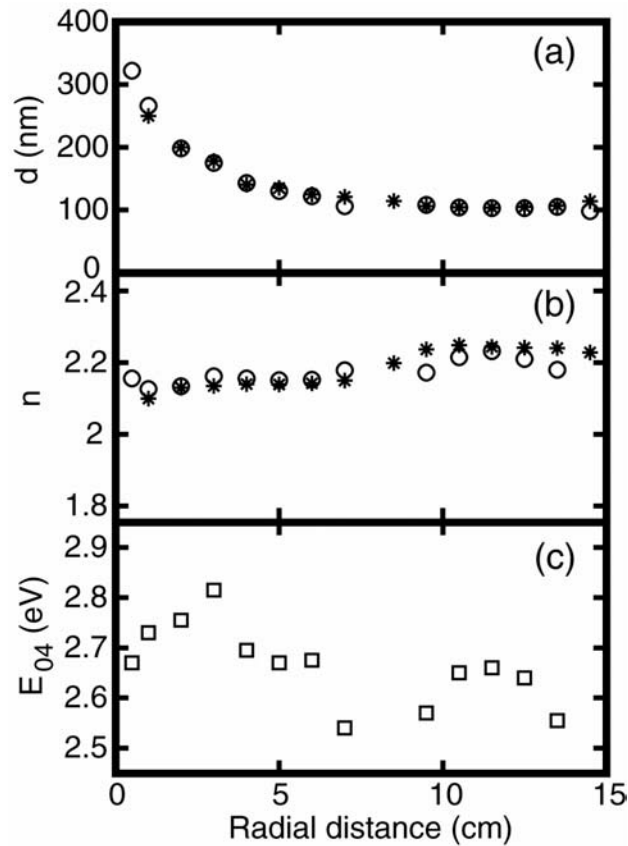


Figure 7.5 The distributions of film thickness (d), refractive index (n) at a wavelength of 632.8 nm and optical gap E_{04} along the sample 2C as a function of radial distance. Stars denote the results obtained from ellipsometry measurements at 632.8 nm, circles and squares denote the results obtained from transmittance measurements.

The thicknesses of samples 1C show a relatively slight decrease at the edge of the electrode and then start to decrease rapidly until the center of the electrode as shown in Figure 7.4(a). The refractive index is observed to be increasing at the center of the electrode as shown in Figure 7.4(b). E_{04} of samples 1C are plotted in Figure 7.4(c) and is found to be exhibiting a very slight decreasing behavior towards the center of the bottom electrode. On the other hand, although a rapid decrease in thickness is observed for 1C samples, thickness dispersion of 2C samples becomes negligible around the center as shown in Figure 7.5(a). Similar effects are observed both for n and E_{04} apart from some modulation of E_{04} values in comparison to 1C samples.

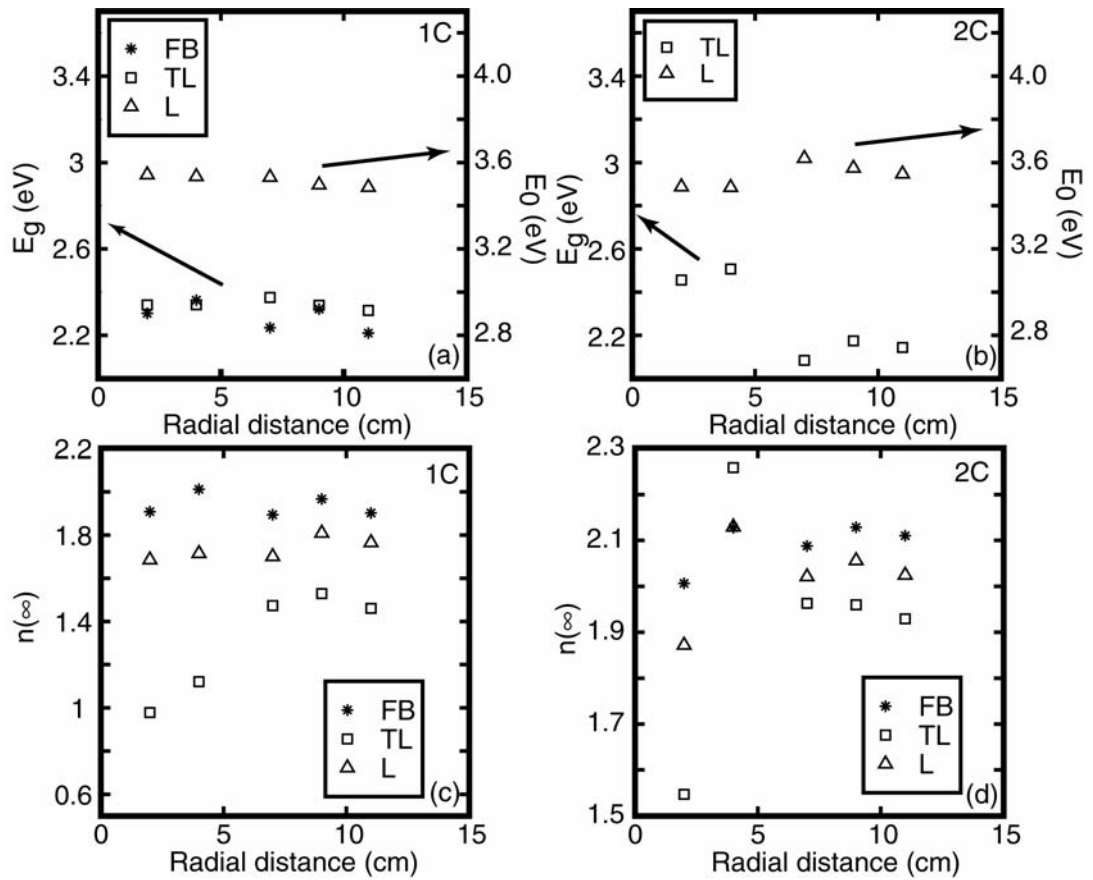


Figure 7.6 Optical gap (E_g) and resonance energies (E_0) of depositions 1C (a) and 2C (b) plotted as a function of radial distance. E_g values are obtained by fitting FB and TL dispersion relations (7.1-7.2), while E_0 values are obtained from L dispersion relations (7.3). Similarly, refractive index at high energy, $n(\infty)$, as a function of radial distance are obtained from FB, TL and L models for depositions 1C (c) and 2C (d).

In addition, the spectral behaviors of refractive indices and the absorption coefficients obtained by applying the optimization method to the transmittance measurements taken at various positions on the samples are fitted by the FB, TL and L models. Optical gap E_g and resonance energy E_0 of the films determined from these models are plotted as function of radial distance in Figure 7.6(a) and 7.6(b) for depositions 1C and 2C, respectively. However, optical gaps obtained by FB model are excluded in Figure 7.6(b) since these values are too low and consequently, unphysical.

Although band gaps and resonance energies of sample 1C show a slight decreasing behavior as a function of radial distance in Figure 7.6(a), sample 2C do not exhibit an apparent increasing or decreasing behavior in Figure 7.6(b). If it is reminded that resonance energy can be considered as an average energy band gap in the framework of single oscillator model, the similar behaviors of E_g and E_0 for 1C is not surprising [160]. On the other hand, high energy refractive indices are observed to be increasing towards the center of the bottom electrode in Figure 7.6(c) for sample 1C. This effect is similarly observed for sample 2C apart from a sharp discontinuous increase of $n(\infty)$ as shown in Figure 7.6(d).

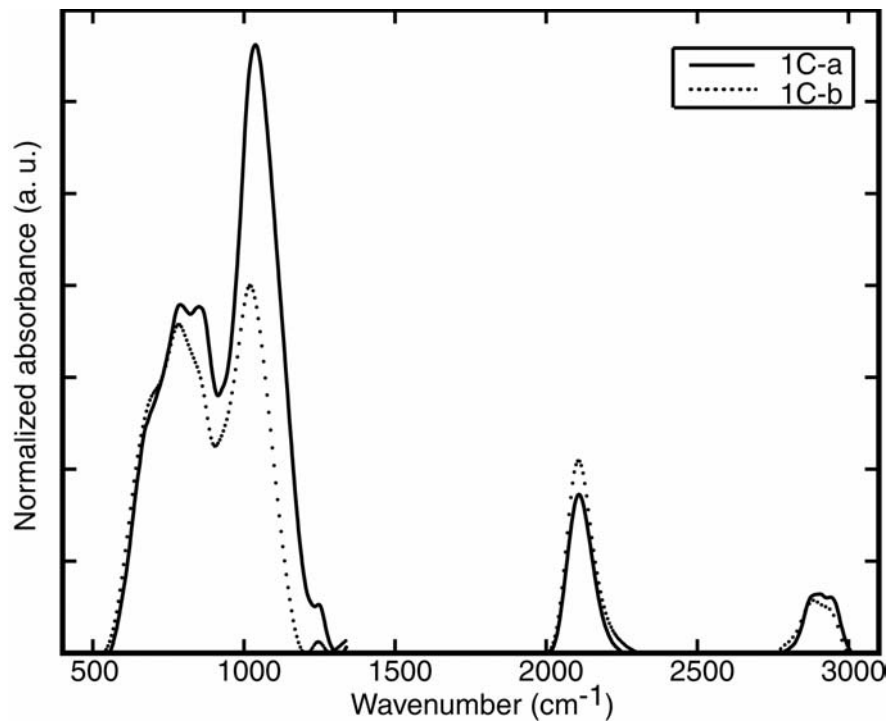


Figure 7.7 IR spectra of two $a\text{-SiC}_x\text{:H}$ samples, 1C-a and 1C-b, grown at positions 3 cm and 8 cm radially apart from the center of the bottom electrode of the PECVD system, respectively. The IR spectra are normalized according to the thicknesses of the films.

7.4.3 Discussion.

The effects of thickness nonuniformity in bonding structure of the films were analyzed by IR analysis. The spectra of the deposition 1C, as shown in Figure 7.7, were taken from the films grown on two different crystalline Si substrates placed at radial distances of 3 cm and 8 cm from the center of the bottom electrode. It is clearly seen in the figure that the spectra have absorption peaks with characteristic vibrational frequencies of a-SiC_x:H films for both samples [161-163]. The rough comparison of these spectra points out a drastic decrease, from near the center of the bottom electrode to the edge, in amplitudes of absorption peaks in the band of 900-1300 cm⁻¹ referred to wagging, rocking and bending motions of the bonds of type CH₂ and CH₃. Similarly, peaks in the band 2800-3000 cm⁻¹, referred to stretching vibrations of CH₂ and CH₃ have the same tendency. This reduction in the absorption amplitude can be attributed to a decrease of incorporated hydrogen amount moving from center to the edge of the bottom electrode. On the other hand, the peak at around 670 cm⁻¹, referred to stretching motion of both Si-C and Si₃CH structure slightly increases or at least stays unchanged. When this is compared with a general decrease in H content along the film, it may reflect enhanced C incorporation along the same direction [154].

On the contrary of the above situation, a slight increase of the peak height around 2100 cm⁻¹ associated with Si-H stretching vibration might be considered as a sign of at least no hydrogen depletion in the plasma medium towards the electrode edge [164]. Consequently, the reduction of carbon related H incorporation in the deposited films toward the edge of the electrode might be due to etching of loose H bonds especially in the form of CH₂ and CH₃ [136, 165].

The thickness variation of the film along the electrode might be caused by an eventual nonuniform distribution of the radicals responsible for film growth in the plasma between the electrodes although the pressure is kept constant. In other words, generation of these radicals should continue during the flow of the gases along the reactor due to secondary reactions between plasma species and radicals produced by

primary dissociation of gas molecules upon collisions with energetic plasma electrons. The primary products are atomic and molecular hydrogen together with the radicals of type C_2H_2 and C_2H_3 [166-168] for ethylene and SiH_2 and SiH_3 [169-170] for silane molecules. The generation rates of secondary radicals depend on both their mutual reaction rates and the ones between them and primary products [167-168, 171-172]. Therefore, building up the density of suitable radicals takes time after gas molecules are introduced into the plasma region. In this respect, growth rate variation is drawn as a function of time spent in the plasma rather than radius of the bottom electrode as shown in Figure 7.8.

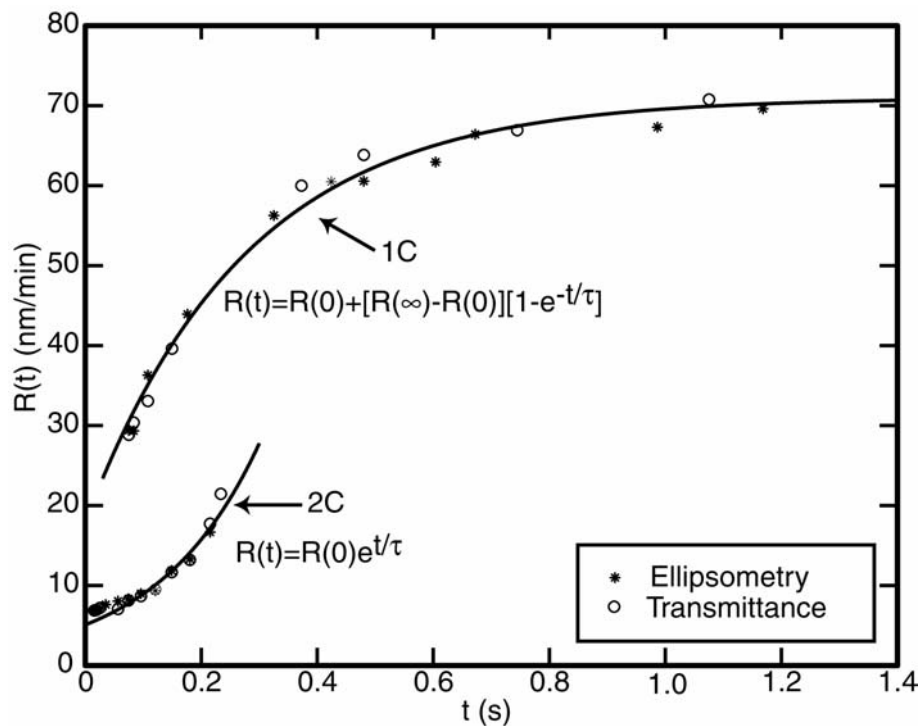


Figure 7.8 Deposition rates $R(t)$ for samples 1C and 2C as a function of residence time (t).

In Figure 7.8, the time spent by the molecules in the plasma (residence time) is determined by the expression $P\frac{V}{F}$ given in Section 7.3. In our reactor, gas molecules enter the plasma region through a circular shower with radius of 3 cm at the center of the upper electrode as illustrated in Figure 7.3. Thus, the residence time for a minimum volume of a vertical cylinder with the radius of 3 cm is taken as the lower limit of the residence time and found to be 0.075 s and 0.015 s for films 1C and 2C, respectively. This rough approximation is in agreement with an exponential dependence of the deposition rates which is molecule dissociation limited [170]. In this approximation, the generation rates of the radicals are taken directly proportional to density of gas molecules and thus, the deposition rate can be expressed by $R(t)=R(0)+(R(\infty)-R(0))(1-e^{-t/\tau})$ where $R(\infty)$ is the maximum deposition rate when all molecules are dissociated and $R(0)$ is the initial deposition rate when the molecules enter the plasma medium. The above expression is fitted for deposition 1C for $\tau=0.28$ s, $R(0)=53$ nm/min and $R(\infty)=71$ nm/min as shown in Figure 7.8. This fitting carries out the density of active radicals in the deposition is saturated beyond about $t = 1$ s for film deposition at 0.5 Torr. The limitation in the generation rates of radicals might be imposed by their available density since gas molecules are sufficiently abundant and immediately available. In other words, this approximation leads to an exponential time distribution of radical density. In turn, exponential growth rate $R(t)=R(0)e^{t/\tau}$ is reasonable. In this respect, the growth rate for 2C is fitted with values of $\tau=0.16$ s, $R(0)=4.7$ nm/min as shown in Figure 7.8. In the frame of this small time interval, this fitting supports the above rate analysis.

Higher CH_2 and CH_3 concentration in the film deposited near the center would be related to the smaller residence time and favorable direction of gas molecules entering vertically the chamber through the shower. In other words, gas molecules are directed toward lower electrode and hence molecules and primary plasma products may have higher probability to reach the surface of the growing film beneath the shower. Therefore, the radicals SiH_2 , C_2H_2 , C_2H_3 , C_2H_5 , $\text{SiH}_2\text{C}_2\text{H}_4$, $\text{SiH}_2\text{C}_2\text{H}_2$, $\text{SiH}_2\text{C}_2\text{H}_3$ may have a greater chance to be incorporated into the film structure by keeping majority of bonded hydrogen [166-169, 173-174]. When plasma species move toward outer edge of

the electrode, their effect gradually decreases due to enhanced density of secondary products including H atoms by radical-ion, radical-radical interactions. Since silane radicals, SiH_2 and SiH_3 , are more reactive than ethylene counterparts, SiH_3 reaction with ethylene radicals dominates plasma density due to its higher density than SiH_2 as time elapsed [175]. Thus, silane radicals generally react with ethylene radicals, but the latter may have chance to react with each other and result in higher C containing radicals [171-172]. In the free radical dominant regime of the plasma, these radicals, $\text{SiH}_3\text{C}_2\text{H}$, $\text{SiH}_3\text{C}_2\text{H}_2$, $\text{SiH}_2\text{C}_2\text{H}_4$ and $\text{SiH}_3\text{C}_2\text{H}_4$, are found to be responsible for a- $\text{SiC}_x\text{:H}$ film growth [173, 175-176]. It is also worth stating that unsaturated ethylene radicals with carbon number up to 7 are reported for microwave plasma which is known as high density plasma [173]. Thus, increased number of C atoms in the radicals promotes incorporation of more carbon atoms into the structure of growing film, and oppositely reduces C- H_n bond density by relative increase of C/H ratio in the radicals [132, 173].

Consequently, both decrease in refractive index and increase in optical gap towards the edge of the bottom electrode are probably due to this increase in atomic carbon fraction in the film which causes stronger Si-C σ bonds in comparison to Si-Si σ bonds.

7.5 Conclusion

In this study, a relatively recent method, consisting of numerical minimization on the transmittance spectra with or without a clear fringe pattern, is primarily and successfully used for determination of thickness and optical constants of amorphous thin films. These results are backed by the analysis of single wavelength (632.8 nm) ellipsometry measurements. Optical parameters, especially optical gap of the grown a- $\text{SiC}_x\text{:H}$ films, defined slightly different within the frame of each approach, become available for comparison with relevant literature.

An important inhomogeneity of samples originating from their position on the bottom electrode of the PECVD reactor along the radial direction has been

experimentally carried out. This anomaly has been attempted to be interpreted in terms of radical formation rates and their residence time during growth process.

In this work, although commonly used growth parameters have been chosen, this spatial inhomogeneity was revealed. In order to reduce such anomaly, the growth parameters should be readjusted, that is, an increase of either pressure or power might remedy this drawback. However, one should keep in mind that both higher pressure and power might generate excessive polymerization in plasma medium, leading to “powdered” films; consequently, a fine compromise seems indispensable.

CHAPTER 8

MODULATION OF OPTICAL CONSTANTS OF HYDROGENATED AMORPHOUS SILICON CARBON ALLOY ($a\text{-Si}_{1-x}\text{C}_x\text{:H}$) BY CARBON CONTENT

8.1 Introduction

As outlined in Section 7.1, hydrogenated amorphous silicon carbon alloy ($a\text{-Si}_{1-x}\text{C}_x\text{:H}$) thin film is a promising material especially in large area electronics. They are used in flat panel displays, as a high band gap window component in solar cells, in light emitting devices, in micro-electro-mechanical systems (MEMS), color sensors etc... The band gaps and refractive indices of amorphous carbon alloys can be continuously controlled by changing their composition. However, as carbon is incorporated in the films, the density of electronic localized states increases which results in degraded photoelectronic properties. This effect has been attempted to be reduced by hydrogen dilution [177]. Carbon atoms tend to form mixture of diamondlike σ bonds and graphitelike π bonded clusters to reach its lower energy configuration [178]. If SiC network is not allowed to relax (tetrahedrally coordinated) to a more stable configuration with incorporation of sp^2 states, the material becomes highly strained which leads to an increase in the width of the valence band tail. However, such a stress is not always a disadvantage in optoelectronic applications because stress produces potential fluctuations in the material which localize photocreated carriers [179]. Eventually, this effect increases the quantum efficiency of photoluminescence. The chemical bonding and band structure of $a\text{-Si}_{1-x}\text{C}_x\text{:H}$ thin films depend primarily on the

value of x . However, their properties depend also on the deposition technique and growth conditions in particular for carbon contents approaching or exceeding stoichiometry ($x \approx 0.5$) [158]. The published results of different authors are widely different due to of the great sensitivity of a-Si_{1-x}C_x:H to preparation conditions and consequently, the plot of a physical quantity as a function of x is not well defined [179].

In this chapter, the structural and optical properties of a-Si_{1-x}C_x:H deposited by plasma enhanced chemical vapor deposition (PEVCD) at different carbon gas concentrations and rf powers are investigated. Optical properties are examined by transmittance, reflectance and ellipsometry measurements. Besides, structural properties are analyzed by Fourier transform infrared (FTIR) spectroscopy.

Let us first review some possible deposition mechanisms of both a-Si:H and a-C:H films with SiH₄ and hydrocarbon source gases, respectively, in a glow discharge, then the case of a-Si_{1-x}C_x:H will be subsequently undertaken.

8.1.1 Deposition of a-Si:H thin films in SiH₄ plasma

The main reactions initiated by the collisions between electrons and SiH₄ gas molecules can be given as follows [2, 169]:



The reaction (8.1b) is the fastest reaction. However, SiH₂ radicals are extremely reactive and can easily react with other radicals in the plasma. In contrast to SiH₂, SiH₃ does not react with SiH₄. The only reaction of SiH₃ in addition to hydrogen is its recombination in the form of Si₂H₆ [180]. Therefore, the dominant radical in the plasma

is SiH_3 . Moreover, SiH_3 is very stable after its collision with SiH_4 and its lifetime in SiH_4 plasma is significantly longer than that of any other radicals and atoms [181]. Apart from the reactions between electrons and SiH_4 (primary reactions) at the initial stage of the plasma, secondary reactions occur between generated species, SiH_4 molecules, photons and electrons. SiH_3 is found to be at least 80% of the gas radicals in the silane plasma. [2]. Various experiments show that SiH_2 and SiH_3 are generated in the plasma with the highest efficiency whereas the other generated species such as SiH and Si require larger energies, that is, they have relatively limited efficiencies. The cross-sections for generation of ions (SiH^+ , SiH_2^+ , SiH_3^+) and excited species have much lower values than generation of neutral radicals such as SiH_2 , SiH_3 , SiH and Si [181].

If one considers that SiH_3 radicals, which are dominant in the plasma, contain 75% H, the resulting deposited films must have similar hydrogen contents. However, typical hydrogen content of a-Si:H films is 5-25%. Such a huge difference requires an elimination, i.e., a release of hydrogen from the surface during the growth [182].

Neutral species impinging onto growing film surface may lose their kinetic energy via energy transfer to the atoms of the solid and become trapped in a bound state at the surface. The sticking coefficient is the probability for a particle becoming bound at the growing surface via energy transfer, that is, participating in film growth. There are two types of bound states: physisorbed and chemisorbed bound states. Physisorbed state is a weaker type of bound state of binding energy less than 0.5 eV due to dipole-dipole intractions (van der Waals type) without exchange of electrons, while chemisorbed state has a binding energy larger than 0.5 eV and adsorbed species forms a covalent or ionic chemical bond by sharing or exchanging electrons with local surface species [183].

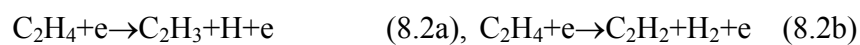
It is generally accepted that the growth of a-Si:H initiated by the physisorption of SiH_3 onto hydrogen-terminated a-Si:H surface site ($\equiv\text{SiH} + \text{SiH}_3 \rightarrow \equiv\text{SiHSiH}_3$) by forming a three-center Si-H-Si bond. This SiH_3 may diffuse over the surface for a suitable site and then a hydrogen molecule is desorbed from the surface Si-H bond leaving behind a silicon dangling bond. Another SiH_3 radical may be subsequently

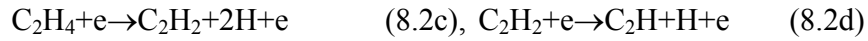
physisorbed and diffuses on the surface and then chemisorbed by an already created Si dangling bond on the surface [184]. The experimental observations of very low density of dangling bonds at the surface may be at first surprising if it is compared to the relatively high sticking coefficient (~ 0.1) of SiH_3 radicals, corresponding to a dangling bond density of the order of 10%. However, the physisorption of SiH_3 radicals followed by diffusion prior to the chemisorption by a dangling bond resolves this contradiction. Diffusive behavior of radicals to find a preferred site is expected to result in smooth surface which is in agreement with experiments [185]. Sticking without diffusion corresponds to physical vapor deposition conditions. Recent calculations have slightly modified the above outlined mechanism stating that the SiH_3 is not bound to the Si:H surface, but a-Si:H may grow by forming a direct Si-Si bond between SiH_3 radical and the surface Si site by displacing the surface hydrogen to a bond center of a neighboring surface Si-Si bond [186].

At higher plasma power densities, ion bombardment might be enhanced and these energetic ions can reduce the hydrogen surface coverage and break up polymeric chains with increasing the concentration of monohydride bonds [113]. Such a decrease in hydrogen coverage may increase the deposition rate because the surface of a-Si:H does not allow direct Si-Si bonding for SiH_3 radical if the surface is fully terminated by hydrogen. Besides, increasing the power density also increases the micro-columnar structure [187-188] and formation of microcrystalline silicon causing a sharp decrease in both the hydrogen content and the optical band gap.

8.1.2 Deposition of a-C:H thin films in C_2H_4 plasma

The mass spectra of dissociation of pure ethylene (C_2H_4) in a PECVD system detect mainly H, C, C_2H , C_2H_3 , C_2H_5 , C_2H_6 species and some other vinyl together with high-order hydrocarbon radicals. The dissociation of C_2H_4 initiated by electron collisions are as follows [168,171,173-174,189-190]:





As H atoms are available in the plasma medium the following reactions are expected:



Since both the reaction rate and sticking coefficient of CH_3 molecule are low, its density in the plasma increases and the following reactions become more probable [171]:



If these radicals collide with ethylene (C_2H_4) or acetylene (C_2H_2) molecules, radicals with more hydrogen can be formed [191]. Consequently, polymerization in gas phase might be initiated leading to the formation of particulates (dusts); if these dusts stick on the growing film surface, the film becomes structurally more disordered. Unsaturated ethylene based complexes containing carbon atoms up to 7 are reported for microwave plasma, known as high density plasma [173].

The plasma species reaching the growing film surface and then sticking on it are expected to be the neutral C_2H , C_2H_3 and C_3H_5 radicals as being the main precursors leading to film growth. These radicals might lose some of their hydrogen atoms as they form a bond on the growing film surface. However, it is known that deposited films involves a substantial amount of hydrogen. [192-194].

Apart from the C_2H_4 , various hydrocarbon source gases may be used such as CH_4 , C_2H_2 , C_2H_6 . The optical properties of films grown by different source gases in rf plasma is found to be differing only at low ion energies. However, in contrast to rf plasma, the choice of the source gas is observed to be influencing the optical properties of films grown in electron cyclotron resonance (ECR) discharges at both low and high energies. One of the reasons for such an insensitivity to source gases for films grown in rf discharge at high power is suggested to be the presence of very broad ion energy distribution in rf discharge, in contrast to ECR discharge, which might smear out all source gas related effects [195]. Similar to the case of SiH_4 plasma, as hydrocarbon molecules are dissociated and ionized in the plasma, radicals and ions lead to film growth by impinging on the surface of the substrate. Incident ions, impinging on the surface, displace the predominantly bonded hydrogen on the surface due to its smaller threshold energy for displacement compared to the case of carbon [196]. The displaced hydrogen atoms can diffuse and then physisorbed on the surface or recombine with another displaced H atom to form H_2 molecule. These H_2 molecules may become trapped in internal voids or desorp. A displaced hydrogen atom at the surface of the film forms a surface dangling bond which is a chemisorption site for subsequent incoming radicals [196]. Atomic hydrogen has a low sticking coefficient on many materials because the energy transfer from this light species to heavy target (surface) is small and therefore light species are unable to lose enough kinetic energy to become chemisorbed [183]. The incorporation of ions during the deposition cannot simply describe the total growth rate of films because it is observed by mass spectroscopy that the incoming flux of ions is generally lower than the one required by the observed deposition rate. This observed excessive growth may not solely explained either by neutral species from the plasma due to their small cross-section for the formation of a new chemical bonding by impinging CH_x radical on a hydrogen-terminated film surface. The experimental observation has been explained by introducing synergetic effect between ions and neutral radicals [197]. Initially physisorbed neutral species might be chemisorbed in a second step by the interaction with impinging ions. In this combined modeling of the surface and the plasma, the impinging ions transfer the necessary energy to form a new chemical bond by overcoming the activation barrier. Another kind of growth synergism

is observed between methyl radicals (CH₃) and hydrogen. Simultaneous interaction of the hydrogen atoms and CH₃ radicals increases the sticking coefficient of methyl radical from about 3×10^{-5} to about 3×10^{-3} [198]. On a surface not exposed to ion bombardment, it is observed that unsaturated hydrocarbon radicals such as C₂H and C₂H₃ can significantly contribute to the film growth since their reaction probability is much higher than that of saturated hydrocarbon radicals such as CH₃ and C₂H₅ [199]. C₂ clusters (ethylene groups) occur more frequently in a-Si_{1-x}C_x:H thin films prepared under low ion fluxes [200] and this result seems in agreement with the studies of Hopf *et al.* [199].

8.1.3 Deposition of a-Si_{1-x}C_x:H thin films

Finally, let's discuss the deposition mechanism of amorphous hydrogenated silicon carbon alloys produced in rf discharge by using SiH₄ and C₂H₄ as source gases. If SiH₄ and C₂H₄ source gases are introduced into the plasma medium, the radicals formed due to both gases might start to react with each others [132, 168, 176]. Essential ones of such reactions can be given as follows:



Although, the reactions (8.5a) and (8.5b) are reported to be observed in SiH₄-CH₄ plasma [168,176], the same reactions are also possible for SiH₄-C₂H₄ plasma via reactions 8.3c and 8.3d. As a result of other probable reactions 8.2, 8.3 and 8.4, the radicals of the form C₂H, C₂H₂, CH₃, SiH₂ and SiH₃ can also be expected to incorporate in the film structure.

Keeping in mind the complexities of previously outlined deposition mechanisms of a-Si:H and a-C:H films separately, it is not a surprise to have an even more complex deposition mechanism for hydrogenated amorphous silicon carbon alloys. Nevertheless, the formation and the amount of dangling bonds on the growing surface might be considered as an essential part which determines the deposition with various aspects since radicals easily become bound on the surface through dangling bonds. As the C₂H₄ and SiH₄ radicals react with H atoms on the growing surface, become physisorbed on the surface and then desorbed, leaving a dangling bond on the growing surface. On the other hand, the presence of unsaturated dangling bonds on the growing surface decreases the diffusion coefficient of the adsorbed radicals and hence deteriorates the film properties by causing columnar structure which include voids, stressed bonds, sp² type bonds etc. In addition, it is difficult to eliminate H from the surface in comparison to the a-Si:H deposition since C-H bonds are stronger than the Si-H bonds. Therefore, a-Si_{1-x}C_x:H films contain more H than a-Si:H films and most of the H atoms are found to be bonded to C. It should be noted that hydrogen dilution during the growth compensates elimination of hydrogen from the growing surface by saturating dangling bonds (163-177). Besides, hydrogen dilution is observed to lead to in high photoconductivity, the deposition rate is decreased as a drawback [201].

8.2 Experimental

8.2.1 Preparation of a-Si_{1-x}C_x:H thin films

a-Si_{1-x}C_x:H thin films are deposited on the grounded bottom electrode of a parallel plate PECVD system at 13.56 MHz (Plasma Lab μ P 80). Crystalline silicon and Corning 7059 glass substrates are used for infrared and ultraviolet-visible optical analyses, respectively.

Silicon wafers first boiled in trichloroethylene for 5 min and then rinsed in ultrasonically agitated deionized water (DIW) for 5 min. Second after they dipped in hot H₂O-H₂SO₄-H₂O₂ (2:1:1) solution for 5 min, they rinsed in DIW for 5 min. Third, they

dipped in hot DIW-HCl:H₂O₂ (2:1:1) solution for 15 min and then rinsed in ultrasonically agitated DIW for 5 min. Finally, wafers dipped in DIW-HF (10:1) solution for 15 s. at room temperature and rinsed in ultrasonically agitated DIW for 5 min. On the other hand, first glass substrates dipped in isopropil alcohol for 5 min and rinsed in ultrasonically agitated DIW. Then they are heated for 5 minutes just prior to deposition.

After the cleaning process, they were loaded into the deposition system as quick as possible to prevent the substrates from atmospheric contamination. Finally, the reactor was pumped down to a base pressure below 1 mtorr and the temperature of the bottom electrode was adjusted to 250 °C before letting flow of source gases, ethylene (C₂H₄) and silane (SiH₄), into the system. Growth process was started after total source gas flow rate (F), hydrogen flow rate and pressure are adjusted to values of 20 ccm, 200 ccm (H dilution ratio will be 91%) and 0.5 torr, respectively. Other deposition parameters such as relative gas concentration of C₂H₄ ($M_{C_2H_4}$), flow rates of ethylene ($F_{C_2H_4}$) and SiH₄ (F_{SiH_4}) and power density (P) for eight different samples are given in Table 8.1

Table 8.1. Eight different depositions under a pressure of 0.5 Torr at substrate temperature of 250 °C for the following deposition parameters such as relative C₂H₄ concentration ($M_{C_2H_4}$), SiH₄ (F_{SiH_4}) and C₂H₄ ($F_{C_2H_4}$) flow rates and power density (P). The last two letters “lp” and “hp” denote films grown at low and high powers, respectively.

Sample	$M_{C_2H_4}$	F_{SiH_4} (ccm)	$F_{C_2H_4}$ (ccm)	P (mW/cm ²)	d_{av} (nm)
0lp	0	20	0	30	226.5
0hp	0	20	0	90	642.0
2lp	0.2	16	4	30	523.4
2hp	0.2	16	4	90	548.2
5lp	0.5	10	10	30	230.7
5hp	0.5	10	10	90	713.6
7lp	0.7	6	14	30	240.8
7hp	0.7	6	14	90	748.9

8.2.2 Measuring procedures and equipments

The thickness and optical constants of the films are obtained by transmittance measurements (double beam Perkin Elmer Lambda 2s Spectrometer) at normal incidence. All measurements are performed as soon as (few minutes) the samples are brought out from the growth chamber in order to reduce eventual atmospheric contamination on the surfaces of the films.

Since no essential inhomogeneity effect is noticed at transmittance and reflectance spectra of the films, optical model used in the analysis is an ideal case, that is, the films are assumed to have homogeneous distribution of thicknesses and optical constants within the area of probing beam of the spectrometer (It is well known that eventual inhomogeneity causes shrinking of interference fringes and reduce their maxima or increase their minima with respect to the bare substrate transmittance as presented in Chapter 6 [62]).

Structural analysis of a-Si_{1-x}C_x:H films is performed by FTIR transmission spectroscopy (Nicolet 520). Effect of interference due to multiple transmissions and reflectances in the thin films are eliminated by interpolating the IR absorption free regions of the spectrum.

8.2.3 Determination of optical constants.

The transmittance spectra of the films are analyzed by a commercial characterization software OptiChar [202]. The generally accepted inaccuracies of transmittance measurements are of the order of 0.1%. As previously discussed in Section 3.4, such an uncertainty is not meaningful unless the film thicknesses are measured with inaccuracies that are unrealistically small. Therefore accuracies of optical constants obtained from transmittance measurements can be improved by decreasing the uncertainty in the determination of the film thickness [71]. On the other hand, the numerical inversion methods may result in multiple solutions, that is, several physically

reasonable complex refractive indices ($N(\lambda)$) and thicknesses (d). In this respect, in order to avoid such an ambiguity, instead of performing additional measurements, we analyzed the spectra with another method, namely envelope method which is given in Subsection 3.4.1, and compared the thicknesses obtained by these two approaches.

The transmittance spectra of all the eight $a\text{-Si}_{1-x}\text{C}_x\text{:H}$ thin films display enough number of interference fringes in their transparent spectral region to apply envelope methods [67-68, 73-74] for the determination of optical constants. First, transmittance spectra of the films are analyzed by OptiChar. Second, thicknesses of the films are determined from transmittance measurements within envelope approach in the wavelength range where the films are not absorbing. The agreement between the thicknesses of the films determined by envelope method (d_{env}) and by OptiChar software (d_{fit}) is quite good as shown Figure 8.1. The average thicknesses (d_{av}) of the films, obtained by arithmetic average of d_{env} and d_{fit} , are given in Table 8.1.

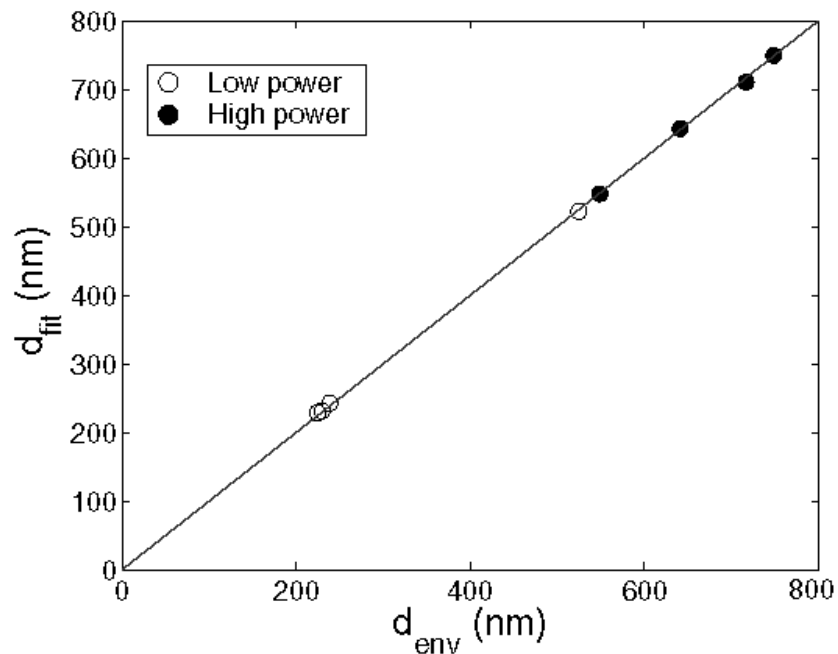


Figure 8.1 The thicknesses d_{fit} is plotted as a function of thicknesses d_{env} to exhibit the agreement in thicknesses determined from fitting and envelope method.

8.2.4 Dispersion relations used in the characterization

The smooth behavior of dielectric functions of amorphous solids, in contrast to sharp features for their crystal counterparts, suggests that dielectric functions with few parameters, such as single Lorentz oscillator (L), Forouhi-Bloomer (FB) and Tauc-Lorentz (TL), are expected to be adequate to simulate the experimental spectrum. These models are outlined in Chapter 7. However, it is observed in Chapter 7 that Lorentzian broadening function has too wide wings leading to excessive absorption near the fundamental edge. Similar behaviors have been observed previously [203-205]. Afromowitz [203] showed why single oscillator model fails for energies approaching the direct gap by expanding the Kramers-Kronig relations. It is seen that the expansion weights the low energy part of the ϵ_2 spectrum and this effect becomes significant only for energies approaching direct band gap. Although harmonic oscillator model automatically satisfies the Kramers-Kronig relations, they do not necessarily represent the dielectric responses in the most efficient way due to appearance of optical absorption below fundamental absorption edge which is generally the case for amorphous materials [150].

Recently, a relatively improved model is suggested [159], which is first quoted in subsection 7.2.3, and involves an energy dependent broadening parameter Γ' for each oscillator in the form:

$$\Gamma' = \Gamma e^{-\beta \left(\frac{E-E_0}{\Gamma} \right)^2} \quad (8.6)$$

where E_0 is the resonance energy and β is a parameter which determines, together with Γ , the Lorentzian broadening. This modification of Lorentz oscillator model, giving excellent agreement with experimental data for Si_3N_4 , SiO and amorphous and crystalline SiO_2 , is called modified single Lorentz oscillator model (ML) [159].

In this study, L, ML, FB, TL dispersion relations are fitted to the retrieved refractive index and absorption coefficient values. This fitting is mostly reliable in the transparent region for refractive index and in the strong absorption region for absorption coefficient due to the insensitivity of transmittance measurements. Therefore, dispersion relations are fitted to the retrieved refractive index and absorption coefficient data simultaneously for transparent and strongly absorbing spectral regions, respectively, similar to the procedure followed in Chapter 7. Although, these dispersion relations are used in the literature especially to fit the measured data such as transmittance, reflectance and ellipsometry, here the retrieved optical constants are fitted directly to compare them and confirm the Kramers-Kronig consistency.

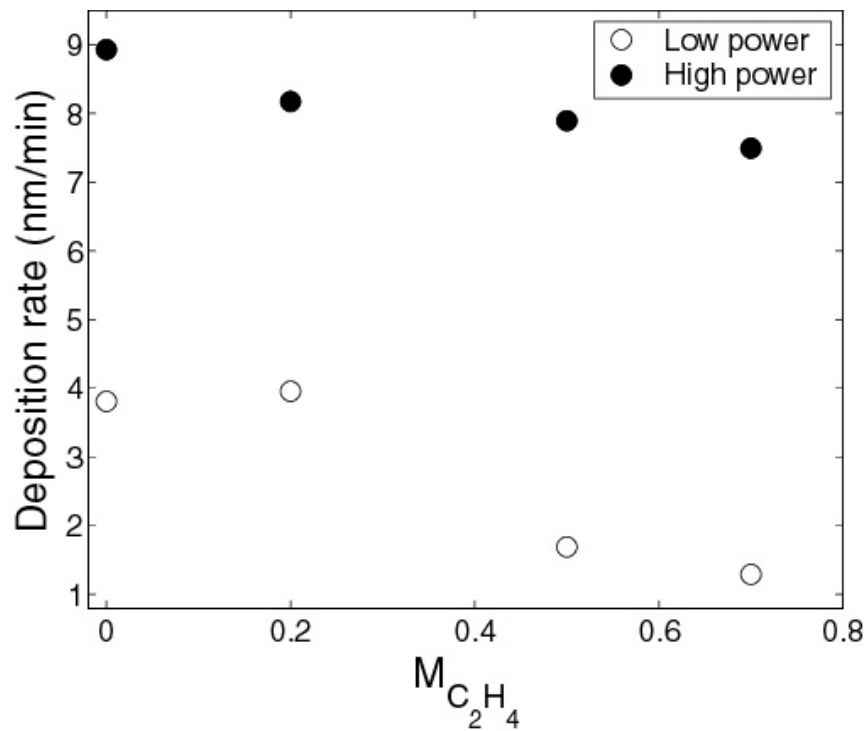


Figure 8.2 Deposition rate of a-Si_{1-x}C_x:H thin films as function of C₂H₄ relative gas concentration $M_{C_2H_4} = C_2H_4 / (C_2H_4 + SiH_4)$.

8.3. Results

8.3.1 The influence of carbon content and rf power on deposition rate

The deposition rate of a-Si_{1-x}C_x:H thin films are plotted as a function of $M_{C_2H_4} = C_2H_4 / (C_2H_4 + SiH_4)$ relative gas concentration in Figure 8.2. For both power densities the deposition rates are observed to be decreasing as $M_{C_2H_4}$ increases, in agreement with some results obtained in the literature [163]. However, others have measured slightly different behaviors: D. Kuhman *et al.* deposited a-Si_{1-x}C_x:H films by C₂H₄ at a power density of 200 mW/cm² and also observed a slight decrease in deposition rate as $M_{C_2H_4}$ increases up to about 0.4, followed by a relatively sharp decreasing behavior beyond $M_{C_2H_4} = 0.4$ [206]. On the other hand, Ferreira *et al.* observed first an increase in deposition rate up to $M_{C_2H_4}$ of about 0.3 and then a decreasing behavior [157].

The deposition rates of films grown at high power density (90 mW/cm²) are seen to be substantially higher than those of the films grown at low power density (30 mW/cm²), similar to the results of Ambrosone *et al.* [158-207]. The ratios of deposition rates being about 2.5 for lower values of $M_{C_2H_4}$, reaches 10-15 for higher values. The effect of such a power change on deposition rate is remarkably large. Although deposition rate decreases as the $M_{C_2H_4}$ increases for both power densities, the decrease at high power is much smaller than the decrease at low power. In other words, at high power density, the deposition rate is relatively independent of $M_{C_2H_4}$ in the range $0 < M_{C_2H_4} < 0.7$. It should be noted that “low power” and “high power” terms in this work should not mixed with the “low power regime” used for films produced by CH₄/SiH₄ gas mixtures. C₂H₄ is an unsaturated hydrocarbon in contrast to CH₄ and it has a high dissociation rate similar to SiH₄. In this respect, for C₂H₄ whatever the power of the plasma is, a-Si_{1-x}C_x:H thin films can not be produced in the “low power regime” which corresponds to a plasma power less than the threshold (~300 mW/cm²) of primary

decomposition of CH_4 [179]. The threshold for primary decomposition of C_2H_4 is much smaller than that of CH_4 . Nevertheless, a decreasing behavior in deposition rates for $\text{a-Si}_{1-x}\text{C}_x\text{:H}$ thin films produced by $\text{CH}_4\text{-SiH}_4$ plasma has been observed [158]; a more rapid decrease for films grown at a power density of 60 mW/cm^2 than for films grown at a power density of 10 mW/cm^2 has been measured on the contrary of present work. Consequently, these results suggest that power regimes do not alone determine the growth mechanisms independent to other deposition parameters and conditions.

These macroscopic effects may be interpreted microscopically as follows: The incorporation of radicals in the film can be characterized by their surface loss probabilities which describe the probability of losing reactive particle in a surface collision. It is defined as the sum of sticking coefficient and the probability γ to react at the surface to form a nonreactive volatile molecule. SiH_3 radicals have surface loss probability of about 0.25 on Si-H growing film surface. On the other hand, CH_3 radicals have very low surface loss probability of about 0.001 on C-H growing surface which increases with hydrogen dilution. This difference may be attributed to the ability of SiH_3 to insert into strained surface bonds [183] which requires also binding and surface diffusion otherwise the surface would not be smooth [186].

The surface loss probabilities of sp^1 -hybridized C_2H , sp^2 -hybridized C_2H_3 , sp^3 -hybridized C_2H_5 precursors have been approximately estimated [199] as 0.9, 0.35 and 0.001. The relatively larger values of surface loss probabilities of sp^1 - and sp^2 -hybridized precursors in comparison to sp^3 -hybridized ones might be due to the electrons in π orbitals which are exposed on the outside of the molecules making them much more reactive or unsaturated than molecules with only single σ bonds between carbons. In subsection 8.1.2, it is stated that since both the reaction rate and sticking coefficient of CH_3 is low its density in the plasma is high. In this respect, the decrease in deposition rate can be attributed to the increase of C_2H_5 concentration and hence, CH_3 concentration (through reactions 8.3c and 8.3d) with smaller surface loss probabilities in the gas mixture and their higher dissociation energy [157].

8.3.2 Carbon incorporation in the films: Statistical approach for compositional analysis.

The carbon content (x) of the films are determined by comparing their optical gaps and refractive indices separately with the values published in the literature as shown in Table 8.2. The published values used for reference are for a-Si_{1-x}C_x:H thin films grown by PECVD systems, generally at substrate temperatures between 200 and 300 °C, powers between 10 W and 50 W and with carbon source gases C₂H₄, C₂H₂ and CH₄. Only in [208] x values are obtained from an empirical relationship. In the references [209-211, 156], carbon contents are determined from one or combination of techniques such as Auger spectroscopy [209-212,156], microprobe analysis [212], Rutherford back-scattering spectroscopy [156, 158] and x-ray photoelectron spectroscopy [213]. It should be kept in mind that although the absolute concentrations obtained from most of these methods are generally not in quite agreement [214] relative measurements for each method are likely to be more reliable [160]. In this respect, a statistical approach might be envisaged as a reliable alternative technique for a first order evaluation instead of using an empirical relation for x .

Hydrogen incorporation during the growth of a-Si_{1-x}C_x:H films affects the optical constants such as refractive index and optical gap. Hydrogen content in the films is observed to be increasing as carbon content increases independent of source gases [158, 212] and decreasing as substrate temperature increases, similar to the observations for a-Si:H films [209]. The sharp increase in the hydrogen concentration is observed to be occurring for low x ($x < 0.2$) [211]. In this respect, the hydrogen concentrations of films are expected to be not essentially different for substrate temperature and rf power of 200-300 °C and 10-50 W, respectively. Nevertheless, the final x compositions are determined by at least 13 independent comparisons for each film. Since refractive index seems relatively insensitive to changes in the deposition parameters as long as the carbon incorporation in the film is not changed, refractive index values are generally believed to be more reliable in comparison to optical gap values for estimations of x [215].

Table 8.2 Table of optical constants and carbon content x of various films determined by comparing these optical constants with relevant published results in the literature. For each film, a set of x values is first determined either from E_g^{Tauc} or E_{04} values and listed in the column denoted by E_{04}, E_g . Similarly, the x values which are determined either from refractive indices at $E=2\text{eV}$ (n_1) or $\lambda = 1100 \text{ nm}$ (n_2) are listed in the column denoted by n . The average values $\langle x \rangle$ of x together with their standard deviations σ are added at the bottom of the table. The indices lp and hp are used for low power (30 mW/cm^2) and high power (90 mW/cm^2).

	2lp	2hp	5lp	5hp	7lp	7hp
E_g^{Tauc} (eV)	2.03	2.03	2.40	2.28	2.55	2.71
E_{04} (eV)	2.18	2.18	2.42	2.48	2.60	2.91
n_1	3.21	3.18	2.63	2.49	2.29	2.07
n_2	2.91	2.89		2.36	2.16	2.02

2.43

	E_{04}, E_g	n	E_{04}, E_g	n	E_{04}, E_g	n	E_{04}, E_g	n	E_{04}, E_g	n	E_{04}, E_g	n
x^a [209]	0.22	0.20	0.22	0.20	0.42	0.30	0.37	0.32	0.53	0.44	0.63	0.48
x^b [210]	0.22	0.15	0.22	0.15	0.32	0.32	0.33	0.35	0.38	0.44	0.61	0.54
x^a [208]	0.16		0.16		>0.23							
x^c [211]	0.20	0.20	0.20	0.20	0.40	0.43	0.45	0.47	0.50	0.52	0.57	0.62
x^c [212]	0.15	0.17	0.15	0.17	0.39	0.37	0.45	0.40	0.48	0.48	0.53	0.53
x^c [158]	0.22	0.18	0.22	0.18	0.33	0.30	0.35	0.33	0.40	0.45	0.50	0.52
x^d [213]	0.18	0.18	0.18	0.18	0.27	0.32	0.39	0.36	0.46	0.43	0.54	0.50
x^c [156]	0.20		0.20		0.28		0.35		0.40		0.55	
$\langle x \rangle$	0.19	0.18	0.19	0.18	0.34	0.34	0.38	0.37	0.45	0.46	0.56	0.53
σ	0.025		0.025		0.054		0.050		0.047		0.048	

^a determined by comparing Tauc gap and n_2 at $\lambda=1100 \text{ nm}$. ^b determined by comparing Tauc gap, E_{04} and n_2 at $\lambda=1100 \text{ nm}$.

^c determined by comparing E_{04} and n_2 at $\lambda=1100 \text{ nm}$.

^d determined by comparing E_{04} and n_1 at $E=2 \text{ eV}$.

However, the estimated x 's by using either refractive indices or optical gaps are found to be in quite agreement in this work. The absolute content (x) obtained from different publications differs at most 15% (each column in the Table 8.2) whereas the average values for each deposition obtained by comparing both optical gaps and n separately agree within 3% (last row of the Table 8.2). In order to show how diverse the x values are obtained from each reference, standard deviations σ are also given at the bottom of Table 8.2.

Finally, carbon content of the films is plotted as function C_2H_4 gas concentration as shown in Figure 8.3. Although the variation of x as a function of the C_2H_4 relative concentration is approximately linear, the slope is substantially increased by the power (see Figure 8.3). This is in agreement with the previous discussion on the growth rate.

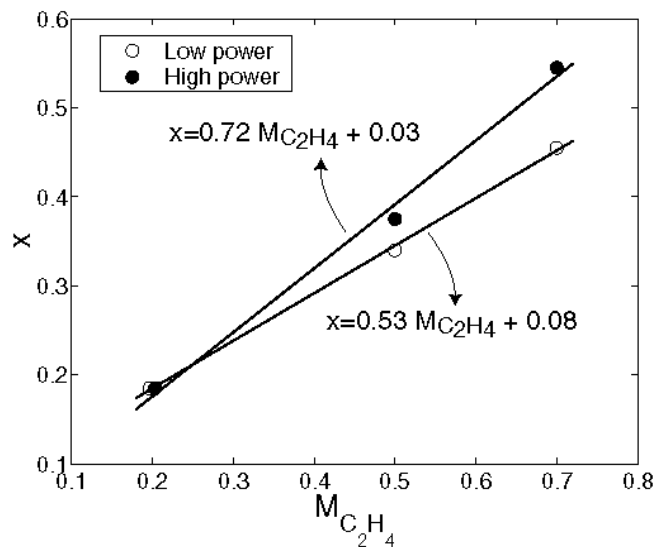


Figure 8.3. Carbon content of $a-Si_{1-x}C_x:H$ thin films as function of C_2H_4 gas concentration $M_{C_2H_4}$.

8.3.3 UV-VIS Transmittance Analysis of the Films

The energy dependence of refractive indices of the thin films deposited at low and high power densities are shown in Figures 8.4. As carbon content in the film increases, the refractive indices are observed to be decreasing. Besides, at each carbon content for $x > 0$, refractive indices of the films grown at high power (hp) are smaller than the refractive indices of the films grown at low power (lp). This is a consequence of more carbon incorporation in the films at high powers. However, for $M=0$ (a-Si:H, $x=0$), the effect of power is reverse, that is, the refractive indices increase by increasing the power. On the other hand, for a-Si_{1-x}C_x:H films with $x \neq 0$, the effect of power on refractive indices has been found to be growing as carbon content in the films increases. In addition, as x increases, refractive index spectra of the films are observed to be less dispersive because the spectral region, where films are transparent, widens within the measured wavelength range.

The refractive indices are successfully simulated by the dispersion relations even for energies just above the optical gaps E_g^{Tauc} of the films as shown in Figure 8.4. The deviations of the fittings appear at corresponding high energies are probably due to sub gap absorptions which are not taken into account in the fittings of dispersion relations. FB dispersion relations are known to be leading to excessive absorption below E_g^{Tauc} constituting one of the problems of FB model. In this respect, although the sub gap absorption is not introduced additionally in FB model, it is expected that FB might fit the spectra better than TL but, this is not the case, generally TL model simulates the refractive indices better. On the other hand, it should be kept in mind that the refractive indices at corresponding high energy regions are not as reliable as the ones in the transparent region.

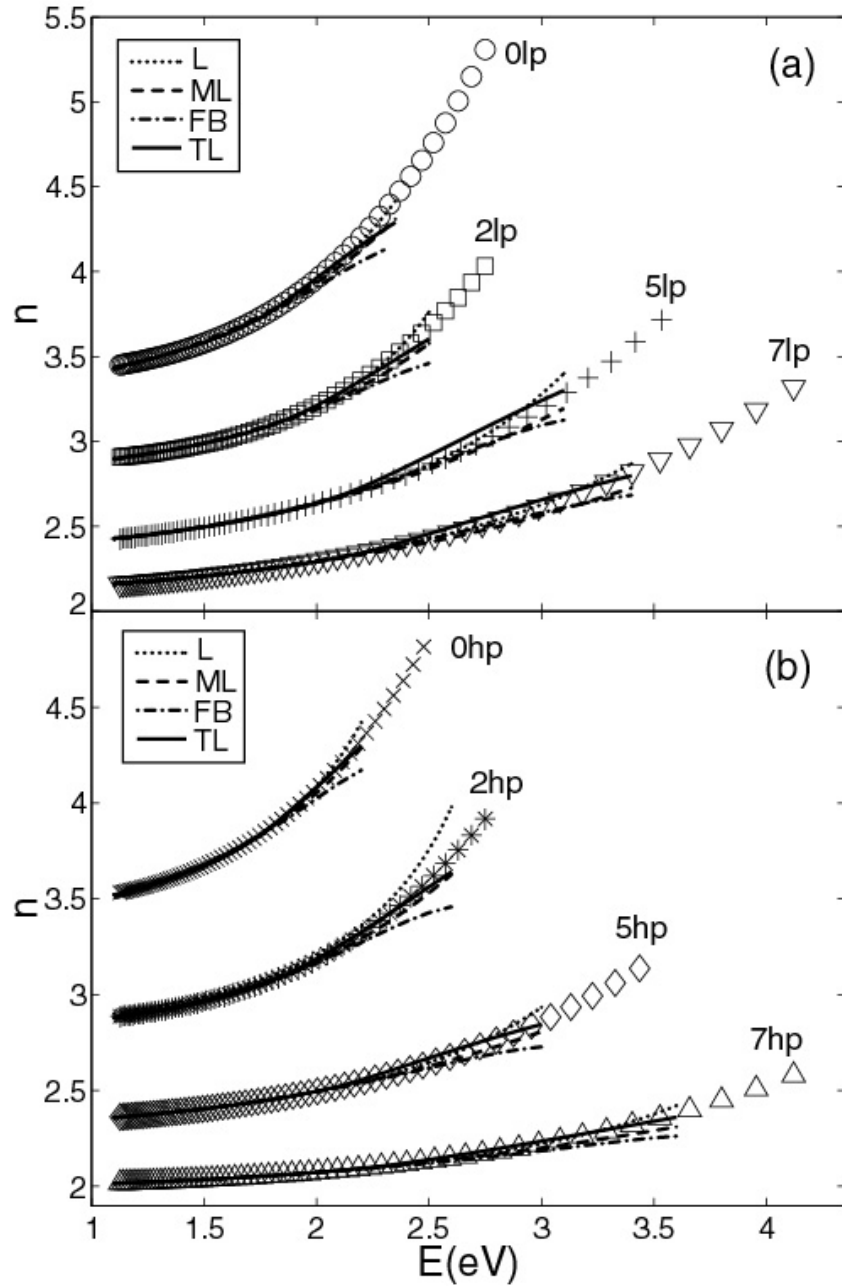


Figure 8.4 Refractive indices of $a\text{-Si}_{1-x}\text{C}_x\text{:H}$ thin films as function photon energy together with fittings of dispersion relations by Lorentz (L), Modified Lorentz (ML), Forouhi-Bloomer (FB) and Tauc-Lorentz (TL) models. (a) low and (b) high power.

(or islands) separated from each other by sp^3 dominant boundaries (tissues). Therefore, in amorphous carbon (a-C) localized to localized transitions are strongly probable since the initial and final states are lying on the same cluster and consequently, an optical absorption up to more than 10^4 cm^{-1} may be due to transitions only between localized states. In this respect, the smooth absorption spectrum observed for 7hp might be due to a distribution of cluster sizes in carbon rich a-Si_{1-x}C_x:H film.

Refractive index below the band gap can be described by the single Lorentz oscillator model [148-149] as $n^2(E) = 1 + (n^2(0) - 1) \frac{E_0^2}{E_0^2 - E^2}$ where the full width at half maximum of the imaginary part ε_2 of the dielectric constant $\varepsilon(E) = \varepsilon_1(E) - i\varepsilon_2(E)$ is taken as zero. E_0 is the resonance energy which approximately corresponds to the maximum of $\varepsilon_2(E)$ and represents the average separation between valence and conduction bands. $n(0)$ is the refractive index extrapolated to zero energy. In the energy interval where a-Si_{1-x}C_x:H thin films are transparent, by plotting $1/(n^2-1)$ as a function E^2 and extrapolating to the $E=0$, one can calculate the static refractive index $n(0)$ as shown Figure 8.5(a). The refractive indices at both $E=0$ and $E=2$ eV are plotted as a function of carbon content in the films in Figure 8.5(b). Deviations from linear relation in Figure 8.5(a) are signs of absorption onset and become more remarkable as the C₂H₄ relative gas concentration decreases.

Figure 8.6 shows the absorption coefficient spectra $\alpha = 4\pi\kappa/\lambda$ for all the films determined from transmittance measurements. As x increases, the optical absorptions in the films are observed to be decreasing at high energies. For samples 2hp and 5hp grown at high power, an additional shoulder like behavior is observed at low energy part of the spectra. Such a variation in α is not apparent for 7hp which is the film of largest carbon content.

In amorphous semiconductors, the optical transitions between localized states depend whether or not the initial and final states are confined within the same regions (large overlapping of wave functions) or at distant regions (small or zero overlapping of

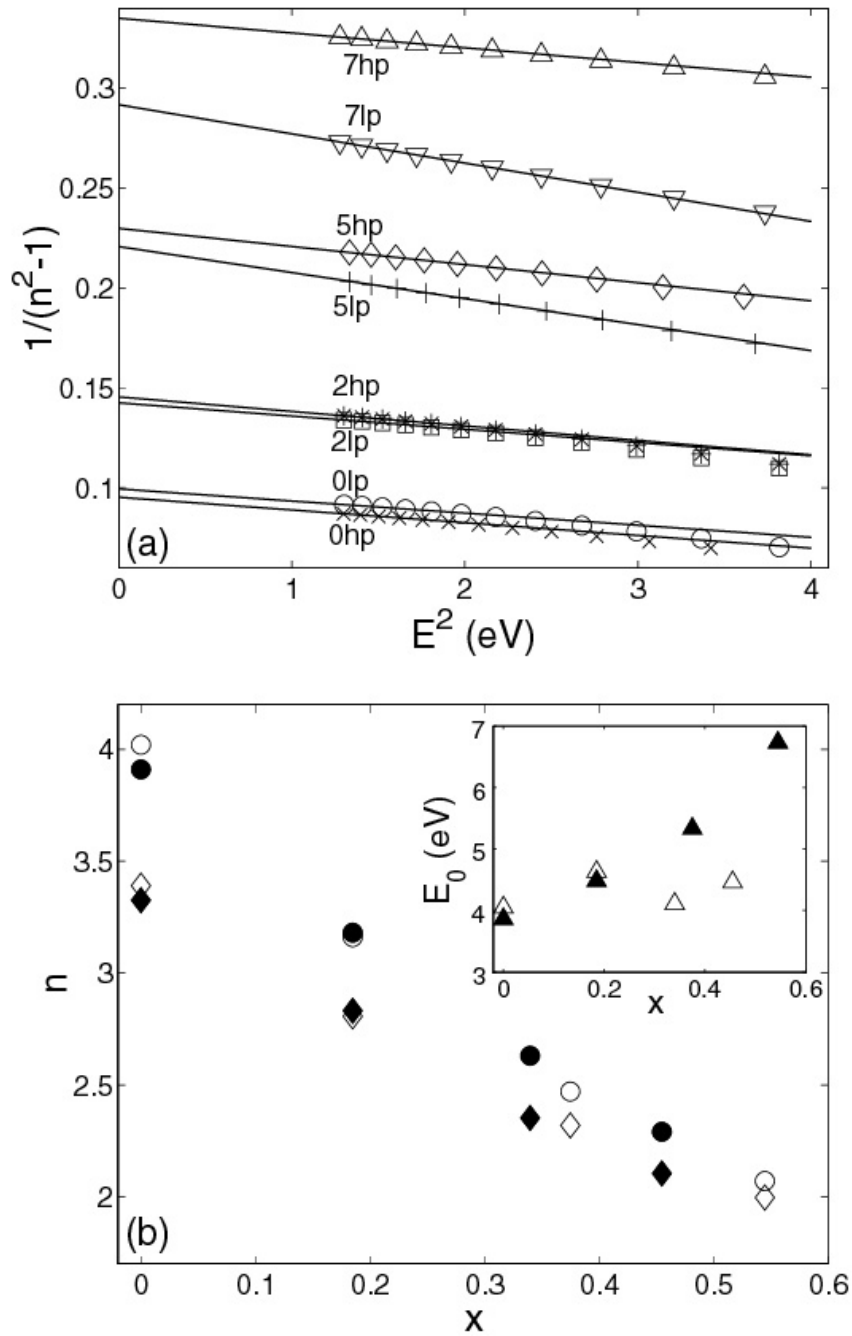


Figure 8.5 (a) $1/(n^2-1)$ is plotted as a function E^2 to determine the static refractive indices $n(E=0)$ of $a\text{-Si}_{1-x}\text{C}_x\text{:H}$ thin films from the intercept of the linear fitting. (b) Refractive indices at both $E=0$ (diamonds) and $E=2$ eV (circles) are plotted as a function of carbon content. The resonance energies found from the fittings are plotted as a function of x as an inset. Full diamonds, circles and triangles denote films produced at high power density whereas the empty markers denote films produced at low power density.

wave functions). In amorphous silicon, the transitions between different parts of the sample, in general, lead to very small transition matrix elements; that's why such transitions are negligible and the spectrum is dominated by both transitions from extended states to extended states and localized states to extended states (or vice versa). On the other hand, the presence of an optical gap in an amorphous carbon (a-C) film requires that the a-C film could not be continuously aromatic (sp^2 like bonded) character but instead it must be built by a random distribution of medium size sp^2 bonded clusters

Dispersion relations of L, ML, FB lead to excessive absorption below the optical gaps of the films. ML model relatively simulates better than L model which is the most deviating model from the data near the absorption edge. In contrast to these models, TL represents the absorption of the films better, that is, it always leads to less absorption than observed one below the optical gap.

The various measures of optical gaps E_g^{Tauc} , E_g^{Cody} and E_{04} , which are defined in Subsection 2.3.3, are plotted as a function of x as shown in Figure 8.7(a). Optical gaps E_g^{Tauc} and E_g^{Cody} increase at low and high power densities as the carbon incorporation in the films increases. However, the rate of increase of the optical gaps of the films grown at low power density is first larger than the ones grown at high power density but it starts to decrease beyond $x \sim 0.35$. The difference between E_g^{Tauc} and E_g^{Cody} is about 0.1 eV for $x=0$ and increases up to about 0.3 eV as x approaches 0.5. Moreover, the difference between E_{04} values of films grown at low power and high power is negligibly small, when it is related to carbon content of the films.

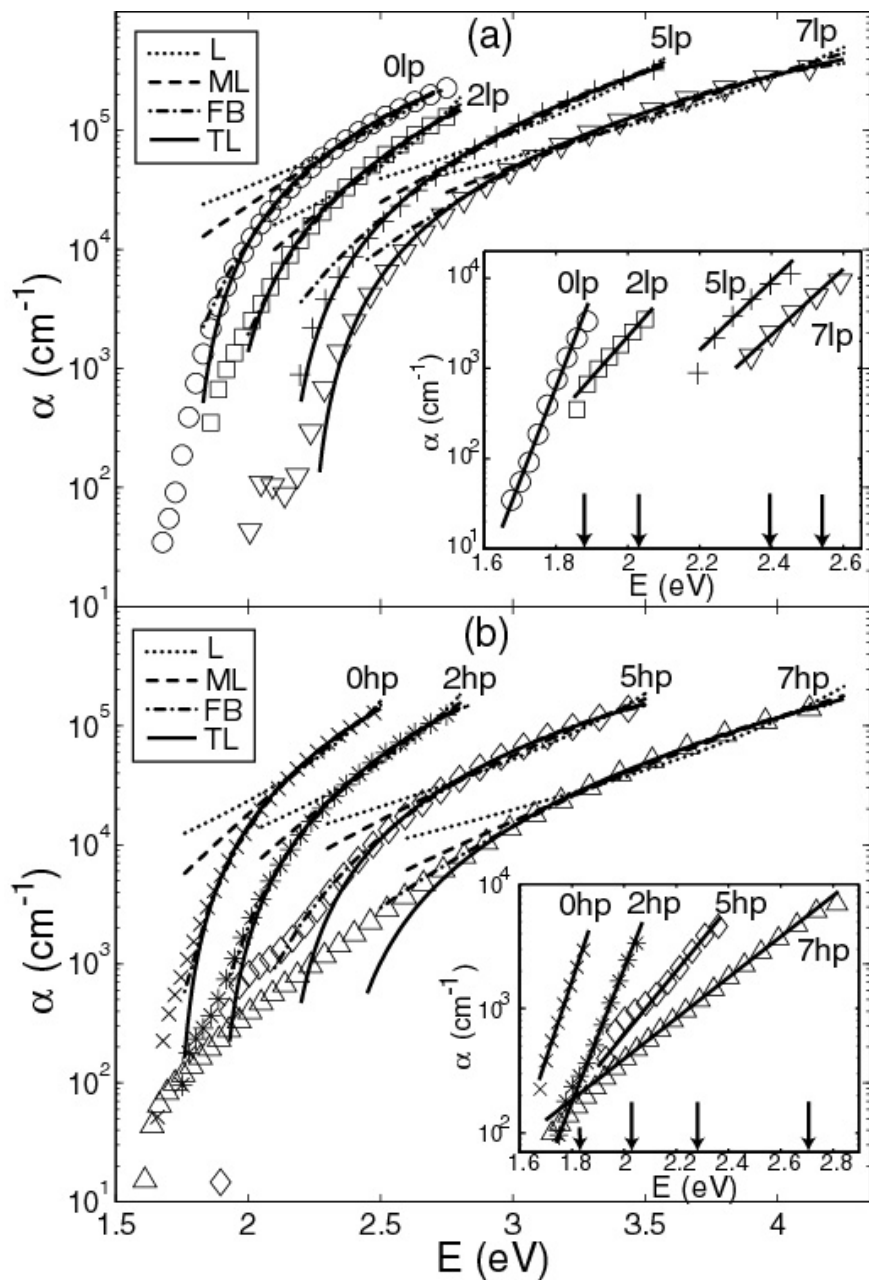


Figure 8.6 Absorption coefficients as a function of energy for $a\text{-Si}_{1-x}\text{C}_x\text{:H}$ thin films grown at (a) low and (b) high power densities together with fittings of dispersion relations of Lorentz (L), Modified Lorentz (ML), Forouhi-Bloomer (FB) and Tauc-Lorentz (TL) models. Close-up drawings of the Urbach edges of the films are plotted as insets where the arrows along the absciss point the corresponding Tauc optical gaps.

The increase in optical gaps as a function of carbon content can be due essentially to increasing number of strong Si-C bonds. However, this factor alone could not explain the whole increase. It should be kept in mind also that part of the increase in optical gap may be resulted from the increased number of Si-H bonds but this last contribution remains limited since in silicon rich alloys, the valence band can be characterized by Si p orbitals and the maximum change of valence band tail upon hydrogenation is about 0.7 eV [216]. Therefore the large increase in optical gaps can not explained solely by hydrogenation either.

The slope parameters B^{Tauc} and B^{Cody} appearing in equations (2.60) and (2.62) are plotted as a function of x as an inset in Figure 8.7(a). B^{Tauc} and B^{Cody} are observed to be decreasing and this behavior is prominent especially for films grown at high power density. B^{Tauc} (B^{Cody}) depends on both the joint density of states and the momentum (dipole) matrix element. This B factor is taken as a measure of the structural disorder, that is, high value of B indicates a smaller degree of structural disorder [217]. According to Mott (215,218), parameter B is inversely proportional to the width of the conduction band tail.

The introduction of the carbon component in structurally disordered a-Si:H alloy increases further the level of disorder due to the eventual contribution of chemical disorder. For relatively low C content ($x < 0.2$), the alloy is observed to be preferring homonuclear bonds. As carbon increases, heteronuclear bonds are dominant [129,216,219].

In the subgap absorption region ($E < E_g$) for both amorphous and crystalline semiconductors, the absorption coefficient $\alpha(E)$ exhibits an exponential variation proportional to $e^{\frac{E}{E_U}}$, as discussed in Section 2.4 (equation (2.53)), with a characteristic energy parameter E_U , called Urbach energy. Although the fundamental basis of this phenomenon is controversial, there has been a considerable theoretical and experimental

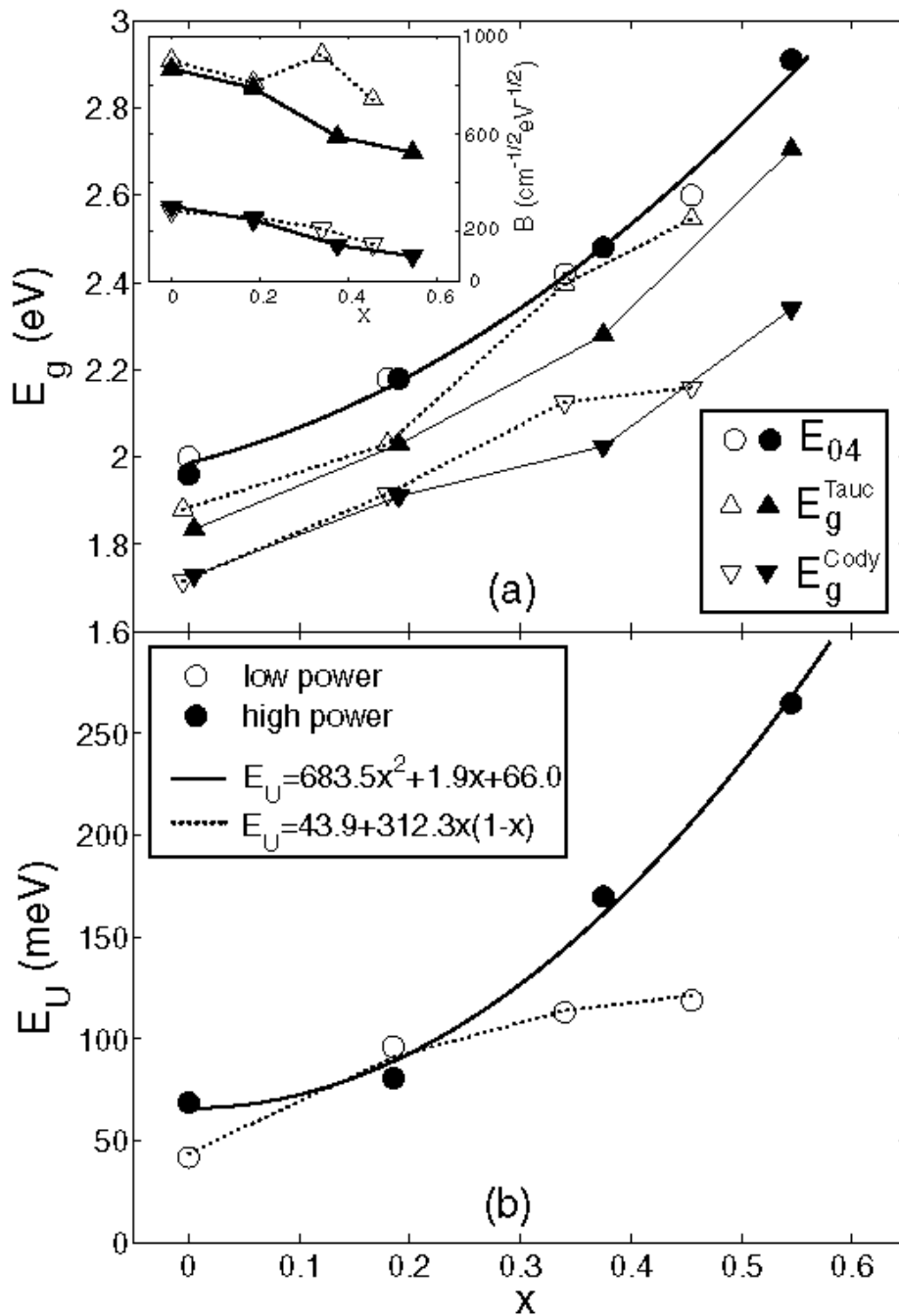


Figure 8.7. (a) E_g^{Tauc} , E_g^{Cody} and E_{04} optical gap values for a-Si_{1-x}C_x:H thin films grown at low (empty markers) and high (full markers) power densities are plotted as function of carbon content x . The variation of slope parameters B^{Tauc} and B^{Cody} are given as an inset. (b) Urbach parameters E_U is plotted as a function of x for both power densities together with suitable representative fittings.

effort to explain the exponential behavior in hydrogenated amorphous silicon (a-Si:H) by exponential behavior of density of states at the valence band. It has not been yet proved that such behavior for a-C is due to the same physical mechanism as in a-Si:H [220]. However, similar microscopic mechanisms generally observed for a-Si:H might be expected to be occurred for silicon rich a-Si_{1-x}C_x:H alloys with $x \leq 0.5$.

In the subgap absorption region ($E < E_g$) for both amorphous and crystalline semiconductors, the absorption coefficient $\alpha(E)$ exhibits an exponential variation proportional to $e^{\frac{E}{E_U}}$, as discussed in Section 2.4 (equation (2.53)), with a characteristic energy parameter E_U , called Urbach energy. Although the fundamental basis of this phenomenon is controversial, there has been a considerable theoretical and experimental effort to explain the exponential behavior in hydrogenated amorphous silicon (a-Si:H) by exponential behavior of density of states at the valence band. It has not been yet proved that such behavior for a-C is due to the same physical mechanism as in a-Si:H [220]. However, similar microscopic mechanisms generally observed for a-Si:H might be expected to be occurred for silicon rich a-Si_{1-x}C_x:H alloys with $x \leq 0.5$.

E_U is proportional to the width of the band tail which is, in turn, a result of disorder and therefore the increase in E_U can be envisaged as the increase in the degree of disorder. Moreover, since valence band tail is generally broader than the conduction band tail, E_U is usually accepted to be representing valence band tail width. The Urbach parameter E_U is observed to increase significantly for films grown at high power as shown in Figure 8.7(b). On the other hand, for the films grown at low power E_U exhibits a sharp increase at low carbon content while it does not significantly change at larger values of x . At low power, this saturation like behavior in E_U suggests interplay between disorders (structural or electronic disorder) and relaxation of the overconstrained network by different configurations of sp , sp^2 and sp^3 bonding configurations. First, E_U may increase due to electronic disorder in the solid but later, as x approaches 0.5 (stoichiometry), solid may start to be consisting of all three types of covalent 2-center hybrid σ -like sp , sp^2 and sp^3 bondings together with π -like

delocalized (or multicenter) bonding which may lead to relaxation of network; or in other words structural disorder may be reduced, leading to steeper Urbach tail [221]. However, as this relaxation occurs (decrease of structural disorder), the number of heteronuclear bonds starts to increase which enhances the electronic disorder due to the greater electronegativity of carbon. It is observed that addition of carbon in the PECVD grown $a\text{-Si}_{1-x}\text{C}_x\text{:H}$ alloys leads to increase in E_U but not considerable change in bond-angle distribution [221]. Therefore, the material is relatively strained at low power. As it seen from Figure 8.7(a), the rate of increase of optical gaps for films grown at low power decreases as x approaches 0.5. In contrast, for the films grown at high power, the increase in the optical gaps becomes stronger as x approaches 0.5 which is similar to the behavior of E_U shown in Figure 8.7(b). In this respect, such a similarity in the behavior of E_g and E_U suggests a linear relationship between them. At low carbon content, the increase in carbon content in the films causes strong fluctuations at the top of the valence band which leads to increase in disorder [222].

For a random-alloying, the probabilities of finding Si-Si, Si-C and C-C bonds in $a\text{-Si}_{1-x}\text{C}_x\text{:H}$ can be given as $(1-x)^2$, $2x(1-x)$ and x^2 , respectively. Complete chemical ordering in a silicon carbon alloy corresponds to a maximum possible number of Si-C bonds in the films with no Si-Si bond for $x \geq 0.5$ (C-rich) and no C-C bonds for $x \leq 0.5$ (Si-rich). In a chemically ordered structure, the probabilities of finding Si-Si, Si-C and C-C for $x \leq 0.5$ become $(1-2x)$, $2x$ and 0 , respectively, whereas for $x \geq 0.5$ the corresponding probabilities become 0 , $2(1-x)$ and $2x-1$, respectively. In the case of phase separation, the probabilities of finding Si-Si and C-C bonds are $(1-x)$ and x , respectively [178]. For a completely random structure, the probabilities of finding Si-Si, Si-C and C-C bonds are x^2 , $2x(1-x)$ and $(1-x)^2$, respectively [216]. It was reported that carbon can be brought into the solid only by a reaction with silicon radical which involves the participation of at least one silicon atom in the low power regime of $\text{CH}_4\text{-SiH}_4$ plasma. Therefore, x is limited in this special case of chemical order, that is, x is always below 0.5 and deposition rate reduces to zero as x reaches 0.5 [179]. In this case, the probabilities of finding Si-Si, Si-C and C-C become $1-x$, x and 0 [178]. On the other hand, potential fluctuations due to carbon incorporation in the film result in

compositional disorder in addition structural and thermal disorder, introduced in Section 2.4 (equation (2.80)). Assuming the distribution of potential fluctuations is Gaussian, Urbach energy E_U can be described by the sum of the variances σ^2 of the potentials:

$$E_U = A \left[\underset{\substack{\text{STRUCTURAL} \\ \text{DISORDER}}}{\sigma_S^2} + \underset{\substack{\text{THERMAL} \\ \text{DISORDER}}}{\sigma_T^2} + \underset{\substack{\text{COMPOSITIONAL} \\ \text{DISORDER}}}{\sigma_C^2} \right] \quad (8.7)$$

If the structural disorder and thermal disorder is assumed to be constant, E_U is only determined by the strength of compositional disorder. Within this approximation, E_U can be given as for an uncorrelated two component alloy, that is, completely random structure [208, 223]

$$E_U = C_1 + C_2 x(1-x) \quad \text{with} \quad C_1 = A(\sigma_x^2 + \sigma_T^2), \quad C_2 x(1-x) = A\sigma_C^2 \quad (8.8)$$

The experimentally determined Urbach parameters of films grown at low power are fitted by equation $E_U = C_1 + C_2 x(1-x)$ as shown in Figure 8.7(b). The contribution of structural and thermal disorder is found to be 43.9 meV. On the other hand, Urbach parameters of films grown at high power can be represented by a function $683.5x^2 + 1.9x + 66$ which can be alternatively written in terms of $(1-x)^2$ and $x(1-x)$. If it is reminded that the factors x^2 , $(1-x)^2$ and $2x(1-x)$ are bond probabilities for a completely random structure, it can be suggested that the films grown at high power involves C-C bonds. In contrast to low power case, potential fluctuations due to presence of C-C bonds can be seen as a source of disorder in addition to the one due to Si-C bonds.

8.3.4 Reflectance and Ellipsometry analysis of the films

Reflectance spectra of the a-Si_{1-x}C_x:H thin films are obtained by using the reflectance unit which is illustrated as an inset in Figure 5.4. Tauc-Lorentz (TL) dispersion relations are preferred in the analysis of the reflectance spectra because it is

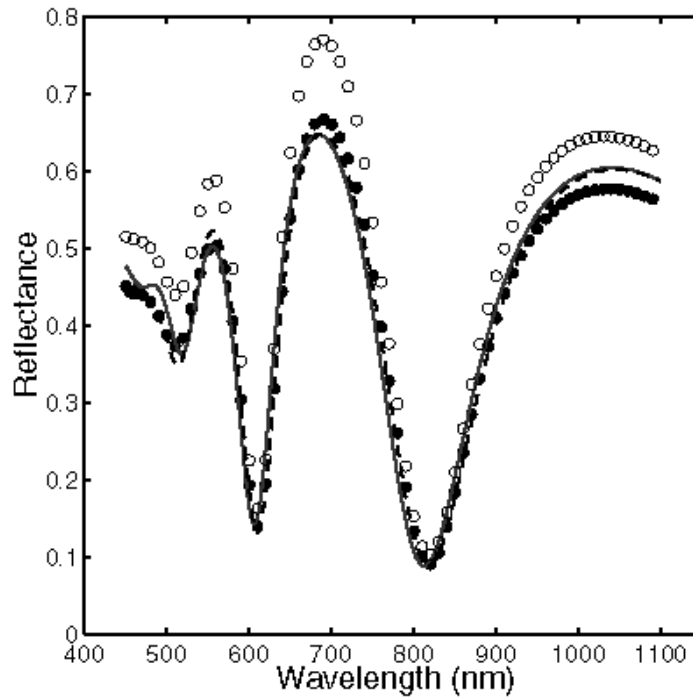


Figure 8.8 Reflectance spectrum (open circles) of the sample 0lp is normalized (full circles) by a common factor for all samples. Solid line denotes the reflectance spectrum simulated by using the optical constants obtained from the analysis of transmittance spectrum. Dashed line denotes the fitting of TL dispersion relations to the normalized reflectance spectrum (full circles) and single wavelength ellipsometry.

observed that they represent the refractive indices and absorption coefficients of the films relatively better than the others given in Section 7.2 and do not violate the fundamental physical constraints. However, all the fittings of the reflectance spectra by the TL model simulate poorly the reflectance spectra of all films, and result in lower thicknesses and higher refractive indices in comparison to the results of transmittance measurements given previously in this chapter. In order to solve this problem, the reflectances of the films are simulated by using the optical constants obtained from the transmittance measurements to compare with the reflectance measurements. It is found that the reflectance spectra of the films are all observed to shift upwards (to higher intensities) systematically for all the films. Then, it is realized that this is not a shift but

rather a multiplication of intensities by a wavelength dependent common factor which is more or less valid for all reflectance spectra. An example of such a spectrum is shown for the sample 0lp in Figure 8.8 and the equivalent spectra for the rest of the samples are given in Appendix D. As the measured reflectances of the films multiplied with the common factor the reflectance spectra of the films (normalized or corrected spectra) are found to be approximately in agreement with the simulated reflectance spectra as shown for sample 0lp in Figure 8.8.

Prior to the measurement of the reflectance of the sample at hand, the reflectance of the calibrating mirror is measured to determine the background radiation and the reflected intensity at all wavelengths is calibrated as 100% reflectance. This measured quantity, called the baseline signal, is used as reference for subsequent measurements on samples. The reflected intensity is expected to be overestimated if the baseline signal is underestimated. For example, if the quality of mirror is degraded and consequently, some of the intensity of the reflected light is lost upon reflection on the mirror, the baseline signal is expected to be decreased. In this respect, the amplification of the reflectance spectra by a common fraction of intensity for all films can be explained by the shift in the baseline signal and the source of such a systematic error is probably due to the mirror used for calibration. It should be noted that this kind of systematic error might be due to instability of light source, but this possibility is eliminated from consideration because there is no observed systematic error in the intensities of transmission measurements.

Single wavelength ellipsometry measurements at a wavelength of 632.8 nm on the previously described a-Si_{1-x}C_x:H thin films are performed at least 9 different angle of incidences by using the setup introduced in Section 5.3. The normalized reflectance spectra (denoted by full circles in Figure 8.8) and ellipsometric angles of the samples are simultaneously fitted by TL dispersion relations. The resulting fitted reflectance (denoted by dashed lines) by TL dispersion relations for sample 0lp is shown in Figure 8.8 and is in agreement with the simulated reflectance (denoted by solid line) by using the optical constants obtained by the transmittance measurements. The measured

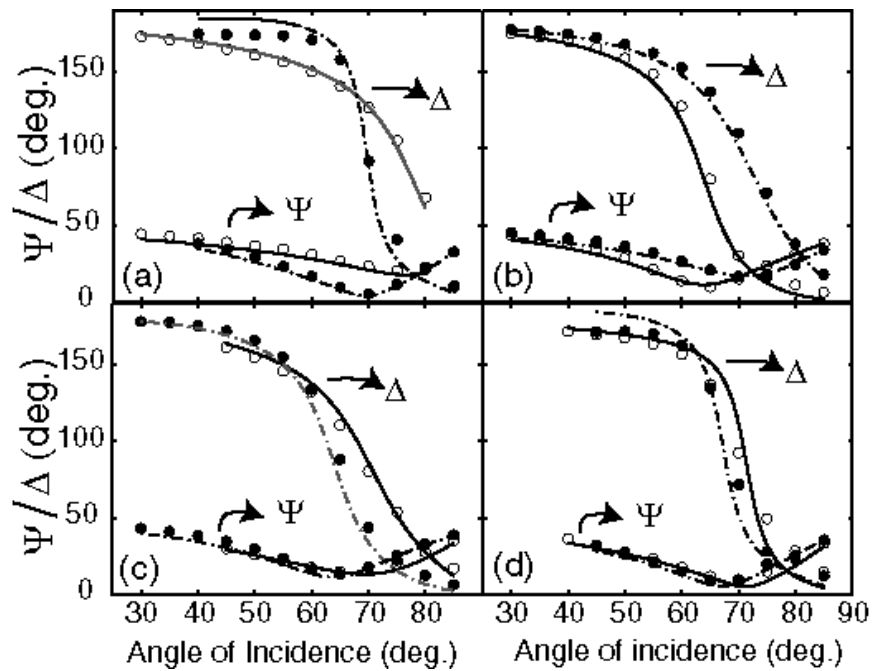


Figure 8.9 Measured ellipsometric angles ψ and Δ of samples (a) 0lp, 0hp; (b) 2lp, 2hp; (c) 5lp, 5hp; (d) 7lp, 7hp. The solid and dash-dot (-.) lines denote the fitting results of the normalized reflectance and ellipsometry angles simultaneously of films grown at low power (empty circles) and high power (full circles), respectively.

ellipsometric angles ψ and Δ of the samples together with the fitting results are shown in Figure 8.9.

The retrieved refractive indices and absorption coefficients of $a\text{-Si}_{1-x}\text{C}_x\text{:H}$ thin films from reflectance and ellipsometry measurements are plotted as a function energy in Figure 8.10. The results are in agreement with transmittance measurement results. However, disagreement of refractive indices obtained by two approaches at energies greater than the optical gaps of the films might be an expected result because at those energies transmittance is determined mainly by absorption coefficient. Therefore, refractive indices might be overestimated at high energies. As the optical gap increases, the energy interval where refractive indices obtained by two approaches are in

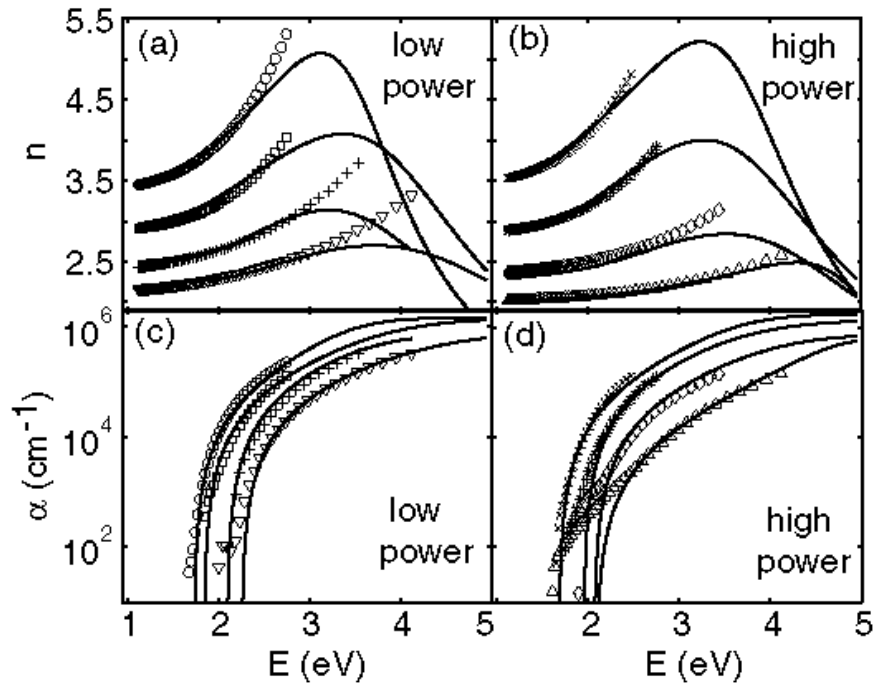


Figure 8.10 Comparison of optical constants obtained from transmittance and reflectance/ellipsometry measurements. Solid lines denote the optical constants retrieved by fitting the normalized reflectance spectra and single wavelength ellipsometry results simultaneously. Circles, squares, pluses, reverse triangles, crosses, stars, diamonds, triangles denote optical constants (Figures 8.4 and 8.6) of the samples 0lp, 2lp, 5lp, 7lp, 0hp, 2hp, 5hp and 7hp, respectively, obtained from the transmittance measurements.

agreement widens. The thicknesses obtained from the fitting of normalized reflectance and ellipsometry measurements are given in Table 8.3.

Table 8.3 Table of thicknesses of samples obtained by fitting the normalized reflectance and single wavelength ellipsometry measurements simultaneously by TL dispersion relations.

Sample	0lp	0hp	2lp	2hp	5lp	5hp	7lp	7hp
d(nm)	228.2	634.6	509.1	538.9	227.3	725.3	243.3	749.4

8.3.5 FTIR spectroscopy analysis of the films

The IR spectra of the a-Si_{1-x}C_x:H thin films are shown in Figures 8.11 and 8.12 for 3 main absorption bands observed in the wavenumber ranges of 500-1500 cm⁻¹, 1900-2200 cm⁻¹ and 2800- 3000 cm⁻¹. Since each band consists of different vibration modes summarized in Table 8.4, they are deconvoluted as shown in Figures 8.11 and 8.12.

It is clearly seen that absorption peaks beyond 700 cm⁻¹ start to appear for both power densities as carbon is incorporated in the films. Especially, the concentration of the vibration mode at about 770 cm⁻¹ (area under this peak) increases as x increases as shown in Figure 8.13(a). Although the position of this peak does not change for films grown at low power density, it is observed a linear increase for films grown at high power density in the range of 763-778 cm⁻¹. The concentrations of this mode for films grown at high power density are always larger than the ones for films grown at low power density. This is almost agreement with the results of Ambrosone *et al.* who observed all absorption modes between 600 cm⁻¹ and 1000 cm⁻¹ to be increasing with rf power [224-225] although this increase is clearly apparent for our films only at 770 cm⁻¹. However, the FWHM values at this frequency are found to be not much differing for both power densities but increases from about 90 cm⁻¹ to 180 cm⁻¹ as carbon is incorporated in the film. The FWHM of this peak is thought mainly correlated to the angular distortion of atomic bonds. It is reported in the literature for unhydrogenated amorphous silicon carbon alloys, an angular spread of 25° and 22° around the bond angle of 109.5° between neighboring atoms corresponds to FWHM values of 245 cm⁻¹ (stressed amorphous) and 220 cm⁻¹ (fully relaxed), respectively [238]. In light of this information the angular distortion of bonds in our films may be interpreted as smaller than the one in unhydrogenated a-Si_{1-x}C_x thin films due to the relaxation role of hydrogen.

Table 8.4 Assignments of absorption peaks in FTIR spectra of a-Si_{1-x}C_x:H thin films.

Peak No:	Wavenumber (cm ⁻¹)	Bond type and mode of vibration
P1	640	Si-H, Wagging [157, 200, 216]
P2	670	Si-H _n Wagging [226, 227-229, 215] Si-C Stretching [230, 229,215, 233]
P3	770	Si-C Stretching [226, 237, 231, 227, 162, 232, 157, 216] Si-CH ₃ Rocking and/or Wagging [227, 229, 215, 233, 162, 232]
P4	850-900	(Si-H ₂) _n Bending [215, 234, 216]
P5	1000	C-H _n Wagging and/or rocking [226, 227, 229, 215, 231, 157, 216]
P6	1245	Si-CH ₃ , Bending (symmetric) [215, 233, 234, 157]
P7	1350	Si-CH ₃ , Bending (asymmetric) [215, 233] C-H ₂ Wagging [215]
P8	1400	C-H ₂ , Bending, Scissoring [215]
P9	2000	Si-H, Stretching [227, 229, 233, 235, 234, 216]
P10	2090 2060-2100	Si-H ₂ , Stretching [227, 226, 229, 235, 234] CSi-H, Stretching [226, 227, 229, 233, 235, 234]
P11	2150	CSi-H ₂ , Stretching [234, 236]
P12	2800	C-H, Stretching [226, 215, 234, 216]
P13	2850	C-H ₂ , Stretching (symmetric) [226, 215, 237, 232, 157]
P14	2880	C-H ₃ , Stretching (symmetric) [226, 215, 233, 237, 162, 232]
P15	2910	C-H ₂ , Stretching (asymmetric) [226, 215, 233, 237, 232]
P16	2950	C-H ₃ , Stretching (asymmetric) [226, 215, 233, 237, 162, 232]
P17	2970	C-H, C-H ₂ , Stretching (sp ²) [232]

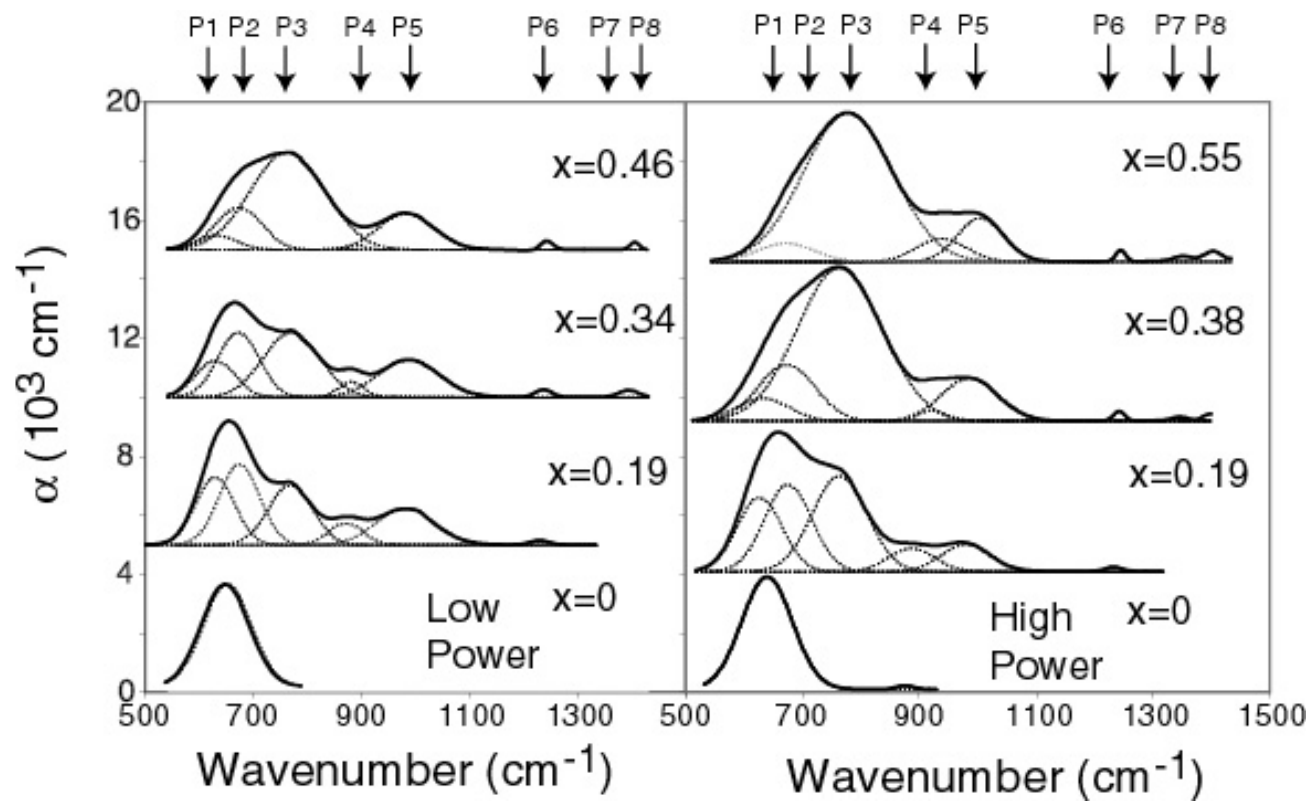


Figure 8.11 First IR absorption band of $a\text{-Si}_{1-x}\text{C}_x\text{:H}$ thin films grown at low and high power with deconvolutions of the peaks according to the assignments given in Table 8.4

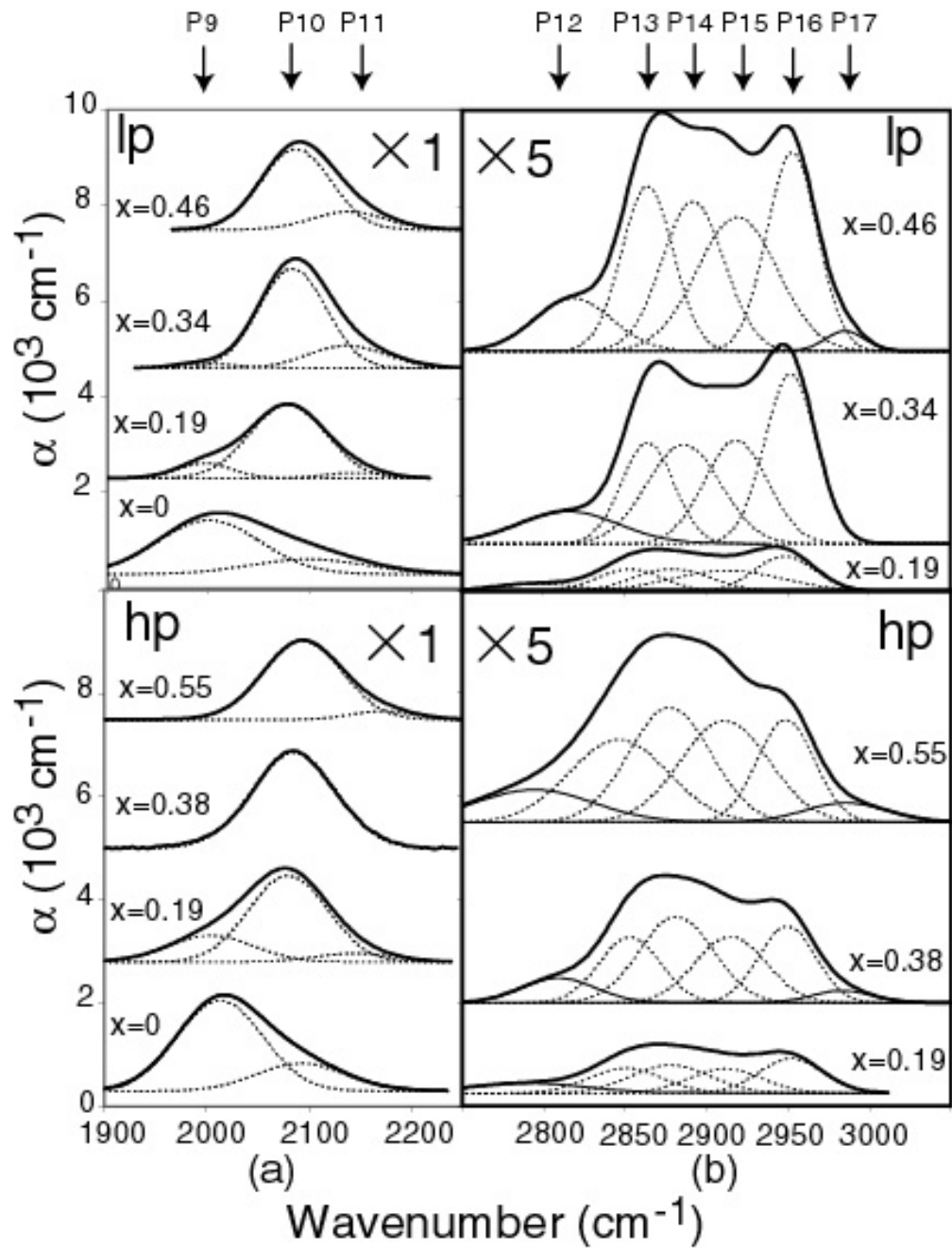


Figure 8.12 Second (a) and third (b) IR absorption bands of $a\text{-Si}_{1-x}\text{C}_x\text{:H}$ thin films grown at low and high power with deconvolutions of the peaks according to the assignments given in Table 8.4.

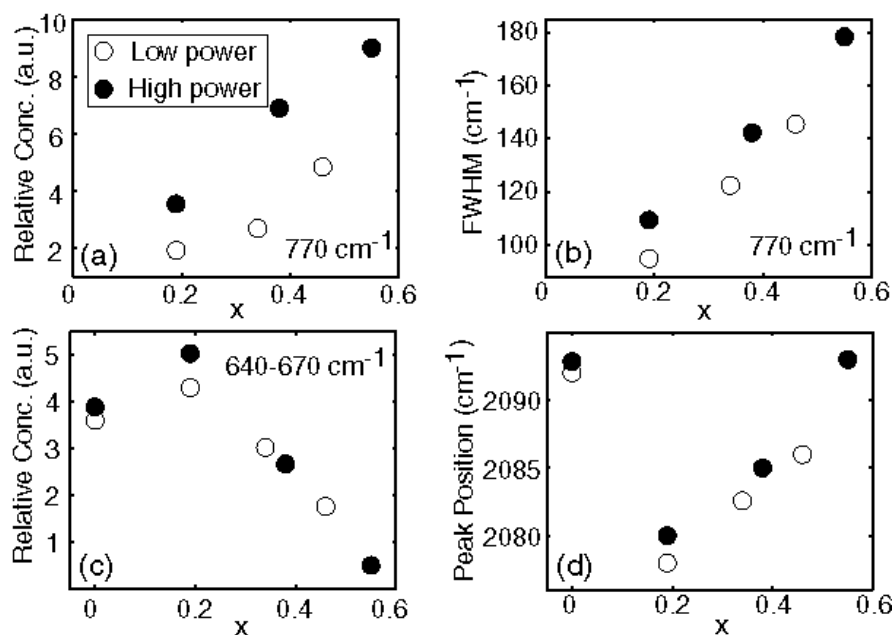


Figure 8.13 The change of peak parameters as a function of carbon content in $a\text{-Si}_{1-x}\text{C}_x\text{:H}$ thin films. (a) the concentration of the vibration mode at about 770 cm^{-1} , (b) FWHM of the absorption peak at 770 cm^{-1} , (c) the sum of concentrations of vibration modes at about 640 and 670 cm^{-1} , (d) peak position of Si-H stretching mode at 2090 cm^{-1} .

The concentration of Si-H wagging mode at a wavenumber of about 640 cm^{-1} reported for $a\text{-Si:H}$ thin films generally decreases and becomes zero as x increases. This behavior may misleadingly be envisaged as an elimination of Si-H bonds in the film structure although such a strong elimination is not observed for their stretching modes at wavenumbers of about $2000\text{-}2150\text{ cm}^{-1}$. On the other hand, the peaks seen at around 670 cm^{-1} involving Si-H_n and Si-C vibration modes are observed to be decreasing as x increases. In this respect, this peak is thought to represent only Si-H_n bonds whose frequency would be shifted from 640 cm^{-1} to 670 cm^{-1} due to replacement of Si neighboring atoms with carbon atoms as their content in the films increases. Therefore, the sum of the concentrations of these two peaks are given in the Figure 8.13(c) where their sum reflects similar character to the total concentration of Si-H stretching modes at about 2000 cm^{-1} . The above interpretation denies the widely adopted assignment of 670

cm^{-1} peak to the Si-C stretching mode whose concentration should have risen when x increases.

The amplitudes, positions and FWHM values of absorption bands at about 980 cm^{-1} for films grown at low power do not change apparently. In addition, the peaks at about 1245 cm^{-1} , 1350 cm^{-1} and 1400 cm^{-1} are not appreciably strong and mutual comparison is difficult. However, it is observed that there is no absorption detected at about 1350 cm^{-1} for films grown at low power in contrast to the films grown at high power with $x=0.38$ and $x=0.55$. The weak nature of bands seen at about 1245 cm^{-1} and 1350 cm^{-1} suggests that the absorption mode at about 770 cm^{-1} can be assigned solely to S-C stretching modes. It should be noted that the absorption band at $1200\text{-}1400 \text{ cm}^{-1}$ is observed to be decreasing with H_2 dilution [136].

Let's examine the second absorption band at about $2000\text{-}2100 \text{ cm}^{-1}$ which represents mainly Si-H and Si-H₂ stretching modes. The absorption peak at 2000 cm^{-1} assigned to the Si-H stretching mode disappears as carbon is incorporated in the films. In addition, the peaks at about 2090 cm^{-1} are substantially present in the films grown at both low and high power for all carbon contents. The replacement of Si neighbors with more electronegative carbon atoms might lead to an increase in the frequency of Si-H stretching mode from 2000 cm^{-1} towards 2070 cm^{-1} depending on the number of carbon atoms bonded to Si of Si-H bond. This effect is clearly seen in the Figure 8.13(d) as a shift from 2078 cm^{-1} to higher frequency of 2092 cm^{-1} as a function of carbon content [235], without any appreciable change in their FWHM values. In other words, the reduction in the length of Si-H bond due to the higher electronegativity of carbon results in an increase in the vibration frequency of this bond. On the other hand, the concentration of this peak reaches its maximum value at about $x\sim 0.35$, similar to the results of Chew *et al.* where they found the intensity of this peak is strongest at intermediate x [239]. The broad absorption peak around 2150 cm^{-1} might correspond to shifted frequency of Si-H₂ stretching mode (whose original frequency is about 2090 cm^{-1} observed in the films without carbon). In this respect, these peaks might shift to higher wavenumbers as carbon is incorporated in the films and their FWHM values do not

differ much. Finally, most of the hydrogen atoms are bonded to silicon in the form of monohydride Si-H and their concentration goes through maximum at about $x \sim 0.35$; besides, a general decrease in hydrogen content is observed as power increases.

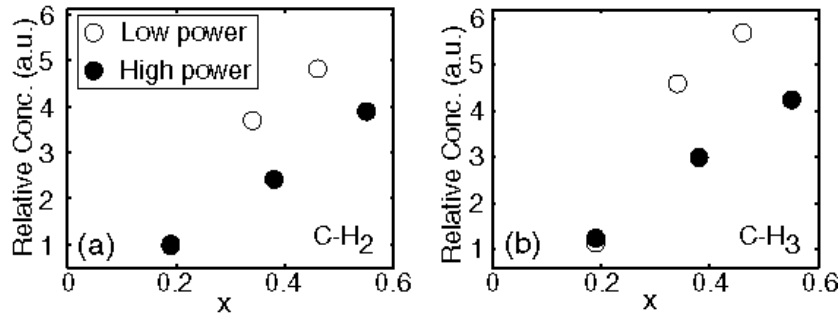


Figure 8.14 Sum of the relative concentrations of symmetric and asymmetric stretching modes of (a) C-H₂ and (b) C-H₃ bonds.

The absorption band between wavenumbers of about 2800-3000 cm^{-1} shown in Figure 8.12 is assigned to C-H_n ($n=1,2$ or 3) stretching vibration modes for films with $x > 0$. Since the frequencies of stretching modes are not mixed with other modes of vibrations in the region of 600-1000 cm^{-1} , the area of peaks may reflect the density of C-H_n bonds similar to stretching modes of Si-H_n bonds in a-Si:H films. Here, the small peaks at around 2800 cm^{-1} and 2970 cm^{-1} attributed to sp^3 type C-H bond and sp^2 type C-H_n ($n=1,2$) bonds, respectively, have the same character as other type of bonds, C-H₂ and C-H₃. However, they are not considered in the analysis of relative concentration due to their weak intensity makes them difficult to distinguish from background absorption, especially for films with low carbon content.

The dominant peaks in the region between 2850-2950 cm^{-1} are deconvoluted into four peaks as expected from peak assignments given in Table 8.4. The amplitude of all peaks increase with a little change in their frequencies and almost no change in their FWHM values as x increases. In order to see the change in concentration C-H_n ($n=2,3$) bonds, symmetric and asymmetric absorption peak intensities of each bond type are

added up and results are given in Figure 8.14. It is clear in the Figure 8.14 that concentration of both C-H₂ and C-H₃ bonds increases as x increases. Especially, a sharp increase in the concentration of C-H₃ is found as x changes from 0.2 to 0.4. It is also clear from the Figure 8.14 that the concentration of C-H₃ is observed to be always greater than that of C-H₂ whereas their ratio is lowered for the films prepared by high power opposed to Si-H bonds in a-Si:H. Additionally, in contrast to increase of carbon content as power increases, relative concentration of hydrogen atoms bonded to carbon decreases which reveals the reduction of hydrogen content as power increases. This might be due to the high dissociation of mixture of source gases (SiH₄ and C₂H₄) in the plasma which usually results in observation of linear dependence of film composition on gas flow ratio M [214]. As a result, most of the hydrogen atoms incorporated in the structure have sp³ type C-H₂ and C-H₃ bonds and concentration of sp³ type C-H and C-H₂ bonds reduces at high power.

The peak at about 3000 cm⁻¹ is attributed to sp² C-H₂ stretching mode. This peak at low power appears only for x=0.46. As for the high power case, this peak appears for both x=0.38 and 0.55. Its concentration increases as x rises. This behaviour might be interpreted by the enhanced dissociation rate of radicals which promotes formation of aromatic clusters in the plasma leading to sp² type bonds in the film structure.

8.4 Conclusion

Eight a-Si_{1-x}C_x:H samples are produced with different carbon concentrations at two different power densities and analyzed with transmittance, reflectance, ellipsometry and FTIR measurements. The effects of carbon content and power density on the refractive index, optical gap, Urbach parameter and bonding configurations are assessed in the frame of possible deposition mechanisms. Reflectance spectra of the films are suffered from a systematic error occurred in the measurements and are corrected by multiplying the reflection intensities with a common wavelength dependent factor. The optical constants obtained from transmission measurements and reflectance/ellipsometry measurements are quite in agreement.

CHAPTER 9

EFFECTS OF DOPING ON THE OPTICAL CONSTANTS OF SILICON BASED AMORPHOUS THIN FILMS

9.1 Introduction

Dual dopability (both n and p type) of a semiconductor is an indispensable requirement for the production of p-n (or p-i-n) junction which is the building stone of modern (opto)electronics. Without this achievement, a semiconductor remains a mediocre material with restricted application.

Among various advantages of silicon based alloys, the possibility of dual dopability renders this family of amorphous semiconductors, in the “state” of thin solid films, basic materials for large area optoelectronic applications. However, the intentional electrical conductivity modulation of these materials by foreign atom doping although feasible, seems a very complex process. Generally, in amorphous material, there is no rigidly defined site, on the contrary of crystalline case, such that an impurity atom can adapt itself to local environment to optimize its own bonding following the N/8-N rule [240]. This suggests that the conventional dopants for the crystal Si (phosphorus for n-type, boron for p-type) should be three-fold coordinated in amorphous medium and therefore they are mainly inactive as electronic dopants; in other words, actually is not forbidden but severely limited. That is, as a partial derivation from N/8-N rule, a small fraction of dopant concentration might have four-fold coordination leading to a doping site. This tetrahedral sp^3 configuration whose formation energy is too high, might be energetically slightly favored only in the presence of a charge compensating deep state capturing the anti-bonding electron of the donor or transferring electron to the bonding

acceptor. This does not mean that this dopant defect pair is necessarily on adjacent sites. They may be very distant from each other, but they may interact with the charge carrier distribution (Fermi sea) whose energy is defined by the Fermi energy E_F . This carrier exchange with the Fermi sea modifies the relative position of E_F within the pseudo gap, by the way doping effect is resulted.

The above outline carries out the complexity of the doping mechanism without mentioning the indispensable effect of hydrogenation which transforms the mediocre non-dopable pure amorphous material into a relatively dopable one by enormously reducing (over 10^5 times) the dangling bond based deep states [2].

It is reasonable that the eventual doping mechanism(s) is expected to be much more complex in silicon based alloys such as a-SiC_x:H. The doping process of silicon based amorphous thin solid films alloys grown by PECVD has been intensively attempted in the Solid State Electronic Laboratory (Phys. Dept.-METU). But in this chapter only optical characterizations of some such doped films in comparison with the non-doped ones are undertaken as a brief survey.

A variety of diagnostic measurements are performed to determine and control different properties of these films. Some measurements techniques may be considered as complementary, revealing different aspects of the films whereas some others may be used for confirmation purposes. In addition to the previously presented optical techniques, spectroscopic ellipsometry, atomic force microscopy and x-ray photoemission spectroscopy measurements are performed in Chemistry Department of University of North Carolina at Chapel Hill under the kind hospitality of Prof. Eugene A. Irene.

9.2 Preparation of Samples

Films are deposited on glass and silicon substrates. UV-VIS transmittance and reflectance measurements are performed on thin films grown on glass substrates whereas

thin films grown on crystalline silicon substrates are used for spectroscopic ellipsometry, atomic force microscopy, Fourier transform infrared spectroscopy and x-ray photoemission spectroscopy measurements. Deposition parameters of the thin films are given in Table 9.1.

Table 9.1. Deposition parameters such as doping ratios ($M_B = B_2H_6/SiH_4$, $M_P = PH_3/SiH_4$), relative gas concentration of the C_2H_4 ($M_{C_2H_4} = C_2H_4/(C_2H_4+SiH_4)$), total gas flow rates (F), pressure (p), substrate temperature (T) and power density (P) for eight different depositions.

Sample	Undoped	B ₂ H ₆ doped	Undoped	B ₂ H ₆ doped	PH ₃ doped
	a-Si:H	(p-type) a-Si:H	a-SiC _x :H	(p-type) a-SiC _x :H	(n-type) a-SiC _x :H
M_B	0	0.01	0	0.01	0
M_P	0	0	0	0	0.01
$M_{C_2H_4}$	0	0	0.5	0.16	0.16
F_{SiH_4} (ccm)	30	6	30	15	15
$F_{C_2H_4}$ (ccm)	0	0	30	3	3
$F_{B_2H_6}$ (ccm)	0	60*	0	180*	0
F_{PH_3} (ccm)	0	0	0	0	180*
p (Torr)	0.3	0.3	0.1	0.5	0.5
P (mW/cm ²)	15	20	60	60	60
T (C°)	250	250	250	250	250

*inside 1000 ppm hydrogen.

9.3 UV-VIS Transmittance and Reflectance Analysis

Figure 9.1(a) shows the spectral dependence of refractive indices of a-Si:H and a-Si:C_x:H films deposited on glass substrates. It is observed that undoped a-Si:C_x:H thin film has small refractive index values ($\approx 2.00-2.25$ in most of the spectra) in comparison to other films. The refractive indices for a-Si:H thin films are observed to be more dispersive than a-SiC_x:H thin films. While B₂H₆ doped a-Si:H exhibits a similar refractive index to B₂H₆ doped a-SiC_x:H thin film in the large wavelength part of the

spectrum, its refractive indices start to approach the refractive index values of PH_3 doped $\text{a-SiC}_x\text{:H}$ film. The decrease in refractive index values of undoped $\text{SiC}_x\text{:H}$ can be attributed to the larger atomic carbon concentration since C_2H_4 gas ratio for undoped $\text{SiC}_x\text{:H}$ is more than three times larger than the p-type and n-type $\text{a-SiC}_x\text{:H}$ thin films. Refractive indices of B_2H_6 doped a-Si:H are found to be much smaller than the undoped a-Si:H . Similarly, Srinivasan *et al.* observed a sharp decrease in refractive index values of undoped a-Si:H as the film is sufficiently boron doped [241]. Such a reduction of refractive indices may not be explained solely by boron doping because it is observed that an increase in hydrogen content may result in the reduction of refractive indices. However, D. Jousse *et al.* did not observe a correlation between hydrogen content and gas phase boron doping concentration [242].

Figure 9.1(b) shows the spectral dependence of absorption coefficient of the films. The thicknesses, optical gaps E_g^{Cody} and E_{04} (defined in subsection 2.3.3) obtained from the analysis of reflectance and transmittance measurements are given in Table 9.2. Undoped $\text{SiC}_x\text{:H}$ thin film has the largest band gap E_{04} confirming that it has large carbon atomic concentration. While B_2H_6 and PH_3 doped $\text{a-SiC}_x\text{:H}$ samples have almost the same E_{04} values, B_2H_6 doped a-Si:H has a larger E_{04} value than undoped a-Si:H .

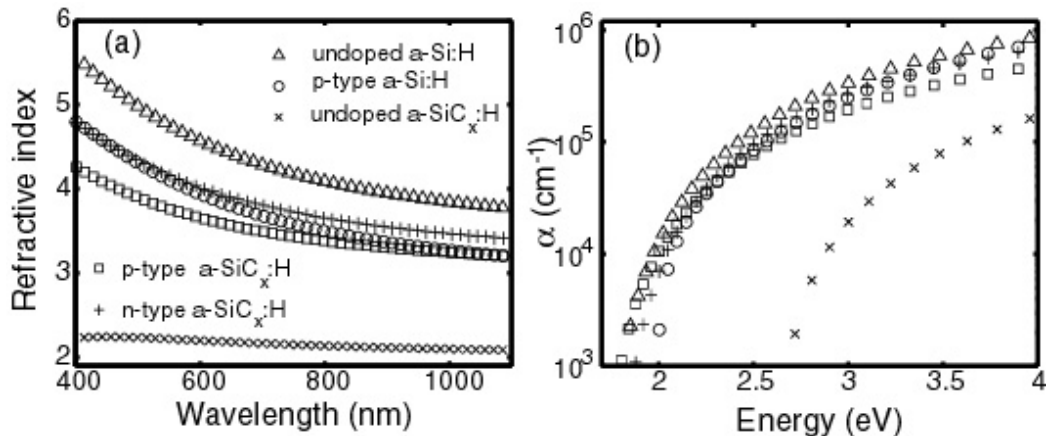


Figure 9.1 (a) Spectral dependence of refractive index n and absorption coefficient α for undoped a-Si:H , B_2H_6 doped a-Si:H , undoped $\text{a-SiC}_x\text{:H}$, B_2H_6 doped $\text{a-SiC}_x\text{:H}$ and PH_3 doped $\text{a-SiC}_x\text{:H}$ thin films, obtained from transmittance and reflectance measurements.

Table 9.2. Optical gaps E_g^{Cody} , E_{04} and film thicknesses d_l calculated from transmittance and reflectance measurements. Thicknesses d_l (bulk layer) and d_2 (roughness layer) of the films calculated from spectroscopic ellipsometry measurements

Sample	Undoped a-Si:H	B ₂ H ₆ doped a-Si:H	Undoped a-SiC _x :H	B ₂ H ₆ doped a-SiC _x :H	PH ₃ doped a-SiC _x :H
E_g^{Cody} (eV)	1.75	1.78	2.52	1.70	1.80
E_{04} (eV)	1.97	2.07	2.87	2.00	2.05
d (nm)	142	66	106	262	206
d_l (nm)	-	89.1	-	289.6	243.0
d_2 (nm)	-	6.6	-	4.3	3.7
x			0.45-0.55	0.05-0.15	0.05-0.15

Optical gaps E_g^{Cody} of the films are determined by plotting the square root of the imaginary part of the dielectric function ($\epsilon_2^{1/2}$) as a function of energy as shown in Figure 9.2. E_g^{Cody} values are about 0.2 eV is less than the E_{04} values. J. Ristein *et al.* showed for a-Si:H films that the E_{04} values and hydrogen content exhibit similar behaviors as a function of boron source gas concentration [243]. Therefore, the increase in E_{04} for B₂H₆ doped a-Si:H suggests an increase in hydrogen concentration. Carbon content x of the films are estimated from Table 8.2 and are given in Table 9.2.

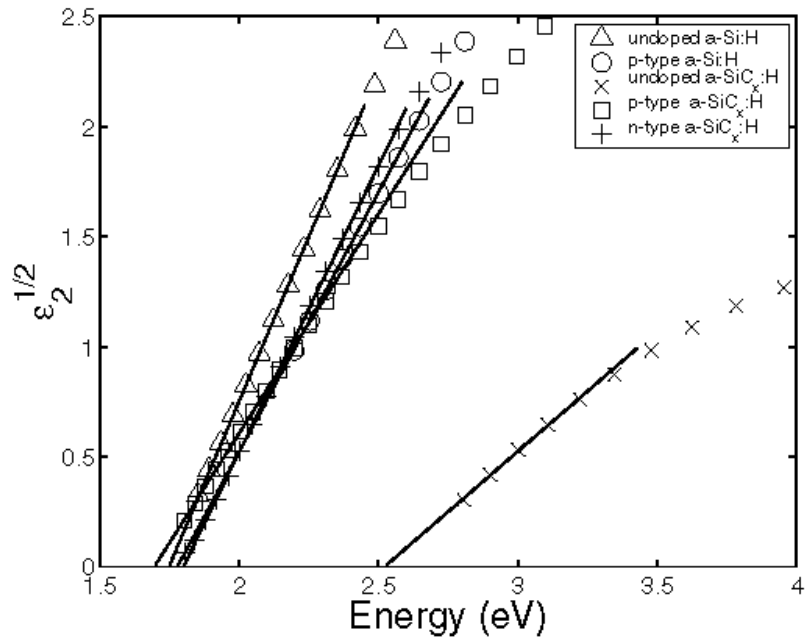


Figure 9.2 Determination of optical gaps E_g^{Cody} of the films by fitting $\epsilon_2^{1/2}$ to a linear function and extrapolating to $\epsilon_2^{1/2} = 0$.

9.4 Spectroscopic Ellipsometry Analysis

Spectroscopic ellipsometry measurements were performed with the experimental setup given in Section 5.4. The angle of incidence is chosen as 70° . Real and imaginary parts of the pseudodielectric functions ($\epsilon = \epsilon_1 - i\epsilon_2$) of the B_2H_6 doped a-Si:H, undoped a-SiC_x:H, B_2H_6 doped a-SiC_x:H and PH_3 doped a-SiC_x:H thin films, grown on <100> s-Si substrates, are derived from the measured ellipsometric angles ψ and Δ by means of a two-phase model (substrate/ambient) and plotted as a function of energy in Figure 9.3.

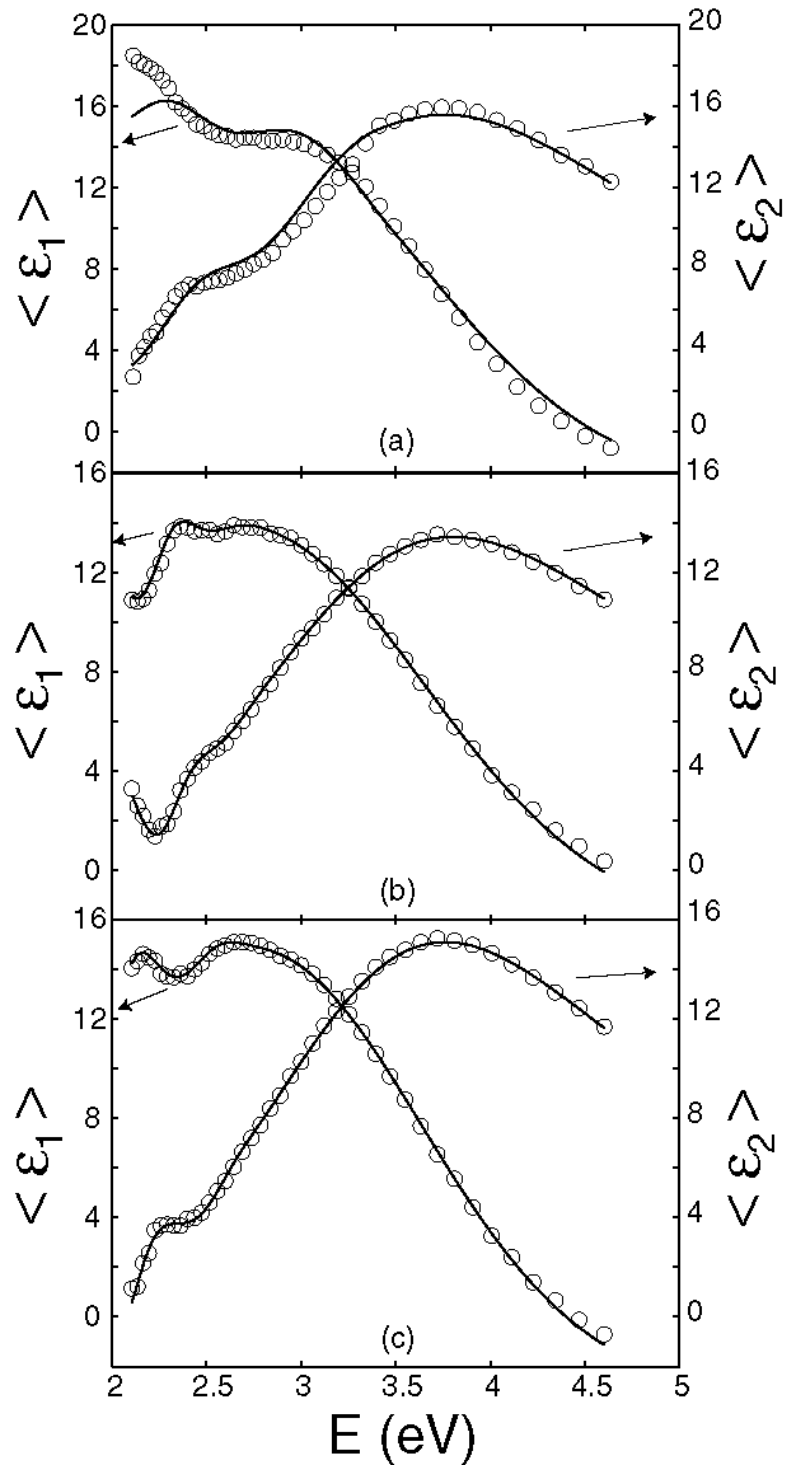


Figure 9.3 Real and imaginary parts of the pseudodielectric functions ($\varepsilon = \varepsilon_1 - i\varepsilon_2$) of the (a) B_2H_6 doped a-Si:H, (b) B_2H_6 doped a-SiC_x:H and (c) PH_3 doped a-SiC_x:H thin films (circles) together with the fitting results (solid lines).

As the films are deposited in PECVD reactor and taken out to air, they eventually become oxidized at the room atmosphere. Therefore a thin native oxide layer is expected on the surface of all films. Generally expected thickness of a native oxide on a crystalline silicon substrate is about 3 nm [244]. However, a-Si:H is known to be more resistive against oxide formation than crystalline silicon. It is reported that thickness of native oxide on a-Si:H increases proportional to $t^{0.4}$ where t is the exposure time to ambient atmosphere [245]. On the other hand, surfaces of ‘real’ films are known to be not perfectly smooth. In this respect, the surface roughness layers are assumed to be mixtures of 50% SiO₂ and %50 void ($n=1, \kappa=0$) in the frame of Bruggeman effective medium approximation (BEMA) [246]. In this approximation, the roughness is microscopic where the dimensions of irregularities and all correlation lengths associated with the roughness are smaller than the wavelength of the light. Within the frame of BEMA, the effective dielectric constant ε of a two-component mixture can be given by

$$(1-c) \frac{\varepsilon_1 - \varepsilon}{\varepsilon_1 + 2\varepsilon} = c \frac{\varepsilon - \varepsilon_2}{\varepsilon_2 + 2\varepsilon} \quad (9.1)$$

where c is the concentration of the spheres with complex dielectric constant ε_2 in a matrix with complex dielectric function ε_1 .

To represent the refractive index values of SiO₂ layer, a Sellmeier function of the following form is used [125]:

$$n^2 = \text{offset} + \frac{a\lambda^2}{\lambda^2 - b^2} - c\lambda^2 \quad (8.2)$$

where $\text{offset}=1.4923$, $a=0.61497$, $b=0.115 \mu\text{m}^2$ and $c=0.01059 \mu\text{m}^{-2}$. This is a fitting result to the tabulated data of optical constants given in Handbook of Optical Constants [247]. The oxide layer of the films can be removed by chemical etching methods, but etching introduces an additional roughness on the surface of the films as it is suggested in subsection 5.3.4 [248].

Within the frame of optical model described above, the pseudodielectric functions of the films are fitted by using TL dispersion relations which are briefly introduced in subsection 7.2.2. Since dielectric constants are complex numbers, the determination of effective dielectric function ε of the surface layer from equation (9.1), which is a quadratic equation, requires the selection of the correct branch of the complex solution. A practical procedure for this purpose is given in reference [249] which simplifies determination of ε by allowing vectorization of the computer code used in the analysis of experimental data. The optical constants given by Sopra (Figure 5.13) are used for <100> crystalline silicon substrate in the regression analysis. The results of the regression analysis (solid lines) are plotted in Figure 9.3 together with the experimental measured data.

Volume fractions of voids on the surface layer of the films are fixed to $c=50\%$ in order to simplify the model. This is the value of typically chosen for thin roughness layers in the absence of additional information. This approximation is justified experimentally for a-Si:H thin films [250].

The spectral dependence of refractive index and absorption coefficient values of the films are plotted in Figure 9.4. Due to carbon incorporation in B_2H_6 and PH_3 doped a-SiC_x:H thin films, their refractive indices are lower than the ones of B_2H_6 doped a-S:H. However, absorption coefficients of the films are observed to be almost same. The thicknesses of the films (d_1) and the roughness layer (mixture of 50% void and 50% SiO₂) on the surface (d_2) are given in Table 9.2. The only d_1 values of the films are observed to be almost independent of the model chosen for the roughness layer. Therefore, the d_2 values should not be considered as absolute values of roughness instead they can be used for the assessment of the variation of surface roughnesses from sample to sample.

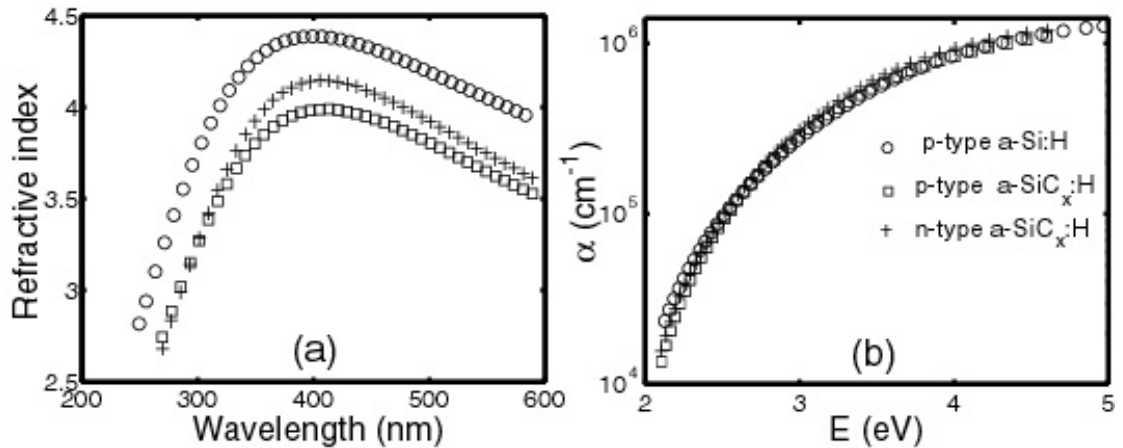


Figure 9.4 (a) Spectral dependence of refractive index n and absorption coefficient α for undoped a-Si:H, B₂H₆ doped a-Si:H, undoped a-SiC_x:H, B₂H₆ doped a-SiC_x:H and PH₃ doped a-SiC_x:H thin films, obtained from spectroscopic ellipsometry measurements.

9.5 Atomic Force Microscopy Analysis

Atomic Force Microscopy (AFM) is a useful technique for analyzing the surface topography which gives quantitative information about the surface features. Characterization of interfaces of thin film devices such as solar cells is essential to improve the performance of the devices. For example, field emission arrays (FEA) produced by using amorphous silicon leads to smoother surfaces in comparison to FEA's produced by polycrystalline silicon which leads to cause problems in terms of uniformity, reliability and electrical stability [251]. On the other hand, the microstructure of amorphous and microcrystalline thin films leads to microscopically rough surfaces which can be difficult to observe by using traditional electron microscopy techniques [252].

9.5.1 Principles of Atomic Force Microscopy

In this technique, a sample surface is scanned under a stationary sharp tip (a couple of microns long and typically less than 20 nm in diameter) which is affixed to the end of a

flexible force-sensing cantilever stylus (100 to 200 μm long). The AFM operates by measuring the forces between the tip and the sample when these are brought in close proximity. As the sample is scanned under the tip, any surface irregularities will cause minute deflections of the tip-cantilever system which are detected, translated and finally displayed as an image [119].

Height variations are chosen to be in the direction of z-axis in an orthogonal x-y-z coordinate system. x-y plane coincides with a perfectly flat surface perpendicular to the z-axis. A mean surface is defined as the plane which separates the surface data by leaving equal volumes at above and below this plane in the $\pm z$ directions. The height variations are measured with respect to this defined mean surface which is parallel to the horizontal x-y plane [119].

9.5.2 Vertical Roughness Parameter: Root Mean Square (rms) Roughness

One of the most commonly used vertical roughness statistical parameter is the root-mean-square (rms) roughness, σ . Let's, first, define the average z_{ave} of z values as

$z_{ave} = \sum_{i=1}^N z_i$. The rms roughness, σ , is defined as the square root mean value of the

squares of the distances of the height-data points, z_i , from the z_{ave} :

$$\sigma = \sqrt{\frac{1}{N} \sum_{i=1}^N (z_i - z_{ave})^2}$$

where z_i represents the z-height value and N denotes the number of equally spaced discrete height-data points of the profile [119].

9.5.3 Lateral Roughness Parameter: Power Spectral Density

There is no unique rms roughness value for a surface because rms roughness depends on the profile length or the area size (maximum surface spatial wavelength) and the distance between the data points. Indeed, different profiles having different frequencies and amplitudes might have the same rms values. Therefore, additional roughness parameters are needed to quantify surface profile. For example, power spectral density is a frequently used quantity to quantify spatial lateral structures of the surface profiles [253-254] and defined as

$$G_{2D}(f_x, f_y) = \lim_{L \rightarrow \infty} \frac{1}{L^2} \left| \int_{-L/2}^{L/2} \int_{-L/2}^{L/2} z(x, y) e^{-2\pi i(f_x x + f_y y)} dx dy \right|^2$$

where L is the length of the profile, $z(x, y)$ is the surface height function and the f_x and f_y are the spatial frequencies of the surface roughness which are related the lateral dimensions of the surface features. Since the measurements at hand are discrete data sets for a limited area of surface, the above expression is needed to be given in the following form:

$$G_{2D}(f_x, f_y) = \frac{1}{L^2} \left| \sum_{m=1}^N \sum_{n=1}^N (\Delta L)^2 z_{mn} e^{-2\pi i(f_x m + f_y n)} \right|^2$$

where z_{mn} discrete height data at positions (m, n) , and $\Delta L = L/N$ is the sampling interval. Since the samples are assumed to be isotropic, $G_{2D}(f_x, f_y)$ has a polar symmetry. Thus, $G_{2D}(f_x, f_y)$ can be expressed in polar coordinates (f, θ) and averaged over azimuthal angle as

$$G_{2D}^i(f) = \frac{1}{2\pi} \int_0^{2\pi} G_{2D}(f, \theta) d\theta$$

This averaged density is called two dimensional isotropic power spectral density. It is suggested that such an averaging of power spectral density has reducing effect of measurement errors [254].

9.5.4 Height Distributions: Skewness and Kurtosis

Another roughness parameter, which is a height distribution function, is skewness. It is a measure of the symmetry of a surface about the mean surface level and is defined as:

$$Skewness = \frac{1}{\sigma^3} \frac{1}{N} \sum_{i=1}^N z_i^3$$

Since the height value has a power of 3, this parameter is more sensitive to points with large z values which correspond to points that are farther from the mean plane. If the Skewness is zero, an even distribution of data around the mean data plane can be concluded. If the Skewness is much far from zero, an asymmetric one-tailed distribution is suggested, such as a smooth surface with a small sharp bump or a small deep hole.

Last height distribution function, which is used in this work, is kurtosis. It is a measure of sharpness of the height distribution function and is defined as

$$Kurtosis = \frac{1}{\sigma^4} \frac{1}{N} \sum_{i=1}^N z_i^4$$

If a profile involves a considerable amount of bumps and holes, there will be larger fractions of the total number of points in the two wings of the height distribution function resulting in a kurtosis value greater than 3. On the other hand, if most of the surface roughnesses are concentrated close to the mean surface plane the kurtosis will be less than 3. Since a perfect Gaussian distribution has a kurtosis of 3, it is possible to obtain information about the randomness of a surface relative to that of a perfectly

random Gaussian surface by computing the kurtosis value of the surface. Thus, kurtosis also describes the randomness of the surface shape relative to that of a perfectly random Gaussian surface [119].

9.5.5 AFM Measurement Results

Surface roughnesses of the films deposited on silicon (100) substrates are measured by Digital Instruments NanoScope III atomic force microscopy. The instrument is operated in tapping mode in order to avoid any modification of a surface by a contacted probe tip and scan area is fixed to 5 μm and 5 μm . The number of data points is 512 x 512 for each measurement. Surface topography is assumed to be random and isotropic in the analysis of the surfaces.

Table 9.3 Rms, skewness and kurtosis values of the film surfaces.

Sample	B ₂ H ₆ doped a-Si:H	Undoped a-SiC _x :H	B ₂ H ₆ doped a-SiC _x :H	PH ₃ doped a-SiC _x :H
Rms (nm)	1.09	0.46	0.87	0.28
Skewness	0.52	0.75	0.35	0.29
Kurtosis	4.55	4.82	3.37	3.62

The calculated rms roughness values of the films are given in Table 9.3. In order to obtain the general surface characteristic of the surfaces, all the parameters in Table 9.3 are calculated from regions where there is no exceptional huge bumps which are probably due to contamination of surface by particulates. All thin films are found to have smooth surface with σ in the range of ~0.3-1.1 nm and therefore they might be suitable for integration in device structure. The thickness of the roughness layers given in Table 9.2 are relatively larger than the ones given in Table 9.3. Rms roughnesses

deduced from spectroscopic ellipsometry are generally found to be larger than rms roughness deduced from AFM [250, 255]. However, the difference in the rms roughness values are quite large. This might be due to two reasons: First, surface roughness and native oxide layer are represented simply by a single layer which might result in high rms roughness values. In addition, a native oxide on the c-Si substrate might have affected the results. Second, exceptional features like sharp bumps and holes on the surface, which are not considered in the determination of values reported in Table 9.3, might be an alternative explanation for such a large discrepancy.

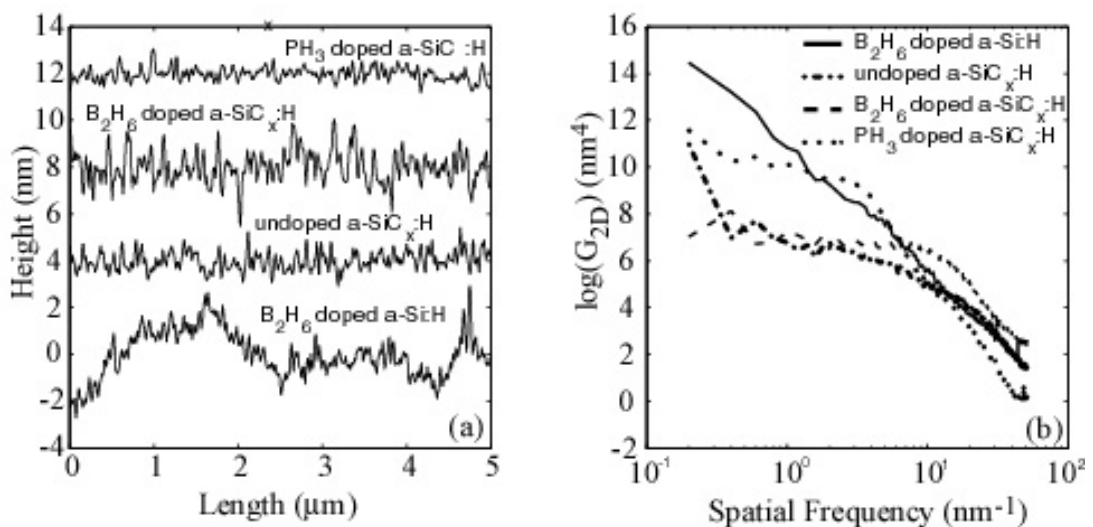


Figure 9.5 (a) One dimensional sectional surface profile and (b) two dimensional isotropic power spectrum density of B₂H₆ doped a-Si:H, undoped a-SiC_x:H, B₂H₆ doped a-SiC_x:H, PH₃ doped a-SiC_x:H thin films.

Sectional profiles of the films are given in Figure 9.5(a) where the heights are measured relative to mean surface level. It is easily noticed that PH₃ doped a-SiC_x:H thin film has the least rough surface whereas the most rough surface is the surface of B₂H₆ doped a-Si:H. These observations are in agreement with rms values given in Table 9.4. It is reported that phosphorus doping of a-Si:H leads to smoother surfaces with less rms roughness values [256] whereas boron doping to either to a-Si:H or a-SiC_x:H increases

the roughness [257]. Power spectral densities of the surfaces are given in Figure 9.5(b). Power spectral densities of PH_3 doped $\text{a-SiC}_x\text{:H}$ and B_2H_6 doped a-Si:H thin films exhibit different behaviors in comparison to undoped $\text{a-SiC}_x\text{:H}$ and B_2H_6 doped $\text{a-SiC}_x\text{:H}$ thin films. It is observed that power spectral density decreases from low to high spatial frequencies which is a common observation for most of the isotropic surfaces.

9.6 FTIR Spectroscopy Analysis

IR spectra of the thin films normalized to thicknesses of the films in two different wavenumber intervals, $500\text{-}1200\text{ cm}^{-1}$ and $1900\text{-}2200\text{ cm}^{-1}$ are shown in Figures 9.6(a) and 9.6(b), respectively. Effect of interference due to multiple transmissions and reflectances in the thin films are eliminated by interpolating the IR absorption free regions of the spectrum. It is observed that the absorption in the $500\text{-}1200\text{ cm}^{-1}$ interval is stronger than the absorption in $1900\text{-}2250\text{ cm}^{-1}$ for all the films.

A-Si:H has intense and narrow absorption peaks in the absorption band between 600 cm^{-1} and 800 cm^{-1} in comparison to $\text{a-SiC}_x\text{:H}$ thin films due to absence of Si-C bonds. These peaks mainly consists of wagging mode vibrations of Si-H and Si-H_n bonds at $\sim 640\text{ cm}^{-1}$ and 670 cm^{-1} , respectively and is observed to be stronger for B_2H_6 doped a-Si:H in comparison to undoped one which is probably a result of unavoidable hydrogen dilution of dopant gas. In addition, the same behavior is observed for the peak in the interval $850\text{-}900\text{ cm}^{-1}$, assigned to Si-H₂ and (Si-H₂)_n bending modes [242,258]. The Si-C stretching mode observed at about 770 cm^{-1} for the $\text{a-SiC}_x\text{:H}$ films is most intense for the undoped $\text{a-SiC}_x\text{:H}$ film but rather weak for doped ones due to fact that doped films have very low carbon content of $x=0.05\text{-}0.15$. Besides, the intensity of the peak at about 1000 cm^{-1} , attributed to CH_3 wagging/rocking bonds, is much higher (about 5 times) for the undoped $\text{a-SiC}_x\text{:H}$ film which is known to have the highest carbon content of about $x=0.45\text{-}0.55$. The difference in relative concentration of CH_3 bonds between doped and undoped $\text{a-SiC}_x\text{:H}$ films is similar to the difference between their carbon contents. This is in agreement with the general increasing behavior of hydrogen content as carbon content increases. It is also observed in the Figure 9.8(a) that

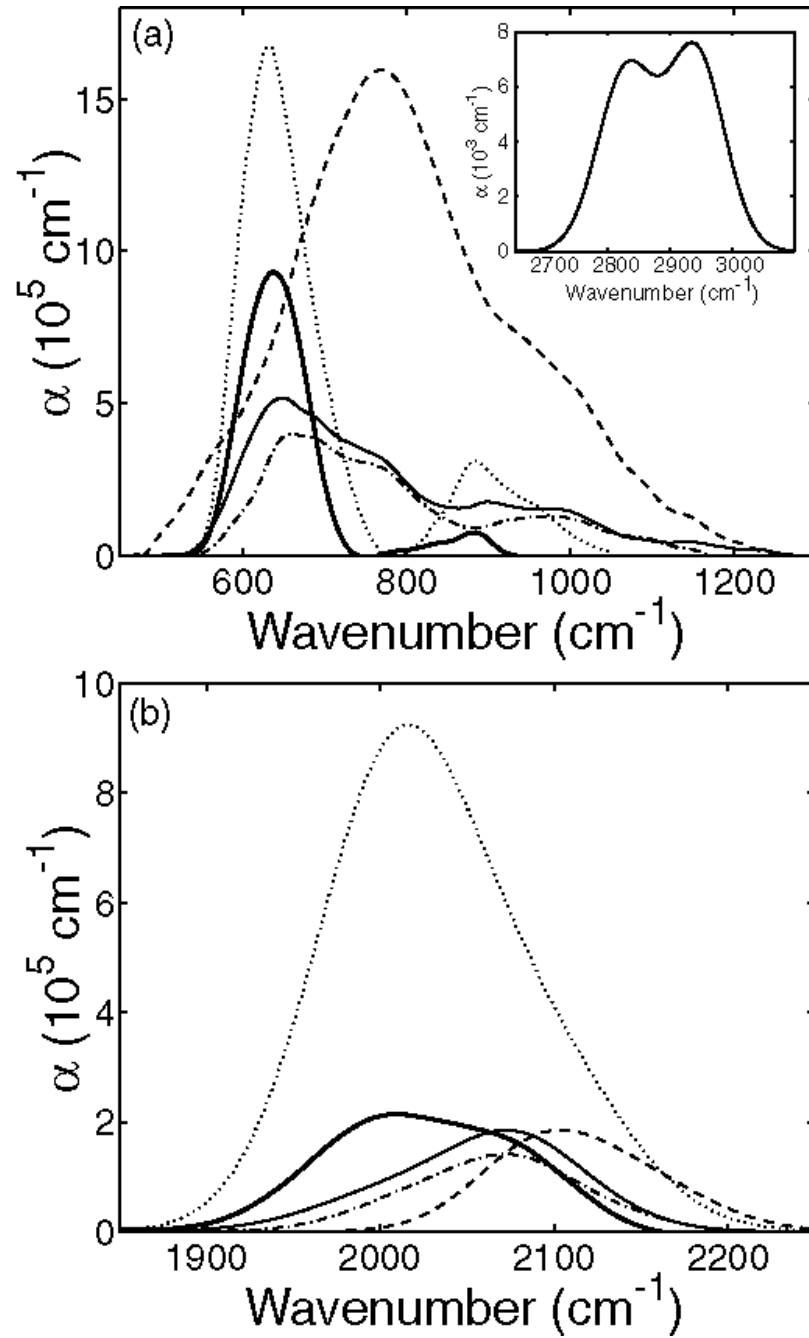


Figure 9.6 IR absorption spectra of undoped a-Si:H (thick solid line), B₂H₆ doped a-Si:H (dotted line), undoped a-SiC_x:H (dashed line), B₂H₆ doped a-SiC_x:H (dash-dotted line) and PH₃ doped a-SiC_x:H (thin solid line) thin films in two different wavenumber intervals of (a) 500-1200 cm^{-1} and (b) 1900-2200 cm^{-1} . IR absorption spectrum of undoped a-SiC_x:H in wavenumber interval of 2800-3000 cm^{-1} is given as an inset in (a).

PH₃ doping enhances the hydrogen incorporation due to more intense peaks at the frequencies at about 640 cm⁻¹ and 890 cm⁻¹. Moreover, PH₃ seems to promote SiH₂ bonding structure which is clear for only n-type a-SiC_x:H film as a tiny peak at 890 cm⁻¹ although both n and p type films have almost same carbon content.

Similarly to the observation given in subsection 8.3.4, the frequency of Si-H stretching mode increases as carbon is incorporated in the film probably due to the replacement of Si neighbors with more electronegative carbon atoms. This shift is observed to be maximum for undoped a-SiC_x:H film due to its highest carbon content. On the other hand, the peak at 2150 cm⁻¹ is assigned to C-Si-H₂ stretching bonds and is only apparent for the undoped a-SiC_x:H film. Such a bond configuration is not observed for hydrogen diluted films considered in Chapter 8. On the other hand, the shift in the frequency of Si-H stretching bond of PH₃ doped a-SiC_x:H film seems somewhat higher than that of B₂H₆ doped one which is in agreement with the same behavior at the wavenumber interval of 600-950 cm⁻¹.

The relative concentration of Si-H stretching modes of B₂H₆ doped a-Si:H is much larger than the undoped a-Si:H. On the other hand, the relative concentration of Si-H₂ with respect to that of Si-H seems higher for undoped a-Si:H film. This observation together with the intensive absorption at about 640 cm⁻¹ confirms the enhanced hydrogen incorporation in B₂H₆ doped a-Si:H film.

A very weak peak at about 2800-3000 cm⁻¹, assigned to C-H_n stretching modes, is detected only for undoped a-SiC_x:H film as shown as an inset in Figure 9.6(a). The weak nature of this peak in comparison to stronger peaks of a-SiC_x:H films in this wavenumber interval, analyzed in Chapter 8, suggests that hydrogen dilution may also increase hydrogen content.

9.7 XPS Analysis

Chemical composition of the films are examined by XPS measurements (Perkin Elmer PHI 5400). Analysis by XPS is accomplished by irradiating a sample with monoenergetic x-rays and analyzing the energy of the detected electrons. These photons have limited penetrating power in a solid on the order of 1-10 micrometers. As a result of interaction of these photon with atoms in the surface region, electrons are emitted by the photoelectric effect. The emitted electrons have measured kinetic energies given by:

$$KE = h\nu - BE - \phi_s$$

where $h\nu$ is the energy of the photon, BE is the binding energy of the atomic orbital from which the electron originates, and ϕ_s is the spectrometer work function defined as follows: The platform on which the sample is placed will give rise to a contact potential equal to the difference in work functions between sample and sample platform ϕ_s . Therefore ϕ_s is needed to be taken into account in the determination of KE of emitted electrons from the surface. The binding energy can be defined as the energy difference between the initial and final states after the photoelectron has left the atom. Since each element has a unique set of binding energies, the elements in the surface can be identified and their concentration can be also determined by XPS [259].

9.7.1 Fundamentals of XPS

The penetration of radiation into the solid is limited by the absorption of radiation in the solid, and produced photoelectrons may lose energy by collisions with the atoms in the solid. Although x-rays can penetrate deeply into the solid, only photoelectrons near to the surface can enter the vacuum without suffering from collisions. The photoelectrons which are originating from the deeper regions below the surface may have enough energy to enter the vacuum by losing some fraction of their energy by colliding with atoms. Such electrons, which are suffering from collisions, do not give a single peak in the photoelectron spectrum but instead they contribute to the

background spectrum. Background spectrum is continuous because the amount of energy lost by each photoelectron is distributed randomly as a function of energy. Escape depth is the maximum depth from which photoelectrons are ejected without losing some of their energy by collisions and result in well defined peaks in photoelectron spectrum. The electrons below this escape depth can be ejected from the surface by losing energy by collisions. As the energy of photoelectron is larger escape depth becomes larger. In other words, greater the excitation energy the greater the escape depth. Typically the escape depth for Mg K α X-rays is of the order of 20 to 100 angstroms. The mass of the atoms in the material is another parameter which determines the amount of energy of lost by the photoelectrons upon collisions with the atoms. Heavier atoms lead to greater energy loss by collision and consequently, smaller escape depth. Therefore, XPS is a technique which is mainly sensitive to surfaces.

As the electrons are emitted from the surface, positively charged ions are left in the surface which attract emitted photoelectrons to the surface and thus, reduce their kinetic energy. Therefore, kinetic energies of electrons are reduced due to some amount of surface charge. This attraction of photoelectrons by the positive surface charge leads to shift of binding energies to higher energies in photoelectron spectrum whereas excessive charge compensation can result in shifts to lower binding energies. Position of C 1s peak from the hydrocarbon that is nearly always adsorbed and present on the sample surface can be used as a reference or calibration for charging effects on the surface. This peak appears at 284.5-285 eV, so any shift from this value can be taken as a measure of the static charge.

In XPS studies, the electron take-off angle, which is measured with respect to the sample surface, is not critical, though it has some effect on the spectra. Very shallow electron take-off angles intensify the spectrum of any component segregated on the surface, whereas a sample mounted at an angle normal to the analyzer axis minimizes the contribution from such a component. This effect can be used to estimate the depth of layers on or in the surface. It is possible to change the angle between the plane of the sample surface and the angle of entrance to the analyzer. At 90° with respect to the surface plane, the signal from the bulk is maximized relative to that from the surface

layer. At small angles, the signal from the surface becomes greatly enhanced, relative to that from bulk [260-262].

When one of the peaks of a wide scan spectrum is examined under conditions of higher energy resolution, the position of maximum is found to depend to a small degree upon the chemical environment of the atom responsible for the peak. That is, variations in the number of valence electrons and the types of bonds they form influence the binding energies of core electrons. These chemical shifts can be observed for the core electrons of all elements except hydrogen (whose single electron is involved in all compounds involving hydrogen and is thus always a valence electron). This means that the photoelectron spectroscopy is a very powerful technique for investigating structure and bonding.

9.7.2 XPS measurements and results

The source of X-ray radiation in XPS measurements is Mg $K\alpha$ (1253.6 eV). $K\alpha$ indicates that a core electron is ejected by directing a highly energetic beam of electrons at Mg surface. Ejected core electron is replaced by a transition within the core levels with the generation of an X-ray. This process gives the $K\alpha$ line corresponding to the transition of a 2p electron to fill a vacancy in the 1s level.

XPS results of the films for peaks of Si, C and O are shown in Figures 9.7-9. Charging effect is eliminated by calibrating binding energy scale with respect to C 1s line (284.5 eV). For undoped a-SiC_x:H film, the take-off angle is 45°. However, for the other films in the region of Si 2p, signals are very noisy to deconvolute. That's why, for these films, measurements in Si 2p energy region are performed at photoelectron take-off angle of 75°. In these spectra, charging shifts are corrected by assuming Si-Si/Si-H binding energy of 99 eV. Such a modification in photoelectron take-off angle led to resolvable Si 2p peak for deconvolution.

The XPS line at ~99 eV corresponds to Si-Si binding energy [263]. Since Si-Si and Si-H binding energies are very close to each other, these two peaks could not be

differentiated. The peak at ~100.8 eV is due to a Si-C bond [259,264]. Similarly, C-C and C-H binding energies could not be separately identified in the C 1s spectra. The peaks at larger energies correspond to oxidized silicon. The peak at ~102 eV might be attributed to suboxides, structures such as O-Si-C and the peak at ~103.1 eV is due to Si-O₂ which can be connected to presence of surface oxidation [265-266]. The relative intensity of Si-C peak to Si-Si/Si-H peak in Si 2p spectra of the films are given in Table 9.5.

Table 9.5 The relative intensities of both Si-C peak to Si-Si/Si-H peak in Si 2p spectra and C-Si peak to C-C/C-H peak in C1s spectra of the films.

Sample	Si – C	C – Si
	Si – Si / Si – H	C – C / C – H
B ₂ H ₆ doped a-Si:H	0.16	4.55
Undoped a-SiC _x :H	0.69	0.70
B ₂ H ₆ doped a-SiC _x :H	0.30	7.15
PH ₃ doped a-SiC _x :H	0.13	3.03

The XPS line at ~283 eV is due to existence of C-Si bonds and the line at ~284.5 eV corresponds to C-C graphitic bonding [264-268]. The next two peaks at ~286 eV and ~287 eV might be due to C-O-H and diamond-like fourfold bond, respectively [264]. Similarly, the relative intensity of C-Si peak to C-C/C-H peak in C 1s spectra of the films are given in Table 9.5.

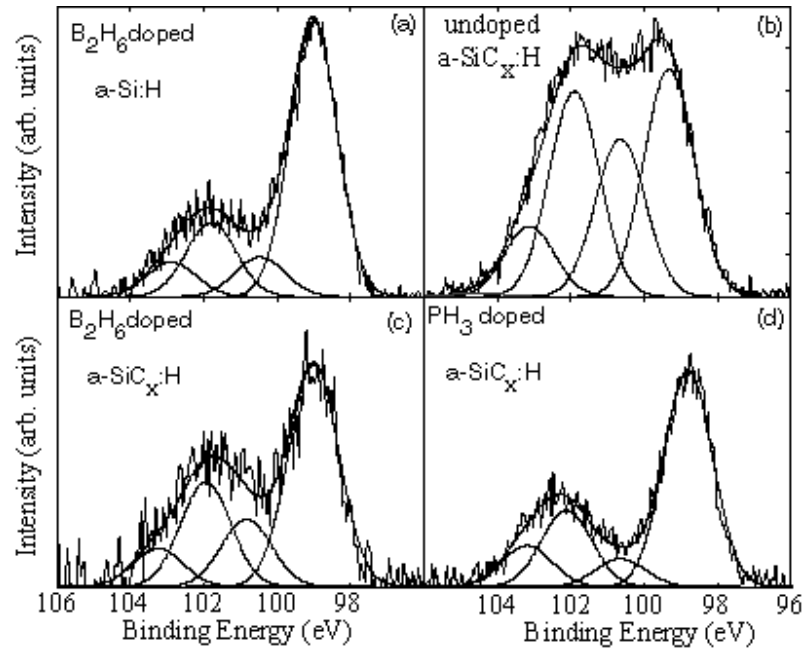


Figure 9.7 Si 2p peaks of (a) B_2H_6 doped a-Si:H (b) undoped a-Si $_x$ C:H (c) B_2H_6 doped a-Si $_x$ C:H (d) PH_3 doped a-Si $_x$ C:H.

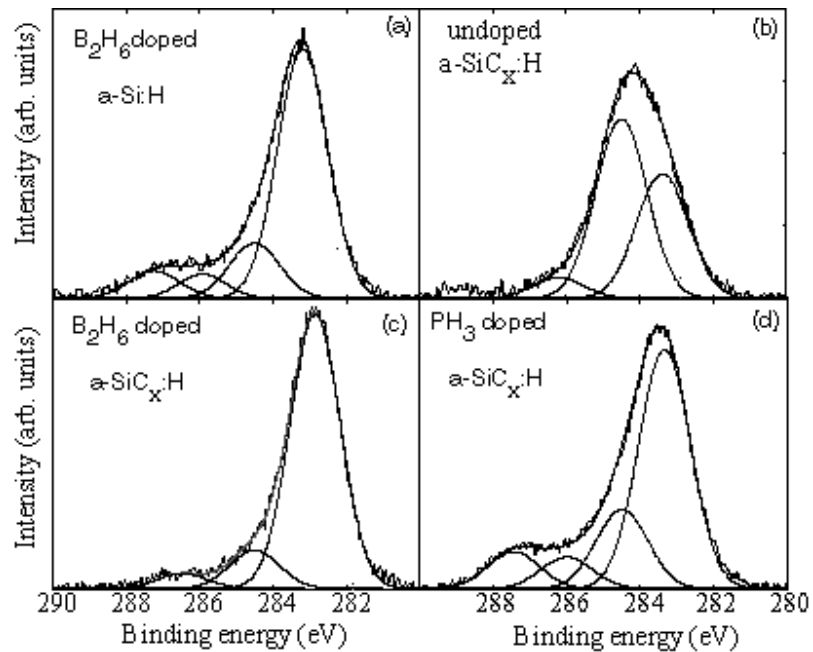


Figure 9.8 C 1s peaks of (a) B_2H_6 doped a-Si:H (b) undoped a-Si $_x$ C:H (c) $B_2H_6_3$ doped a-Si $_x$ C:H (d) PH_3 doped a-Si $_x$ C:H.

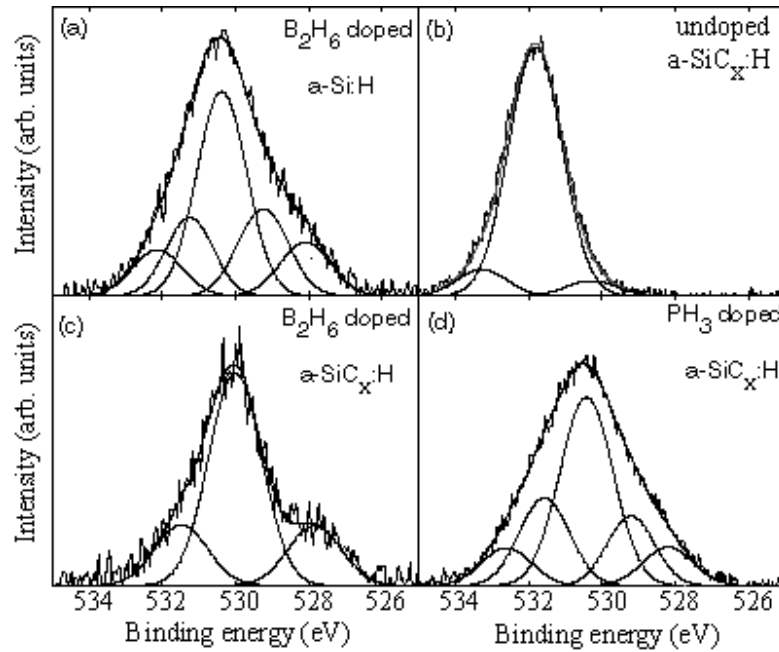


Figure 9.9 O 1s peaks of (a) B₂H₆ doped a-Si:H (b) undoped a-SiC_x:H (c) B₂H₆ doped a-SiC_x:H (d) PH₃ doped a-SiC_x:H

Broadening of the C 1s level is highest for PH₃ doped a-SiC_x:H and lowest for undoped a-SiC_x:H. This might be connected to Si atom content that is highest for PH₃ doped a-SiC_x:H and lowest for undoped a-SiC_x:H. In turn, this might be interpreted in terms of hydrogen concentration in the film. In O 1s spectra, some of the peaks at binding energies of ~528 eV, ~529.2 eV, ~530.3 eV, ~531.6 eV, ~532.4 eV and 533.3 eV are observed. In spectra of undoped a-SiC_x:H and B₂H₃ doped a-SiC_x:H, the peaks at ~529.2 eV and ~533.3 eV are not explicitly identified. The peak at ~532.4 eV corresponds to SiO₂ whereas the low-intensity O1s peak at ~530.3 eV can be attributed to O²⁻ type oxygen [269]. In the low energy side of the O 1s spectra (527.7-530.5 eV) corresponds to oxygen ions all associated with a “2-” formal charge. The peak at 531.6 might be due to OH⁻ type oxygen [269]. Finally, it is possible to conclude O1s spectra is composed of SiO₂, hydroxide (OH⁻) and oxide structures. Generally, an increase of negative charge on the ionized atom leads to a lowering of its core binding energies [270]. Although binding energies are calibrated with respect to C-C/C-H line, it is seen

that the peak at ~ 530.3 eV (O^{2-} /oxide oxygen) might be considered as a reference for correction of charging effects because this binding energy observed to be not shifting. The full width half maximum of the peak at 530.3 eV has relatively large width of 1.7 eV which might indicate more disorder.

9.8 Discussion and Conclusion

Effects of B_2H_6 and PH_3 doping on a-Si:H and a-SiC_x:H thin films are examined with bulk sensitive methods (transmittance, reflectance and Fourier transform infrared spectroscopy) and surface sensitive techniques (spectroscopic ellipsometry, atomic force microscopy and x-ray photoemission spectroscopy). Transmittance and reflectance measurements revealed the absorption properties together with the complex refractive index values of the films. PH_3 doped a-SiC_x:H thin film is found to have a larger optical gap than B_2H_6 doped a-Si_x:H thin film. However, PH_3 doped a-SiC_x:H has larger refractive indices than B_2H_6 doped a-SiC_x:H in agreement with the spectroscopic ellipsometry measurements although B_2H_6 doped a-Si:H is found to be larger in contrast to the results of transmittance and reflectance. IR measurement result suggests that PH_3 doping enhances the hydrogen incorporation. Consequently, enhanced hydrogen incorporation PH_3 doped a-SiC_x:H should have decreased the refractive index as it increases optical gap of a-SiC_x:H. It is observed from the FTIR measurements that PH_3 doping promotes Si-H₂ bonding structure in contrast to B_2H_6 doped sample which suggests an increase in the void fraction of the PH_3 doped a-SiC_x:H. The broadening in the imaginary part of pseudodielectric function of B_2H_6 doped a-SiC_x:H is observed to be slightly larger than the PH_3 doped a-SiC_x:H.

Atomic force measurements revealed that all thin films are found to have smooth surface with σ in the range of ~ 0.3 -1.1 nm. It is observed that phosphorus doping of a-Si:H leads to smoother surfaces with less rms roughness values whereas boron doping to both a-Si:H or a-SiC_x:H increases the roughness. The relative intensities of both Si-C peak to Si-Si/Si-H peak in Si 2p spectra and C-Si peak to C-C/C-H peak in C1s spectra of the films reflect the carbon content in the a-SiC_x:H thin films. The relative intensity of

Si-C to Si-Si/Si-H peak is largest for undoped a-SiC_x:H film in agreement with its large carbon content. The relative intensity of Si-C to Si-Si/Si-H peak of B₂H₆ doped a-SiC_x:H is larger than that of PH₃ doped a-SiC_x:H. The relative intensity of C-Si peak to C-C/C-H peak is strongly related with carbon contamination of the surface.

CHAPTER 10

CONCLUSION

Silicon based hydrogenated amorphous films, with their p and n type dopability, their field effect behavior, their ability to be deposited on large area at low temperature on low cost substrate within the same plasma reactor (PECVD), their compatibility with the existing crystalline silicon based microelectronic technologies, their improved optical properties and their adjustable band gap from IR to UV by various alloying process, constitute a whole so called amorphous silicon technology for large area electronics.

For testing the optimization of the optical properties within a “film growth-analysis” cycle, the UV-Visible transmittance, reflectance, ellipsometry, Fourier transform infrared spectroscopy, atomic force microscopy, x-ray photoemission spectroscopy measurements are adopted as test techniques. In this respect, on one side, a theoretical analysis, on the other side the assessment of experimental results are undertaken.

The interaction of light with amorphous material is described in the frame of semi-classical approach as a theoretical analysis starting from the Schrödinger equation and first order time dependent perturbation theory. Expressions for the spectral dependence of absorption coefficients are derived for transitions between valence and conduction band extended states, and between valence band tail (localized states) and conduction band extended states. Absorption properties of amorphous semiconductors

are compared with the crystalline semiconductors. Although the broad behaviours of absorption edges in amorphous semiconductors do not let to assign a definite threshold for the energy gap, some empirical approaches are described for the determination of optical gaps. Exponential dependence of absorption coefficients is described by potential fluctuations which are discussed in the frame of potential well model by defining their distribution as Gaussian. It is shown that when the decay length of the bound state is of the order of inter-atomic distance the density of states becomes exponentially linear in energy. Urbach parameter is defined proportional to the standard deviation of local potential wells from the mean.

Theoretical description of the interaction of light with solid is discussed on the basis of Maxwell's equations. Transmittance and reflectance of thin absorbing film on a transparent substrate is derived both for finite and infinite substrate thickness. Characteristic matrix approach in determining transmission and reflection coefficients is developed as a practical tool in the analysis of multilayer coatings. Method of envelopes and a numerical approach for the determination of optical constants of thin films are introduced.

Real films may deviate considerably from the homogeneous, parallel-sided slab model although the deposition parameters may be adjusted to reduce inhomogeneities. Therefore, approximate expressions are derived for various types of inhomogeneities to assess them from the transmittance and reflectance spectra. It is shown that one type of inhomogeneity may not be responsible alone for anomalies in the experimental spectrum of an a-Si:H thin film. Variation of refractive index along the direction perpendicular to the film surface is considered as an alternative type of inhomogeneity in addition to thickness variation within the spot of the probe beam. It is found that a model with two transitional regions at both boundaries of the film describe the experimental spectrum satisfactorily. Such a refractive index profile is found to be suiting well to the generally observed compositional and structural variations throughout the film from the substrate to the ambient boundaries which might lead to refractive index changes.

A variation in optical constants of a-Si_{1-x}C_x:H thin films as a function of the sample position on the bottom electrode of the PECVD reactor along the radial direction is observed and has been attempted to be interpreted in terms of radical formation rates and their residence time during the growth process.

Eight a-Si_{1-x}C_x:H thin film samples are produced with different carbon concentrations and at two different power densities. The films are analyzed with transmittance, reflectance, single wavelength ellipsometry and FTIR measurements. The effects of carbon content and power density on the refractive index, optical gap, Urbach parameter and bonding configurations are assessed in the frame of possible deposition mechanisms.

Deposition rate of the films grown at high power (90 mW/cm²) are found to be substantially higher than the films grown at low power (30 mW/cm²). This behavior is attributed to the increase of C₂H₅ concentration, in turn, CH₃ concentration, with smaller surface loss probabilities in the gas mixture and their higher dissociation energy. Besides, the deposition rate decreases for both power densities as the C₂H₄ relative gas concentration increases.

The carbon contents of the films are determined by comparing their refractive indices and optical gaps separately with the values published in the literature. It is observed that carbon contents of the films are increased by the increase in power density. As the carbon content increases refractive indices of the films decrease whereas the optical gaps of the films increase. Refractive indices and absorption coefficients of the films are fitted by various dispersion relations of which TL is observed to simulate the optical constants better. The decrease in Tauc (Cody) slope B^{Tauc} (B^{Cody}) and the increase in Urbach parameter E_U as carbon content increases is attributed to the increase of the degree of disorder. However, the increase in E_U is stronger for films grown at high power whereas E_U values of films grown at low power exhibit saturation like behavior as carbon content increases. The incorporation of the carbon in structurally disordered a-Si:H alloy increases further the degree of disorder due to eventual composition disorder.

FTIR measurements revealed that most of the hydrogen atoms are bonded to silicon in the form of monohydride Si-H and their concentration goes through maximum at about $x \sim 0.35$. In contrast to increase of carbon content as power increases, relative concentration of hydrogen atoms bonded to carbon decreases which reveals the reduction of hydrogen content as power increases. Most of the hydrogen atoms incorporated in the structure have sp^3 type C-H₂ and C-H₃ bonds and concentration of sp^3 type C-H and C-H₂ bonds reduces at high power.

As the reflectance spectra of the films are observed to shift to higher intensities, they are corrected by multiplying with a wavelength dependent common factor. The reason of such a systematic error is explained by the decrease of the baseline signal which is probably due to the loss of light upon reflection on the calibrating mirror. The corrected reflectance spectra and single wavelength ellipsometry measurements are analyzed to compute the optical constants of the films. The results are approximately in agreement with the results of the transmittance measurements.

Optical characterization of undoped, B₂H₆ and PH₃ doped, both a-Si:H and a-SiC_x:H thin films are undertaken and effects of doping on optical and surface properties of the thin films are analyzed. Refractive indices and optical gaps of the films are determined by spectroscopic ellipsometry analysis where Bruggemann effective medium theory is applied to represent both the eventual native oxide and roughness layer present on the surface of the films. The relative change in the thickness of the roughness layers is found to follow the same behavior observed by atomic force microscopy. PH₃ doping is observed to promote SiH₂ bonding structure.

APPENDIX A

A.1 Inclusion of Material Properties in Maxwell's Equations

The Maxwell's equations in free space (vacuum) are

$$\vec{\nabla} \cdot \vec{E} = 4\pi\rho \quad (\text{A.1}) \quad \vec{\nabla} \cdot \vec{B} = 0 \quad (\text{A.2})$$

$$\vec{\nabla} \times \vec{E} = -\frac{1}{c} \frac{\partial \vec{B}}{\partial t} \quad (\text{A.3}) \quad \vec{\nabla} \times \vec{B} = \frac{4\pi}{c} \vec{J} + \frac{1}{c} \frac{\partial \vec{E}}{\partial t} \quad (\text{A.4})$$

where \vec{E} and \vec{B} are electric field and magnetic induction (sometimes called magnetic-flux density), ρ and \vec{J} are total charge and total current densities, c is the velocity of light in free space, respectively. Since $\vec{\nabla} \cdot \vec{B} = 0$, \vec{B} can be defined in terms of a vector potential \vec{A} as $\vec{B} = \vec{\nabla} \times \vec{A}$. Use of this definition leads to $\vec{\nabla} \times (\vec{E} + \frac{1}{c} \frac{\partial \vec{A}}{\partial t}) = 0$. Then, $\vec{E} - \frac{1}{c} \frac{\partial \vec{A}}{\partial t}$ can be written in terms of a scalar function φ and \vec{E} can be expressed in terms of \vec{A} and φ as follows:

$$\vec{E} = -\frac{1}{c} \frac{\partial \vec{A}}{\partial t} - \vec{\nabla} \varphi \quad (\text{A.5})$$

The total charge density in a solid can be given by $\rho = \rho_{ext} + \rho_{pol}$ where ρ_{ext} is the external charge density (macroscopic excess or free charge introduced by an external source) in the medium and ρ_{pol} is the charge density due to the spatially variation of polarization (dipole moment per unit volume). As electromagnetic field is applied to a solid, each charge in the solid medium respond to the applied field and the charge

density is distorted. Such a distortion in the charge density can be understood by formation of dipole moments due to the applied field. If the polarization is constant in all over the solid, then polarization charge density ρ_{pol} is zero. On the other hand, if the polarization changes spatially, there may be a net increase or decrease of charge within any small volume [59]. In this respect, ρ_{pol} can be expressed as $\rho_{pol} = -\vec{\nabla} \cdot \vec{P}$.

Using the general continuity equation $\vec{\nabla} \cdot \vec{J} + \frac{\partial \rho}{\partial t} = 0$ for charge and current, one can find the current density \vec{J}_{pol} due to the polarization as $\vec{J}_{pol} = \frac{\partial \vec{P}}{\partial t}$. Similar to polarization concept, in the presence of electromagnetic field, electron spin gives rise to magnetization \vec{M} (magnetic moment density). This magnetization leads to a current and can be expressed as $\vec{J}_{mag} = c\vec{\nabla} \times \vec{M}$. Total current density \vec{J}_{bound} due to charges restricted to localized motion (bound to nuclei) can be expressed by

$$\vec{J}_{bound} = \vec{J}_{pol} + \vec{J}_{mag} = \frac{\partial \vec{P}}{\partial t} + c\vec{\nabla} \times \vec{M} \quad (\text{A.6})$$

Another type of current density in a solid arises from electrons free to move through the solid and can be split into two parts. First, motion of conduction electrons in the presence of electric field is a possible type of current. Such a current density is denoted by \vec{J}_{cond} . Second, \vec{J}_{ext} is a current density introduced into the solid by an external source [147].

As a result, total current density can be written as $\vec{J} = \vec{J}_{pol} + \vec{J}_{mag} + \vec{J}_{cond} + \vec{J}_{ext}$. However, it should be kept in mind that categorizing the current densities as in this form is not unique because the degree of localization of electrons depends on the energy of the electromagnetic radiation. In other words, electrons which are bound at one energy of the electromagnetic radiation might be better described as free at a higher energy [147].

Consequently, we can rewrite the first and fourth Maxwell's equations as follows

$$\vec{\nabla} \cdot \vec{E} = 4\pi(\rho_{ext} - \vec{\nabla} \cdot \vec{P}) \quad \text{or} \quad \vec{\nabla} \cdot (\vec{E} + 4\pi\vec{P}) = 4\pi\rho_{ext} \quad (\text{A.7})$$

$$\vec{\nabla} \times \vec{B} = \frac{4\pi}{c} \left(\frac{\partial \vec{P}}{\partial t} + c\vec{\nabla} \times \vec{M} + \vec{J}_{cond} + \vec{J}_{ext} \right) + \frac{1}{c} \frac{\partial \vec{E}}{\partial t} \quad (\text{A.8})$$

Defining polarization by $\vec{P} = \chi_e \vec{E}$ where χ_e is the dielectric susceptibility, we can define the electric displacement \vec{D} as $\vec{D} = (1 + 4\pi\chi_e)\vec{E} = \epsilon_1 \vec{E}$ where $\epsilon_1 = 1 + 4\pi\chi_e$ is called the dielectric constant (or electric permittivity). Similarly, the equation

$$\vec{\nabla} \times (\vec{B} - 4\pi\vec{M}) = \frac{4\pi}{c} (\vec{J}_{cond} + \vec{J}_{ext}) + \frac{1}{c} \frac{\partial}{\partial t} (\vec{E} + 4\pi\vec{P})$$

becomes

$$\vec{\nabla} \times \vec{H} = \frac{4\pi}{c} (\vec{J}_{cond} + \vec{J}_{ext}) + \frac{1}{c} \frac{\partial \vec{D}}{\partial t} \quad (\text{A.9})$$

where \vec{H} is called magnetic field and defined as $\vec{H} = \vec{B} - 4\pi\vec{M}$. If magnetization is linearly related to magnetic field as $\vec{M} = \chi_m \vec{H}$ where χ_m is called magnetic susceptibility. Then, $\vec{B} = \mu \vec{H}$ where μ is the magnetic permeability and is defined as $\mu = 1 + 4\pi\chi_m$. After these rearrangements and definitions, Maxwell's equations in a solid become:

$$\vec{\nabla} \cdot \vec{D} = 4\pi\rho_{ext} \quad (\text{A.10})$$

$$\vec{\nabla} \cdot \vec{B} = 0 \quad (\text{A.11})$$

$$\vec{\nabla} \times \vec{E} = -\frac{1}{c} \frac{\partial \vec{B}}{\partial t} \quad (\text{A.12}) \quad \vec{\nabla} \times \vec{H} = \frac{4\pi}{c} \vec{J}_{cond} + \frac{1}{c} \frac{\partial \vec{D}}{\partial t} \quad (\text{A.13})$$

One can interpret \vec{D} in equations (A.10) and (A.13) as $\vec{D} = \vec{E}_{ext}$ where \vec{E}_{ext} resembles the external field which is usually used as a probe and induces an electric field in the solid. \vec{E} , in equation (A.12), can be interpreted as $\vec{E} = \vec{E}_{total}$ where \vec{E}_{total} is the sum of external field and induced field.

APPENDIX B

B.1 Definitions of Coefficients Appearing in Expressions of Transmittance and Reflectance:

Transmittance T_i and reflectance R_i for air/film/semi-infinite substrate system at $\phi_i = 0$:

$$T_i = \frac{A_i x}{B_i - C_i x + D_i x^2}, \quad R_i = \frac{E_i - C_i^+ x + G_i x^2}{B_i - C_i^- x + D_i x^2}$$

where

$$A_i = 16n_s(n^2 + \kappa^2),$$

$$B_i = [(n+1)^2 + \kappa^2][(n+n_s)^2 + \kappa^2]$$

$$C_i = [(n^2 - 1 + \kappa^2)(n^2 - n_s^2 + \kappa^2) - 4n_s k^2]2 \cos(4\pi d / \lambda)$$

$$- \kappa[2n_s(n^2 + \kappa^2 - 1) + 2(n^2 - n_s^2 + \kappa^2)]2 \sin(4\pi d / \lambda)$$

$$D_i = [(1-n)^2 + \kappa^2][(n-n_s)^2 + \kappa^2]$$

$$E_i = [(1-n)^2 + \kappa^2][(n+n_s)^2 + \kappa^2]$$

$$G_i = [(n-n_s)^2 + \kappa^2][(1+n)^2 + \kappa^2]$$

$$C_i^\pm = [(1-n^2 - \kappa^2)(n^2 - n_s^2 + \kappa^2) \pm 4n_s k^2]2 \cos(4\pi d / \lambda)$$

$$+ \kappa[2n_s(1-n^2 - \kappa^2) \pm 2(n^2 - n_s^2 + \kappa^2)]2 \sin(4\pi d / \lambda)$$

$$x = e^{-\alpha d}$$

For a beam incident normally on the film from the substrate side

$$T_i' = T_i, \quad R_i' = \frac{E_i' - C_i^{+'} x + G_i' x^2}{B_i' - C_i^{-'} x + D_i' x^2}$$

where

$$E'_i = [(n_s - n)^2 + \kappa^2][(n+1)^2 + \kappa^2]$$

$$G'_i = [(n_s + n)^2 + \kappa^2][(n-1)^2 + \kappa^2]$$

$$C_i^\pm = [n^2 - n_s^2 + \kappa^2](n^2 - 1 + \kappa^2) \pm 4n_s k^2] 2 \cos(4\pi nd / \lambda) \\ + \kappa[-2(n^2 - n_s^2 + \kappa^2) \pm 2n_s(n^2 - 1 + \kappa^2)] 2 \sin(4\pi nd / \lambda)$$

$$B'_i = [(n_s + n)^2 + \kappa^2][(n+1)^2 + \kappa^2]$$

$$D'_i = [(n_s - n)^2 + \kappa^2][(n-1)^2 + \kappa^2].$$

Transmittance T and reflectance R for air/film/substrate/air system at $\phi_i = 0$:

$$T = \frac{Ax}{B - Cx + Dx^2}, \quad R = \frac{E_i - C_i^+ x + G_i x^2}{B_i - C_i^- x + D_i x^2} + \frac{1}{B_i - C_i x + D_i x^2} \frac{A_r x}{B_r - Cx + Dx^2}$$

$$A = 16n_s(n^2 + \kappa^2)$$

$$B = [(n+1)^2 + \kappa^2][(n+1)(n+n_s^2) + \kappa^2],$$

$$C = [(n^2 - n_s^2 + \kappa^2)(n^2 - 1 + \kappa^2) - 2\kappa^2(n_s^2 + 1)] 2 \cos(4\pi nd / \lambda) \\ - \kappa[2(n^2 - n_s^2 + \kappa^2) + (n_s^2 + 1)(n^2 - 1 + \kappa^2)] 2 \sin(4\pi nd / \lambda)$$

$$D = [(n-1)^2 + \kappa^2][(n-1)(n-n_s^2) + \kappa^2]$$

$$A_r = 64n_s(n^2 + \kappa^2)(n_s - 1)^2, \quad B_r = [(n+1)^2 + \kappa^2][(n+1)(n+n_s^2)^2 + \kappa^2]$$

APPENDIX C

C.1 Definitions of Coefficients Given by Equation (5.15)

Reflection coefficients r_p and r_s can be written as in equation (3.8). The definitions in this representation are listed below:

$$X = e^{-i2\delta},$$

$$a = r_{1p}, \quad b = r_{2p}, \quad c = r_{1s}, \quad d = r_{2s}$$

$$A = a, \quad B = (b + acd), \quad C = bcd, \quad D = c,$$

$$E = (d + abc), \quad F = abd.$$

APPENDIX D

D.1 Normalized reflectance spectra of a-Si_{1-x}C_x:H thin films with simulated reflectances

The normalized reflectance spectra of the films (or corrected spectra) are obtained by multiplying the measured reflectances of the films with a common factor. Measured reflectance spectrum is denoted by empty circles whereas the normalized one is denoted by full circles. Solid line denotes the reflectance spectrum simulated by using the optical constants obtained from the analysis of transmittance spectrum. Dashed line denotes the fitting of TL dispersion relations to the normalized reflectance spectrum (full circles) and single wavelength ellipsometry.

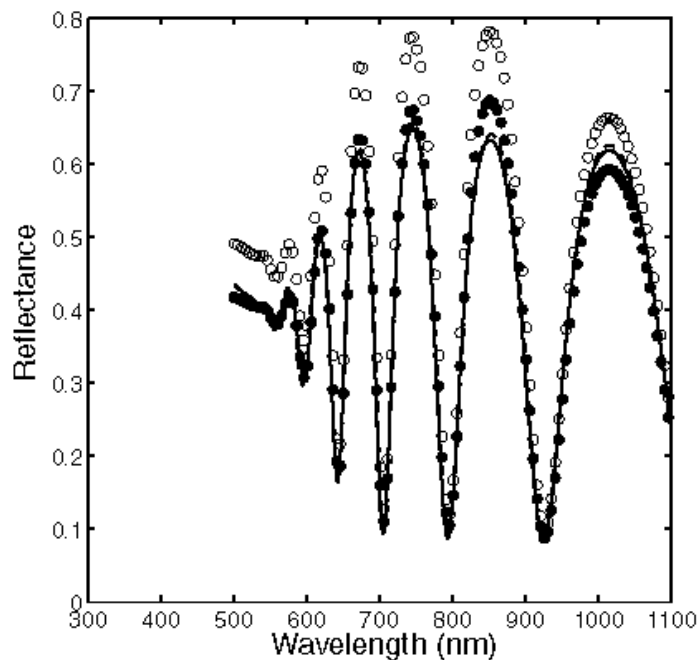


Figure D.1 Reflectance spectra of the sample 0hp.

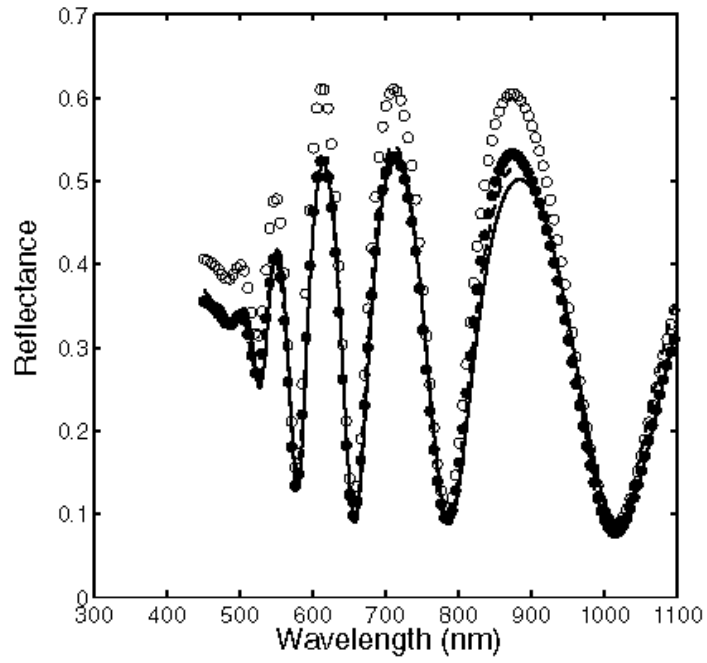


Figure D.2 Reflectance spectra of the sample 2lp.

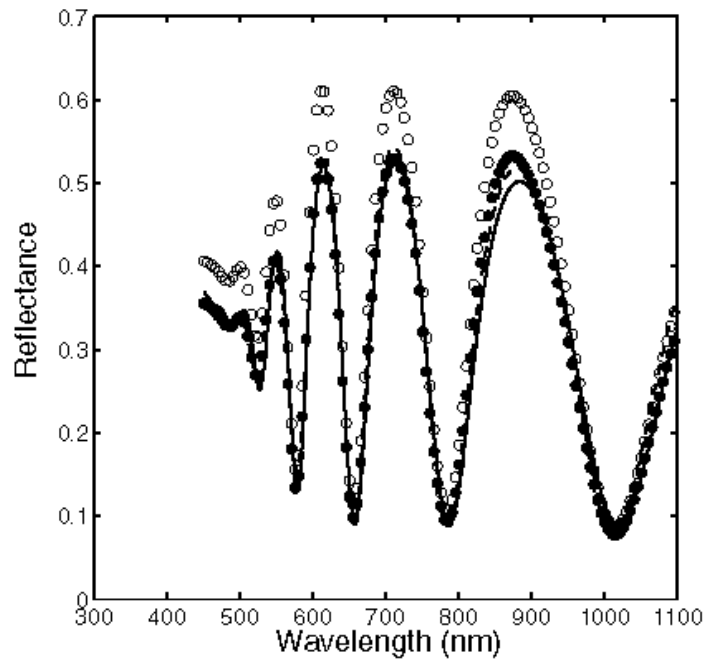


Figure D.3 Reflectance spectra of the sample 2hp.

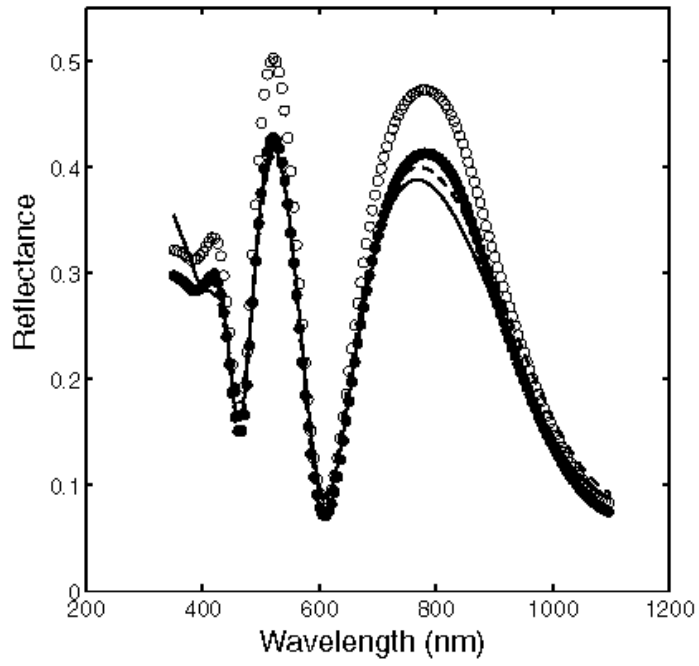


Figure D.4 Reflectance spectra of the sample 5lp.

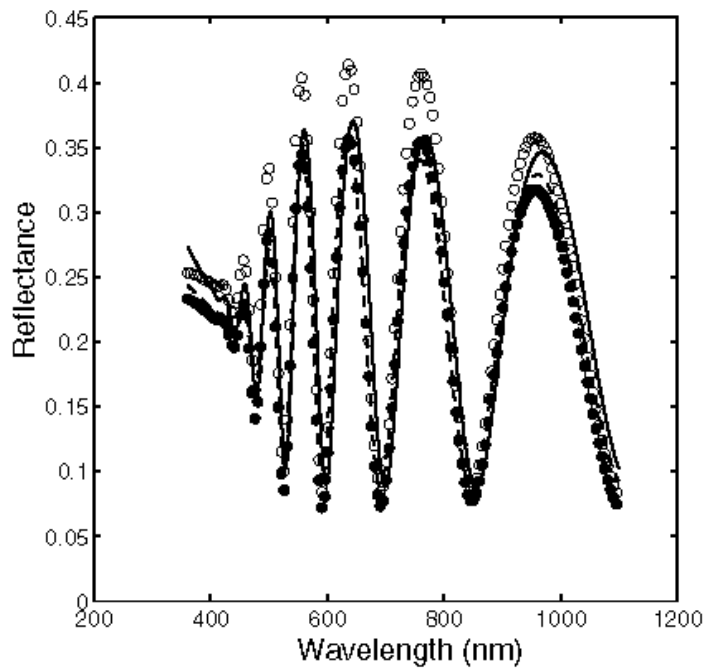


Figure D.5 Reflectance spectra of the sample 5hp.

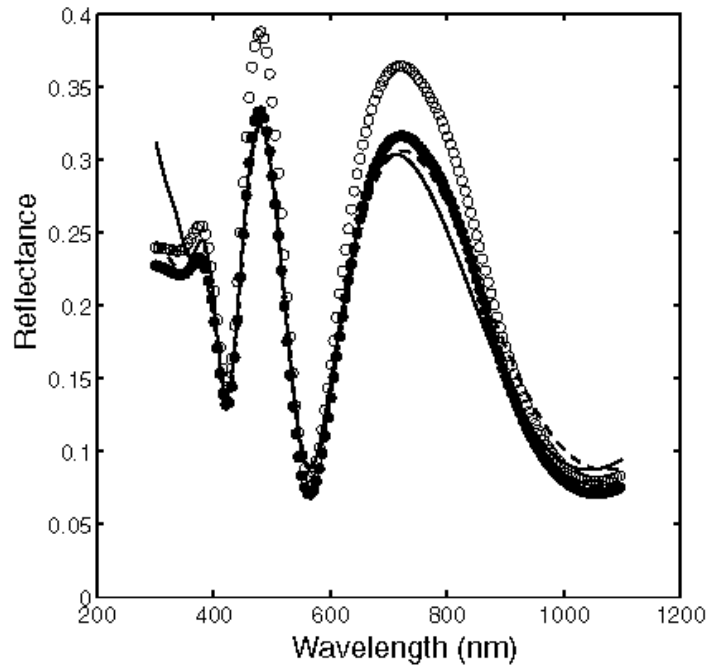


Figure D.6 Reflectance spectra of the sample 7lp.

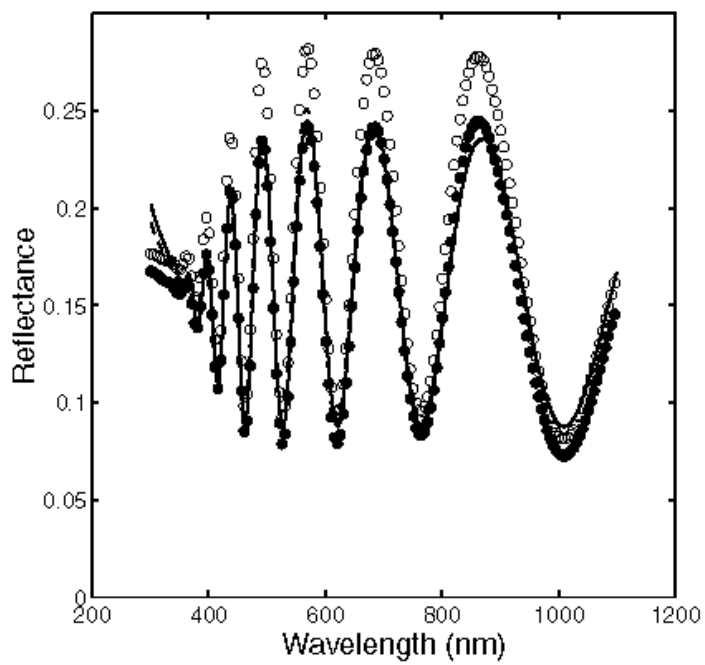


Figure D.7 Reflectance spectra of the sample 7hp.

REFERENCES

- [1] Y. Hamakawa, *Solar and Wind Technology*, vol. 7 (1989), p. 235.
- [2] R.A. Street, *Hydrogenated Amorphous Silicon* (Cambridge University Press, Cambridge, 1991).
- [3] D.E. Carlson, in: *Semiconductor and Semimetals*, ed. by J.J. Pankove, vol. 21, Part D, 1984, p. 7.
- [4] W.G. Hawkins, D.J. Drake, N.B Goodman, and P.J. Hartmann, *Mat. Res. Soc. Symp. Proc.*, vol. 33, p. 231 (1984).
- [5] W.G. Hawkins, *Mat. Res. Soc. Symp.*, vol. 49, p.443, 1985.
- [6] B. Katircioğlu, İ. Atılgan, S. Özder and R. Turan, Project no. TUBITAK-TBAG-1538 (1998).
- [7] *Hydrogenated Amorphous Silicon, Part B*, in: *Semiconductor and Semimetals*, vol. 21, ed. by J.J. Pankove, Academic Press, New York, 1984.
- [8] *Physical Properties of Amorphous Materials*, ed. by D. Adler, B.B. Schwartz, M.C. Steele, Plenum Press, New York, 1985.
- [9] H. Tuan, *Mat. Res. Soc. Symp. Proc.*, vol. 33, p.247 (1984).
- [10] R.C. Mc. Phedran, L.C. Botten, D.R. Mckenzie, and R.P. Netterfield, *Appl. Opt.*, vol. 23, no. 8, p. 1197 (1984).
- [11] J.C. Jans, R.W. Hollering and M. Erman, *Analysis of Microelectronics Materials and Devices*, ed. By M. Grasserbauer and H.W. Warner, John Wiley & Sons (1991), p. 681.
- [12] K. Vedam, *Thin Solid Films*, vol. 313-314 (1998), p.1
- [13] P.J. McMarr, K. Vedam, J. Narayan, *J. Appl. Phys.*, vol. 59 (1986), p.694.
- [14] D.E Aspnes, *Thin Solid Films*, vol. 455-456 (2004), p. 3.
- [15] F. Seitz, *The Modern Theory of Solids*, Mc-Graw-Hill, New York (1940), p. 215.

- [16] T. Dereli, A. Verçin, *Kuantum Melanîği 2*, Metu Press, Ankara (2000), p.86.
- [17] J.J. Sakurai, *Modern Quantum Mechanics*, Addison-Wesley Publishing, (1994), p. 130.
- [18] F. Wooten, *Optical Properties of Solids*, Academic Press, New York (1972), p. 112.
- [19] P.Y. Yu, M. Cardona, *Fundamentals of Semiconductors*, Springer-Verlag, Berlin (1996), p. 247.
- [20] F. Bassani, G.P. Parravicini, R.A. Ballinger, *Electronic States and Optical Transitions in Solids*, Pergamon Press, Oxford (1975), p.152.
- [21] G.D. Cody, *Semiconductor and Semimetals*, Vol. 21, part B, (1984), p.11.
- [22] D. Weaire, *Phys. Rev. Lett.*, vol. 26 (1971), p.1541.
- [23] W.B. Jackson, S.M. Kelso, C.C. Tsai, J.W. Allen, S.J. Oh, *Phys. Rev. B*, vol. 31 (1985), p. 5187.
- [24] S.K. O’Leary, *Appl. Phys. Lett.*, vol. 82 (2003), p. 2784.
- [25] J. Tauc, R. Grigorovici, A. Vancu, *Phys. Stat. Sol.*, vol. 15 (1966), p. 627.
- [26] G.D. Cody, B.G. Brooks, B. Abeles, *Solar Energy Mater.*, vol. 8 (1982), p. 231.
- [27] V.Vorliceck, M. Zatetova, S.K. Pavlov, L. Pajasova, *Journal of Non-Crystalline Solids*, vol. 45 (1981), p. 289.
- [28] K. Rerbal, J.N. Chazalviel, F. Ozanam , I. Solomon, *Phys. Rev. B*, vol. 66 (2002), p. 184209.
- [29] G.D. Cody, T. Tiedje, B. Abeles, B. Brooks, Y. Goldstein, *Phys. Rev. Lett.*, vol. 47 (1981), p. 1480.
- [30] F. Urbach, *Phys. Rev.*, vol. 92 (1953), p. 1324.
- [31] W. Franz, *Z. Naturforsch*, vol. 13a (1958), p. 484.
- [32] L.V. Keldish, *Sov. Phys. –JETP*, vol. 34 (1958), p. 788.
- [33] J.D. Dow, D. Redfield, *Phys. Rev. Lett.*, vol. 26 (1971), p. 762.

- [34] J.D. Dow, D. Redfield, *Phys. Rev. B*, vol. 5 (1972), p. 594.
- [35] G.D. Cody, *Journal of Non-Crystalline Solids*, vol. 141 (1992), p. 3.
- [36] C.H. Grein, S. John, *Phys. Rev. B*, vol. 41 (1990), p. 7641.
- [37] J. Tauc, *Optical Properties of Solids*, ed. by S. Nudelman, S.S. Mitra, Plenum Press, New York, 1969, p123.
- [38] A. Papoulis, *Probability, Random Variables, and Stochastic Processes*, McGraw-Hill, Singapore, 1991, p.214.
- [39] D.E. Newland, *An Introduction to Random Vibrations, Spectral and Wavelet Analysis*, Prentice Hall, Harlow, England, 1993, p. 80.
- [40] E.N. Economou, C.M. Soukoulis, M.H. Cohen, S. John, *Disordered Semiconductors*, ed by M.A. Kastner, G.A. Thomas, S.R. Ovshinsky, Plenum Press, New York, 1987, p. 681.
- [41] L. I. Schiff, *Quantum Mechanics*, 2nd ed., McGraw-Hill, New York, 1955, p. 76.
- [42] S. Gasiorowicz, *Quantum Physics*, John Wiley & Sons, Singapore, 1974, p. 179.
- [43] S.K. O'Leary, P.K. Lim, *Applied Physics A*, vol. 66, 1998, p. 53-58.
- [44] D. Monroe and M.A. Kastner, *Phys. Rev. B* vol. 33, 1986, p. 8881.
- [45] C.M. Soukoulis and E.N. Economou, *Waves in Random Media*, vol. 9, 1999, p. 255-269.
- [46] W. Sritrakool, V. Sayakanit and H.R. Glyde, *Phys. Rev. B*, vol. 33, 1986, p. 1199.
- [47] B. Abeles, C.R. Wronski, T. Tiedje, G.D. Cody, *Solid State Commun.*, vol. 36 (1980), p. 537.
- [48] N. Bacalis, E.N. Economou and M.H. Cohen, *Phys. Rev. B* vol. 37, 1988, p. 2714.
- [49] B.I Halperin, M. Lax, *Phys. Rev.*, vol. 148 (1966), p. 722.
- [50] M. Schreiber, Y. Toyozawa, *Journal of the Physical Society of Japan*, vol. 51 (1982), p.1544.

- [51] C.H. Grein, S. John, Phys. Rev. B, vol. 36 (1987), p. 7457.
- [52] C.H. Grein, S. John, Phys. Rev. B, vol. 39 (1989), p. 1140.
- [53] C.H. Grein, S. John, Solid State Communications, vol. 70 (1989), p. 87.
- [54] S. Abe, Y. Toyozawa, Journal of the Physical Society of Japan, vol. 50 (1981), p. 2185.
- [55] Q. Li, C.M. Soukoulis and E.N. Economou, Phys. Rev. B, vol. 37, 1988, p. 8289.
- [56] J. Tauc, in: Optical Properties of Solids, ed. by F. Abeles, North-Holland, Amsterdam, (1972), p. 277.
- [57] H. Oheda Jap. J. Appl. Phys., vol. 18, 1979, p. 1973.
- [58] W.B. Jackson, C.C. Tsai, S.M. Kelso, J. Non-Crystalline Solids, Vol. 77&78 (1985), p. 281.
- [59] J.D. Jackson, Classical Electrodynamics, 3rd ed., John Wiley & Sons, (1999).
- [60] R.M.A. Azzam, N.M. Bashara, Ellipsometry and Polarized Light, North Holland, Amsterdam, (1989).
- [61] O.S. Heavens, Physics of Thin Films, ed. by G. Hass, R.E Thun, Academic, New York, (1964), p. 46-63.
- [62] B. Akaoglu, İ. Atılgan, B. Katırcıoğlu, Appl. Opt., vol. 39 (2000), p.1611.
- [63] E.G. Steward, Fourier Optics: An Introduction, Halsted Press, New York (1987).
- [64] K. Lamprecht, W. Papousek, and G. Leising, Applied Optics, vol. 36 (1997), p. 6364.
- [65] M. Born, E. Wolf, Principles of Optics, 7th ed. Cambridge University Press, Cambridge (1999).
- [66] S.A. Furman, A.V. Tikhonravov, Basics of Multilayer Systems, Editions Frontiers, Gif-Sur-Yvette Cedex, Paris, (1992).
- [67] J.C. Manificier, J. Gasiot and J.P. Fillard, J. Phys. E: Sci. Instrum., vol. 9 (1976), p. 1002.
- [68] R. Swanepoel, J. Phys. E: Sci. Instrum. Vol. 16 (1983), p. 1214.

- [69] J.I. Cisneros, *Appl. Opt.*, vol. 37 (1998), p.5262.
- [70] R. Swanepoel, *J. Phys. E: Sci. Instrum.* Vol. 17 (1984), p. 896.
- [71] D.E Aspnes, H.G. Craighead, *Appl. Opt.*, vol. 25 (1986), p. 1299.
- [72] A.V. Tikhonravov, M.K. Trubetskov, M.A. Kokarev, T.V. Amotchkina, A. Duparre, E. Quesnel, D. Ristau, S. Gunster, *Appl. Opt.*, vol. 41 (2002), p. 2555.
- [73] D.A. Minkov, *J. Phys. D: Appl. Phys.* Vol. 22 (1989), p. 1157.
- [74] D.A. Minkov, *J. Phys. D: Appl. Phys.* Vol. 22 (1989), p. 199.
- [75] I. Chambouleyron, J. M. Martinez, A.C. Moretti, M. Mulato, *Appl. Opt.*, vol. 36 (1997), p.8238.
- [76] I. Chambouleyron, J. M. Martinez, A.C. Moretti, M. Mulato, *Thin Solid Films*, vol. 317 (1998), p. 133.
- [77] E.G. Birgin, J.M. Martinez, I. Chambouleyron, *Tech. Dig. Ser.-Opt. Soc. Am.*, vol. 9 (1998), p.132.
- [78] E.G. Birgin, I. Chambouleyron, J.M. Martinez, *J. Comput. Phys.*, vol. 151 (1999), p. 862.
- [79] M. Mulato, I. Chambouleyron, E.G. Birgin, J.M. Martinez, *Appl. Phys. Lett.*, vol. 77 (2000), p.2133.
- [80] E.G. Birgin, I.E. Chambouleyron, J.M. Martinez, S.D. Ventura, *Applied Numerical Mathematics*, vol. 47 (2003), p. 109.
- [81] P. Drude, *Ann. Phys.*, vol. 32 (1887), p. 584.
- [82] K.Vedam, *Thin Solid Films*, vol. 313-314 (1998), p. 1.
- [83] E.A. Irene, *Thin Solid Films*, vol. 233 (1993), p. 96
- [84] D.E. Aspnes, 3rd International Conference on Spectroscopic Ellipsometry, Vienna, July 6-11, 2003.
- [85] D.E Aspnes, *Optical Properties of Solids: New Developments*, edited by B.O. Seraphin (North Holland, Amsterdam, 1976), p. 801.

- [86] D.E Aspnes, Handbook of Optical Constants of Solids (Academic Press, 1985), p.89.
- [87] D.E. Aspnes, P.S. Hauge, J. Opt. Soc. Am., vol. 66 (1976), p. 949---R.W. Collins, Rev. Sci. Instrum., vol. 61 (1990), p. 2029.
- [88] S. Huard, Polarization of Light, John Wiley&Sons, Paris, 1996.
- [89] D.S. Kliger, J.W. Lewis, C.E. Randall, Polarized Light in Optics and Spectroscopy, Academic Press, San Diego, 1990.
- [90] D.E. Aspnes, Thin Solid Films, vol. 89 (1982), p. 249.
- [91] V.S. Nguyen, in: Handbook of Thin-Film Deposition Processes and Techniques, ed. by K.K. Schuegraf, Noyes Publications, William Andrew Publishing, New York (1988).
- [92] D.C. Shram, J.A.M. van der Mullen, M.C.M. van de Sanden, Plasma Phys. Control. Fusion, vol.36 (1994), p. B65.
- [93] W.J. Goedheer, Plasma Sources Sci. Technol., vol. 9 (2000), p. 507.
- [94] N. St J. Braithwaite, Plasma Sources Sci. Technol., vol. 9 (2000), p. 517.
- [95] Bayram Katircioğlu, Radio Frequency Plasma Lecture Notes, unpublished.
- [96] Orhan Özdemir, Ph.D. Thesis, Middle East Technical University, 2004.
- [97] W. Luft, Y.S. Tsuo, Hydrogenated Amorphous Silicon Alloy Deposition Processes, Marcel Dekker Inc., New York (1993).
- [98] İ. Atılgan, Ph.D. Thesis, Middle East Technical University, 1993.
- [99] Lambda 2 UV/VIS Spectrometer Operator's Manual, Bodenseewerk Perkin-Elmer GmbH, 1990.
- [100] M.D. Seyer, RS-232 Made Easy, Prentice Hall, 1984.
- [101] S.Y. Kim, L. Spanos, E.A. Irene, J. Korean Phys. Soc., vol. 28 (1995), p. 420.
- [102] D. Goncalves, E.A. Irene, Quim. Nova, vol. 25 (2002), p. 794.
- [103] L. Spanos, Phd Thesis, 1994, Chem. Dept., Univ. North Carolina at Chapel Hill.

- [104] P.S. Hauge, F.H. Dill, IBM J. Res. Develop., vol. 17, (1973), p. 472.
- [105] W. Budde, Appl. Opt., vol. 1 (1962), p. 201.
- [106] B.D. Cahan, R.F. Spanier, Surf. Sci., vol. 16 (1969), p. 166.
- [107] D.E. Aspnes, A.A. Studna, Appl. Opt., vol. 14 (1975), p. 220.
- [108] D.E. Aspnes, A.A. Studna, Phys. Rev. B, vol. 27 (1983), p. 985.
- [109] C.M. Herzinger, B. Johs, W.A. McGahan, J.A. Woollam, W. Paulson, J. Appl. Phys., vol. 83 (1998), p. 3323.
- [110] <http://www.spectra.com/sopra.html>.
- [111] D.E. Aspnes, Thin Solid Films, vol. 89 (1982), p. 249.
- [112] D. Poelman, P.F. Smet, J. Phys D: Appl. Phys, vol. 36 (2003), p. 1850.
- [113] R. Jacobsson, in Progress in Optics, ed. by E.Wolf, (Noth-Holland, Amsterdam, 1965), Vol. 5, p.247.
- [114] H. Bremmer, The Theory of Electromagnetic Waves, ed. by M. Kline, Dover Publications (New York), (1951), p. 105.
- [115] A.V. Tikhonravov, M.K. Trubetskov, B.T. Sullivan, J.A. Dobrovolski, Applied Optics, vol. 36 (1997), p. 7188.
- [116] J.P. Borgogno, B. Lazarides, E. Pelletier, Appl. Opt., vol. 21 (1982), p. 4020.
- [117] G. Myburg, R. Swanepoel, Journal of non-Crystalline Solids, vol. 89 (1987), p. 13.
- [118] M. Montecchi, R.M. Montereali, E. Nichelatti, Thin Solid Films, vol. 396 (2001), p. 262.
- [119] M. Yamaguchi, K. Morigaki, Philos. Mag B, vol. 79 (1999), p. 387.
- [120] E.C. Freeman, W. Paul, Phys. Rev. B, vol. 20 (1979), p.716.
- [121] M.H. Brodsky, R.S. Title, K. Weiser, F.D. Pettit, Phys. Rev. B, vol. 1 (1970), p. 2632.
- [122] M. Harris, H.A. Macleod, S. Ogura, Thin Solid Films, vol. 57 (1979), p.173.

- [123] W.M.M. Kessels, R.J. Severans, M.C.M. Van de Sanden, D.C. Schram, *J. Non-Cryst. Solids*, vol. 227-230 (1998), p. 133.
- [124] D.Das, S.M. Iftiqar, A.K. Barua, *J. Non-Cryst. Solids*, vol. 210 (1997), p. 148.
- [125] A. Masuda, K. Itoh, K. Matsuda, Y. Yonezawa, M. Kumeda,, T. Shimizu, *J. Appl. Phys.*, vol. 81 (1997), p. 6729.
- [126] J.R. Elmiger, M. Kunst, *Appl. Surf. Sci.*, vol. 103 (1996), p. 11.
- [127] R. Ruther, J. Livingstone, N. Dytlowisky, D. Cohen, *J. Appl. Phys.*, vol 79 (1996), p. 175.
- [128] B. Akaoglu, B. Katircioğlu, İ. Atılgan, *Thin Solid Films*, vol. 437 (2003), p. 257.
- [129] J. Robertson, *Phil. Mag. B*, vol. 66 (1992), p. 615.
- [130] J. Sotiropoulos and G. Weiser, *J. Non-Cryst. Solids*, vol. 97&98 (1987), p. 1087.
- [131] T. Stapinski, G. Ambrosone, U. Coscia, F. Giorgis and C. F. Pirri, *Physica B*, vol. 254 (1998), p. 99.
- [132] J.M. Dieguez Campo, M. Lenski, F.J. Comes, *Thin Solid Films*, vol. 323 (1998), p. 115.
- [133] W.K. Choi, Y.M. Chan, C.H. Ling and Y. Lee, *J Appl. Phys* 77 (1995), p. 827.
- [134] F. Giorgis, F. Giuliani, C.F. Pirri, E. Tresso, J.P. Conde and V. Chu, *J. Non-Cryst. Solids*, vol. 227-230 (1998), p. 465.
- [135] R. Zedlitz, E. Lotter and M. Heintze, *J. Non-Cryst. Solids*, vol. 164-166 (1993), p. 1031.
- [136] Z. Yu, J. Pereyra and M.N.P. Correno, *Solar Energy Materials & Solar Cells*, vol. 66 (2001), p. 155.
- [137] G.E. Jellison, *Thin Solid Films*, vol. 313-314 (1998), p. 33.
- [138] A.R. Forouhi and I. Bloomer, *Phys. Rev. B*, vol. 34 (1986), p. 7018.
- [139] S.A. Alterovitz, N. Savvides, F.W. Smith and J.A. Woollam, in: E. D. Palik (Ed.), *Handbook of Optical Constants of Solids II*, Academic Press, New York, 1991, p. 837.

- [140] W.A. McGahan, T. Makovicka, J. Hale and J.A. Woolam, *Thin Solids Films*, vol. 253 (1994), p. 57.
- [141] T. Yamaguchi, Y. Kaneko, A.H. Jayatissa, A. Aoyama, A. V. Zotov, V.G. Lifshits, *J. Appl. Phys.* 77 (1995) 4673.
- [142] T. Yamaguchi, Y. Kaneko, A.H. Jayatissa, M. Aoyama, *Thin Solid Films* vol. 279 (1996), p. 174.
- [143] G.E. Jellison, Jr. and F.A. Modine, *Appl. Phys. Lett.*, vol. 69 (1996), p. 371.
- [144] G.E. Jellison, Jr. and F.A. Modine, *Appl. Phys. Lett.*, vol. 69 (1996), p. 2137.
- [145] D. Franta, I. Ohlidal, M. Frumar, J. Jedelsky, *Appl. Surf. Sci.*, vol. 175-176 (2001), p. 555.
- [146] D. Franta, L. Zajickova, I. Ohlidal, J. Janca, K. Veltruska, *Diamond Relat. Mater.*, vol. 11 (2002), p. 105.
- [147] F. Wooten, *Optical Properties of Solids*, Academic Press, New York, 1972.
- [148] S.H. Wemple, M. DiDomenico, *Phys. Rev. B*, vol. 3 (1971), p. 1338.
- [149] S.H. Wemple, *Phys. Rev. B*, vol. 7 (1973), p. 3767.
- [150] J. Leng, J. Opsal, H. Chu, M. Senko, D.E. Aspnes, *Thin Solid Films*, vol. 313-314 (1998), p. 132.
- [151] M. Gorn, P. Lechner, H.D. Mohring, H. Rubel, B. Scheppat, N. Kniffler, *Philos. Mag. B*, vol. 64 (1991), p. 101.
- [152] A. Hadjadj, P. St'ahel, P.R.I. Cabarrocas, V. Paret, Y. Bounouh, J. C. Martin, *J. Appl. Phys.*, vol. 83 (1998), p. 830.
- [153] P. Roman, *Advanced Quantum Theory*, Addison-Wesley, Reading, Massachusetts, 1965, p. 200.
- [154] F. Demichelis, G. Crovini, F. Giorgis, C. F. Pirri, E. Tresso, V. Rigato, U. Coscia, G. Ambrosone, S. Catalanotti, P. Rava, *Solid State Commun.*, vol. 98 (1996), p. 617.

- [155] D. E. Sweenor, S. K. O’Leary, B. E. Foutz, *Solid State Communications*, vol. 110 (1999), p. 281.
- [156] R. Carius, *Phil. Mag. B*, vol. 80 (2000), p. 741.
- [157] I. Ferreira, M. E. V. Costa, L. Pereira, E. Fortunato, R. Martins, A. R. Ramos, M. F. Silva, *Appl. Surf. Sci.*, vol. 184 (2000), p. 8.
- [158] G. Ambrosone, U. Coscia, S. Ferrero, F. Giorgis, P. Mandracci, C. F. Pirri, *Phil. Mag. B*, vol. 82 (2002), p. 35.
- [159] A.B. Djurusic, E.H. Li, *Appl. Opt.*, vol. 37 (1998), p. 5291.
- [160] I. Solomon, M. P. Schmidt, C. Senemaud, M. D. Khodja, *Phys. Rev B*, vol. 38 (1988), p. 13263.
- [161] F. Giorgis, F. Giuliani, C.F. Pirri, V. Rigato, E. Tresso, S. Zandolin, *EMIS Datareviews Series No. 19, INSPEC, London, 1998*, p. 74.
- [162] S. Lin, S. T. Chang, *J. Phys. Chem. Solids*, vol. 59 (1998), p. 1399.
- [163] C. Chu, J.P. Conde, J. Jarego, P. Brogueira, J. Rodriguez, N. Barradas, J. C. Soares, *J. Appl. Phys*, vol. 78 (1995), p. 3164.
- [164] P. A. Longeway, in: J. I. Pankove (Ed.), *Semiconductor and Semimetals 21 part A*, Academic Press, London, 1984, p. 179.
- [165] A. Tabaka, H. Kamijo, Y. Suzuoki, T. Mizutani, *J. of Non-Cryst. Solids*, vol. 227-230 (1998), p. 456.
- [166] H. Kobayashi, M. Shen, A. T. Bell, *J. Macromol. Sci.-Chem*, vol. A8 (1974), p. 373.
- [167] I. Ferreira, V. Silva, H. Aguas, E. Fortunato, R. Martins, *Appl. Surf. Sci.*, vol. 184 (2001), p. 60.
- [168] Y. Catherine, G. Turban, B. Grolleau, *Thin Solid Films*, vol. 76 (1981), p. 23.
- [169] G. Turban, Y. Catherine, B. Grolleau, *Thin Solid Films*, vol. 67 (1980), p. 309.
- [170] A. Gallagher, *J. Appl. Phys.*, vol. 63 (1988), p. 2406.
- [171] D. G. Dagel, C. M. Mallouris, J. R. Doyle, *J. Appl. Phys.*, vol 79 (1996), p. 8735.

- [172] J. R. Doyle, *J. Appl. Phys.*, vol. 82 (1997), p. 4763.
- [173] T. Fujii, H. S. Kim, *Chem. Phys. Lett.*, vol. 268 (1997), p. 229.
- [174] Y. Catherine, G. Turban, *Thin Solid Films*, vol. 60 (1979), p. 193.
- [175] N. Al-Rubaiey, R. Walsh, *J. Phys. Chem.*, vol. 98 (1994), p. 5303.
- [176] J. M. Jasinski, R. Becerra, R. Walsh, *Chem. Rev.*, vol. 95 (1995), p. 1203.
- [177] A. Matsuda, K. Tanaka, *J. Non-Cryst. Solids*, vol. 97&98 (1987), p. 1367.
- [178] L. R. Tessler, I. Solomon, *Phys. Rev. B*, vol. 52 (1995), p. 10962.
- [179] I. Solomon, *Applied Surface Science*, vol. 184 (2001), p. 3.
- [180] A. Roth, F.J. Comes, W. Beyer, *Thin Solid Films*, vol. 293 (1997), p. 83.
- [181] K. Tanaka, E. Maruyama, T. Shimada, H. Okamoto, T. Sato, *Amorphous Silicon*, John Wiley&Sons, Chichester, 1999.
- [182] W.M.M. Kessels, A.H.M. Smets, D.C. Marra, E.S. Aydil, D.C. Schram, M.C.M. van de Sanden, *Thin Solid Films*, vol. 383 (2001), p.154.
- [183] A. von Keudell, *Plasma Sources Sci. Technol.*, vol. 9 (2000), p. 455.
- [184] J. Robertson, M.J. Powell, *Thin Solid Films*, vol. 337 (1999), p. 32.
- [185] C.C. Tsai, J.C. Knight, G. Chang, B. Wacker, *J. Appl. Phys.*, vol. 59 (1986), p. 2998.
- [186] R. Dewarrat, J. Robertson, *Thin Solid Films*, vol. 427 (2003), p.11.
- [187] J.C. Knights, R.A. Lujan, M.P. Rosenblum, R.A. Street, D.K. Biegelsen, J.A. Reimer, *Appl. Phys. Lett.*, vol. 38 (1981), p. 331.
- [188] F.J. Kampas, *J. Appl. Phys.*, vol. 53 (1982), p.6408.
- [189] D. Kruangam, in “Amorphous and Microcrystalline Semiconductor Devices II: Optoelectronic Devices”, Ed. by J. Kanicki, Artech House, London, (1991).
- [190] N. Inagaki, *Plasma Surface Modificaiton and Plasma Polymerization*, Technomic Publishing Company Inc., Basel (1996).
- [191] H. Kobayashi, A.T. Bell, M. Shen, *Macromolecules*, vol. 7 (1974), p. 277.

- [192] F. Giorgis, C.F. Pirri, E. Tresso, P. Rava, *Philosophical Magazine B*, vol. 75 (1997), p. 471.
- [193] J. Robertson, *J. Non-Crystalline Solids*, vol. 137-138 (1991), p. 825.
- [194] M. Koos, *Diamond and Related Materials*, vol. 8 (1999), p. 1919.
- [195] T.Schwartz-Sellinger, A. von Keudell, W. Jacob, *J. Appl. Phys.*, vol. 86 (1999), p.3988.
- [196] A. von Keudell, M. Meier, C. Hopf, *Diamond and Related Materials*, vol. 11 (2002), p.969.
- [197] A. von Keudell, W. Jacob, *J. Appl. Phys*, vol. 79 (1996), p. 1092.
- [198] A. von Keudell, T. Schwarz-Selinger, M. Meier, W. Jacob, *Appl. Phys. Lett.*, vol. 76 (2000), p. 676.
- [199] C. Hopf, T. Schwarz-Selinger, W. Jacop, A. von Keudell, *J. Appl. Phys.*, vol. 87 (2000), p. 2719.
- [200] Y. Catherine, A. Zamouche, J. Bullo, M. Gauthier, *Thin Solid Films*, vol. 109 (1983), p. 145.
- [201] A. Matsuda, T. Yamaoka, S. Wolff, M. Koyama, Y. Imanishi, H. Kataoka, H. Matsuura, K. Tanaka, *J. Appl. Phys.*, vol. 60 (1986), p. 4025.
- [202] A.V. Tikhonravov, M.K Trubetskov, *OptiChar Software*, <http://www.optilayer.com>, Version 4.13, 2002.
- [203] M.A. Afromowitz, *Solid State Communications*, vol. 15 (1974), p.59.
- [204] B.G. Martin, R.F. Wallis, *Solid State Communications*, vol. 21 (1977), p. 21.
- [205] M. Erman, J.B. Theeten, P. Chambon, S.M. Kelso, D.E. Aspnes, *J. Appl. Phys.*, vol. 56 (1984), p. 2664.
- [206] D. Kuhman, S. Grammatica, F. Jansen, *Thin Solid Films*, vol. 177 (1989), p. 253.
- [207] G. Ambrosone, U. Coscia, S. Lettieri, P. Maddalena, C. Privato, S. Ferrero, *Thin Solid Films*, 403-404 (2002), p.349.

- [208] A. Skumanich, A. Frova, N.M. Amer, *Solid State Communications*, vol. 54 (1985), p. 597.
- [209] R.S. Sussman, R. Ogden, *Philos. Mag. B*, vol. 44 (1981), p. 137.
- [210] K. Mui, D.K. Basa, F.W. Smith, R. Corderman, *Phys. Rev. B*, vol. 35 (1987), p. 8089.
- [211] W. Siebert, R. Carius, W. Fuhs, K. Jahn, *Phys. Stat. Sol. (b)*, vol. 140 (1987), p. 311.
- [212] J. Sotiropoulos, G. Weiser, *J. Non-Cryst. Solids*, vol. 92 (1987), p. 95.
- [213] E. Pascual, J.L. Andujar, J.L. Fernandez, E. Bertran, *Diam. and Rel. Mat.*, vol. 4 (1995), p. 1205.
- [214] B. Racine, A.C. Ferrari, N.A. Morrison, I. Hutchings, W.I. Milne, J. Robertson, J. *Appl. Phys.*, vol. 90 (2001), p. 5002.
- [215] J. Bullot, M.P. Schmidt, *Phys. Stat. Sol. (b)*, vol. 143 (1987), p.345.
- [216] P.I. Rovira, F. Alvarez, *Phys. Rev. B*, vol. 55 (1997), p. 4426.
- [217] J. Chui, Rusli, S.F. Yoon, E.J. Teo, M.B. Yu, K. Chew, J. Ahn, Q. Zhang, T. Osipowicz, F. Watt, *J. Appl. Phys.*, vol. 89 (2001), p. 6153.
- [218] N.F. Mott, E.A. Davis, *Electronic Processes in Non-Crystalline Solids*, 2nd ed., Clarendon Press, Oxford, 1979.
- [219] S.Pascarelli, F. Boscherini, S. Mobilio, F. Evangelisti, *Phys Rev. B*, vol.45 (1992), p. 1650.
- [220] G. Fanchini, S.C. Ray, A.Tagliaferro, *Diamond and Related Materials*, vol. 12 (2003), p. 891.
- [221] A. R. Zanatta, M. Mulato, I. Chambouleyron, *J. Appl. Phys*, vol 84 (1998), p. 5184.
- [222] M. De Seta, S.L. Wang, P. Narducci, F. Evangelisti, *J. Non-Cryst. Solids*, vol. 137-138 (1991), p. 851.

- [223] A. Frova, A. Selloni, in: *Tetrahedrally-Bonded Amorphous Semiconductors*, ed. by D. Adler, H. Fritzsche, Plenum Press, New York, 1985.
- [224] G. Ambrosone, P. Capezzuto, S. Catalanotti, U. Coscia, S. Mormone, *Philosophical Magazine B*, vol. 80 (2000), p.497.
- [225] G. Ambrosone, V. Ballarini, U. Coscia, S. Ferrero, F. Giorgis, P. Maddalena, A. Patelli, P. Rava, V. Rigato, *Thin Solid Films*, vol. 427 (2003), p. 279.
- [226] Y. Katayama, K. Usami, T. Shimada, *Philos. Mag. B*, vol. 43 (1981), p.283.
- [227] F. Demichelis, C.F. Pirri, E. Tresso, T. Stapinski, *J. Appl. Phys.*, vol. 71 (1992), p.5641.
- [228] D. R. McKenzie, *J. Phys. D:Appl. Phys.*, vol. 18 (1985), p.1935.
- [229] R.A. C. M. M. van Swaaij, A.J.M. Berntsen, W.G.J.H.M. van Sark, H. Herremans, J. Bezemer, W.F. van der Weg, *J. Appl. Phys.*, vol. 76 (1994), p.251.
- [230] H. Herremans, Grevendonk, R.A. C. M. M. van Swaaij, W.G.J.H.M. van Sark, A.J.M. Berntsen, W.M. Arnold Bik, J. Bezemer, *Philos. Mag. B*, vol.66 (1992), p. 787.
- [231] G. Leo, G. Galluzzi, G. Guattari, R. Viicenzoni, F. Demichelis, G. Ciovini, C.F. Pirri, E. Tresso, *J. Non.Cryt. Solids*, vol. 164-166 (1993), p. 1035.
- [232] F. Demichelis, F. Giorgis, C.F. Pirri, E. Tresso, *Phil. Mag. A*, vol. 72 (1995), p. 913.
- [233] H. Weider, M. Cardona, C.R. Guarnieri, *Phys. Stat. Solid. B.*, vol. 62 (1979), p. 99.
- [234] Y. Tawada, K. Tsuge, M. Condo, H. Okamoto, Y. Hamakawata, *J. Appl. Phys.*, vol. 53 (1982), p. 5273.
- [235] G. Lucovsky, *Solid State Communications*, vol. 29 (1979), p. 571.
- [236] B.K. Agrawal, *J. Non-Cryst. Solids*, vol. 114 (1989), p. 519.
- [237] Y.M. Li, B.E. Fieselmann, *Appl. Phys Lett.*, vol. 59 (1991), p. 1720.
- [238] G. Foti, *Appl. Surf. Sci.*, vol. 184 (2001), p. 20.

- [239] K. Chew, Rusli, S.F. Yoon, V. Ligatchev, E. J. Teo, T. Osipowicz, F. Watt, J. Appl. Phys., vol. 92 (2002), p. 2937.
- [240] N.F. Mott, Philos. Mag., vol. 19 (1969), p.835.
- [241] G. Srinivasan, A.S. Nigavekar, Materials Science and Engineering B, vol.8 (1991), p. 23.
- [242] D. Jousse, E. Bustarret, A. Deneuve, J.P. Stoquert, Physical Review B, vol. 34 (1984), p. 7031.
- [243] J. Ristein, G. Weiser, Solar Energy Materials, vol. 12 (1985), p. 221.
- [244] L. Zajickova, K. Veltruska, N. Tsud, D. Franta, Vacuum, vol. 61 (2001), p. 269.
- [245] A. Lehner, G. Steinhoff, M.S. Brandt, M. Eickhoff, M. Stutzmann, J. Appl. ., vol. 94 (2003), p. 2289.
- [246] D.E. Aspnes, J.B. Theeten, F. Hottier, Phys. Rev. B, vol. 20 (1979), p. 3292.
- [247] H.R. Philipp, in Handbook of Optical Constants of Solids, ed. by E.D. Palik, Academic, New York, 1985, p. 749.
- [248] C.M. Herzinger, P.G. Snyder, B. Johs, J.A. Woollam, J. Appl. Phys., vol. 77 (1995), p. 1715.
- [249] Ph. J. Roussel, J. Vanhellefont, H.E. Maes, Thin Solid Films, vol. 234 (1993), p. 423.
- [250] H. Fujiwara, J. Koh, P. I. Rovira, R.W. Collins, Phys. Rev. B, vol. 61 (2000), p. 10832.
- [251] J.D. Lee, B.C. Shim, H.S. Uh, B. Park, IEEE Electron Device Letters, vol. 20 (1999), p.215.
- [252] K.L. Westra, D.J. Thomson, Thin Solid Films, vol. 257 (1995), p. 15.
- [253] J.M. Elson, J.M. Bennett, J. Opt. Soc. Am., vol. 69 (1979), p. 31—J.M. Elson, J.M. Bennett, Appl. Opt., vol. 34 (1995), p. 201.
- [254] Angela Duparre, J. Ferre-Borrull, S. Gliech, G. Nothi, J. Steinert, J.M. Bennett, Appl. Opt., vol. 41 (2002), p. 154.

- [255] J. Koh, Y. Lu, C.R. Wronski, Y. Kuang, R.W. Collins, T.T. Tsong, Y.E. Strausser, *Appl. Phys. Lett.*, vol. 68 (1996), p. 1297.
- [256] J.D. Lee, B.C. Shim, H.S. Uh, B. Park, *IEEE Electron Device Letters*, vol. 20 (1999), p.215.
- [257] Z.Y. Wu, B. Drevillon, M. Fang, A. Gheorghiu, C. Senemaud, *J. Non-Cryst. Solids*, vol. 137-138 (1991), p. 863.
- [258] M.H. Brodsky, M. Cardona, J.J. Cuomo, *Physical Review B*, vol. 16 (1977), p. 3556.
- [259] *Handbook of X-Ray Photoelectron Spectroscopy*, Perkin Elmer Corporation, Physical Electronics Division.
- [260] Skoog, Leary, *Principles of Instrumental Analysis*, 4th Ed., Saunders College Pub., 1992.
- [261] J.M. Hollas, *Modern Spectroscopy*, 3rd Ed., J. Wiley, New York, 1996.
- [262] *Spectroscopy*, Ed. by B.P. Straughan, S. Walker, Chapman and Hall, New York, 1976.
- [263] A. Tabata, S. Fujii, Y. Suzuoki, T. Mizutani, M. Ieda, *J. Phys. D: Appl. Phys.*, vol. 23 (1990), p. 316.
- [264] W.K. Choi, T.Y. Ong, L.S. Tan, F.C. Loh, K.L. Tan, *J. Appl. Phys.*, vol. 83 (1998), p. 4978.
- [265] J.-W.He, X. Xu, J.S. Corneille, D.W. Goodman, *Surface Science*, vol. 279 (1992), p. 119.
- [266] A. Toneva, Ts. Marinova, V. Krastev, *Journal of Luminescence*, vol. 80 (1999), p. 455.
- [267] F. Ibrahim, J.I.B. Wilson, P. John, A.G. Fitzgerald, A. Cook, *J. Non-Cryst. Solids*, vol. 175 (1994), p.195.
- [268] Z.Y. Wu, B. Drevillon, M. Fang, A. Gheorghiu, C. Senemaud, *J. Non-Cryst. Solids*, vol. 137-138 (1991), p. 863.

[269] I.D. Welsh, P.M.A. Sherwood, *Physical Review B*, vol. 40 (1989), p. 6386.

[270] J. Dupin, D. Gonbeau, P. Vinatier, A. Levasseur, *Phys. Chem. Chem. Phys.*, vol. 2 (2000), p. 1319.

VITA

Bariş Akaoğlu was born in Bursa on May 14, 1974. He received his B.S. and M.S. degree in Physics from the Middle East Technical University in 1996 and 1998, respectively. Since 1996 he has been a teaching/research assistant in the Department of Physics. He worked for 3 months as a visiting researcher in University of North Carolina at Chapel Hill in 2002. His main area of interest is characterization of silicon based amorphous thin films for optoelectronic applications by transmittance, reflectance and ellipsometry measurements.